Development and application of multi-atlas attenuation correction for brain imaging with simultaneous PET-MR

Inès Mérida

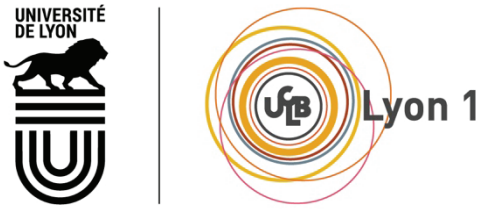

N°d'ordre NNT : 2017LYSE1116

THESE de DOCTORAT DE L'UNIVERSITE DE LYON
opérée au sein de
l'Université Claude Bernard Lyon 1

Ecole Doctorale N° 476
Neurosciences et cognition

Spécialité de doctorat : Neurosciences

Soutenue publiquement le 23/06/2017, par:

Inés Mérida

Development and application of multi-atlas attenuation correction for brain imaging with simultaneous PET-MR

Devant le jury composé de:

Irène Buvat	Directeur de recherche (CNRS)	Rapporteur
Stefaan Vandenberghe	Professeur (University of Gent)	Rapporteur
Carole Lartizien	Chargée de recherche (CNRS)	Examinateur
Marine Soret	Physicienne médicale (AP-HP)	Examinateur
Luc Zimmer	Professeur (Université Lyon1, HCL)	Examinateur
Olivier Bertrand	Directeur de recherche (INSERM)	Directeur de thèse
Nicolas Costes	Ingénieur de recherche (CNRS)	Co-directeur
Alexander Hammers	Professeur (King's College London)	Co-directeur
Matthieu Lepetit-Coiffé	Ingénieur (Siemens Healthineers)	Invité

UNIVERSITE CLAUDE BERNARD - LYON 1

Président de l'Université	M. le Professeur Frédéric FLEURY
Président du Conseil Académique	M. le Professeur Hamda BEN HADID
Vice-président du Conseil d'Administration	M. le Professeur Didier REVEL
Vice-président du Conseil Formation et Vie Universitaire	M. le Professeur Philippe CHEVALIER
Vice-président de la Commission Recherche	M. Fabrice VALLÉE
Directeur Général des Services	M. Alain HELLEU

COMPOSANTES SANTE

Faculté de Médecine Lyon Est – Claude Bernard	Directeur : M. le Professeur J. ETIENNE
Faculté de Médecine et de Maïeutique Lyon Sud – Charles Mérieux	Directeur : Mme la Professeure C. BURILLON
	Directeur : M. le Professeur D. BOURGEOIS
Faculté d'Odontologie	Directeur : Mme la Professeure C. VINCIGUERRA
Institut des Sciences Pharmaceutiques et Biologiques	Directeur : M. le Professeur Y. MATILLON
Institut des Sciences et Techniques de la Réadaptation	Directeur : Mme la Professeure A-M. SCHOTT
Département de formation et Centre de Recherche en Biologie Humaine	

COMPOSANTES ET DEPARTEMENTS DE SCIENCES ET TECHNOLOGIE

Faculté des Sciences et Technologies	Directeur : M. F. DE MARCHI
Département Biologie	Directeur : M. le Professeur F. THEVENARD
Département Chimie Biochimie	Directeur : Mme C. FELIX
Département GEP	Directeur : M. Hassan HAMMOURI
Département Informatique	Directeur : M. le Professeur S. AKKOUCHE
Département Mathématiques	Directeur : M. le Professeur G. TOMANOV
Département Mécanique	Directeur : M. le Professeur H. BEN HADID
Département Physique	Directeur : M. le Professeur J-C PLENET
UFR Sciences et Techniques des Activités Physiques et Sportives	Directeur : M. Y.VANPOULLE
Observatoire des Sciences de l'Univers de Lyon	Directeur : M. B. GUIDERDONI
Polytech Lyon	Directeur : M. le Professeur E.PERRIN
Ecole Supérieure de Chimie Physique Electronique	Directeur : M. G. PIGNAULT
Institut Universitaire de Technologie de Lyon 1	Directeur : M. le Professeur C. VITON
Ecole Supérieure du Professorat et de l'Education	Directeur : M. le Professeur A. MOUGNIOTTE
Institut de Science Financière et d'Assurances	Directeur : M. N. LEBOISNE

Remerciements

Ce travail de thèse a été mené au CERMEP, dans le cadre du projet LILI (Lyon Integrated Life Imaging), et financé par une bourse CIFRE issue de la collaboration entre le CERMEP et Siemens Healthcare.

Je remercie sincèrement mes trois directeurs de thèse, Olivier Bertrand, Nicolas Costes et Alexander Hammers pour leur encadrement chaleureux et encourageant pendant ces trois dernières années. Merci Olivier de m'avoir accueille au sein de ton équipe DYCOG, au CRNL. Merci de ton écoute et tes conseils. Nicolas, Alexander, merci pour la confiance que vous m'avez accordée dès mon arrivée. Votre disponibilité et votre soutien ont été précieux pour moi. Vous m'avez transmis votre philosophie de travail avec vos approches différentes et pourtant si complémentaires l'une de l'autre, elles continuent à m'inspirer dans mes recherches aujourd'hui**.** J'espère avoir encore la chance de travailler avec vous dans les années à venir.

Je souhaite également remercier les membres de mon jury, Irène Buvat et Stefaan Vandenberghe, Carole Lartizien, Marine Soret et Luc Zimmer d'avoir accepté de lire et juger mes travaux de thèse.

Ce travail n'aurait pas abouti sans l'aide essentielle d'Anthonin Reilhac et de Jérôme Redouté. Merci de m'avoir fait profiter de votre expertise pointue en imagerie TEP. C'est un réel plaisir de travailler avec vous !

Je tiens vivement à remercier Marjorie Villien. Merci pour tes conseils qui m'ont aidé à visualiser mon projet de thèse dans sa globalité et à me projeter toujours vers l'avant. Ma thèse au quotidien n'aurait pas été aussi amusante sans nos échanges scientifiques et psychologiques et bien-sûr sans nos fous rires, au labo et en conférence. Ravie de t'avoir rencontrée !

Un grand merci à Zacharie, Nikos, Justine, Flora pour avoir rendu ces dernières années à LILI si agréables.

Je remercie également l'ensemble de l'équipe du CERMEP pour leur accueil chaleureux durant ces années thèse.

Merci à Thomas Troalen, Matthieu Lepetit-Coiffé, Anne Chevalier et Nicolas Maurice pour les heures de formation et les échanges enrichissants autour de l'IRM-TEP.

Mes remerciements vont aussi à Clara Fonteneau et Marie-Françoise Suaud-Chagny de l'équipe PSYR2 du CRNL, avec qui j'ai eu l'opportunité de collaborer sur les premières données cérébrales d'IRM-TEP simultanée acquises au CERMEP.

Je n'oublie pas l'équipe de King's College London, Colm McGinnity et Jane MacKewn, pour leur aide dans la validation de la méthode et l'intérêt qu'ils ont porté à ce projet.

Merci à Natalia, Marie-Pierre et José-Luís, ma petite famille qui m'a toujours soutenue et encouragée.

Merci à toi, Emmanuel, pour tout ce que l'on vit ensemble.

Abstract

Simultaneous PET-MR imaging brings new perspectives for understanding many aspects of brain function. To achieve PET-MR's full potential, accurate brain attenuation correction (AC) is required for absolute PET quantification. In PET-MR scanners, radiodensity maps are not directly available unlike in PET/CT, and the attenuation map has to be derived from the MR data (MRAC methods). In this thesis, I have developed a multi-atlas procedure that produces a subject-specific μ-map for brain imaging (*MaxProb*) via multiple registrations of CT-MR atlas pairs to an MR target. The solution proposed only requires a T1-weighted MRI of the subject, commonly acquired in clinical and research protocols, and a CT-MR atlas database.

The *MaxProb* method permits generating pseudo-CT images for brain MRAC with high accuracy. Results obtained show very good performance of the method and a bias in reconstructed PET of less than 2%. I have also demonstrated for the first time that an inaccurate attenuation correction map, combined with inhomogeneous spatial tracer distribution as is regularly encountered in dynamic brain PET, can lead to a non-constant bias of the activity measure across time, and this can distort kinetic parameter estimation. *MaxProb* AC is not affected by this phenomenon. Accurate quantification is also achieved with *MaxProb* on physiological parameters estimated from kinetic modelling, even when cerebellum (surrounded by bone) is used as reference region. In a simulation study, I have shown that compared to a standard approach (*UTE*), *MaxProb* multi-atlas MRAC enhances sensitivity to detect physiological variations in binding parameters, opening the way for new dynamic PET studies on simultaneous PET-MR systems.

Résumé

L'imagerie simultanée IRM-TEP ouvre de nouvelles perspectives pour l'exploration *in vivo* des fonctions cérébrales. Pour une quantification du signal de tomographie par émission de positons, il est indispensable de corriger l'atténuation tissulaire des photons. En l'absence de mesure tomodensitométrique en IRM-TEP, les cartes de radiodensité ne sont pas disponibles. Il est nécessaire de trouver une méthode fiable et exacte pour générer une carte d'atténuation du sujet à partir des données disponibles TEP ou IRM. Dans cette thèse, j'ai développé une technique qui génère une carte d'atténuation propre à un sujet par une approche multi-atlas (*MaxProb*) passant par de multiples recalages de paires d'atlas IRM-CT. Cette méthode utilise uniquement l'image IRM T1 du sujet, couramment acquise dans les protocoles cliniques et de recherche, ainsi qu'une base de données d'atlas IRM-CT.

L'évaluation de *MaxProb* montre de très bonnes performances, le biais de quantification de l'image TEP étant réduit à moins de 2% pour des images TEP reconstruites. Cette évaluation pratiquée sur une acquisition dynamique TEP a en outre montré, pour la première fois, qu'une carte d'atténuation imparfaite, combinée à une distribution spatiale du traceur inhomogène au cours du temps (comme c'est le cas dans la plupart des études dynamiques), peut produire un biais non-constant des cinétiques TEP. Cela impacte les paramètres biologiques estimés par modélisation sur les cinétiques TEP. La méthode *MaxProb* n'est cependant pas affectée par ce phénomène. *MaxProb* fournit une quantification fiable des paramètres physiologiques estimés par modélisation même lorsque le cervelet (entouré par les os du crâne) est utilisé comme région de référence. Mon évaluation a aussi porté sur la reproduction par simulation d'une étude réaliste d'imagerie TEP d'une décharge dynamique d'un neurotransmetteur. Par rapport à la méthode de correction d'atténuation standard (UTE), *MaxProb* améliore la sensibilité de détection des variations physiologiques, même faibles. Ceci ouvre la voie à de nouveaux protocoles d'imagerie dynamique et simultanée en IRM-TEP, augmentant la puissance de détection, et réduisant les nombres de sujets nécessaires à la mise en évidence d'un phénomène neurophysiologique ou d'un dysfonctionnement physiopathologique.

Contents

Introduction

In vivo tomographic imaging is a powerful tool to explore brain anatomy and study brain function of living organisms. Various imaging modalities have been developed and refined in the last decades, in particular single-photon emission computed tomography (SPECT), positron emission tomography (PET), and magnetic resonance imaging (MRI). These tools are used to understand neuronal mechanisms involved in basic functions and cognitive processes, characterize pathophysiological functions, and elaborate clinical diagnoses. Increasing our knowledge about cerebral dysfunction opens the possibility to find appropriate treatments.

Besides tomographic imaging, brain neuronal activity can be explored by the neurophysiological techniques electroencephalography (EEG), which has been among the first approaches introduced for cerebral *in vivo* exploration, and magnetoencephalography (MEG). These techniques record electrical or magnetic activity of the brain with an excellent temporal resolution (few milliseconds) but present a limited spatial resolution to localise the brain areas involved in the neural activity recorded. PET using intra-vascular injection of water labelled with O-15 ($[^{15}O]H_2O$-PET) is another technique that has initially been employed to measure cerebral blood flow (CBF). CBF indirectly reflects brain activity with a better spatial resolution than EEG. However, the development of functional magnetic resonance Imaging (fMRI) that provides another indirect measure of brain activity via the dynamic blood oxygenation with a better compromise between spatial and temporal resolution than PET, has largely replaced PET for this application. Modern applications of PET imaging are based on labelling molecules with a positron-emitting isotope, and thus also offers the capacity to visualise molecular activity of the brain. The isotopes C-11 (~20 min half life) and F-18 (~2h half life) allow the labelling of a large variety of molecules probing metabolic processes, protein deposition, and neurotransmission. PET measures the spatial and temporal distribution of a tracer injected into the venous circulation, with a spatial resolution of few millimetres on a time scale of few seconds. PET is also unique because it produces quantified measurement of the tracer concentration with a sensitivity of pmol/mL. PET allows characterizing physiological mechanisms by modelling the tracer uptake in tissues *via* kinetic modelling, which explains the local use of the tracer. Its neurochemical specificity depends on the tracer used, and can be very high (e.g. probing subtypes of neuroreceptors). $[^{18}F]$FDG is an analogous of endogenous glucose, and provides an image of the cellular glucose metabolism in the whole brain. Measures of glucose metabolism are very widely used clinically for cancer diagnosis and therapeutic evaluation. The expansion of $[^{18}F]$FDG PET

scanning has helped to further develop radiochemistry and pharmacology. A large variety of molecules labelled with positron emitter has been produced, and PET imaging has become a method of reference to study neuroreceptors and synaptic transmission. PET has also been used for the development of new drugs and understanding their mechanism of action. For example, [^{11}C]raclopride, an antagonist at dopaminergic D2 receptors, and with a lower affinity at D3 receptors, produces very specific images widely used for the understanding of physiology and pathophysiology of the dopaminergic system and its functions. Because some receptor subtype expression can be very localized in the brain, PET needs to be associated to a structural image in order to obtain a precise localization of the surrounding brain regions.

In the 2000s, a complementary structural imaging modality, x-ray computed tomography (CT), has been added to PET to overcome PET's deficit in terms of anatomical localisation (Beyer et al., 2000). PET/CT is now part of routine diagnosis, especially in clinical oncology, and also largely used in brain research. In those combined systems, CT and PET images are acquired consecutively. The CT image provides the anatomical information required to localize the tracer uptake, but with a limited contrast in soft tissues. It also fulfils the requirement of measuring tissular radiodensity needed for PET attenuation correction. However, in many applications in the brain imaging context, PET/CT still needs the acquisition of a structural MR image. Ten years later simultaneous PET-MR scanners have emerged (Delso et al., 2011). These new devices combine PET and MR technologies within the same field of view, so both imaging modalities can be acquired simultaneously. MRI ensures high spatial resolution and its excellent soft tissue contrast is particularly interesting to distinguish brain anatomy. In addition to the large panel of structural sequences, MR imaging is a versatile technique that provides functional information. For example, and as mentioned above, MRI allows the measurement of brain activity patterns and oxygen consumption by the means of fMRI. The blood oxygen level dependent (BOLD) signal is commonly associated to neuronal activity in brain, even if the neurovascular mechanisms involved are not completely understood for now. Functional connectivity of brain areas is also studied with MRI via resting-state fMRI. Arterial spin labelling (ASL) is another technique that provides a quantitative measure of cerebral blood flow. MRI can also offer information about structural connectivity using diffusion imaging. Another capability of MR is proton spectroscopy, employed to map metabolites in tissues according to their characteristic resonance frequency.

The development of PET-MR devices represented an important technological challenge, since the photo-multipliers traditionally used in the PET detection system are incompatible with the high field strength of the MRI. This difficulty has been overcome thanks to avalanche photodiodes (APDs) or

highly sensitive silicon photomultipliers (SiPMs). Two commercial systems that allow acquiring simultaneous PET and MRI data are now available: the mMR Biograph (Siemens Healthcare) and the SIGNA PET-MR (General Electrics). The new simultaneous PET-MR scanners have multiplied the possibilities of exploration achievable within only one examination and allow, for the first time, not only multi-modal but also simultaneous acquisition of the two modalities.

However, it must be borne in mind that constraints related to both modalities have now to be considered in a protocol set up. This includes radioprotection measures due to the manipulation of radioactive tracers used in PET and the constraints imposed by the high field strength of the MRI (i.e. use of MR-compatible material). Obvious workflow advantages of hybrid PET-MR are linked to easier organisation of the two examinations (i.e. a single appointment), patient comfort and reduction of radiation exposure, which is particularly interesting for longitudinal studies and paediatric imaging. The intrinsic coregistration between PET and MRI is also a gain brought by the simultaneous PET-MR system. In addition, several applications of PET-MR for clinical diagnosis have been highlighted in the last years (Catana et al., 2012; Werner et al., 2015). Numerous publications discuss the clinical interest of multi-modality in areas such as neuroncology (Bisdas et al., 2013; Pirotte et al., 2006), dementia disorders (Drzezga et al., 2014), neurovascular diseases (Werner et al., 2015), epilepsy (Galazzo et al., 2016) and neuropsychiatric syndromes (Schultz et al., 2012).

Moreover, simultaneous PET-MR appears to be a promising tool for exploring some areas of neuroscience that are not yet completely understood. Interesting studies have started to investigate the relationship between changes in neuroreceptor occupancy measured with PET and changes in brain activity detected with fMRI (Sander et al., 2013; Wey et al., 2014). Other groups have worked on the comparison of brain metabolism (FDG-PET) and brain perfusion (ASL) (Galazzo et al., 2016), on a new method to explore functional changes in brain metabolism (Villien et al., 2014) or on the characterization of brain connectivity (Tomasi et al., 2013) and resting-state networks (Savio et al., 2017). PET-MR is also seen as a tool for the cross-validation of multiple MRI and PET parameters improving data quality of either PET or MRI aided by the other modality (Andersen et al., 2015; Stegger et al., 2012). A significant advance in basic and clinical brain research by way of PET-MR can also be expected from the development of multimodal tracers and probes that can be detected by both modalities (Uppal et al., 2011). Definitively, there is a rising interest for the enormous potential of simultaneous PET-MR, and novel studies related to these new questions are emerging.

From a methodological point of view, PET-MR also opens interesting perspectives. Some methodological questions benefit from the information provided by the MRI data acquired

simultaneously to PET. This is the case for PET image reconstruction (Tahaei and Reader, 2016), motion correction (Fayad et al., 2016; Manber et al., 2016), correction of partial volume effect (Gutierrez et al., 2012; Hutton et al., 2012; Le Pogam et al., 2013), image-derived input function estimation (Chen et al., 2016; Fung and Carson, 2013; Sari et al., 2015) and new kinetic modelling approaches (Jiao et al., 2016).

However, other methodological aspects become a new challenge with PET-MR, as it is the case notably for attenuation correction (AC). PET data needs to be corrected for photon attenuation by the tissues in order to obtain accurate PET quantification. In PET/CT systems, AC used to be computed straightaway from the CT image. With PET-MR systems, the MRI has replaced the CT and a new strategy has to be found to generate substitute attenuation map from the MR image (MR-based AC). It has been reported (Andersen et al., 2014) that initial MR-based approaches produce spatially biased PET images relative to CT-based AC. However, accurate AC is essential to continue brain research with simultaneous PET-MR protocols, in particular when small variations of the PET signal are investigated and compared across brain regions.

The work presented in this thesis introduces a novel AC method and validates it on static and dynamic PET data. Its impact on sensitivity is then investigated in a real PET-MR study.

In the first chapter, the physical basis of MR and PET imaging are introduced. The attenuation phenomenon is explained and the need for correcting PET data for attenuation is presented. Methods used for attenuation correction on transmission PET systems and PET/CT scanners are described. Finally, techniques for PET-MR AC, presented in the literature in the last decade, are examined at the end of this section.

The second chapter presents the multi-atlas AC approach developed during my PhD (*MaxProb*). A detailed evaluation that assesses pseudo-CT accuracy and precision of static PET data quantification using standard [^{18}F]FDG is provided. Several complementary metrics are used to validate the AC method at global, regional and voxel levels.

In the third chapter, the impact of MR-based AC on various tracers that have different spatial distribution in brain is explored with dynamic PET data.

Finally, in chapter 4, the *MaxProb* method is applied to a bolus-infusion PET protocol using [^{11}C]raclopride. The sensitivity of *MaxProb* to distinguish differences in tracer uptake between groups is investigated with simulated and real PET data. Results are compared to those obtained with the vendor-provided AC technique.

The thesis is concluded by a short chapter synthesising the main insights gained during this work, and suggestions for future work.

1 Chapter 1
MR-based attenuation correction for brain PET-MR imaging: State-of-the-art

Photon attenuation is a physical phenomenon that impacts PET measurements and that tends to introduce bias in the quantification of the PET image. To understand the need for AC, it is essential to understand the physical basis of PET imaging, the mechanisms that allow measuring the tracer in the organism, and the techniques used to recover the tracer distribution in biological tissues from the photon detection. After introducing the physical basis of MR and PET imaging, this chapter focuses on the attenuation phenomenon and on the necessity of correcting PET data for attenuation to obtain an accurate image quantification. This chapter also aims to explain how AC approaches have been historically implemented in conventional PET and PET/CT scanners, and what the new difficulties are that occur in hybrid PET-MR devices. Finally, the state-of-the-art of the different solutions proposed in the literature for MR-based brain AC is described, providing the background of my PhD work.

1.1 Physical principles of MR imaging

The magnetic properties of proton nuclei abundant in the human body is the basis of the physical generation of signal in structural and functional MR images.

1.1.1 MR signal

Atoms with non-zero spins can absorb and emit electromagnetic radiation. They are employed in MR imaging. Due to its great abundance in biological tissues, hydrogen is the most frequently imaged nucleus. The MR signal is thus based on proton densities (i.e. hydrogen nucleus). When inserted in a strong external magnetic field B_0, some of the spins align with the field direction (parallel orientation), and some align against the filed (anti-parallel orientation). The sum of spins results in a macroscopic magnetization (M_0) parallel to B_0. At this equilibrium state, the spins rotate around the B_0 axis, drawing a cone, at a precession frequency (the Larmor frequency), which is proportional to

the magnetic field strength. Since a slight excess of spins are in the B_0 orientation, M_0 has a positive longitudinal component, whereas it has a null transverse component because the spins do not rotate in phase, so the macroscopic transverse component is cancelled out (Figure 1 **A**).

In those conditions, a radio-frequency (RF) pulse tuned to the Larmor frequency can be applied to excite the system and disturb the equilibrium state. An exchange of energy occurs between the RF and the nuclei, which results in a tip down of the net magnetization vector (Figure 1 **B**). During the excitation, the longitudinal magnetization decreases, and a transverse magnetization appears (except for a 180° flip angle). The flip angle (α) depends on the intensity, waveform and duration of the RF pulse. Relaxation is the dynamic physical process in which the system of spins returns to equilibrium. Relaxation can be broken down into two phases: 1) the longitudinal magnetization, aligned with B_0, which is recovered following an exponential curve characterized by time constant T1, and 2) the transverse magnetization, due to spins getting out of phase, which decays according to an exponential function with a time constant T2 (Figure 1 **C**). The time constants T1 and T2 are specific to the surrounding biological tissues, typically influenced by their chemical composition, but also depend on the strength of B_0.

Once the RF transmitter is turned off, the electromagnetic signal produced by the M_0 relaxation is recorded with specific MR coils (Figure 1 **D**). In practice, T2*, an effective value of expected T2, is measured. T2* results principally from inhomogeneities in B_0. These inhomogeneities may be the result of intrinsic defects in the magnet itself or from susceptibility-induced field distortions produced by the tissue or other materials placed within the field. An MR sequence is based on a repetition of RF pulses and the signal recorded is sampled at several time intervals. The echo time (TE) is defined as the time between the RF pulse and the MR signal sampling, and the repetition time (TR) is the time between two excitation pulses. Depending on the MR sequence parameters, e.g. the chosen TE/TR values, the tissue signal will exhibit various contrasts on the MR image (Figure 2).

The two main families of MR sequences are spin-echo and gradient-echo sequences. Many techniques based on these two families of sequences, including hybrid sequences, have been developed to acquire different MR contrast images (not detailed in this work) (Bitar et al., 2006; Gibby, 2005; Hoa et al., 2008).

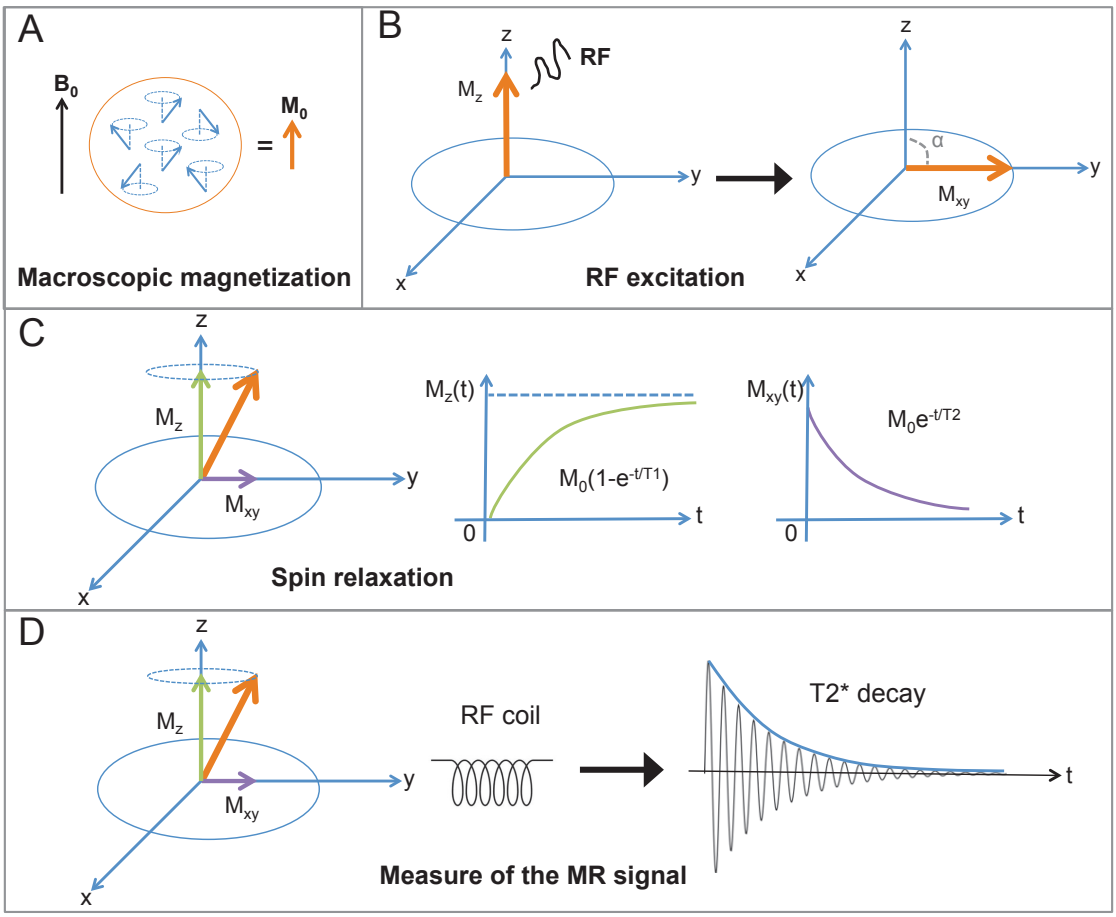

Figure 1: Physical basis of the MR signal. Macroscopic magnetization at equilibrium including precession (A), Radio-frequency applied to disturb the equilibrium (B), Spin relaxation: recover of longitudinal compound and decay of transverse compound (C), Measure of the MR signal (D).

1.1.2 Contrasts in MR imaging

Considering the wide variety of MRI sequences that provide different tissue contrasts, in this section we focus on and briefly describe four sequences often used in the context of PET-MR AC: T1 and T2-weighted images, the two-point Dixon-Water-Fat sequence, and the ultra-short echo time sequence.

T1 and T2-weighted sequences are two standard image contrasts widely employed in a clinical context. T1-weighted images (Figure 2 **A**) are obtained by using a short TR and a short TE. With this image contrast, due to a short T1 time constant, fat appears with a hyper signal in white, while soft tissues are in grey. Water, air and bone all appear dark grey and black due to the hypo-signal they produce, so they cannot be correctly distinguished in the image. For T2-weighted images (Figure 2 **B**),

long TR and long TE are employed. In this weighting, water is white, fat appears grey, soft tissue dark grey, and both air and bone appear black. Again, air and bone cannot be differentiated.

Taking advantage of the differences in resonance properties of water and lipids, the two-point Dixon-Water-Fat sequence (Dixon) separates water and fat signals by exploiting the different resonance frequencies of the two (Coombs et al., 1997). By adding and subtracting phase-corrected images obtained from two excitations (Dixon in-phase and Dixon out-of-phase), a “water image” and a “fat image” are generated**.** Figure 2 **(C - F)** shows an illustration of the Dixon sequence.

The last sequence described here is the ultra-short echo time (UTE) sequence (Tyler et al., 2007). It is used to detect signals from tissues with very short T2* relaxation time (T2* in the range of 0.05–2 ms), such as cortical bone. UTE sequences consist in the acquisition of two consecutive images (UTE1 and UTE2) at two different echo times, typically TE1 = 60 μs and TE2 = 2.24 ms. The signal from the bone is present in the UTE1 but not in the UTE2, whereas the signals from other tissue classes (i.e., soft tissue and air) are similar in both cases. (We follow the established terminology and refer to the materials in body as “tissue” classes, even though air is not actually a tissue). Hence, bone signal can be highlighted by subtracting UTE1 and UTE2 images. An example of the UTE sequence is shown in Figure 2 **(G and H)**.

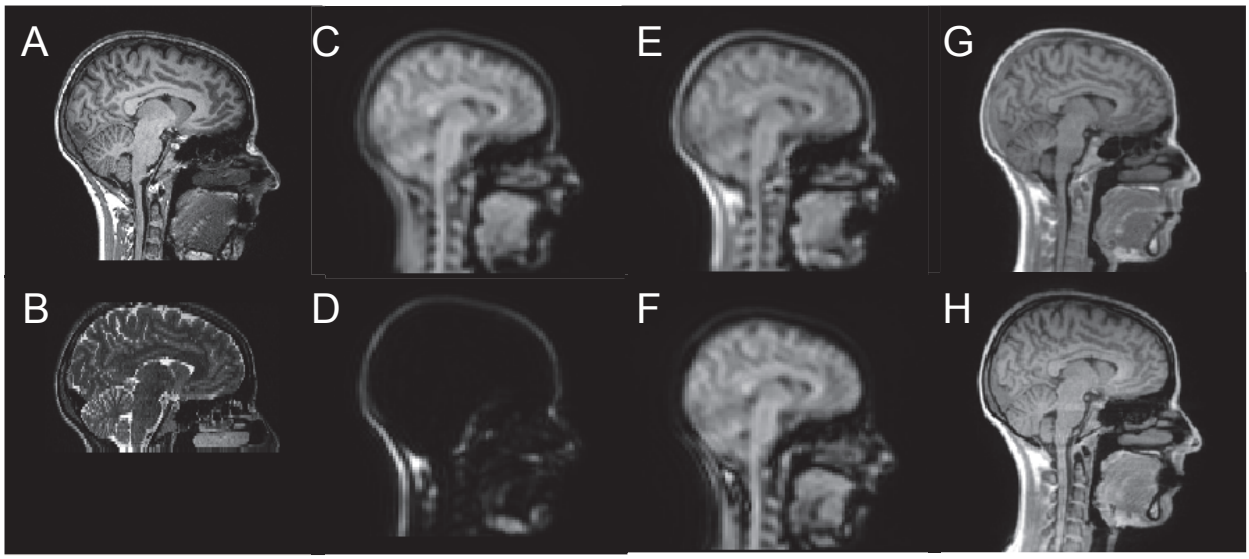

Figure 2: MRI contrasts: T1-weighted (A), T2-weighted (B), Dixon-Water (C), Dixon-Fat (D), Dixon in-phase (E) and Dixon out-of-phase (F), UTE1 (G), UTE2 (H).

1.2 Physical principles of PET imaging

In PET imaging, molecules labelled with a positron-emitting isotope are employed as tracer of endogenous physiological processes in the human body. PET aims to recover a tracer's temporal and spatial distribution in the body to characterize and quantify the physiological phenomenon of interest. The imaging modality is based on several physical properties of the matter and requires various processing steps before a quantitative image can be obtained: radiotracer synthesis, venous injection, data acquisition, and image reconstruction.

1.2.1 Radiotracer

The radiotracer consists of a chemical compound into which a radioactive isotope has been incorporated. The chemical compound is usually chosen to be chemically and functionally close to an endogenous molecule. Once incorporated, it binds the specific tissues or simply follows a metabolic process, as the homologous endogenous molecule. The radiotracer hence allows targeting the physiological function of interest. The radioactive isotope is the element that can be detected by the PET scanner, following the isotope's disintegration process, through the ensuing radio emission that can be detected outside of the body. The tracer is normally injected into the subject by the intravenous route and behaves as a probe that can be followed by the PET system. It is important to use it at very low quantities in order not to trigger a physiological reaction in the organism.

Radioactive positron emitter isotopes are usually produced by nuclear reaction in a relatively small circular particle accelerator, a 9-18 MEv cyclotron. Protons or deuterons are accelerated with the cyclotron to form a beam. The targeted atoms are bombarded with the accelerated particles. This reaction creates the positron-emitting isotopes. The most common isotopes used in PET imaging are: Oxygen-15 (^{15}O), Nitrogen-13 (^{13}N), Carbon-11 (^{11}C), Fluorine-18 (^{18}F), and have a half-life of 2, 10, 20 and 109 minutes, respectively.

The radioactive isotopes are then incorporated into the chemical compound. This step is called the radiosynthesis. Some chemical compounds mentioned in this work are 1) Fluoro-deoxy-glucose labelled with F18 ([^{18}F]FDG) which is an analogue of endogenous glucose, 2) MPPF, also labelled with F18 ([^{18}F]MPPF), which is a selective antagonist of the serotoninergic 5-HT$_{1A}$ receptors and 3) raclopride labelled with C11 ([^{11}C]raclopride) which is an antagonist at the dopaminergic D2 receptor,

and – with lower affinity – at D3 receptors. [^{18}F]FDG provides an image of the cellular glucose metabolism, whereas [^{18}F]MPPF and [^{11}C]raclopride are tracers depicting specific neurotransmission systems. An example of radiotracer structure is shown in Figure 3, and Figure 4 shows PET images obtained with [^{18}F]FDG, [^{18}F]MPPF and [^{11}C]raclopride.

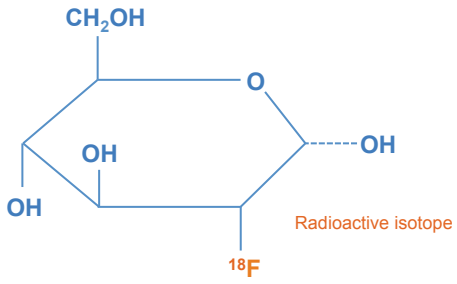

2-deoxy-2[^{18}F]-D-glucose

Figure 3: The [^{18}F]FDG molecule consisting of the chemical compound incorporating the radioactive isotope.

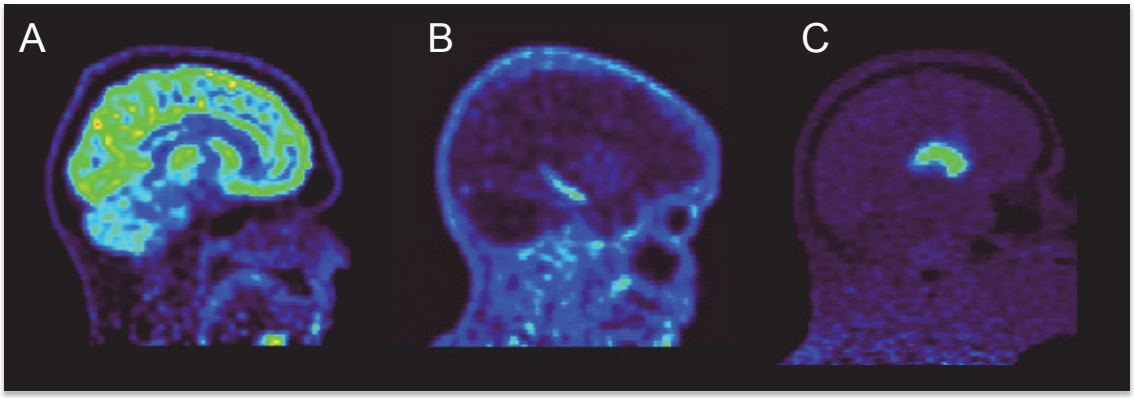

Figure 4: Examples of PET [^{18}F]FDG (A), [^{18}F]MPPF (B) and [^{11}C]raclopride (C).

1.2.2 Annihilation reaction

The radioisotope coupled to the tracer disintegrates to a more stable state. In this process, a proton is transformed into a neutron, and additionally, a neutrino (ν) and a positron (e+) are emitted. This positron emitted with an initial energy (depending on the isotope) travels some distance across the human body, loses energy and interacts with an electron of the matter via an annihilation reaction.

The annihilation results in the emission of two secondary gamma photons of 511 keV, in opposite directions (Figure 5).

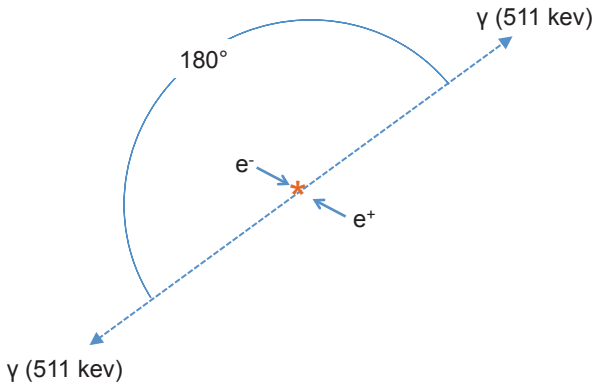

Figure 5: Annihilation reaction.

1.2.3 Detection of coincidences

The two photons from the annihilation reaction are detected simultaneously by the detection system of the PET scanner. This coincident detection is an event called true coincidence. The coincidence detection serves to determine the projection of the photon emission location. A line of response (LOR) is the imaginary segment that joins the two detection points. Other types of coincidences can be collected by the scanner: scatter and random coincidences. In scatter coincidences one of the two photons undergoes Compton scattering during its transportation in the body. It loses a part of its initial energy and is deviated from its initial direction (see section 1.3.2), so it is highly likely that the resulting coincidence event will be assigned to the wrong LOR. Random coincidences occur when two photons not arising from the same annihilation event are detected as a coincidence (Figure 6).

The PET tomograph is made of scintillation detectors coupled to electronic circuits that convert the energy of the incident photons into an electrical signal. The PET tomograph records the coincidence events into a list mode file or a sinogram (usually called PET raw data). The list mode archives each coincidence detected, its arrival time, and the coordinates of the detectors involved in the detection. The sinogram is a simpler file that contains the projections of the events acquired for each angle, on a temporal frame. An example of sinogram and its corresponding PET image are shown in Figure 7.

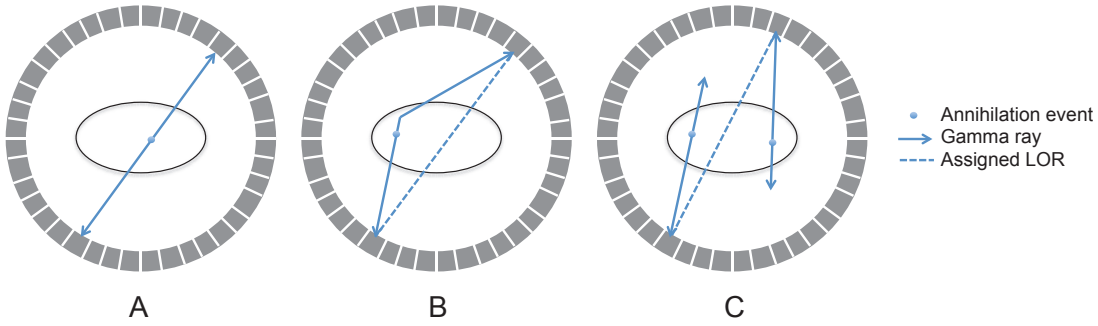

Figure 6: PET detector ring (dark grey) and object to be imaged (oval). Three coincidence types: true coincidence (A), scatter coincidence (B) and random coincidence (C).

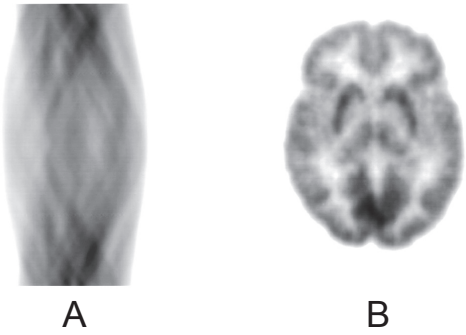

Figure 7: Sinogram (A) and reconstructed brain image (B) corresponding to sinogram. Source: (Fahey, 2002).

Scatter and random coincidences add bias to the data, whereas several aspects from the instrumentation measure chain contribute to add statistical noise to PET data. To limit scatter and random coincidences, both temporal and energetic windows are introduced. The temporal window (between 6 and 15 ns depending on the detection system) permits selecting photons that come from the same annihilation, whereas the window on the energy (usually 350-650 keV) ensures that only photons with an energy superior to a given threshold will be accepted.

1.2.4 Image reconstruction

Image reconstruction is the step that aims to recover the image of tracer spatial distribution from the projections collected with the PET scanner. There are two main reconstruction algorithms: analytic and iterative.

Analytic reconstruction algorithms offer a direct mathematical solution for the formation of an image. Filtered-back projection (FBP) (Rogers et al., 1987) is the analytical method most commonly used, and is fast and straightforward to implement. The drawback is that FBP provides inconsistent results at low counts and amplifies statistical noise inherent to acquired data. By contrast, iterative reconstruction schema can integrate a more realistic model of the system and can account for the noise structure in the observations. These improvements are based on a more complicated mathematical solution requiring multiple steps to obtain an image. This iterative process results in a potentially more accurate estimate than analytical reconstruction methods, at the cost of greater computational demands. Advances in computation speed and faster algorithms have helped to overcome the computational burden of iterative approaches allowing them to receive growing clinical acceptance. The Ordered Subset Expectation Maximization (OSEM) algorithm (Hudson and Larkin, 1994) based on maximum likelihood is largely implemented in clinical routine today. Figure 8 shows an example of a PET image reconstructed with the analytic FBP2D and the iterative OP-OSEM3D algorithms.

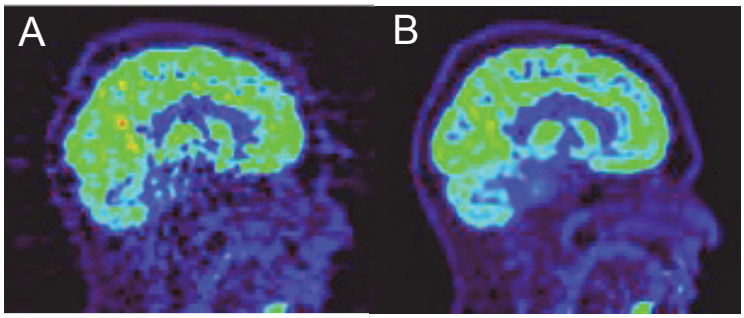

Figure 8: Example of PET image reconstructed with the FBP2D algorithm (A) and OP-OSEM3D algorithm (B).

Now that the main steps required in the creation of a PET image have been introduced, we will examine the interaction between photons and matter, and zoom in on the attenuation phenomenon.

1.3 Interaction of photons with matter

The two photons emitted by the annihilation can interact with particles from human tissues before they reach the detectors. In this case, they can be absorbed or scattered. The absorption results in a reduction of counting statistics, whereas the scattering produces a bias in the localisation of the

events. Both phenomena induce a degradation of the image quality and have to be corrected for as far as possible to ensure an accurate quantification of the PET signal. At PET energies (i.e. 511 keV) photons interact with human body tissues essentially by two mechanisms: the photoelectric effect and Compton scattering.

1.3.1 Photoelectric effect

In photoelectric absorption, the incident photon is totally absorbed by an atom of the matter. As a consequence, due to the energy transfer, an electron is ejected from one of its bound shells. The probability that a photon be absorbed is given by (**Equation 1**):

$$\frac{\mu}{\rho} = constant.\frac{Z^{4.5}}{E^3} \qquad \text{(Equation 1)}$$

where μ/ρ gives the mass attenuation coefficient, Z the atomic number and E the photon energy. This means that tissues with high Z values, such as bone that contains a relatively large percentage of calcium (Z=20), are more attenuating than water or soft tissues (Z=1 for hydrogen and Z=8 for oxygen), and even more so than air (Kinahan et al., 1998).

1.3.2 Compton scattering

In Compton scattering, a photon interacts with an electron in the absorber material. Part of the photon energy is transmitted to the electron and the latter is ejected from the atom with an angle ϕ (Figure 9). The photon loses energy, and it is deviated from its initial direction with an angle θ as follows (**Equation 2**):

$$E' = \frac{1}{1+\frac{E}{m_0c^2}(1-cos\theta)} \qquad \text{(Equation 2)}$$

E' gives the energy of the scattered photon, E represents the energy of the incident photon, m_0c^2 is the rest mass of the electron and θ the deviation angle of the incident photon. The probability of Compton scattering is proportional to Z and has a slight inverse dependence (albeit nonlinear) on

photon energy. Again, bone is more likely to contribute to Compton scattering than water, due to the atomic number of this material.

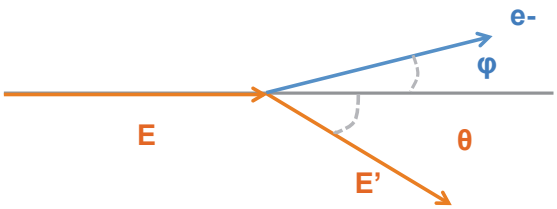

Figure 9: Compton scattering.

1.3.3 Linear attenuation coefficients

The effect of the interactions that contribute to photon attenuation can be summarized with linear attenuation coefficients. The total probability that a photon of a particular energy will undergo an interaction with matter, when travelling across a unit distance through a given substance, is called the linear attenuation coefficient (μ) of the substance. The attenuation law of a photon beam across a medium of distance *d* is given by the following exponential relation (**Equation 3**).

$$I(d) = I_0 e^{-\int_0^d \mu_E(\mathrm{x}).\mathrm{dx}} \qquad \text{(Equation 3)}$$

I(d) represents the number of photons transmitted through a distance *d*, I_0 the number of incident photons, μ the linear attenuation coefficient and E, the photon energy. From **Equation 3** we see that the attenuation depends on the photons' energy and the material that they travel through. However, as the attenuation is integrated along the LOR, it does not depend on the location of the photon emission in this LOR. The attenuation correction factor (ACF) gives the total attenuation for the LOR and is defined as follows (**Equation 4**):

$$ACF(LOR) = e^{\int_{LOR} \mu(r)dr} \qquad \text{(Equation 4)}$$

1.4 The need to correct for photon attenuation

As shown in the previous section, attenuation alters photon detection and thereby can have an important impact on the PET signal measured. It has been estimated that around 70% of the photons emitted at the middle of the brain interact with tissues and do not reach the detectors (Figure 10). This proportion is even higher for whole body PET imaging. In the absence of correction, the image obtained in PET underestimates tracer uptake in deep regions (less photons than those really emitted are detected) and overestimates the activity at the edges (due to the relative lack of attenuation at the edges compared to deeper structures). Those problems are illustrated in Figure 10. Attenuation correction has to be applied in order to re-establish a representative image of the real tracer distribution in the volume studied. It may also be noted that other corrections, such as correction for scatter, random coincidences, count-rate losses due to dead time of the detectors, and variations in detector efficiency, are not described in this work, but are also required to accurately quantify the PET image (Alessio and Kinahan, 2006; Buvat et al., 2014; Hutton et al., 2006; Nuyts and Matej, 2015).

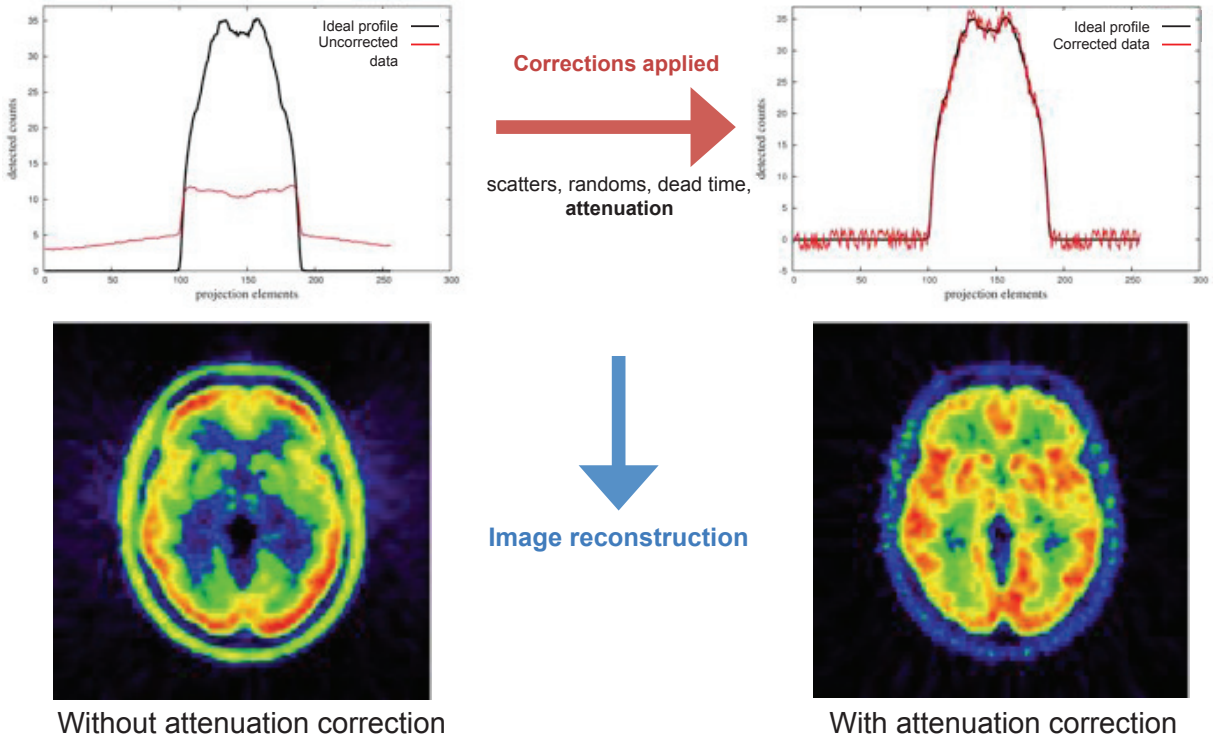

Figure 10: Errors induced in the PET image by the absence of attenuation correction (Source: courtesy from Anthonin Reilhac).

1.5 AC for different modalities

In the past, several approaches have been developed for attenuation correction in PET imaging. In this paragraph the AC implementations for transmission PET, PET/CT, and new PET-MR scanners are described.

Above all, to correct the photon attenuation by the tissues, it is necessary to have available the distribution of the attenuation coefficients for the volume studied (μ-map) or at least the attenuation coefficient factor for all LOR explored, which corresponds to the projection of the μ-map. Several strategies, described in the following, can be used to determine the μ-map, depending on the available acquisition modality. The AC can be performed pre or post data reconstruction, but it is generally integrated in the reconstruction process to ensure a more efficient and accurate correction.

1.5.1 Transmission PET scanners

The most evident way of measuring tissue attenuation map for a 511 keV gamma photon is to directly measure the absorption rate of an external known positron source along all the lines of response of the PET scanner. To this purpose the first conventional PET scanners included a preliminary acquisition, performed before PET emission scan, called transmission scan. During transmission, one (or more) external source(s) of 511 keV photons produced by a positron emitter, generally ^{68}Ge or ^{68}Ga, rotates around the subject, and is used to assess the transmitted signal intensity across the field of view (FOV). Since the source strength is generally not known, a scan acquired without the patient in the gantry is also necessary to determine the measured signal in the absence of attenuation (blank scan). In 2D, the probability of transmission along a given LOR can be determined as the ratio of the number of coincidences counted in the LOR with and without the attenuating object (McKee and Hiltz, 1994). This method directly provides the attenuation coefficients at PET photon energy. However the measuring time is generally long and suffers from statistical noise that is subsequently propagated to the emission PET image. An example of transmission μ-map is shown in Figure 11.

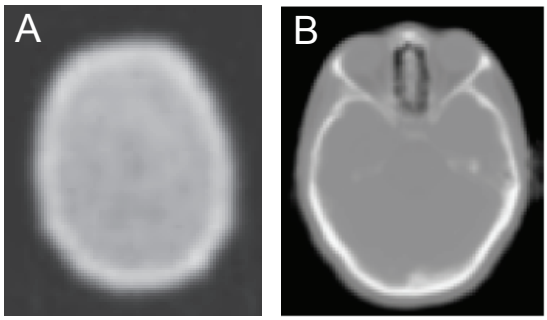

Figure 11: Examples of transmission (A) and CT-based (B) μ-maps corresponding to 511 keV attenuation used for PET AC. Different axial slices are shown.

1.5.2 PET/CT scanners

In more recent PET scanners, a tomodensitometric X ray scanner (CT) is coupled with the PET system to replace the external rotating source. In PET/CT scanners, an x-ray CT image is acquired by a rotating X-ray beam. This CT image, expressed in Hounsfield Units (HU), is used to derive the attenuation map. Compared to transmission PET AC, CT AC is acquired in only few seconds and has the advantage of having a high flux of photons, so the CT scan does not suffer from contamination by 511 keV photons if the subject has already been injected with the radiotracer. In addition, CT images have lower statistical noise and are quickly acquired. Since the attenuation coefficients are energy-dependent, coefficients measured at CT energies (from 30 to 140 keV) must be converted to the appropriate values at 511 keV (μ_{PET}) in order to correct PET emission data. The x-ray source in CT emits photons with a broad energy spectrum from 30 keV to 140 keV whereas PET produces mono-energetic 511 keV annihilation photons (Figure 12). This presents two difficulties with the conversion of CT attenuation factors for use with PET data. The first problem is the difference between the monochromatic 511 keV and wide-band CT energy spectra, while the second is the large difference in photon energies between PET and CT. Photoelectric absorption is the main contributor to the attenuation of photons at lower energies, whereas Compton scattering dominates at higher energies (such as at 511 keV).

Several techniques have been proposed to convert the CT image to μ_{PET}: segmentation of the CT image into tissue classes, dual-energy CT scan, intensity scaling with linear relations, or hybrid approaches (Kinahan et al., 1998). The most common of these methods consists in the bilinear scaling proposed by Carney et al. (2006) (**Equation 5**). The bilinear relation between CT intensities

(HU) and attenuation coefficients at PET energies is shown in Figure 13. An example of a CT-based μ-map, compared to transmission μ-map, is shown in Figure 11.

Despite its limitations, CT-based AC is considered as the ground truth and is generally used as the reference method to validate new AC approaches.

$$\mu^{PET} = \begin{cases} \mu_{H_20}^{PET} \frac{(CT+1000)}{1000}, CT \leq 0\ HU \\ \mu_{H_20}^{PET} + CT\ \frac{\mu_{H_2O}^{CT}(\mu_{Bone}^{PET} - \mu_{H_2O}^{PET})}{1000\ (\mu_{Bone}^{CT} - \mu_{H_2O}^{CT})}, CT > 0\ HU \end{cases} \quad \text{(Equation 5)}$$

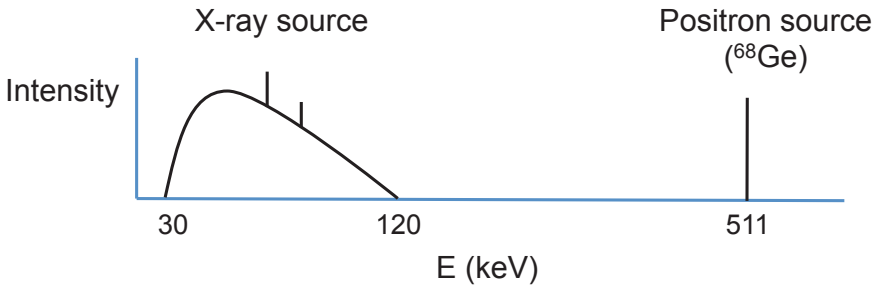

Figure 12: Spectral distributions for x-ray and PET photons (not to scale). X-ray sources produce a polychromatic spectrum. The peaks in the characteristic x-rays represent discrete energies corresponding to the transition of orbital electrons in the target material.

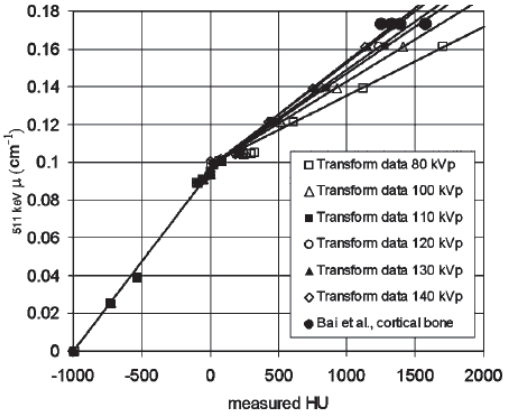

Figure 13: Bilinear scaling to convert CT intensities (HU) into attenuation coefficients (cm^{-1}) for PET energies (lower energies than 80 kVp not in diagram, lines not always on points but uncertainty not estimated). Some manufacturers use different scaling. Source (Carney et al., 2006).

1.5.3 PET-MR scanners

In current PET-MR scanners, neither the PET transmission, nor the CT image are available anymore and the μ-map needs to be estimated from the MR information. However, contrary to CT, the MR image does not directly measure electron density, and the relation between MRI intensities and attenuation coefficients is not obvious. Furthermore, as it has been noticed in section 1.1.2, contrast between air and bone is generally poor in MR images so it is difficult to discriminate these tissues on MRI despite their very different attenuation properties. In the following section, the state-of-the-art of methods for brain PET-MR AC proposed in the literature is detailed.

1.6 State-of-the-art in PET-MR AC

State-of-the art may be operationally defined as the methods that are actually used on the two commercially available fully integrated PET-MR systems. At the moment, there are two different AC solutions available on the Siemens PET-MR system (Biograph mMR). Both are based on the segmentation of MR images into several tissue classes. In the first approach, the Dixon sequence is segmented into air, lung tissue, fat and water (Martinez-Möller et al., 2009) (Figure 14 **B**), whereas the second approach segments the UTE sequence into air, soft tissue and bone (Catana et al., 2010) (Figure 14 **C**). The lack of bone in the Dixon method tends to produce important quantification errors, in particular in the brain regions around the skull (Andersen et al., 2014), and the UTE method suffers from segmentation errors in air and bone boundaries (Aasheim et al., 2015; Dickson et al., 2014). Recent studies (Ladefoged et al., 2016) reported regional (such as in cerebellum and parietal cortex) underestimation of around -15% for Dixon and -8% for UTE. For these reasons, the current versions of those solutions are not accurate enough for neurological PET-MR quantification. A new procedure that combines the UTE sequence with a CT template to improve bone segmentation is currently being validated by the vendor (Koesters et al., 2016; Paulus et al., 2015). AC on the General Electrics (GE) PET-MR system (SIGNA) is based on a more recent template approach (Sekine et al., 2015) (detailed in section 1.6.3.3) which provides regional PET quantification errors of around 3 to 4%, however, local errors of 10% have been reported at the voxel level (Sekine et al., 2016).

To reduce the quantification problems mentioned above, AC for hybrid PET-MR systems has been an active area of investigation in the last decade. Many research teams have worked on this field and a large number of approaches based on different techniques have been proposed. Here we present a

review of the literature to highlight the state-of-the-art for PET-MR AC and discuss the advantages and disadvantages of each solution. We group the methods into three main families: PET-based techniques; methods that rely on MR segmentation; and solutions that use a database of images. Quantification errors are given in an indicative fashion for some of the studies mentioned, but a relevant comparison has to be realized based on the same data and using the same metrics (Ladefoged et al., 2016). We focus on methods dedicated to brain imaging.

1.6.1 PET-MR AC based on the PET signal

The first group of approaches aims to estimate the μ-maps from transmission or emission PET data that inherently contain information about the attenuation properties of the body.

1.6.1.1 Transmission-based methods

Mollet et al. (2014) proposed adding an external positron source in the PET FOV to measure the μ-map by transmission. This system consists in a tube wrapped around a cylinder and filled with a [^{18}F]FDG solution, covering all the FOV. Simultaneous transmission and emission acquisition can be performed to decrease the acquisition time and ensure a better spatial registration between the μ-map and the emission PET image. The transmission data are extracted from the simultaneous transmission–emission scan dataset by employing of the time-of-flight (TOF) information (which is not available on all hybrid PET-MR scanners). Compared to CTAC, errors of 8, 10 and 17% were obtained in PET images for soft tissue, lungs and bone tissues respectively. This approach allows taking into account all objects in the FOV that could attenuate the PET signal, such as MR coils and headphones. It also manages well abnormal anatomies and metallic implants. However, the transmission source device requires particular maintenance and increases the radiation exposure of the subject. Additionally, tissue misclassification on μ-maps during the extraction of transmission data can induce an underestimation of the attenuation coefficients, in particular in regions close to the transmission source (Mollet et al., 2014).

1.6.1.2 Joint estimation of emission and attenuation maps

Methods that jointly estimate the emission and attenuation maps from PET data with iterative algorithms, such as maximum-likelihood reconstruction of attenuation and activity (MLAA) (Nuyts et al., 1999) and MLAA with TOF information (Rezaei et al., 2012), have been initially introduced in the context of transmission PET scans, before the emergence of PET-MR hybrid systems. These iterative estimation techniques alternate the computation of the emission and attenuation map estimates solely using the emission data. They present advantages similar to transmission-based approaches. However, the additional unknown variables in this optimization problem widen the set of possible solutions, and the algorithm may converge on local minima leading to inconsistent emission and attenuation maps and producing crosstalk artefacts resulting from the propagation of activity features into attenuation maps and vice versa.

Recent papers have introduced anatomical information derived from the subject MRI into the MLAA algorithm, in order to guide the optimization process and find a better estimate of the attenuation and emission maps. Salomon et al. (2011) segment a T1 MR image into several clusters whereas Mehranian et al. (2015) segment a Dixon MR image into four classes (lung, fat, air and cortical bone). In this case, bone segmentation is refined with a bone probability map derived from CT images. Finally, Benoit et al. (2016) integrate the UTE image and a discretized version of the T1-weighted MRI as prior information to the iterative algorithm (Figure 14 **D**). Errors reported for these methods, when compared to CTAC, varied from -0.3 to 30% in large brain regions such as cerebellum and frontal lobe. If those approaches help to reduce noise and improve the map estimation, their performance strongly depends on the PET tracer used and in particular on its spatial distribution (Mehranian et al., 2016; Mehranian and Zaidi, 2015). More precisely, a tracer with very localised brain uptake will lead to a poorer performance, as no information will be available for brain areas without tracer uptake. It is to notice that many of these methods require TOF information (Mehranian and Zaidi, 2015; Rezaei et al., 2012; Salomon et al., 2011).

1.6.2 PET-MR AC based on MRI segmentation

1.6.2.1 MRAC with discrete attenuation coefficients

This group of methods segments the subject's MR images into material classes (mostly air, soft tissue and bone) and assigns to each of them a representative constant attenuation coefficient.

Zaidi et al. (2003) segment a T1-weighted MR image into four tissue classes (air, skull, brain, and nasal sinuses) using a fuzzy c-means algorithm. This initial segmentation-based technique produced biases from -2 in occipital lobe to 7% in thalamus (reference method was transmission-based AC in this study). As T1 MR images provide insufficient contrast between air and bone (see section 1.1.2), UTE sequences have been later introduced later by other groups (Tyler et al., 2007) and are now often used in the context of MRAC to better discriminate bone from air-filled cavities. In Anazodo et al. (2015) a bone mask is generated by applying morphological operations to the probabilistic bone map extracted from the T1-weighted MRI with the SPM8 function "New Segment". The bone mask is finally superimposed to the Dixon-based μ-map. This approach led to PET quantification errors of around -7% in parietal and occipital lobes (Ladefoged et al., 2016). Keereman et al. (2010) work on the R2* map, which is the logarithmic difference between UTE1 and UTE2 over the difference of the echo times to enhance bone contrast and distinguish bone from soft tissue. The R2* map is corrected for air with a mask of air voxels derived from the UTE1. Tissue classes are then segmented by thresholding the R2* map. In (Catana et al., 2010), bone and air voxels are enhanced by calculating normalized intensity sum and difference between the two echo images. In both approaches, the MR image is lastly segmented in air, soft tissue and bone tissue classes. Another solution consists in combining the segmentation of two-point Dixon and UTE MR images to generate four tissue classes (bone, air, fat and soft tissue) (Berker et al., 2012). Fat and water images are obtained by decomposing the MR signal of the two-point Dixon sequence (Coombs et al., 1997). This method (mean error over eight brain regions 7.6%) improves the performance of AC based on Dixon (mean error of -14.1%) or UTE only (mean error of 11.4%). In a hybrid procedure, Poynton et al. (2014) combine probabilistic segmentation of T1-weighted and UTE sequences with a probabilistic CT atlas producing an improved segmentation of the MR image into air, soft tissue, and bone, compared to simple segmentation of the T1 or UTE images. After segmentation, this method assumes a constant attenuation coefficient per tissue class. Compared to methods that only rely on the UTE sequence, this segmentation approach guided with a CT template slightly reduced quantification error by 0.5 or 2 percentage points, depending on the brain structures, leading to a regional absolute bias of 1.8% in cingulate and 5.5% in cerebellum.

These techniques are easy to implement and only rely on one or two MR sequences (T1, UTE and/or Dixon). While the Dixon sequence can be acquired in 20 seconds, the UTE and the T1 require at least 4 and 6 minutes, respectively. In addition, the discrete attenuation coefficient assigned to each tissue class, after segmentation, may not be representative of the actual local tissue density, and can induce inaccuracies in reconstructed PET images. This is particularly true for osseous tissues that exhibit a large range of densities, as shown by Catana et al. (2010). For example, cortical bone is a

very dense material whereas mastoid cells consist in an osseous structure filled with small air cavities. Moreover, the reproducibility of the UTE acquisition requires further validation.

1.6.2.2 Continuous coefficients for bone

To account for tissue density variability in bone, some research groups have proposed new solutions that attempt to compute continuous attenuation coefficients for bone, using constant coefficients only for the remaining tissue classes.

Ladefoged et al. (2015) segment the UTE MRI into five tissue classes (brain, cerebrospinal fluid, tissue, air and bone) (Figure 14 **E**). Continuous coefficients for bone are generated by modelling the relationship between UTE intensities (R2* map) and HU (CT images) for a group of 10 subjects with a polynomial fit. In a similar approach (Juttukonda et al., 2015), the MRI is segmented into four tissue classes (air, fat, soft tissue, and bone) using Dixon and UTE images. A polynomial regression is then computed between the R2* map and CT intensities for bone tissue. The evaluation performed in this study led to regional errors around ±1% in brain structures such as parietal, temporal and occipital lobes, cerebellum, thalamus and caudate.

While these techniques have produced encouraging results, their accuracy still strongly relies on the precision of the initial tissue classification. New MR sequences for this purpose have been developed recently (PETRA, (Grodzki et al., 2012) and ZTE (Wiesinger et al., 2016)) and their interest for MRAC is under investigation (Delso et al., 2015; Hsu et al., 2015).

1.6.3 PET-MR AC derived from a database of images

The last family of methods a database of image pairs (for example MR and CT, or MR and PET images) is used to derive a pseudo μ-map or pseudo-CT, which is afterwards easily converted to attenuation coefficients. Unlike MR segmentation-based techniques, this process can generate continuous attenuation coefficients for the whole volume.

1.6.3.1 MR intensity and CT HU fitting

Machine learning algorithms have been proposed to link MR intensities and CT HU. Johansson et al. (2011) and Larsson et al. (2013) build a Gaussian mixture regression model to predict a subject-specific pseudo-CT. In this model, features (mean and standard deviation computed on a 27-voxel neighbourhood) are extracted from UTE, T2 MRI, and CT images. For a new subject, the regression model is applied to its acquired MRI dataset to generate the pseudo-CT. In a similar approach, Navalpakkam et al. (2013) handle a super-vector regression estimation with features (mean, median, standard deviation, minimum and maximum calculated in a 27-voxel neighbourhood) extracted from Dixon, UTE, CT images and an air mask. This model is also used to derive, for each voxel of the subject MRI, the corresponding CT intensity. Those methods obtained regional errors of around 5%. They offer the opportunity to associate MR intensities to CT intensities given a neighbourhood, but rely on images with good contrast to differentiate tissues and can have excessively long processing time for clinical routine (several hours).

1.6.3.2 Patch-based

Patch-based techniques use a database of coregistered MR and CT image pairs to predict a subject-specific pseudo-CT. These approaches perform an intensity-based nearest neighbour search between patches extracted from the subject T1-weighted MRI (Andreasen et al., 2016; Torrado-Carvajal et al., 2015) or UTE MRI (Roy et al., 2014) and patches extracted from a database. Even if those methods do not require any registration to the subject space, the important computational cost (several hours) associated with the patch search has to be addressed. Such approaches are promising but have not yet been evaluated exhaustively.

1.6.3.3 Templates

In this thesis, we use the term atlas to refer to an anatomical image from an individual subject and its associated maps. In contrast, we employ the term template to denote an average of images from several subjects registered to a common space.

Using the concept of single atlas, Schreibmann et al. (2010) propose to work with a multimodality optical flow deformable model to create a simulated CT image that matches the patient anatomy by

mapping the CT image of a single subject to the patient space (T1 or T2 MRI images). The resulting registered CT is the subject-specific pseudo-CT. In this study no detailed assessment on the PET quantification was performed.

Various template approaches have been developed. In Montandon and Zaidi (2005), an [^{18}F]FDG PET and a transmission μ-map template are built with data from 17 subjects. To generate the μ-map of a new subject, the PET template is registered to the subject's PET image (initially reconstructed with an approximate AC method). The deformation found via the PET registration is applied to the template μ-map. This final image gives an attenuation map that is subject-specific to varying degrees. In a similar design (Malone et al., 2011), the PET template is replaced by an MR template built from 10 subjects and in (Izquierdo-Garcia et al., 2014), the transmission μ-map is replaced by a CT template (15 subjects) (Figure 14 **F**). For this type of approaches, regional errors between 0.5 and 6% were reported with CTAC as ground truth. The accuracy of these techniques strongly depends on the quality of the single registration used to map the average template to the single target subject. To refine the registration step, Sekine et al. (2015) propose a CT template generated from 50 subjects and registered to a bone-enhanced liver-accelerated volume acquisition (LAVA) in-phase MRI image via non-rigid B-spine-based elastic registration. However, the gain produced by this algorithm compared to the previous techniques presented in this paragraph is difficult to assess as each study used different data. The regional errors were reported by Sekine et al. (2015) were around 2-3%.

1.6.3.4 Multi-atlas approaches

Finally, true multi-atlas approaches have been introduced in the MRAC context to generate subject-specific pseudo-CTs from a database of MR and CT pairs. In Burgos et al. (2014), the database is registered to the target space by registering each atlas MRI to the target MRI and applying the deformation field to the atlas CT images. Normalised mutual information as a measure of image similarity is calculated at the voxel level between each atlas MRI and the subject MRI. The MR atlases are ranked by decreasing similarity and CT atlases are fused with a weighted average that depends on the similarity rank (Figure 14 **G**). The mean error obtained with this multi-atlas approach in PET data, compared to PET corrected with ground truth CT, was 0.99% in grey matter. Sjölund et al. (2015) investigate a multi-atlas technique by registering 10 MRI and CT pairs to the target space. This step is optimized with an iterative registration of the CT atlases to the average of previously registered atlases. The pseudo-CT is calculated by a simple average of registered CT images. In a different proposition (Torrado-Carvajal et al., 2015), CT atlases are directly registered to the MRI of

the subject (CT-MR intermodality registration) using affine and non-rigid registration with mutual information as similarity metric. Bone tissue is defined by thresholding the CT image and registering to the subject space. Several strategies for multi-atlas fusion are tested and Dice overlap indices (intersection over average) of 72% are obtained between the ground truth CT and the pseudo-CT generated, for bone label. However, this last approach only provides a segmentation of the skull and is not directly suitable for AC in its current version.

In contrast to single atlas and template designs, true multi-atlas approaches register all CT and MR atlas pairs independently, thereby reducing the influence of errors in the individual registrations. To the extent that such errors are uncorrelated, they tend to cancel each other out. Multi-atlas techniques have been proposed originally for image segmentation problems (Rohlfing et al., 2004), in particular for brain segmentation into anatomical regions where it has been shown that they outperform single atlas approaches and methods that use averaging prior to registration (i.e. template procedures) by 20% in terms of similarity index (Heckemann et al., 2006). Independent registrations also give the opportunity to better address inter-subject variability by selecting, in the final step, the most relevant information from the database based on local features. However, anatomical abnormalities or brain lesions that are not represented in the atlas database will be difficult to manage with multi-atlas techniques.

Note that all PET-MR AC methods proposed in the literature and described in this work have been assessed on different datasets, using different references and metrics, making comparison of methods difficult. In addition, until 2016 no real consensus was reached in the international community concerning the optimal performance and the acceptable limits of quantitative errors. Ladefoged et al. (2016) have admonished the need of using a unified quantitative framework with identical metrics, subject cohort, and common CT-based reference to evaluate and compare the approaches proposed in the literature. Their study provides a detailed quantitative evaluation of eleven methods and will be further discussed in the next chapter.

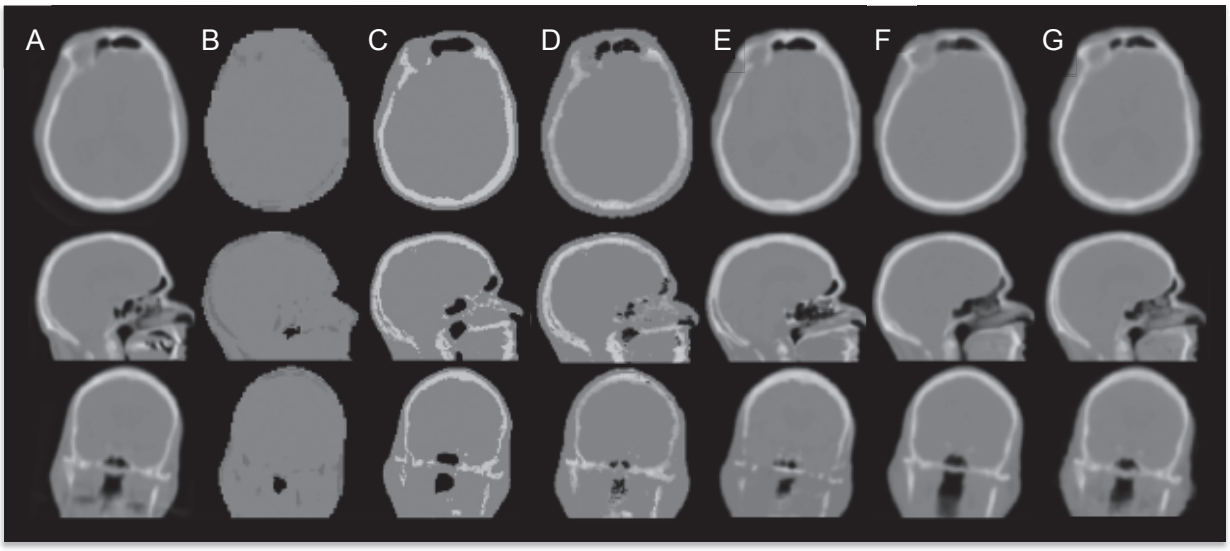

Figure 14: Selection of μ-maps obtained with different techniques. Ground truth CT-based μ-map (A), Dixon-based (Martinez-Möller et al., 2009) (B), UTE-based (Catana et al., 2010) (C), PET-based (Benoit et al., 2016) (D), segmentation-based (Ladefoged et al., 2015) (E), template-based (Izquierdo-Garcia et al., 2014) (F), multi-atlas-based (Burgos et al., 2014a) (G). Adapted from: (Ladefoged et al., 2016).

1.6.4 Hardware AC

Another aspect of photon attenuation in PET imaging concerns the attenuation due to hardware components. Hardware components have been redesigned to minimal attenuation, however, those present in the PET field-of-view during PET acquisition will also attenuate and scatter the annihilation photons and thus reduce and degrade the PET signal measured. For the patient table and the rigid radiofrequency coils that are generally fixed at a defined position, pre-acquired CT-based μ-maps are stored in the system. The position of the RF coil in the PET FOV is detected when the coil is connected to the scanner and the corresponding μ-map is then easily integrated to the subject μ-map for PET AC. However, the scaling transformation to convert the CT HU to attenuation coefficients at 511 keV, usually calibrated for human tissues (Carney et al., 2006), has to be adapted to hardware components that are made of different materials (Paulus et al., 2013). Flexible RF coils (mainly used in whole-body imaging) (Paulus et al., 2013), mobile rigid coils (loops for example) and other hardware components such as headphones (Büther et al., 2016) also contribute to the photon attenuation leading to a lose in PET values of around -11% in the areas close to these hardware objects. Taking into account the attenuation maps of those objects is more difficult, as it requires detecting their position in the FOV and performing accurate registration. New methods are currently under investigation, for example detecting the position of the object via a Kinect depth sensing input

device (Frohwein et al., 2016). Figure 15 shows an example of head coil and headphones that can contribute to the attenuation of PET signal. Hardware AC in PET-MR imaging is an important challenge to keep in mind; however, this aspect is beyond the scope of my PhD work.

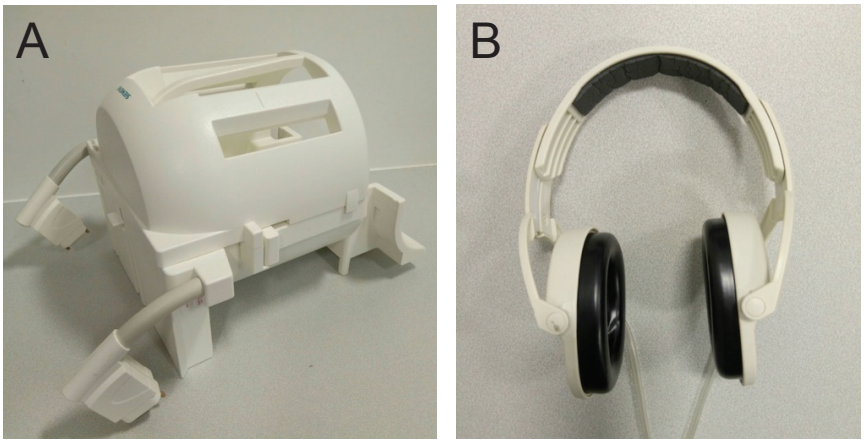

Figure 15: Hardware can contribute to PET attenuation: Head coil MR (A) and headphones (B).

1.7 Conclusion

In PET imaging, photons measured to generate the image suffer from attenuation by the tissues. In the absence of correction for this phenomenon, photon attenuation can lead to wrong quantification and even wrong patterns in the PET image. AC is thus essential to ensure accurate quantification. Due to photoelectric effect and Compton scattering properties, photon interaction with tissues is essentially related to electron densities. As a consequence, attenuation of PET photons is more likely in bone than in water, and not likely in air. As CT measures electron densities and straightforwardly provides a direct estimation of attenuation coefficients for the volume being imaged (despite an energy conversion being required), the MR signal is based on proton densities and there is no obvious link between MR intensities and attenuation coefficients. In addition, traditional MR sequences (such as T1 and T2) provide very low, if any, contrast between air and bone, making the distinction between both materials difficult. For these reasons, deriving the μ-map from the MR data is a real challenge for PET-MR imaging. To solve this issue, many research teams have worked on MR-based AC in the last years, and several methods using different techniques have emerged. Analysing the advantages and disadvantages of the approaches published in the literature, it appears that a good AC method should be subject-specific to accurately match the anatomy of the subject and manage abnormal brain anatomies. In addition, it is important to integrate all tissue

classes; it is now clear than bone cannot be neglected. The solution has to provide continuous coefficients to correctly represent inter-class large variations of densities, in particular for bone. Finally, the method performance should not depend on the tracer used or radioactivity spatial distribution, to be suitable for any brain protocol. In addition to this, an AC approach that can easily be extended to other species, such as non-human primates that are often studied in neurosciences and neuroimaging research, would be a considerable asset.

To address the question of brain AC for PET-MR, I have worked on multi-atlas procedures that generate a subject-specific μ-map for brain imaging. The final proposed solution only requires a T1-weighted MRI of the subject, commonly acquired in clinical and research protocols, and a database of atlases I have collected and pre-processed. The principles of the method, as well as a detailed evaluation of its performance of PET quantification, are presented in the next chapter.

2 Chapter 2

MaxProb multi-atlas method and validation on static [^{18}F]FDG data

As discussed in the previous chapter, AC is essential to obtain accurate and quantitative PET images. In PET-MR scanners, attenuation maps are not directly available, and the μ-map has to be derived from the MR (or the PET) data. This is a challenge as there is no evident link between MR intensities (based on proton densities) and attenuation coefficients (more related to electron densities). In addition, bone and air are difficult to distinguish in the MR images due to the poor contrast, while they are two materials with very different attenuation properties. In the CERMEP, more than 20 research projects for the simultaneous PET-MR mMR system are being planned. Most of these methodological and applicative studies are in the field of neuroscience and will require accurate AC for absolute quantification. In this chapter we introduce a novel multi-atlas approach developed to synthesise a subject-specific pseudo-CT (*MaxProb* method). We took advantage of our experience in multi-atlas techniques for image segmentation and applied them to the framework of brain MR-based AC. Our aim was to develop a solution for both clinical and research contexts, with high accuracy and robustness. A local bias inferior to 5%, compared to ground truth CT AC, was aimed for. The method proposed consists in the individual registration of the atlases contained in the database to the target subject space and the fusion of atlas CT intensities via label propagation and majority voting. A complete evaluation of the *MaxProb* method on quantitative static [^{18}F]FDG PET data is provided. [^{18}F]FDG is a tracer widely used in clinical and research applications to characterize glucose metabolism. Its homogeneous uptake in the whole brain allows a global evaluation of MRAC. Most of the results shown in this chapter have been published in (Merida et al., 2017). Additional analyses are also provided.

2.1 Materials

2.1.1 Atlas database

The atlas database comprised of CT and MR image pairs from 40 subjects (13 male, 27 female) [mean age ± SD, 33.9 ± 13.2 y; range, 16–63 y], selected as a convenience sample from our research database on the basis of the availability of PET/CT and MR. Data were anonymized images of subjects who had participated in various ethically approved research studies. The anonymization procedure was registered under the number 1134516 by the competent authority (Comité de Protection des Personnes Sud-Est III). Subjects had been informed that their anonymized images could be used for methodological development, and had been given the option to oppose this use of their data. The subjects' MR images were visually reviewed for conspicuous brain abnormalities (none found). Each subject had a T1-weighted MR image and a PET/CT brain scan. Three-dimensional anatomical T1-weighted sequences (MPRAGE) were acquired on a Siemens Sonata 1.5 Tesla MR scanner (TE=3.93 ms, TR=1970 ms, flip angle=15°). The images were reconstructed in a 256 × 256 × 176 matrix with voxel dimensions of 1 × 1 × 1 mm^3. CT images were acquired on a Siemens Biograph mCT PET/CT tomograph at the energy of 80 keV. The images were reconstructed in a 512 × 512 × 149 matrix with a voxel size of 0.58 × 0.58 × 1.5 mm^3. MR images were corrected for field inhomogeneities using SPM12 (Statistical Parametric Mapping 12; Wellcome Trust Centre for Neuroimaging, UCL, London, UK). Each subject's field-bias corrected MR image was aligned with the CT image using the affine registration tool *reg_aladin* from the NiftyReg software suite, optimizing normalized cross correlation for the image pair (http://cmictig.cs.ucl.ac.uk/wiki/index.php/NiftyReg (Ourselin et al., 2001)). Coregistered MR images were resampled to their initial resolution using cubic B-spline interpolation. Voxel values in CT images quantitatively represent radiodensity in Hounsfield units (HU). We therefore chose the CT image as the reference space in order to avoid interpolation of these values. We use the term *atlas* to refer to the CT and coregistered T1 MRI image pair (Figure 16).

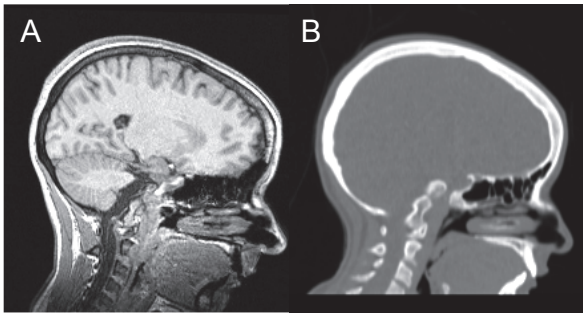

Figure 16: T1 MR image (A) and CT image (B) from one individual. This coregistered pair of images is called an atlas.

2.1.2 Test data

2.1.2.1 PET scanning

From the 40 subjects of the database, twenty-three subjects [mean age ± SD, 35.0 ± 14.5 y; range, 16–63 y] had a 10-minute static [^{18}F]FDG PET scan, obtained from 40 to 50 minutes after the injection of 125 ± 26.4 MBq of [^{18}F]FDG. PET scans were obtained on the same Siemens Biograph mCT PET/CT tomograph as the CT scans. All data were acquired in list mode.

2.1.2.2 PET reconstruction

PET data were reconstructed with an offline version of the Siemens reconstruction software (e7tools, Siemens Medical Solutions, Knoxville, USA). Actual CT images were converted to attenuation maps (μ-maps) by applying a bilinear transformation (Carney et al., 2006) followed by Gaussian blurring (full width at half maximum (FWHM) = 4 mm), and resampled to the PET voxel grid. [^{18}F]FDG data were rebinned into a single 10-minute frame. Images were reconstructed using two different algorithms: 1) 3D ordinary Poisson-ordered subsets expectation maximization (OP-OSEM3D) incorporating the system point spread function using 12 iterations of 21 subsets and 2) 2D Fourier rebinning (FORE) followed by 2D filtered-back projection (FBP2D) using a ramp filter with a cut-off at Nyquist frequency. Data correction (normalization, attenuation and scatter correction) occurred either before reconstruction (FBP2D) or was fully integrated within the reconstruction process (OP-OSEM3D). Time-of-flight was not used, as the PET-MR Siemens Biograph mMR system for which the method is intended does not record time-of-flight information. Gaussian post-reconstruction filtering (FWHM = 4 mm) was applied to all PET images. Reconstructions were performed with a zoom of 3 yielding a voxel size of 1.06 × 1.06 × 2.02 mm^3 in a matrix of 128 × 128 × 109 voxels.

2.1.2.3 MRI segmentation

The T1 MR images were anatomically segmented into 83 regions using a maximum probability atlas in Montreal Neurological Institute (MNI) / International Consortium for Brain Mapping stereotaxic space, based on manual delineations of 30 MRIs of healthy young adults (Hammers_mith maximum probability atlas n30r83, (Gousias et al., 2008; Hammers et al., 2003), available at www.brain-development.org). An 84th region, the cerebellar vermis, was manually added in stereotaxic space (Figure 17 **A**). Deformation fields from the subjects' space to MNI space were determined from the T1 MR image by using the *Segment* function of SPM12. The atlas was back-normalized to each individual MRI space via the inverse transformation. Masks of grey matter (GM), white matter (WM), and cerebrospinal fluid (CSF) were generated in the subject space by combining the Hammers_mith MRI segmentations and the probabilistic "tissue" maps obtained with SPM12 (SPM *Segment*) (Figure 17 **B**).

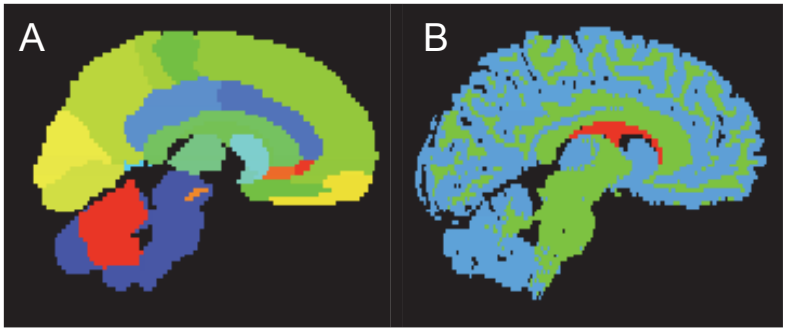

Figure 17: Brain labels from Hammers_mith atlas 84 ROI including cerebellar vermis (A) and mask of tissue classes (GM, WM and CSF) (B).

2.2 Methods

2.2.1 *MaxProb*: multi-atlas generation of a subject-specific pseudo-CT

The general principle of the *MaxProb* approach consists in predicting a subject-specific from its MR image and the atlas database. Firstly, pairwise nonrigid registration of each atlas MR image to the target MR image was computed and used for propagating the atlas CT into the target space. Secondly, the pseudo-CT was generated through voxelwise atlas selection and intensity fusion. The pipeline of the *MaxProb* method is shown in Figure 18; a detailed step-by-step description follows.

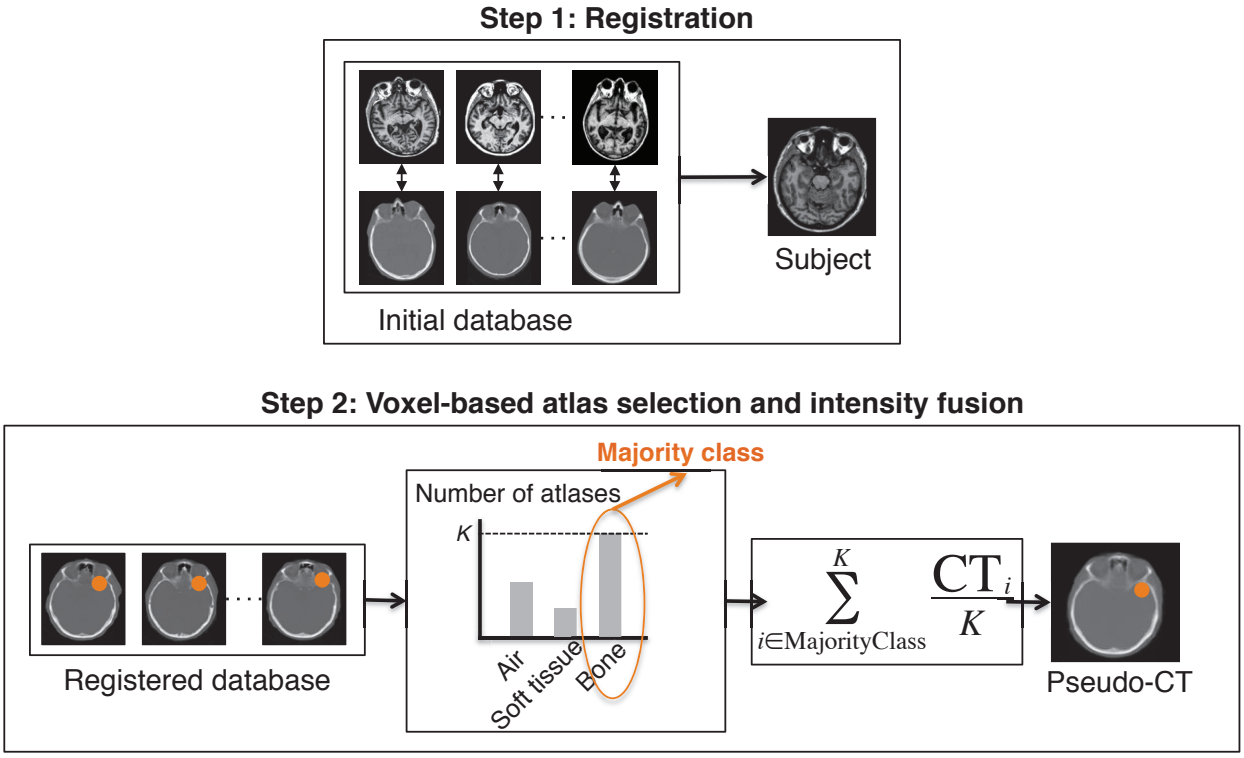

Figure 18: *MaxProb* pipeline to generate a pseudo-CT from the subject's MR image. The example in orange refers to bone; the process classifies all voxels into one of the three classes.

2.2.1.1 Registration

MR images from the original database of co-registered MR-CT pairs (see section 2.1.1) were mapped to each target subject's MR image using affine registration, followed by non-rigid registration (NiftyReg suite: http://cmictig.cs.ucl.ac.uk/wiki/index.php/NiftyReg) (Modat et al., 2010; Ourselin et al., 2001), based on cubic-B-spline, with normalized mutual information as similarity measure and a control point spacing of 5 mm. The transformations obtained from the MR non-rigid registration were then applied to the corresponding co-registered CT. This step yielded the registered database (Figure 18**, Step 1**).

2.2.1.2 Atlas selection and fusion

Registered CT atlases were segmented into three tissue classes, defined by intensity thresholding on the CT images (Poynton et al., 2014):

1 Air: <-500 HU

2 Soft tissue: [-500; 300] HU

3 Bone: >300 HU

For each voxel in the target subject space, majority voting was performed across the registered CT atlases to determine a majority tissue class label (Figure 18**, Step 2**). If there was more than one modal value in the distribution, one of the equiprobable tissue classes was randomly selected (Hammers et al., 2003). Finally, the voxel intensity value of the pseudo-CT was determined by averaging CT HU values of atlases belonging to the majority class for the corresponding voxel (Figure 18**, Step 2**).

In this study, synthetic pseudo-CTs were generated for each subject in a leave-one-out design. Each subject's MR image was used as a target, and the 39 remaining subjects as the atlas database.

2.2.2 *SingleAtlas* pseudo-CT

As a point of reference, I developed a simplified method (*SingleAtlas*), which uses only one atlas (MR and CT pair), randomly selected from the database. The pipeline of the *SingleAtlas* procedure is shown in Figure 19 .The pseudo-CT was built by registering the atlas MRI to the subject space and then warping the CT image (similar to Schreibmann et al. (2010)). The same registration parameters as for the multi-atlas approach were used. The transformed single CT constituted the pseudo-CT (Figure 19). *MaxProb* was compared to *SingleAtlas* to determine whether the complexity of the multi-atlas design yielded any accuracy advantage.

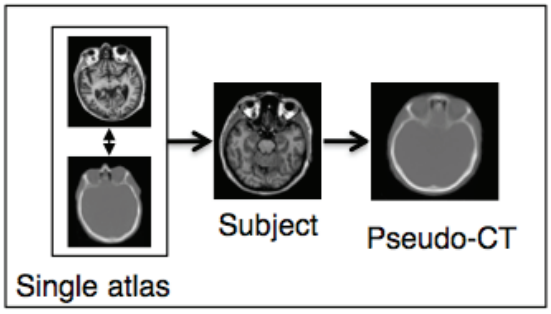

Figure 19: Pipeline for *SingleAtlas* approach.

2.2.3 Pseudo-CT background

The background of real CT images (i.e. atlas images in the context of leave-one-out evaluation) contained the pillow and other components that contributed to the attenuation in the PET images (Figure 20). To account for this additional attenuation, the background in the pseudo-CT image was replaced with the real CT image background for each subject. Note that this background issue will not need to be managed for PET-MR imaging with the mMR scanner, since the hardware μ-map is integrated to the subject attenuation map by the manufacturer's reconstruction software.

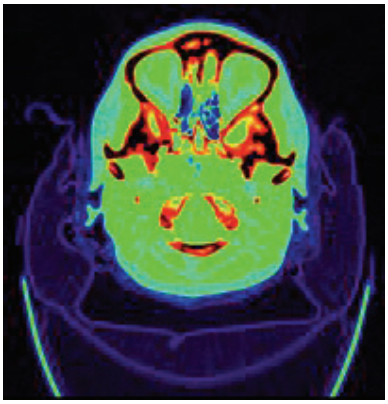

Figure 20: CT image (axial view) of one subject. The background contained the pillow and other components that could contribute to attenuation (intensities for the pillow and other components were around -800 HU in areas in purple, whereas background intensities were close to -1000, in black).

2.2.4 Pseudo-CT evaluation

Evaluation of the synthetized pseudo-CT was restricted to voxels within a head mask. Head masks were generated from the CT images using tools from the software suites FSL (Version 4.1, (Smith et al., 2004)) and NiftySeg (http://cmictig.cs.ucl.ac.uk/wiki/index.php/NiftySeg, (Cardoso et al., 2011)). CTs were thresholded at -500 HU and binarized. The largest connected component was found to eliminate the head support visible in the images. Binary images were blurred using a Gaussian kernel with a standard deviation of 6 mm, and thresholded at 0.4. This filled up the air spaces in the nose and pharynx. Holes were filled using the *seg_maths* tool from NiftySeg. The basal parts of the head masks were finally cut at the foramen magnum in order to eliminate the neck. For this, the head mask for the first subject of the database was manually cut. Then, this cut mask was automatically wrapped to the other subjects by applying a deformation field previously calculated between the two

MR images (affine and non-rigid registration, same parameters used as described in section 2.2.1.1). An example of CT image, head mask and head mask cut at the foramen magnum for one subject is shown in Figure 21.

Figure 21: CT image (A), head mask (B) and head mask cut at the foramen magnum (C).

Each generated pseudo-CT was compared to the subject's real CT (ground truth CT). We computed the Mean Absolute Error (MAE) in HU across the head mask (**Equation 6**).

$$\mathrm{MAE} = \frac{\sum_1^K |pCT_i - rCT_i|}{\mathrm{K}} \qquad \text{(Equation 6)}$$

where pCT_i refers to the value (in HU) for pseudo-CT at voxel i, rCT_i refers to the value (in HU) for ground truth CT at voxel i and K is the total number of voxels in the volume of interest.

In addition, the Jaccard overlap index (Jaccard, 1901; intersection over union) was computed per tissue class (air, soft tissue and bone). The percentage of misclassified voxels in the pseudo-CT compared to the ground truth CT was employed as a metric reflecting the accuracy of the generated pseudo-CT. For this purpose, ground truth CT and pseudo-CT images were labelled by intensity thresholding (see thresholds above). Various thresholds for tissue classification were tested in the evaluation and similar results were found (see section 2.3.1.3.2).

SingleAtlas and *MaxProb* pseudo-CT generation methods were compared on these quality criteria using paired Wilcoxon signed-rank tests. The threshold of statistical significance was set at a p-value of 0.05, divided by the number of comparisons (two in this study) to correct for multiple comparisons (Bonferroni, 1936).

2.2.5 [^{18}F]FDG PET evaluation

The quantitative error induced by the MRAC methods on PET images was assessed by comparing PET data reconstructed with MRAC approaches to PET data reconstructed with real CT, considered as the ground truth. The assessment was performed on activity values for PET [^{18}F]FDG data.

MR images and segmentation labels were registered to the corresponding PET images with SPM12 (*Coregister* function). [^{18}F]FDG images were spatially normalized to MNI space by using SPM12.

The bias introduced by the MRAC methods was calculated as the relative error (**Equation 7)** and the absolute error (**Equation 8**):

$$\text{Relative error } (\%) = \frac{\text{PET}_{\text{MRAC}} - \text{PET}_{\text{CTAC}}}{\text{PET}_{\text{CTAC}}} \times 100 \qquad \text{(Equation 7)}$$

$$\text{Absolute error } (\%) = \left|\frac{\text{PET}_{\text{MRAC}} - \text{PET}_{\text{CTAC}}}{\text{PET}_{\text{CTAC}}}\right| \times 100 \qquad \text{(Equation 8)}$$

where PET_{CTAC} refers to PET data corrected for attenuation with the ground truth CT, and PET_{MRAC} is the PET data corrected with the MRAC *SingleAtlas* or *MaxProb* approaches ($PET_{SingleAtlas}$ or $PET_{MaxProb}$).

2.2.5.1 Global and regional bias

Global mean and standard deviations of [^{18}F]FDG activity were extracted in the subject space for the brain tissue masks (GM, WM, CSF). Regional mean and standard deviations of [^{18}F]FDG were also extracted in 84 regions of the Hammers_mith MRI segmentation. The relative errors between the ground-truth PET_{CTAC} and PET_{MRAC} were calculated for each ROI. Average bias for each cerebral region was computed across the subjects. Statistical significance of the differences in regional evaluation between ground truth and MRAC solutions was determined with a paired Wilcoxon signed-rank test.

2.2.5.2 Parametric image of bias

Voxel-wise parametric maps of the bias were computed for [^{18}F]FDG PET data: for each subject, the image of relative error between PET_{CTAC} and PET_{MRAC} was calculated in the subject space. The images

of relative error were then normalized to MNI space using B-spline interpolation, averaged and finally masked with a brain mask.

2.2.5.3 SPM analysis

Voxel-based analysis to assess differences between PET_{CTAC} and PET_{MRAC} for [^{18}F]FDG PET was performed with SPM12 using an ANOVA with the factors methods and subjects. The resulting statistical parametric maps were thresholded at an uncorrected significance level of $p<0.001$ for illustration, and surviving clusters at a significance level of $p<0.05$ corrected for multiple comparisons (family wise error).

2.3 Results

The computation time required to generate a pseudo-CT with the *MaxProb* method was around 1.5 hours using a single core. Using a six-core machine, the multiple registrations required in the process can be parallelized, reducing the run-time to about 15 minutes.

2.3.1 Pseudo-CT evaluation

In this section we report results obtained for the evaluation of the pseudo-CTs generated with the *SingleAtlas* and *MaxProb* MRAC methods.

2.3.1.1 Qualitative results

Figure 22 shows the ground truth CT and pseudo-CTs generated with the *SingleAtlas* and *MaxProb* approaches for a subject of the database with mean voxel classification error. The difference image between the ground truth CT and each pseudo-CT (pseudo-CT - ground truth CT) is also shown. Pseudo-CTs computed with both methods showed, in general, strong agreement with the ground truth CT. However, the error for the skull was much larger for the *SingleAtlas* technique (error range

from -3000 to 3000 HU) than for the *MaxProb* scheme (error between -500 and 500 HU). The small amount of air in the mastoid cells was not well reproduced in the *MaxProb* pseudo-CTs but misplaced in the *SingleAtlas* approach.

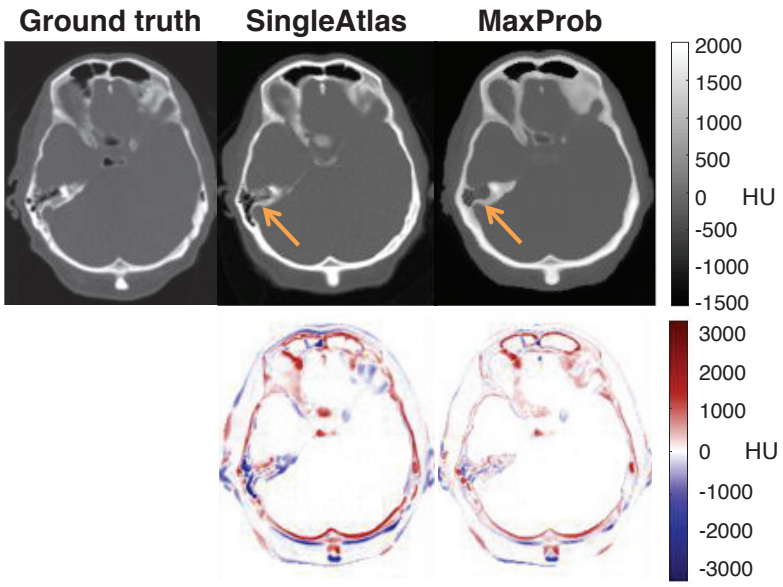

Figure 22: Ground truth CT and pseudo-CT for one subject with average voxel classification error performance (top) and the corresponding image difference (pseudo-CT – ground truth CT) (bottom). A representative axial section is shown. A region with errors in air-filled spaces for some method is pointed out with arrows.

2.3.1.2 Quantitative results

Volumes of the various head tissues and non-tissue components with dissimilar attenuation properties, i.e. air, soft tissue, and bone ("tissues", mean ± standard deviation) within the head mask for all ground truth CTs of the database were 180 ± 36 cm^3 for air, 2309 ± 267 cm^3 for soft tissue and 626 ± 95 cm^3 for bone.

2.3.1.2.1 MAE

Mean absolute errors of pseudo-CT intensities computed voxel-by-voxel, on the head mask per tissue class and for the global head volume, across all subjects are shown in Table 1. Significantly smaller errors were obtained for the *MaxProb* method compared to the *SingleAtlas* approach.

Table 1: Mean absolute error (MAE) in Hounsfield units computed on the head mask and per tissue class. Paired Wilcoxon signed-rank test (*: p<0.05 *MaxProb* vs. *SingleAtlas*).

	SingleAtlas		**MaxProb**		
	mean	sd	mean	sd	
Global	189 ±	16	133 ±	19	*
Air	307 ±	43	269 ±	46	*
Soft tissue	107 ±	15	67 ±	9	*
Bone	458 ±	42	332 ±	61	*

2.3.1.2.2 Jaccard index

A box plot of the Jaccard indices computed per tissue class and methods is shown in Figure 23. Mean values, standard deviations, and results from the statistical comparisons are summarized in Table 2. The mean Jaccard index obtained with *SingleAtlas* was 46% for air, 67 % for bone and 85% for soft tissue. *MaxProb* systematically performed better, with a Jaccard index of around 10 points above the *SingleAtlas* method for air and bone. Paired Wilcoxon signed-rank tests showed that all the differences were statistically significant (Table 2).

Table 2: Jaccard index (mean ± standard deviation) per method and per tissue class. Paired Wilcoxon signed-rank test (*: p<0.05 *MaxProb* vs. *SingleAtlas*).

	SingleCT		**MaxProb**		
Tissue	mean	sd	mean	sd	
Air	46 ±	5	57 ±	5	*
Soft tissue	85 ±	1	90 ±	2	*
Bone	67 ±	3	76 ±	3	*

Paired Wilcoxon signed-ranked test (*: p<0.05)

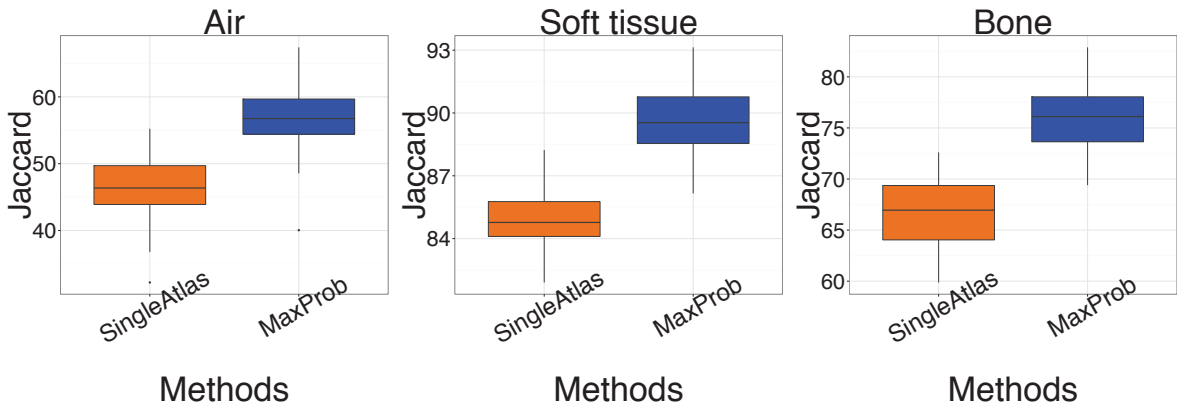

Figure 23: Boxplots of Jaccard index per tissue class and per method. Note that y axis scales differ between plots. Centre lines correspond to medians, boxes to interquartile ranges, and whiskers to robust ranges. Outliers are represented as dots. Note that Jaccard indices obtained with the *SingleAtlas* approach were systematically and significantly lower than with the *MaxProb* method.

2.3.1.2.3 Percentage classification error

The percentage of voxel classification error (mean ± standard deviation) across all subjects, per method and error type, is reported in Table 3. "Bone_as_air" means that a voxel was classified as air in the pseudo-CT when it should have been bone according to the ground truth CT; the remaining row labels are formed in the same manner. Errors are expressed as the percentage of the voxels within the head mask. The total classification error was approximately 12.3% for the *SingleAtlas* approach and decreased to around 8.4% for the *MaxProb* method. Significantly better performance was achieved with *MaxProb* compared to *SingleAtlas*.

2.3.1.3 Additional analysis performed on pseudo-CTs

In addition to the pseudo-CT evaluation presented above, several aspects of the multi-atlas procedure were explored and reported in this section.

2.3.1.3.1 Atlas database resolution

In the atlas database pre-processing pipeline, each atlas MRI had been coregistered to its corresponding CT image. In this coregistration step, two choices were possible: resampling the

coregistered MR image to CT resolution (0.58 × 0.58 × 1.5 mm^3), or keeping the initial MRI resolution (1 × 1 × 1 mm^3). The resolution of the atlas database can have an important impact in computation time, as the registration time increases with the number of voxels to take into account. To a lesser extent, the fusion step is also affected by the matrix size of the images. For this reason, I studied the influence of the atlas database resolution on pseudo-CT accuracy. Each pseudo-CT was generated with both databases (atlas database at MR and CT resolution). A quantitative evaluation of pseudo-CT accuracy is shown in Table 4 (Jaccard index) and Table 5 (voxel error classification). The mean Jaccard index obtained with the *MaxProb* method and database at CT resolution was 57.5% for air, 75.7% for bone and 89.7% for soft tissue, so less than 1% different from results reported for the *MaxProb* method and database at MR resolution. The total classification error with *MaxProb* was 8.31% for the database at CT resolution and 8.34% for the database at MR resolution. In summary, results reported with databases for the two voxel dimensions tested had very little impact on the quality of pseudo-CT generated. The atlas database with the coregistered MR images at their initial resolution was then used in order to reduce the computation time.

Table 3: Mean voxel classification error (in % of all voxels in the head mask) across 40 subjects, per method. Paired Wilcoxon signed-rank test (*: p<0.05 *MaxProb* vs. *SingleAtlas*).

	SingleAtlas		MaxProb		
Error	mean	sd	mean	sd	
bone_as_soft-tissue	3.19 ±	0.79	2.75 ±	0.92	*
bone_as_air	0.13 ±	0.04	0.04 ±	0.03	*
air_as_bone	0.18 ±	0.11	0.13 ±	0.12	*
air_as_soft-tissue	1.85 ±	0.49	1.66 ±	0.57	*
soft-tissue_as_bone	4.79 ±	0.95	2.55 ±	0.66	*
soft-tissue_as_air	2.13 ±	0.56	1.20 ±	0.46	*
Total	12.27 ±	1.17	8.34 ±	1.19	*

Table 4: Mean Jaccard index (%) across 40 subjects, for the *MaxProb* method, with pseudo-CTs generated with two different atlas database resolutions (MRI resolution: 1 × 1 × 1 mm^3 and CT resolution: 0.58 × 0.58 × 1.5 mm3). Paired Wilcoxon signed-rank test (*: p<0.05 MR resolution vs. CT resolution).

	MR resolution		CT resolution		
Tissue	mean	sd	mean	sd	
Air	56.7 ±	5.4	57.5 ±	5.4	*
Soft tissue	89.6 ±	1.5	89.7 ±	1.4	
Bone	76.0 ±	3.3	75.7 ±	3.1	

Wilkoxon test (*: p<0.05 MR resolution vs. CT resolution)

Table 5: Mean voxel classification error (%) across 40 subjects, for the *MaxProb* method, with pseudo-CTs generated with two different atlas database resolutions (MRI resolution: 1 × 1 × 1 mm^3 and CT resolution: 0.58 × 0.58 × 1.5 mm^3). Paired Wilcoxon signed-rank test (*: p<0.05 MR resolution vs. CT resolution).

	MR resolution	CT resolution	
Error	mean sd	mean sd	
bone_as_soft-tissue	2.75 ± 0.92	2.74 ± 0.91	
bone_as_air	0.04 ± 0.03	0.04 ± 0.03	*
air_as_bone	0.13 ± 0.12	0.15 ± 0.14	*
air_as_soft-tissue	1.66 ± 0.57	1.70 ± 0.54	
soft-tissue_as_bone	2.55 ± 0.66	2.56 ± 0.63	
soft-tissue_as_air	0.13 ± 0.12	1.12 ± 0.43	*
Total	8.34 ± 1.19	8.31 ± 1.12	

Wilkoxon test (*: p<0.05 MR resolution vs. CT resolution)

2.3.1.3.2 Thresholds for pseudo-CT segmentation used in the evaluation

The evaluation of pseudo-CTs per tissue class (section 2.2.4) was realized with the same thresholds than those used to fuse the atlases in the *MaxProb* pipeline, i.e. <-500 HU for air, [-500; 300] HU for soft tissue and >300 HU for bone (section 2.2.1.2) (threshold 1).

In order to investigate the influence of those thresholds on pseudo-CT accuracy, and whether using same thresholds for pseudo-CT generation and evaluation favoured *MaxProb*, other thresholds ([-600; 400] (threshold 2) and [-400; 200] (threshold 3) were also studied in the evaluation. Table 6 shows Jaccard indices and voxel classification error for *MaxProb* and my implementation of Burgos et al. (2014a) (called *Ref*) approaches, using three different thresholds for CT classification. The total voxel classification error for *MaxProb* increased from 8.31% to 8.82% respectively with threshold 1 and threshold 3. A similar increase occurred for the *Ref* approach (8.65% of error with threshold 1 and 9.06% with threshold 2). The results demonstrate slight dependence on the thresholds used for the evaluation, with the influence similar for *MaxProb* and the solution described in Burgos et al. (2014a). Using the same thresholds for generation and evaluation of pseudo-CT did not favour *MaxProb* performance.

Table 6: Mean Jaccard index and mean voxel classification error across 40 subjects for pseudo-CT, per MRAC method and threshold used to segment the pseudo-CT. Ref refers to (Burgos et al., 2014a). Paired Wilcoxon signed-rank test (*: p<0.05 *MaxProb* vs. *Ref*).

Jaccard index (%)

Threshold (1): [-500 ; 300] HU

	MaxProb		Ref		
Tissue	mean	sd	mean	sd	
Air	57.5 ±	5.4	57.0 ±	4.7	
Soft tissue	89.7 ±	1.4	89.0 ±	1.1	*
Bone	75.7 ±	3.1	76.1 ±	3.3	

Threshold (2): [-600 ; 400] HU

	MaxProb		Ref		
Tissue	mean	sd	mean	sd	
Air	56.8 ±	6.1	53.9 ±	4.8	*
Soft tissue	89.7 ±	1.3	89.7 ±	1.1	
Bone	74.4 ±	3.5	74.9 ±	3.6	

Threshold (3): [-400 ; 200] HU

	MaxProb		Ref		
Tissue	mean	sd	mean	sd	
Air	56.8 ±	4.8	59.7 ±	4.6	*
Soft tissue	88.9 ±	1.7	88.1 ±	1.2	*
Bone	75.7 ±	2.9	77.2 ±	3.1	*

Voxel classification error (%)

	Ref		MaxProb		
Error	mean	sd	mean	sd	
Total	8.65 ±	0.93	8.31 ±	1.12	*

	Ref		MaxProb		
Error	mean	sd	mean	sd	
Total	8.30 ±	0.93	8.33 ±	1.06	NS

	Ref		MaxProb		
Error	mean	sd	mean	sd	
Total	9.06 ±	0.96	8.82 ±	1.24	NS

2.3.1.3.3 Map of number of atlases fused

To further investigate the behaviour of the fusion step for the *MaxProb* scheme, the parametric map of atlases fused at the voxel level was computed. Figure 24 shows an example of this parametric map for one randomly selected subject. This figure indicates that there was a broad consensus between atlases in the middle of tissue structures, as for example in the middle of the brain, and in this case, most (or even all) of the atlases of the database (i.e. 39 atlases) contributed the average of HU intensities (voxels in white). In other cases, for regions close to boundaries between tissue classes (i.e. soft tissue and bone, or air and bone), the number of atlases fused was around 18 (dark voxels) and 28 (voxels in grey). These results were expected as the inter-subject variability is higher for skull shape and air-filled cavities than for the overall shape of brain.

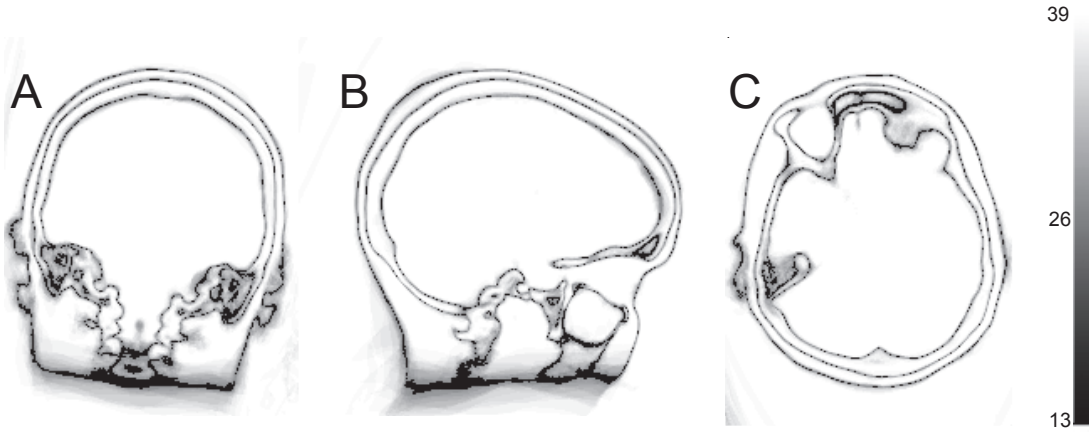

Figure 24: Map of number of atlases fused per voxel with the *MaxProb* method (example for one randomly selected subject). Note that the extracorporal grey areas correspond to the background in CT atlases (see section 2.2.3).

2.3.1.3.4 Joint histogram

Joint histograms provide an indication of the distribution of one variable compared to another one. This tool can be used to analyse the distribution of pseudo-CT intensities in relation to the distribution of ground truth CT intensities, for a given subject. In this section, both *MaxProb* and *SingleAtlas* pseudo-CTs are compared to ground truth CT for the two subjects that had best (5.5%) and worse (11.0%) classification error rate with the *MaxProb* approach (Figure 25). An identification of the error type is proposed.

Overall, intensities for *MaxProb* pseudo-CTs showed better agreement with ground truth CT than *SingleAtlas*, in which distributions were sparser. The joint histograms for *MaxProb* presented holes with missing values in the distribution. This was expected due to the process of classifying the CT atlases into three tissue classes before fusion. An averaging of intensities is performed per tissue class and extreme values of each class are directed towards the centre value of the class. Good correspondence between ground truth CT and *MaxProb* pseudo-CT was found for voxels in the range [-200; 200] HU. Those intensities correspond to soft tissues, which represent an important volume within the head. Low errors were obtained in the middle of the brain due to the low inter-subject variability in this area and thus a good agreement between atlases. Good correspondence was seen for bone structures (dispersion less important around the identity line), despite a slight underestimation of bone intensities in *MaxProb* pseudo-CTs that can be explained by the averaging performed during the fusion process.

In Figure 25 (for the subject with highest classification error, *MaxProb* method only), each type of classification error described in section 2.3.1.3.2 (soft tissue as air, soft tissue as bone, air as soft tissue, air as bone, bone as air and bone as soft tissue) has been reported.

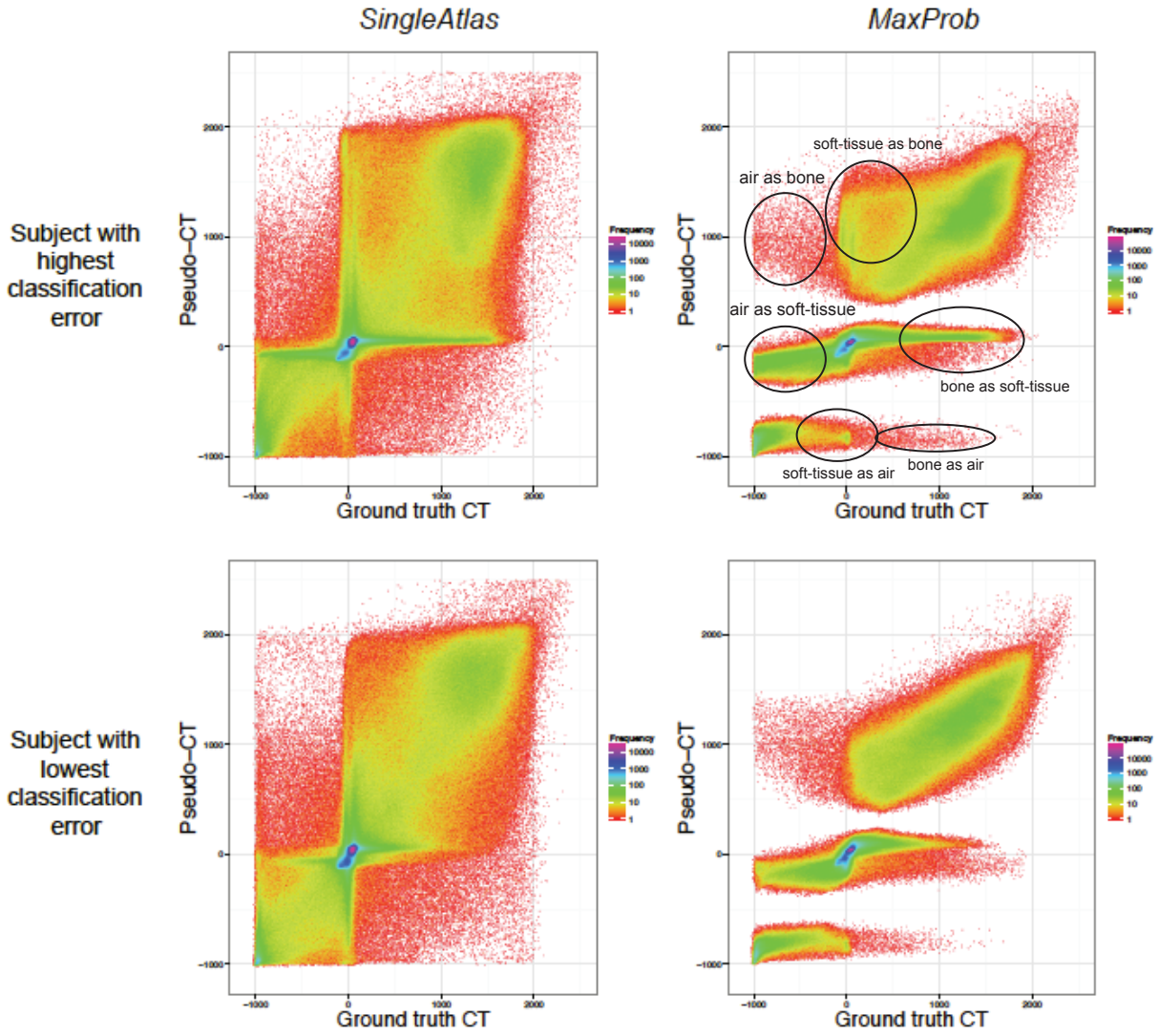

Figure 25: Joint histograms of *SingleAtlas* (left column) and *MaxProb* (right column) pseudo-CT intensities vs. ground truth CT intensities. The subjects with the highest (top) and lowest (bottom) classification error rates were selected for this example. The joint histogram of an ideal pseudo-CT would be distributed along the identity line.

2.3.2 [^{18}F]FDG PET evaluation

In this section, results obtained with the MRAC methods tested are presented in terms of accuracy of the resulting reconstructed PET image. Differences between OP-OSEM3D and FBP2D were negligible. Therefore only results generated with the iterative reconstruction algorithm are shown in their entirety. Part of the results obtained with the filtered back-projection algorithm is provided in section 2.3.2.6 for comparison.

2.3.2.1 Global bias

Figure 26 shows the absolute error (in %) between PET_{CTAC} and each PET_{MRAC} for GM, WM and CSF for static [^{18}F]FDG PET. Table 7 reports both relative and absolute biases per method and tissue class. For a given tissue class, both methods had similar average results. The mean and standard deviation of absolute bias were slightly, but not significantly, higher for *SingleAtlas* than for *MaxProb*. Results also revealed that the performance discrimination between *SingleAtlas* and *MaxProb* is less obvious using metrics computed from the reconstructed images than when they are directly computed from the generated pseudo-CT (difference to the *MaxProb* technique around 10 points using the Jaccard index on the pseudo-CTs vs. less than one point using the reconstructed PET images).

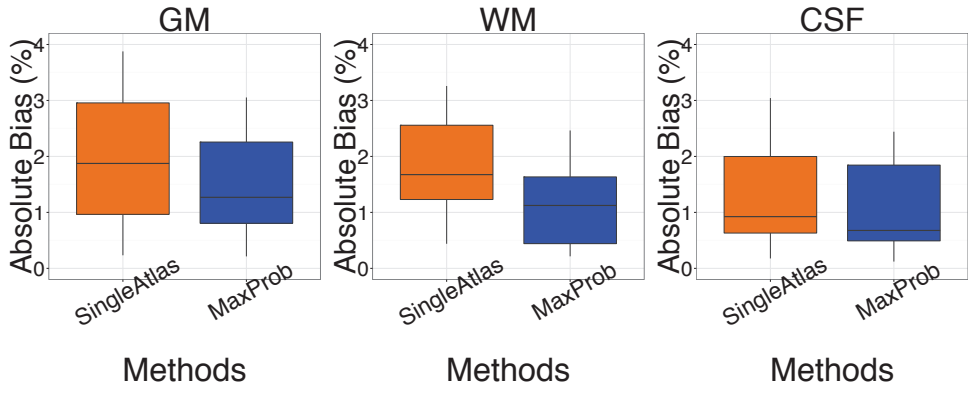

Figure 26: Boxplots of absolute bias per tissue class (in %) between the ground-truth [^{18}F]FDG PET (reconstructed with CT-based attenuation correction) and PET reconstructed with each pseudo-CT method. Plot features as above (Figure 23).

Table 7: Absolute and relative bias (mean ± standard deviation) per method and structure. Paired Wilcoxon signed-rank test (*: p<0.05 *MaxProb* vs. *SingleAtlas*) for both absolute and relative bias.

	Method	SingleAtlas	MaxProb	
	Bias (%)	mean sd	mean sd	
GM	Absolute	1.71 ± 1.05	1.43 ± 0.90	
	Relative	0.99 ± 1.78	0.26 ± 1.70	*
WM	Absolute	1.53 ± 0.88	1.16 ± 0.82	
	Relative	0.99 ± 1.48	0.01 ± 1.44	*
CSF	Absolute	1.17 ± 0.87	1.04 ± 0.70	
	Relative	0.36 ± 1.43	0.26 ± 1.25	

2.3.2.2 Regional bias

The mean regional bias (in %) measured for the 84 brain structures from [^{18}F]FDG images reconstructed with the *SingleAtlas* and *MaxProb* MRAC methods is shown in Figure 27.

With [^{18}F]FDG data, the mean bias obtained with the *MaxProb* method was mostly between 0 and 1% (range from -0.6 to 2.5%), with a slight tendency for overestimation rather than underestimation. Few structures had a bias larger than 2%: lateral part of anterior temporal lobe, middle and inferior temporal gyrus, fusiform gyrus and anterior orbital gyrus. Errors were larger with *SingleAtlas* (range from -2 to 4%) with a high variability that included over- and underestimations. There was substantial localized bias in all regions of the parietal lobe.

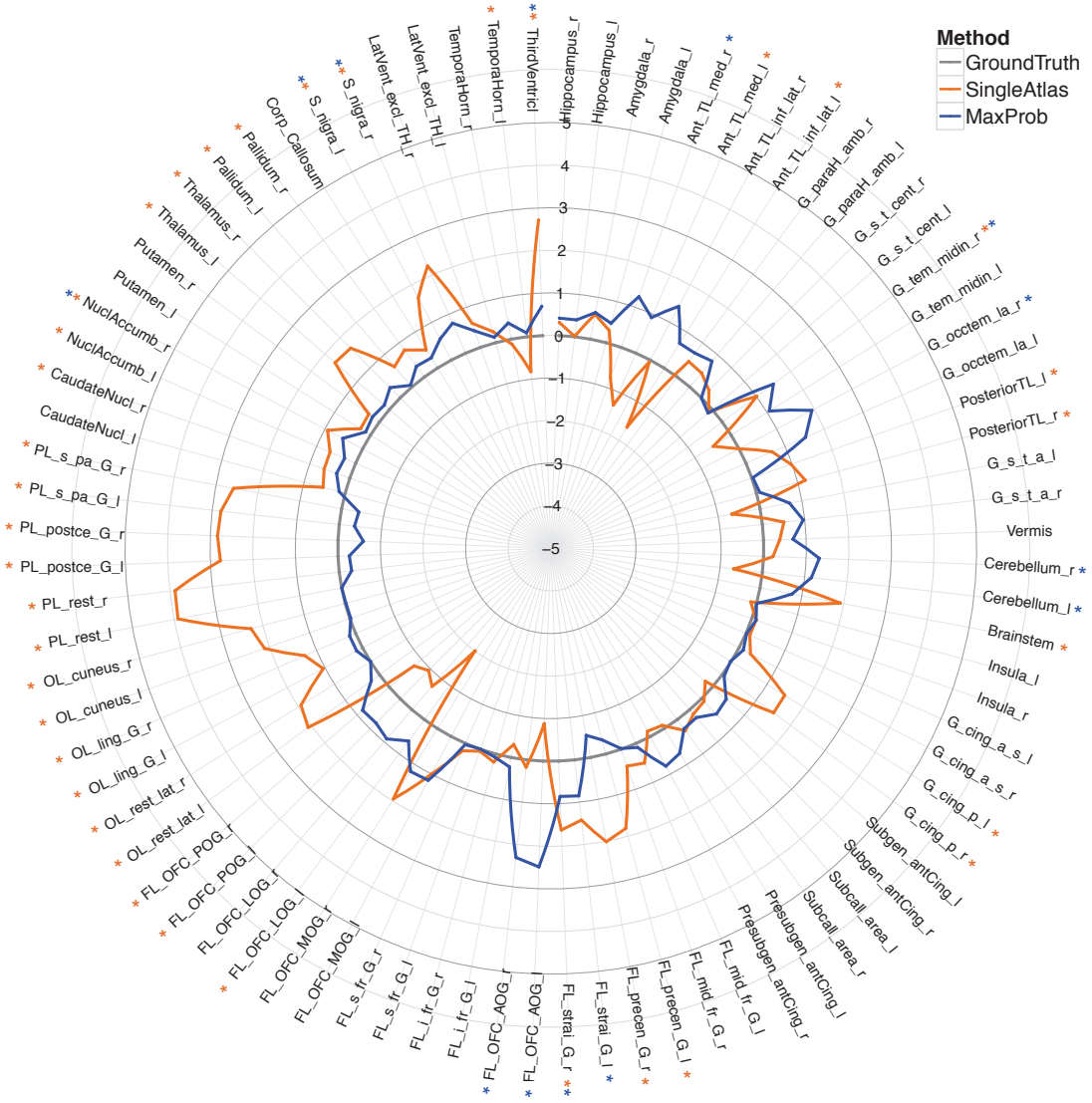

Figure 27: Mean bias for PET [^{18}F]FDG, per ROI and per AC method. Bias (in %) is represented in the radial axis. The regions correspond to the 83-region version of the Hammers_mith atlases (www.brain-development.org), with the cerebellar vermis added (see Methods). R, right; l, left; G, gyrus; TL/FL/OL/PL, temporal/frontal/occipital/parietal lobe; OFC, orbitofrontal cortex. For a full list of abbreviations, see Appendix (Table 10). Paired Wilcoxon signed-rank test (*: p<0.05 at the region level). Asterisks indicate that regional bias was significantly different from ground truth, for *SingleAtlas* (orange) and *MaxProb* (blue asterisks).

2.3.2.3 Parametric image of bias in normalized space

Figure 28 shows the mean voxel-wise difference images (averaged across the 23 subjects in the standard space) between ground truth CT and pseudo-CT (pseudo-CT – ground truth CT) as well as the mean voxel-wise relative error between the [^{18}F]FDG images reconstructed with the ground truth CT and those obtained with *SingleAtlas* and *MaxProb*.

The largest errors in synthetic pseudo-CTs can be seen at the air and bone boundaries. We note that due to the nature of the reconstruction process, there is no direct translation between inaccuracies in the CT image and the resulting bias in the reconstructed image. However, in general, underestimation of the pseudo-CT value leads to underestimation of the activity in the surrounding brain tissues in the PET image, and overestimation of the pseudo-CT value leads to overestimation of the activity in the surrounding brain tissues in the PET image. The *SingleAtlas* approach produces errors up to ±1000 HU in mean image difference. These inaccuracies were localized in bone and air-filled regions. [^{18}F]FDG PET data reconstructed with the *SingleAtlas* pseudo-CT showed local bias around -2 and 2% inside the brain. In some brain regions, the bias was greater than 25%, for example in the postcentral gyrus, the superior frontal gyrus and the cerebellum. With the *MaxProb* method, the error at the voxel level was near 0% throughout most of the brain. Error was predominantly localized in the regions of the brain adjacent to the skull, whereas bias was less substantial in the centre of the brain. Some small clusters of voxels approached 15% error, namely in the inferior temporal lobe, anterior orbital gyrus and the cerebellum. However the cerebellar errors became negligible when averaged over the cerebellar region of interest as a whole (see Figure 27 and Figure 28).

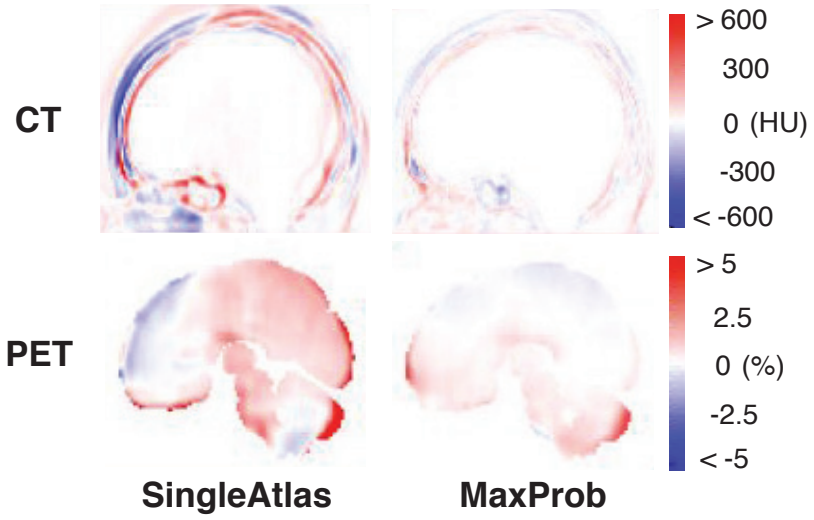

Figure 28: Top row, mean of 23 difference images between ground-truth CT and pseudo-CT (*SingleAtlas* and *MaxProb*), in standard stereotaxic space. Colour scale for CT differences: Hounsfield units. Bottom row, mean of 23 bias images between [^{18}F]FDG PET$_{CTAC}$ and [^{18}F]FDG PET$_{MRAC}$, in standard stereotaxic space. Colour scale for PET bias: percentage. The colour scale for CT image difference is thresholded at -600 and 600 HU to improve the display of local errors, although local difference in *SingleAtlas* images reached +1200 HU (dark red) and -1200 HU (dark blue). The colour scale for PET image bias is thresholded at –5 and 5% to improve the display of local errors, although local bias in *SingleAtlas* images reached 25% (dark red) and –17% (dark blue). A representative sagittal section is shown.

2.3.2.4 SPM analysis

The t score maps of the difference between PET_{CTAC} and the different PET_{MRAC} for the [^{18}F]FDG, thresholded at p<0.001, are shown in Figure 29. [^{18}F]FDG activity image corrected with the *SingleAtlas* AC showed more extensive regions of overestimation with higher t-scores (Figure 29**, 1a**) than those seen with *MaxProb* AC (Figure 29**, 2a**). Regions affected were the main part of parietal lobe, brain stem and orbitofrontal cortex. [^{18}F]FDG images corrected with the *SingleAtlas* AC were also affected by underestimation in disparate regions such as the frontal lobe and the cerebellum (Figure 29**, 1b**). Data corrected with *MaxProb* showed overestimation in few small clusters that were localized in the frontal lobe and orbitofrontal regions (Figure 29**, 2a**). No significant regions of underestimation were found (Figure 29**, 2b**).

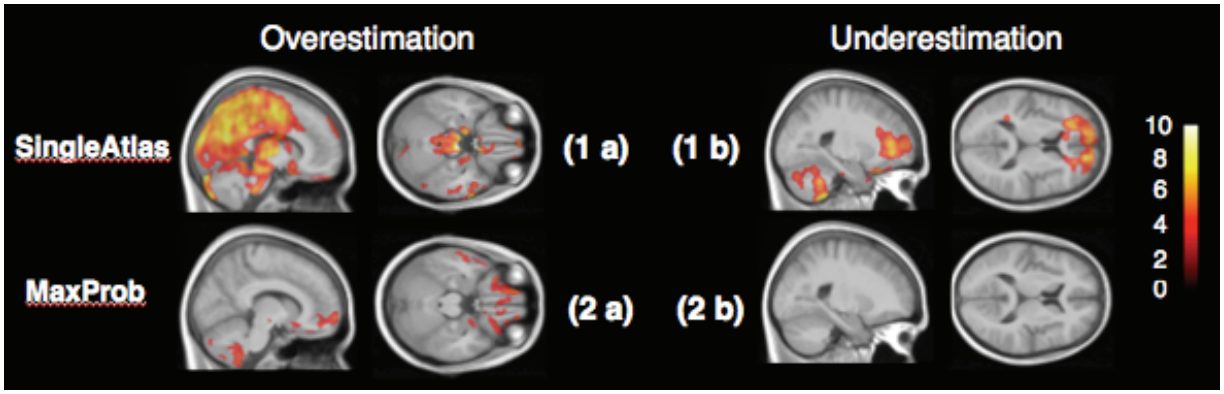

Figure 29: Comparison of static [^{18}F]FDG PET activity concentrations derived from ground truth AC PET data and data obtained with the two MRAC methods *SingleAtlas* (1) and *MaxProb* (2). The images show regions of overestimation (a) or underestimation (b) at a significance level of p<0.001 uncorrected. Colour scale: t statistic.

The illustrative statistical parametric maps shown in Figure 29 were then thresholded at a significance level of p<0.05 corrected for multiple comparisons, and only clusters with an extension exceeding the expected size (<k>=5.75) were retained. *SingleAtlas* yielded 43 significant clusters, covering large areas of the brain; slightly more than half were overestimations. In the cerebellum, the reference region for a number of PET tracers, eight significant clusters of overestimation were found with t-scores up to 7.2, and four significant clusters of underestimation with t-scores up to 6.8. The significant clusters represented more than 328 cm^3 (20%) of the analysed brain volume (1655 cm^3). In contrast, only two significant clusters of overestimation were found with *MaxProb* MRAC (in

the left anterior orbital gyrus, z 5.3, 223 mm^3, and right superior frontal gyrus, z 5.2, 96 mm^3), and no clusters of underestimation. This represented 0.02% of the analysed brain volume.

2.3.2.5 Outliers

We found two significant outlier subjects in the [^{18}F]FDG PET analysis, who had a regional bias exceeding 10% for some labels when *MaxProb* MRAC was used (five outliers with the *SingleAtlas* approach). Figure 30 shows PET data corrected with the *MaxProb* pseudo-CT. For the first subject, an abnormally strong signal in the PET image was observed around the anterior frontal cortex bilaterally, with a gradient in PET bias from the bone towards the centre of the brain. The other subject had a substantial overestimation in the bias map localized around the lateral part of the left temporal lobe, but no signal increase was visible on the PET image.

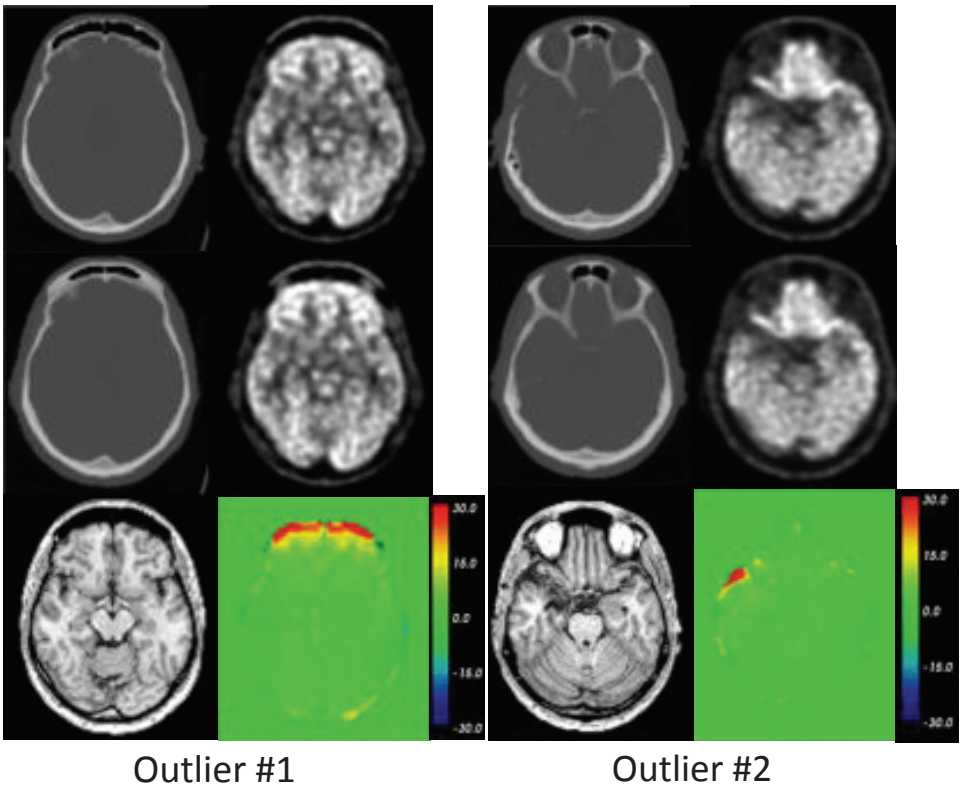

Figure 30: The two outlier subjects (bias exceeding 10% for some regions). All images are in stereotaxic space. First row: Ground-truth CT (left) and the corresponding [^{18}F]FDG PET image (right). Second row: *MaxProb* pseudo-CT (left) and the corresponding [^{18}F]FDG PET image (right). Third row: T1 MRI (left) and PET bias image reconstructed with the *MaxProb* pseudo-CT compared to the ground truth PET image (right). A representative axial section is shown.

2.3.2.6 PET reconstruction with FBP2D algorithm

Results for PET bias, for [^{18}F]FDG PET data reconstructed with the analytic FBP2D algorithm, are reported in Table 8 (global error) and Figure 31 (regional error). Differences between OP-OSEM3D and FBP2D reconstructions for global errors (Table 7 and Table 8) were inferior to 0.6% for both MRAC methods, *SingleAtlas* and *MaxProb*. The regional errors were under 2% for *MaxProb* except for one region (FL_OFC_AOG), similar to results obtained for OP-OSEM3D reconstruction. These few differences observed between reconstruction algorithms were expected, and can be explained by the convergence properties and positivity constraints. In conclusion, no meaningful performance differences of MRAC approaches due to the reconstruction algorithms were noticed. This aspect will be further developed in the next chapter, in the context of dynamic PET data.

Table 8: Absolute and relative bias (mean ± standard deviation) per method and structure for PET data reconstructed with the filtered back-projection algorithm. Paired Wilcoxon signed-rank test (*: p<0.05 *MaxProb* vs. *SingleAtlas*) for both absolute and relative bias. The results obtained with filtered back-projection were very similar to those obtained with the iterative reconstruction algorithm (Table 7).

	Method	**SingleAtlas**	**MaxProb**
	Bias (%)	mean sd	mean sd
GM	Absolute	1.69 ± 1.12	1.48 ± 0.96
	Relative	0.91 ± 1.84	0.32 ± 1.76 *
WM	Absolute	1.49 ± 0.91	1.21 ± 0.85
	Relative	0.86 ± 1.54	0.05 ± 1.50 *
CSF	Absolute	1.11 ± 0.92	1.10 ± 0.82
	Relative	0.00 ± 1.46	0.30 ± 1.36

Paired Wilcoxon signed-ranked test (*: p<0.05)

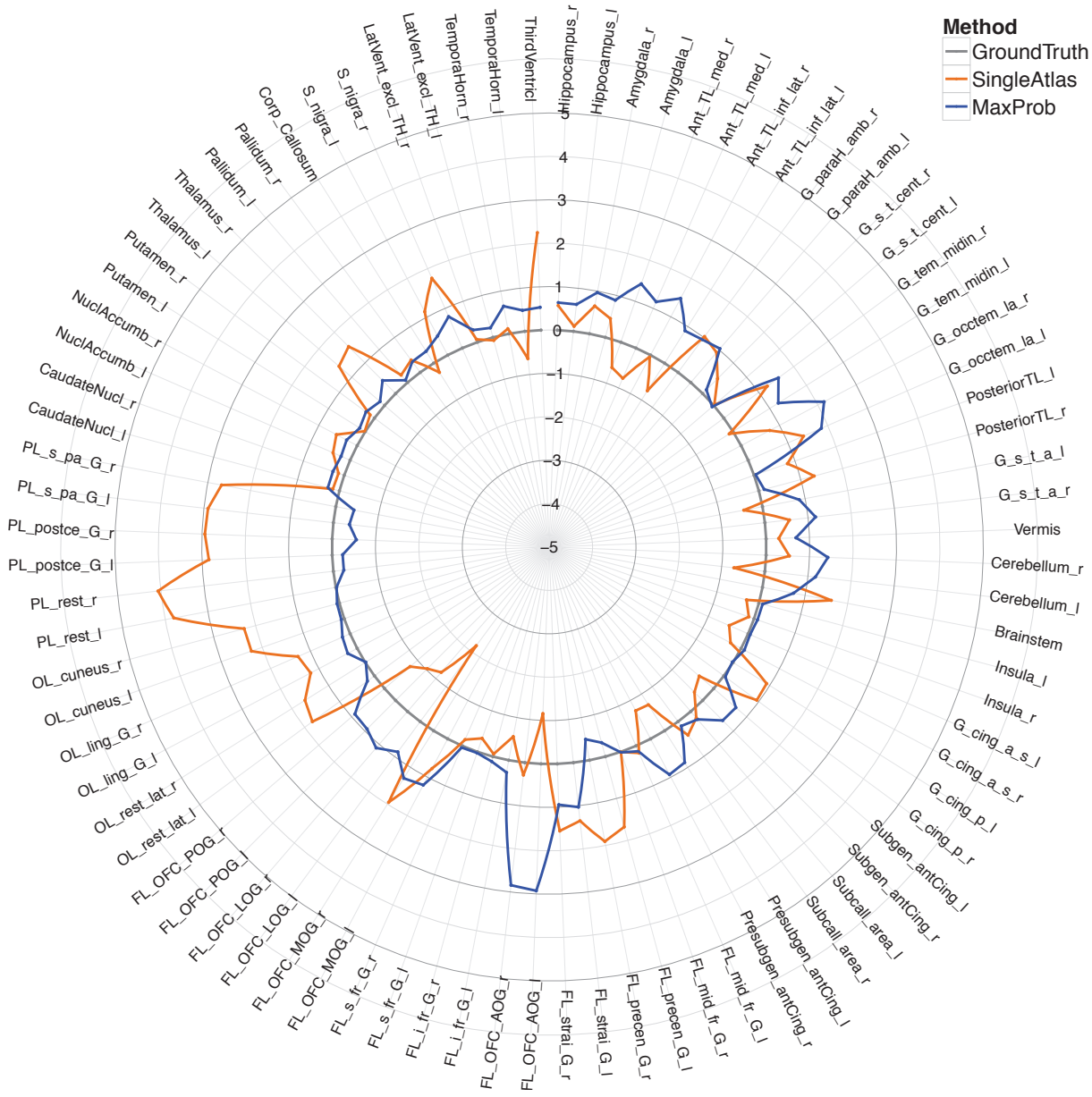

Figure 31: Mean bias for PET [^{18}F]FDG, per ROI and per AC method for PET data reconstructed with the filtered back-projection algorithm. Bias (in %) is represented in the radial axis. The regions correspond to the 83-region version of the Hammers_mith atlases (www.brain-development.org), with the cerebellar vermis added (see Methods). R, right; l, left; G, gyrus; TL/FL/OL/PL, temporal/frontal/occipital/parietal lobe; OFC, orbitofrontal cortex. For a full list of abbreviations, see Appendix (Table 10). The results obtained with filtered back-projection were very similar to those obtained with the iterative reconstruction algorithm (Figure 27).

2.3.2.7 Multi-method, multi-centric study

During my PhD I have participated in a multi-method study (Ladefoged et al., 2016) in which eleven MR-based AC solutions for brain imaging, developed by different research teams in the international community, have been assessed and compared. Part of the evaluation was performed on static [^{18}F]FDG scans of 201 subjects, including global, regional and voxel-wise quantitative criteria on μ-maps and reconstructed PET images. My role in this project was to set up a version of the *MaxProb* software that could be run in Copenhagen. I have also participated to an international meeting that gathered all participants to the multi-centric study to discuss the aims of the study as well as the evaluation strategy and the metrics used in the method comparison. Finally, I have provided the description of the *MaxProb* technique and commented the draft of the paper. Here, some of these results are reported in order to illustrate the performance of *MaxProb* in a different evaluation context.

The Jaccard overlap index was calculated to assess the pseudo-CT quality. For bone tissue, *MaxProb* obtained a Jaccard score of 81% in the multi-centre study, and a score of 76% was achieved in our evaluation (Table 2). Several metrics were used to quantify the bias introduced in PET_{MRAC}, in comparison to PET_{CTAC}. Figure 32 shows the average regional bias for ten anatomical regions defined on the MNI template, for three PET tracers ([^{18}F]FDG, [^{18}F]PiB and [^{18}F]Florbetapir). For [^{18}F]FDG, *MaxProb* produced low regional biases, ranging from -2 to 0%. For a more detailed assessment, the parametric images of relative difference are shown in Figure 33. As in our own study, *MaxProb* produced local errors between -1 and 1% (Figure 28).

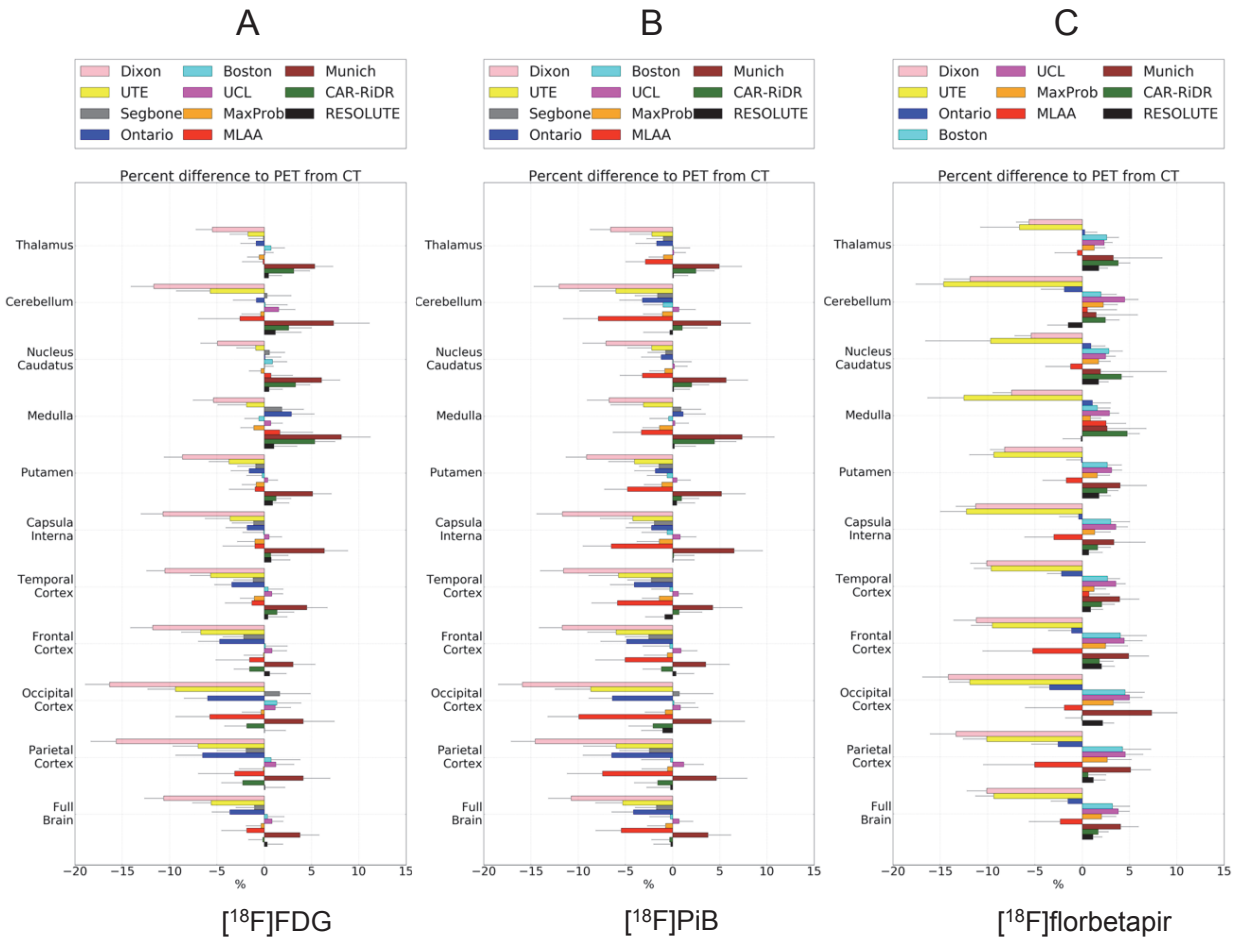

Figure 32: Global and regional ROI analysis across all patients obtained in the multi-centric study: [^{18}F]FDG (n=192, excluding patients with fat/water tissue inversion) (A), [^{18}F]PiB (n=47, excluding patients with fat/water tissue inversion) (B) and [^{18}F]florbetapir (n=85, excluding patients with fat/water tissue inversion) (C). The gray lines indicate 1 SD. Adapted from (Ladefoged et al., 2016).

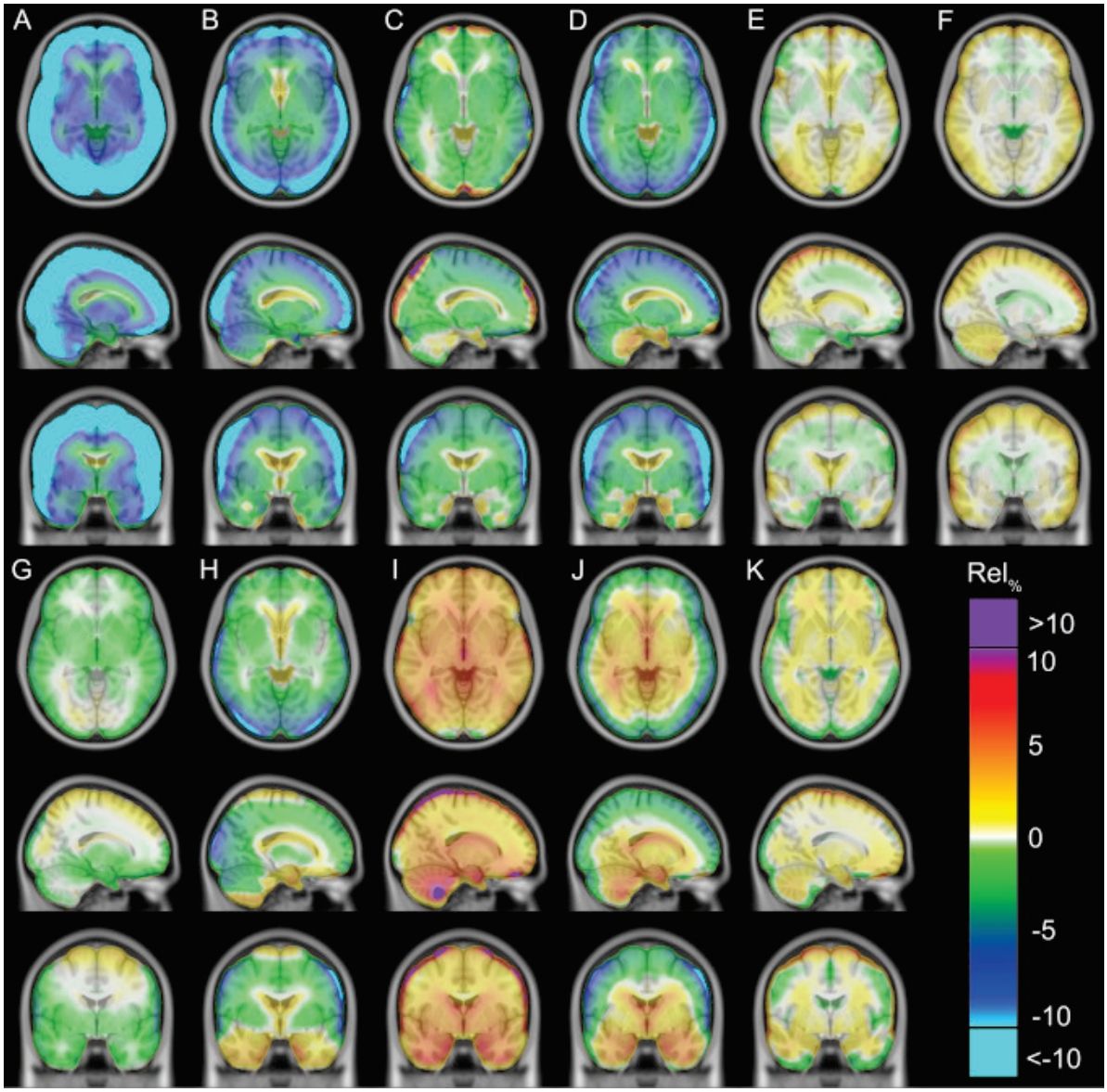

Figure 33: Mean of bias images across all [^{18}F]FDG patients (n=201, including patients with fat/water tissue inversion) for each method compared in the multi-centric study: Dixon (A), *UTE* (B), Segbone (Koesters et al., 2016) (C), Ontario (Anazodo et al., 2015) (D), Boston (Izquierdo-Garcia et al., 2014) (E), UCL (Burgos et al., 2014a) (F), *MaxProb* (G), MLAA (Benoit et al., 2016) (H), Munich (Cabello et al., 2015) (I), CAR-RiDR (Juttukonda et al., 2015) (J), RESOLUTE (Ladefoged et al., 2015) (K). Source: (Ladefoged et al., 2016).

2.4 Discussion

General comments

Pseudo-CTs could be generated with acceptable accuracy with *MaxProb*. *SingleAtlas* produced larger errors as well as many more outliers than the multi-atlas approach, a finding that we expected because a single image cannot reflect inter-subject variability (Heckemann et al., 2006).

We showed that both regional and local evaluation of the errors is relevant, since large bias localized in regions near bone may become averaged and not detected in a global and even a regional evaluation. This point is important for studies in neuroscience that focus on small brain structures, but also for clinical studies, e.g. in the presurgical evaluation for epilepsy, where small cortical abnormalities are sought. The results obtained with the different metrics confirmed strong coherence. Moreover, the detailed evaluation of both pseudo-CT and quantitative PET images allowed discriminating errors induced by the sensitive head regions in terms of attenuation (air and bone) and offered the possibility to locally Identify problems. This allows suggesting specific solutions to further improve the multi-atlas approach (discussed below).

Prior work has shown superiority of multi-atlas techniques over UTE for AC (Burgos et al., 2014a). At the beginning of my PhD, no UTE data was available, so *MaxProb* has not been directly compared to the vendor-provided MRAC solution in this first evaluation. Chapter 4 provides a direct comparison of UTE-based AC and our multi-atlas proposition, in an applicative context.

Atlas database

Our multi-atlas method has been implemented and tested with two different atlas databases. The first database, described in this chapter, contained 40 subjects and initial CT resolution of 0.58 × 0.58 × 1.5 mm^3 (Merida et al., 2015). The second, with 38 atlases and a coarser initial CT resolution (1.37 × 1.37 × 5 mm^3) was used in our preliminary work (Merida et al., 2015) and in the multi-centric study (Ladefoged et al., 2016). The results with both databases were very similar (see Appendix). This is important, as it suggests that the multi-atlas strategy performs similarly across databases. Currently,

a third database with larger FOV that will allow generating the attenuation coefficients for the neck, is under investigation.

Remaining errors on pseudo-CT images

In the MRAC methods, attenuation of brain structures that have boundaries with air cavities or with bone is difficult to estimate because of the low contrast between air and bone in the MR images. Figure 28 shows that CT values in such regions were particularly biased for *SingleAtlas*, but were well managed in the multi-atlas approach despite a slight local overestimation of around 300 HU. The effect of error on bone was generalized in the *SingleAtlas* AC method, and these inaccuracies produced both overestimations and underestimations on PET images all around the cortex. The small residual bias observed on the parametric image for *MaxProb* (Figure 28) may be partially affected by a lack of information around the neck in the atlas database. The new database with extended field of view can be used to address this problem.

Outliers in PET quantification

We found an anatomical explanation for the unusually large local errors in PET data seen in two subjects: outlier #1 had abnormally large frontal sinuses and outlier #2 had undergone a lobectomy via a craniotomy in the lateral skull overlying the temporal lobe. These characteristics can be observed on the real CT images. The multi-atlas methods did not handle these anatomical abnormalities well. However, bias remained localized to the immediate vicinity of the pseudo-CT abnormalities (Figure 30). The cluster showing high quantification error for outlier subject #2 (Figure 30) was located in the CSF, explaining why no difference was visually discernible on the PET images (Figure 30). The outlier detection was based on the regional quantification, which did not handle the postoperative change correctly, while there was no relevant error propagation into the brain image itself.

The signal increase resulting from anatomical variants or postoperative changes may conceivably sometimes be clinically pertinent and would present a risk for misdiagnosis if the AC error was not noticed. In our case, the errors in the pseudo-CTs can be predicted from visual review of the MR image (large frontal sinuses can be seen on T1-weighted MRI) for outlier #1 and from the medical

history (craniotomy) for outlier #2. In PET-MR imaging, similarly to PET/CT but possibly even more so, referring clinicians should take care to provide an accurate request that lists all pertinent history. Similarly to PET/CT, reporting clinicians have to be aware of possible pitfalls, and should be able to simultaneously visualize the PET image, the MR image, and the attenuation map, and perhaps explicitly check for unusually large sinuses or fluid-filled sinuses (for which we did not have examples in our cohort). It is to be expected that reporting clinicians will become accustomed to PET-MR artefacts, just as they already are accustomed to interpreting e.g. FLAIR artefacts, or CT artefacts due to bone or metal. For now, areas close to craniotomies may be difficult to interpret, and clinicians should remain aware of the possibility of large sinuses causing local artifacts. In some special cases, e.g. in the case of brain tumours with craniotomies, it may be preferable to plan for an additional low-dose CT scan.

MaxProb: from limitations to methodological improvement

The *MaxProb* approach was based on a relatively simple scheme. The subject's MRI was only used to perform the registration of the atlas database to the subject space. In general, *MaxProb* provided good (or acceptable) performance and accurate air/bone segmentation. Nonetheless, looking at the detailed evaluation, two main sources of errors could still be identified. First, brain regions close to skull (the cortex) presented errors slightly higher than the other areas of the brain (Figure 28, Figure 33). These errors were probably due to inaccuracies in skull attenuation coefficients assigned by the multi-atlas technique. Second, as shown in section 2.3.2.5, registration errors due to abnormal anatomies not represented in the atlas database or because of artefacts in the MR image could impact the accuracy of the generated pseudo-CT. These errors were then propagated to the PET image.

Taking into account the two main above-mentioned limitations, the *MaxProb* method might be further improved by combining the following ideas: *MaxProb* in its actual version would allow generating the pseudo-CT and compute attenuation coefficients in the whole volume. In addition, bone tissue could be segmented by thresholding the pseudo-CT image. In order to better capture subject particularities in skull densities and improve attenuation coefficients, a fit of MR and CT intensities can be used in bone tissue as proposed by Ladefoged et al. (2015) or Juttukonda et al. (2015). For this step a UTE image of the subject, in addition to the T1-weighted MRI, should be acquired. A second refinement of the multi-atlas scheme could be realized by integrating the MR

information into the atlas selection and fusion step. Different MR sequences could be considered, additionally to the T1, such as the UTE or new ZTE sequences in which bone can be better distinguished than in the T1. MR information could be integrated to the algorithm via simple classification probability maps (e.g. SPM Segment) or by computing more sophisticated confidence maps between MR and CT images. Finally, several techniques to combine the information could be taken into account: simple hierarchy routine; combining probabilities; or machine learning algorithms. Another criterion also interesting to explore would consist in a selection of the atlases based on metadata (age, sex…) prior to the multi-atlas pipeline.

Other ideas for further investigation

The multi-atlas method could also in principle be refined by updating the coordinate system, rather than reslicing the MR in CT space. Another area to investigate is the effect of the degree of smoothing of the pseudo-CT (the pseudo-CT is smoother than the ground truth CT due to its construction process) in the reconstruction process and the impact on quantitative PET analysis. A Gaussian smoothing is usually applied to CT (or pseudo-CT) in the reconstruction pipeline for PET/CT data. As the pseudo-CT is built by averaging several individual atlas CT images, it contains a certain amount of smoothing. So it would be interesting to determine the additional smoothing that we need to apply to fairly compare it to the ground truth CT. This question will be raised again when using the UTE-based attenuation map provided by the vendor.

2.5 Conclusion and perspectives

The *MaxProb* method permitted generating pseudo-CT images for brain MRAC with high accuracy. Performance for PET quantification was achieved within likely acceptable limits established by the community (± 5% of CT-based reference). In the multi-centric study (Ladefoged et al., 2016), *MaxProb* also provided very good results and was among the top three techniques proposed in the literature.

MaxProb was implemented into a Matlab program and shared with two other centres: the Rigshospitalet (Copenhagen) for the multi-centric study and King's College London where the method is currently being validated with their own data and will be used soon in clinical research protocols.

The software is ready to be distributed to other centres and an atlas database will be available for academic collaborations.

Further work will be focused on the extension of the multi-atlas approach developed for adult human brain to paediatric imaging. As children have slightly different head shapes and especially different bone densities compared with adults, we expect that a dedicated database of children atlases will be more appropriate (or several databases per age range to take into account anatomical variability in child development). Such a database is already available at the CERMEP. We are also planning to adapt *MaxProb* to non-human primate (NHP) imaging. Several PET-MR protocols on NHP have started at the CERMEP. The vendor MRAC solution is not optimized for NHP and the μ-map computed by the scanner is generally aberrant. A database of CT and MR image pairs is being acquired for several individuals, and will be used to transpose the *MaxProb* multi-atlas approach to NHP. We expect that the registration will possibly be the more difficult step that will require adapting the registration parameters used.

In the literature, all procedures proposed for attenuation map generation have only been assessed in the context of static PET acquisition, generally using [^{18}F]FDG PET data. In this chapter, we have focused the evaluation of our new multi-atlas solution in a similar context, using a large range of quantitative criteria. Ladefoged et al. (2016) have recently shown that different AC methods can present varying performance depending on the PET tracer used ([^{18}F]FDG, [^{11}C]PiB and [^{18}F]florbetapir). Those results suggest that the AC performance may depend on the tracer spatial distribution (variation of contrast) in brain, and deserve further validation. In the next chapter, this phenomenon is investigated via dynamic PET acquisitions, which are characterized by tracer spatial distribution changes over time.

3 Chapter 3

Impact of MR-based AC on dynamic PET data

Two major observations emerge from previous chapter. First, results showing the dependence of the accuracy of MRAC methods according to the PET tracer used suggest that AC performance may depend on the tracer spatial distribution (variation of contrast) in the brain. As we seek the best AC performance whatever the tracer used, this observation is an obvious limitation and raises the question of the behaviour of MRAC in the context of dynamic PET data. During dynamic acquisition, the spatial distribution of any tracer changes over time. It depends on its transport by blood especially immediately after the injection, and after few minutes increasingly on its specific uptake to targeted molecules or neuronal receptors. Secondly, MRAC methods tend to introduce inhomogeneous local bias: regions close to the skull are often more affected than subcortical areas, and this is particularly true for the cerebellum (Andersen et al., 2014). These inhomogeneities can impact PET quantification studies, for example when a reference region is used in the quantification process. In clinical applications of PET, SUV (standardized uptake value) is often normalized by the activity in the cerebellum (SUVr). In research studies, simplified kinetic modelling also requires a reference region to avoid measuring arterial input function for estimating transport or binding parameters of the tracer. Again, the cerebellum is often chosen as reference region.

Research brain PET studies typically use dynamic acquisitions to characterize physiological parameters of neuronal mechanisms, glucose and oxygen metabolism, or cerebral blood flow. In the last years, interest for dynamic PET imaging on simultaneous PET-MR systems requiring accurate quantification in both clinical and research contexts has increased, and no performance data on MR-based AC for dynamic PET imaging have been published so far.

In this chapter we propose an novel evaluation of dynamic PET data quantification using MR-based AC methods. We characterize and quantify the dependence of PET quantification on tracer spatial distribution, for a tracer with spatially heterogenous specific binding. Dynamic assessment is performed with 2'-methoxyphenyl-(N-2'-pyridinyl)-p-[^{18}F]fluoro-benzamidoethylpiperazine ([^{18}F]MPPF), a selective antagonist at 5-HT$_{1A}$ receptors mainly found in limbic structures. Evaluation presented in this chapter includes accuracy on radioactivity measured and binding parameters estimated from kinetic modelling using a reference region.

3.1 Materials

3.1.1 Atlas database

The same database that the one described in Chapter 2 was used for the study presented in this chapter. The database was composed of CT and MR image pairs from 40 subjects.

3.1.2 Test data

3.1.2.1 PET scanning

Among the 40 subjects of the database, seven subjects [mean age ± SD, 33.4 ± 9.8 y; range, 19–44 y] had a dynamic PET scan during 60 min starting with the injection of 164 ± 42.6 MBq of [^{18}F]MPPF. PET and reference CT scans were obtained on a Siemens Biograph mCT PET/CT. PET data were acquired in list mode.

3.1.2.2 PET reconstruction

[^{18}F]MPPF data were rebinned into 35 time frames (variable length frames, 15 × 20 s, 15 × 120 s, 5 × 300 s) for multi-frame dynamic reconstruction. Both FBP2D and OP-OSEM3D algorithms were used for individual frame reconstruction, and identical reconstruction parameters as for static [^{18}F]FDG data were used (see Chapter 2). The final reconstructed volumes had a voxel size of 1.06 × 1.06 × 2.02 mm^3 in a matrix of 128 × 128 × 109 × 36 voxels.

3.1.2.3 Modelling of [^{18}F]MPPF kinetics

The brain distribution of a radiotracer that crosses the blood-brain barrier (BBB) can be described by a compartmental model. This model is used to explain the dynamic PET kinetic in a tissue volume. The simplest model is a one-tissue compartment model (1TC). For a tracer that specifically binds a receptor, a more realistic model is the two-tissue compartment model (2TC). In the first tissue compartment of a 2TC model, the tracer is free or non-specifically bound. This compartment is called

non-displaceable compartment, as the tracer concentration is not sensitive to a displacement by a pharmacological agent specific to the same receptor as the tracer. The second tissue compartment is the specific compartment, where the tracer is specifically bound to its receptor. The 2TC model is characterized by parameters describing transport across the BBB (K_1 and k_2), and local uptake (k_{on}, k_{off} and B_{max}). In the absence of an arterial input function, parameters of a 2TC compartment model can not been estimated. However, some macro parameters combining the transport and uptake parameters can be derived, considering the 2TC model in target region (region with available receptor for the tracer), and a reference region. In *in vitro* binding studies of a compound to a receptor, the Binding potential (BP) is defined by the ratio of the receptor density (concentration) to compound affinity for the receptor. In *in vivo* PET studies, several BP variants can be defined (Innis et al., 2007). One of them is the non-displaceable binding potential (BP_{ND}) defined as the ratio of specifically bound tracer concentration to non-displaceable tracer concentration ($BP_{ND} = C_S/C_{ND}$).

This BP_{ND} can be computed with the simplified reference tissue model (SRTM) in a two-compartmental framework ((Lammertsma and Hume, 1996); Figure 34). Under several assumptions, the three parameters of the SRTM (R_1, k_2 and BP_{ND}) can be solved using different methods. In our study, the [^{18}F]MPPF data were modelled with SRTM, and the basis function approach developed by Gunn et al. (1997) was used. The reference used in the model was the mean time activity curve of the cerebellar grey matter (excluding the cerebellar vermis), i.e. parts of the cerebellum that are devoid of specific 5-HT_{1A} receptor binding (Parsey et al., 2005). Parametric BP_{ND} images of 5-HT_{1A} receptor distribution were generated. Figure 35 shows the mean parametric BP_{ND} map of 5-HT_{1A} receptor distribution across the seven subjects.

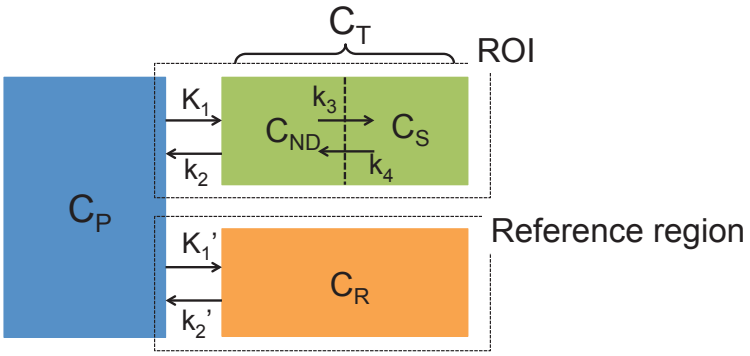

Figure 34: Compartmental model.

The relationship between C_T and C_R is given by (**Equation 9**):

$$\frac{dC_T(t)}{dt} = R_1 \frac{dC_R(t)}{dt} + k_2 C_R(t) - \frac{k_2}{1+BP_{ND}} C_T(t) \qquad \text{(Equation 9)}$$

where:

- C_P: Metabolite-corrected plasma concentration (kBq.ml^{-1})
- C_{ND}: Concentration of free (i.e. not specifically bound) ligand (kBq.ml^{-1})
- C_S: Concentration of specifically bound ligand (kBq.ml^{-1})
- C_T: Concentration in ROI tissue (kBq.ml^{-1})
- C_R: Concentration in reference tissue (kBq.ml^{-1})
- K_1: Rate constant for transfer from plasma to free compartment (ml.ml^{-1}.min^{-1})
- k_2: Rate constant for transfer from free to plasma compartment (min^{-1})
- k_3: Rate constant for transfer from free to bound compartment (min $^{-1}$)
- k_4: Rate constant for transfer from bound to free compartment (min^{-1})
- K_1': Rate constant for transfer from plasma to reference compartment (ml.ml^{-1}.min^{-1})
- k_2': Rate constant for transfer from reference to plasma compartment (min^{-1})
- $R_1 = K_1/K_1$'
- $BP_{ND} = k_3/k_4$

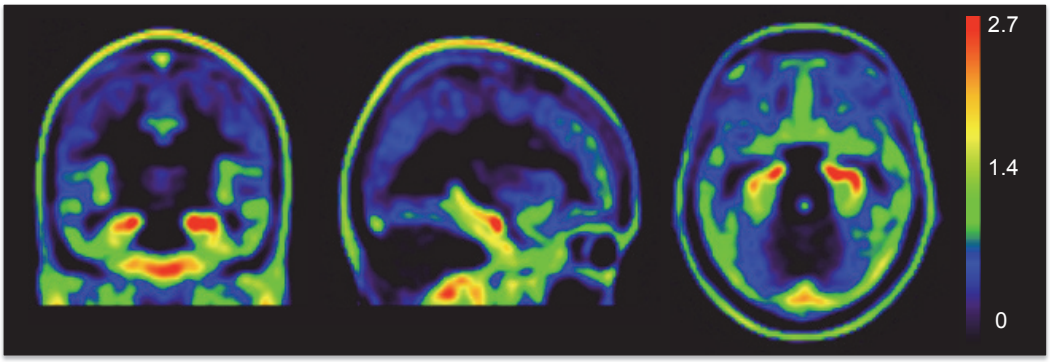

Figure 35: Mean BP_{ND} image across seven subjects, in standard space after spatial normalization. Note the limbic distribution with high BP_{ND} in the mesial temporal lobes, followed by other temporal regions, insula and cingulate gyri.

3.2 Methods

3.2.1 Pseudo-CT generation

SingleAtlas pseudo-CT and *MaxProb* pseudo-CT were generated for the seven test subjects following the methodology detailed in Chapter 2 (sections 2.2.1 and 2.2.2). The multi-atlas approach was computed in a leave-one-out scheme of the seven subjects within the atlas database of 40 subjects.

Dynamic [^{18}F]MPPF data were reconstructed with three different attenuation maps: *SingleAtlas* ($PET_{SingleAtlas}$), *MaxProb* ($PET_{MaxProb}$) and ground truth CT (PET_{ACCT}). The MRAC solutions were compared to ground truth CT in terms of quantitative PET, using several metrics computed on the dynamic PET data.

3.2.2 Evaluation criteria

The bias introduced by the MRAC methods on dynamic [^{18}F]MPPF data was assessed on radioactivity images and parametric images of the physiological parameter extracted from kinetic modelling (BP_{ND}). I also investigated the effect of activity distribution on the accuracy of PET activity quantification with the MRAC methods.

3.2.2.1 Regional analysis

Regional mean and standard deviations of [^{18}F]MPPF and BP_{ND} images were extracted in a selection of regions of the Hammers_mith MRI segmentation (see Chapter 2, section 2.1.2.3) that exhibit specific [^{18}F]MPPF binding, plus the cerebellum. The resulting 44 ROI were masked by the GM. The relative errors between PET_{CTAC} and PET_{MRAC} were calculated for each ROI. Average bias for each cerebral region was computed across the subjects. Statistical significance of the differences in regional evaluation between ground truth and MRAC methods was studied with a paired Wilcoxon signed-rank test.

3.2.2.2 Joint histograms

Joint histograms of the BP_{ND} images generated from dynamic $PET_{SingleAtlas}$ and $PET_{MaxProb}$ were plotted versus the BP_{ND} image from dynamic PET_{CTAC}.

3.2.2.3 Kinetics

[^{18}F]MPPF time activity curves (TAC) were extracted for several ROIs. The first frame was removed because of low count rates close to zero. The bias on TACs was computed by calculating the relative error frame by frame. The frame biases were then averaged across subjects.

3.3 Results

This section describes the impact of the AC approach on the quantification of dynamic [^{18}F]MPPF PET data and the subsequent kinetic modelling. As in the previous evaluation on static [^{18}F]FDG (chapter 2), OP-OSEM3D and FBP2D reconstruction algorithms showed similar tendencies in the dynamic evaluation, therefore only results obtained with the iterative reconstruction algorithm are shown in their entirety. Part of the results obtained with the filtered back-projection algorithm is provided in section 3.3.5 for comparison.

3.3.1 Regional evaluation

Results of regional evaluation using [^{18}F]MPPF are shown in Figure 36 for a selection of 44 regions that exhibit specific [^{18}F]MPPF binding (Costes et al., 2002). To investigate the effects of the inaccuracies produced by the tested MRAC methods on the kinetic modelling step, we present the mean bias computed from the late static [^{18}F]MPPF images (generated by time-weighted averaging over the final ten minutes of the acquisition; shown as dotted lines), as well as the mean bias for the BP_{ND} images (as solid lines).

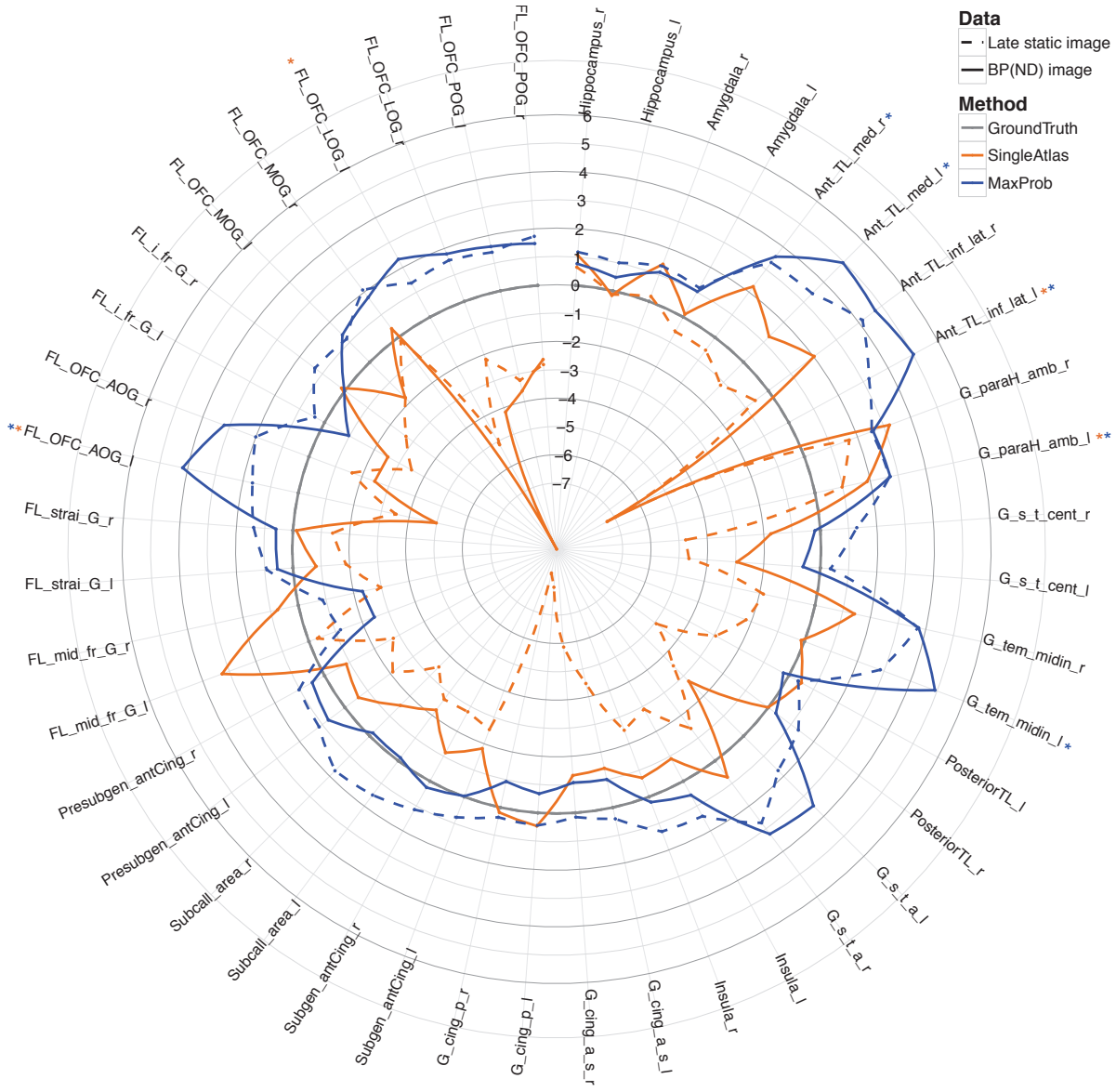

Figure 36: Mean bias for the late static [^{18}F]MPPF images (dotted lines) and for BP_{ND} images (solid lines), per selected relevant ROI and per AC method. R, right; l, left; G, gyrus; TL/FL/PL, temporal/frontal/parietal lobe; OFC, orbitofrontal cortex. For a full list of abbreviations, see Appendix (Table 10). Paired Wilcoxon signed-rank test (*: p<0.05 at the region level), shown for BP_{ND} images only.

The bias measured from late static [^{18}F]MPPF images was higher than for [^{18}F]FDG data (Chapter 2, section 2.3.2.2), with the mean error ranging from -1.2 to 5.0% for *MaxProb*. As for the [^{18}F]FDG evaluation, a general overestimation for most of the assessed regions was also noted. *SingleAtlas* showed bidirectional, but mainly negative, bias (from -8.5 to 1.7%) for the tested brain structures. The variability of the bias was again higher than for the *MaxProb* method.

Bias on the BP_{ND} ranged from –2.5 to 5.0% for *MaxProb*. For *SingleAtlas,* the maximum negative bias reached –9.3% and the positive bias reached 3.3%. Two regions were particularly strongly affected by errors: lateral orbital gyrus (–9.3%) and lateral part of anterior temporal lobe (–7.3%). In the BP_{ND} images, error patterns did not match well with errors in activity values measured in the late static [^{18}F]MPPF images.

Figure 37 shows an example of [^{18}F]MPPF PET image at early and at late-phase of the dynamic acquisition for a randomly selected subject. An example of a late-phase [^{18}F]FDG PET image (from a different subject) is shown for comparison. Note the very different activity distribution in the brain, depending on the tracer used and the time of acquisition relative to injection.

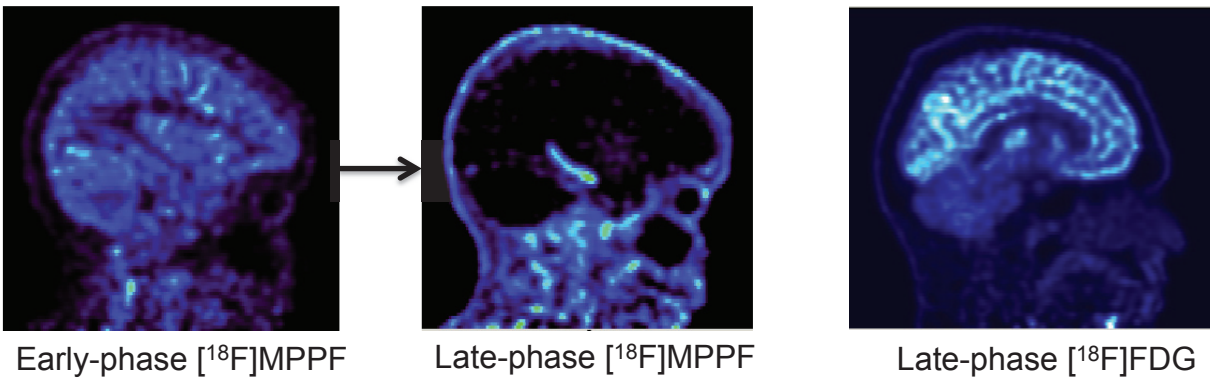

Figure 37: Example of radioactivity spatial distribution at different times for [^{18}F]MPPF, and a late image of the [^{18}F]FDG uptake in the brain.

3.3.2 Evaluation on BP_{ND} images

The joint histograms of mean BP_{ND} $PET_{SingleAtlas}$ and $PET_{MaxProb}$ versus PET_{ACCT} are shown in Figure 38. Linear regressions and goodness-of-fit value (R^2) are reported in the graphs. When no mask was applied to the BP_{ND} images (i.e. the whole image was considered), both MRAC approaches obtained strong correlation compared to CTAC (R^2=0.96 for *SingleAtlas* and R^2=0.99 for *MaxProb*), but the dispersion of BP_{ND} values for *SingleAtlas* was higher than for *MaxProb*. However, if mean BP_{ND} images were masked (i.e. only the 44 ROIs were considered), both MRAC methods provided similar results.

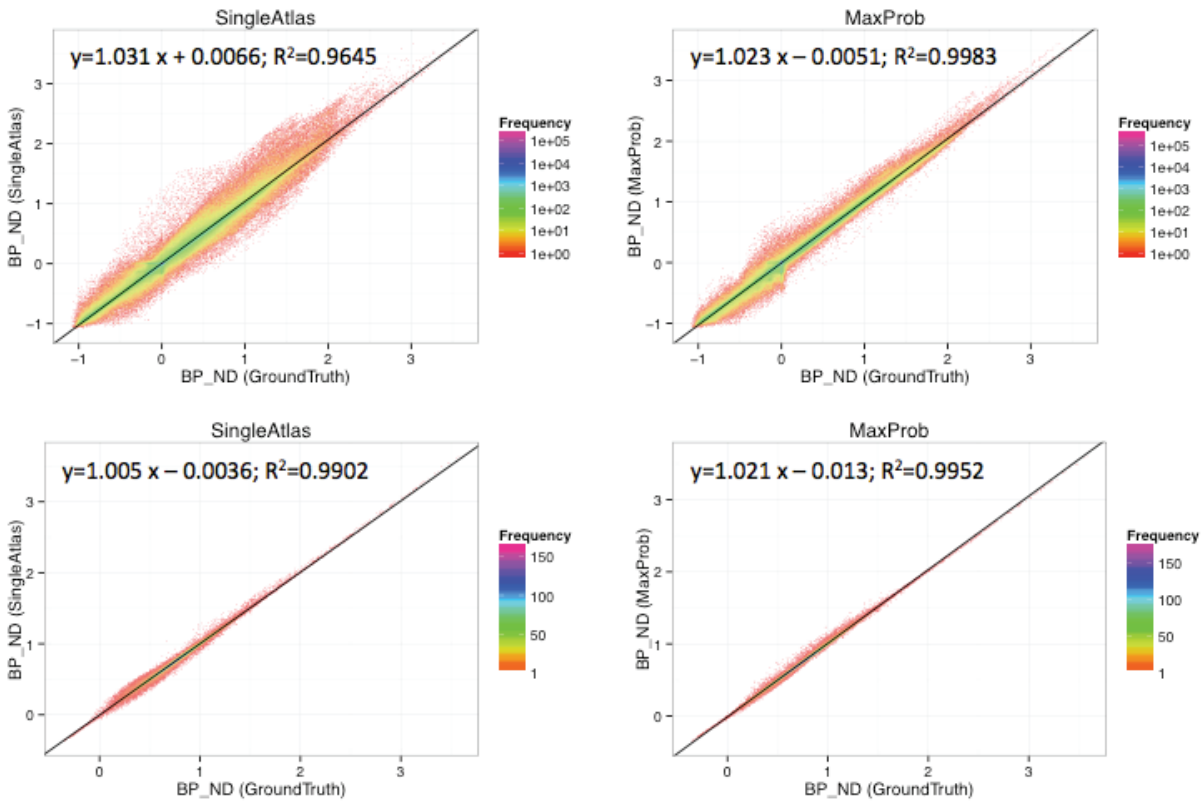

Figure 38: Joint histograms of mean parametric BP_{ND} images across subjects in normalized space. Joint histograms were calculated within the whole image (top row) or within the 44 ROI (bottom row). yBP_{ND} (*SingleAtlas*) vs. BP_{ND} (ground truth CT) (A) and BP_{ND} (*MaxProb*) vs. BP_{ND} (ground truth CT) (B).

3.3.3 Evaluation on time activity curves

The analysis of the measured TACs showed that the mean bias computed from the early static PET image (corresponding to the first three minutes of the dynamic image, during the perfusion of tracer in the tissues) across the 44 investigated regions was 0.2 ± 0.8 % for *SingleAtlas* and 1.0 ± 0.7 % for *MaxProb*, while when computed from the late static PET image (the last ten minutes of the dynamic image) and across the same regions the mean bias was -2.6 ± 2.2 % for *SingleAtlas* and 1.5 ± 1.1 % for *MaxProb*, suggesting first that inaccuracies in AC maps impacted the reconstructed time frames differently and that, overall, the resulting error seemed to increase in magnitude over time with the two MRAC methods tested.

Mean errors computed as a function of time for selected regions that were obtained with *SingleAtlas* and *MaxProb* are shown in Figure 39. The graph reports bias on the time-activity curve across time for the cerebellum excluding vermis (no specific binding, reference region for modelling),

hippocampus (high binding of [^{18}F]MPPF), anterior temporal lobe lateral part (a region where both MRAC methods had substantial bias on BP_{ND}) and posterior temporal lobe (a region where both MRAC methods had weak bias on BP_{ND}). Only labels in left hemisphere are shown here but, in general, similar curves were obtained for the labels in the right hemisphere. Overall, the magnitude of the mean bias tended to increase during the measurement period. This was the case for most of the 44 studied regions. However, the magnitude of bias was lower and less time dependent for the *MaxProb* approach than for the *SingleAtlas* method.

For the cerebellum, the reference region used for [^{18}F]MPPF modelling, the bias on TACs fluctuated over time between -2 and 2% for *SingleAtlas* and 0 and 2% for *MaxProb*. The bias tended to increase slightly over time, in particular for *SingleAtlas*. In the hippocampus, both methods yielded very low and almost constant bias over time and negligible bias for BP_{ND}. For the lateral part of anterior temporal lobe, the magnitude of bias increased over time, with a higher slope in the case of *SingleAtlas*. In this region, the bias reached 4% during the last ten minutes of the acquisition for the *MaxProb* method and -7.5% for *SingleAtlas*. The resulting BP_{ND} was also strongly biased for both MRAC methods. A large increase (around 4%) in bias magnitude was observed in the posterior temporal lobe for the *SingleAtlas* method, whereas the bias remained stable with *MaxProb*. However, the biases obtained for BP_{ND} were very close to 0% for both MRAC methods.

Figure 40 provides a generalized analysis of results highlighted in Figure 39. Figure 40 shows, for each of the seven subjects, the mean bias (in %) averaged across the 44 regions and plotted for each time frame as a function of the intra-frame coefficient of variation (COV = SD*100/mean). The COV represents the activity non-uniformity between regional measurements, i.e. the degree of tracer distribution inhomogeneity, and therefore, for [^{18}F]MPPF, increases with time (cf. Figure 37). For the *SingleAtlas* method there is a strong correlation between the mean bias and the COV of the frame: the bias linearly increased in magnitude with COV. This ultimately suggests a dependence of bias on the spatial distribution of the activity: early frames, corresponding to the perfusion of the tracer, exhibited homogeneous activity distributions (lowest COV) and led to the lowest biases, while late frames are more representative of the specific binding and yielded higher COV and bias. *MaxProb* yielded time activity measurements with errors that were significantly less dependent on the activity distribution. This was confirmed by the computation of the mean slope across the seven subjects included in the study which was -7.0 for *SingleAtlas* and 1.2 for *MaxProb* (Figure 40).

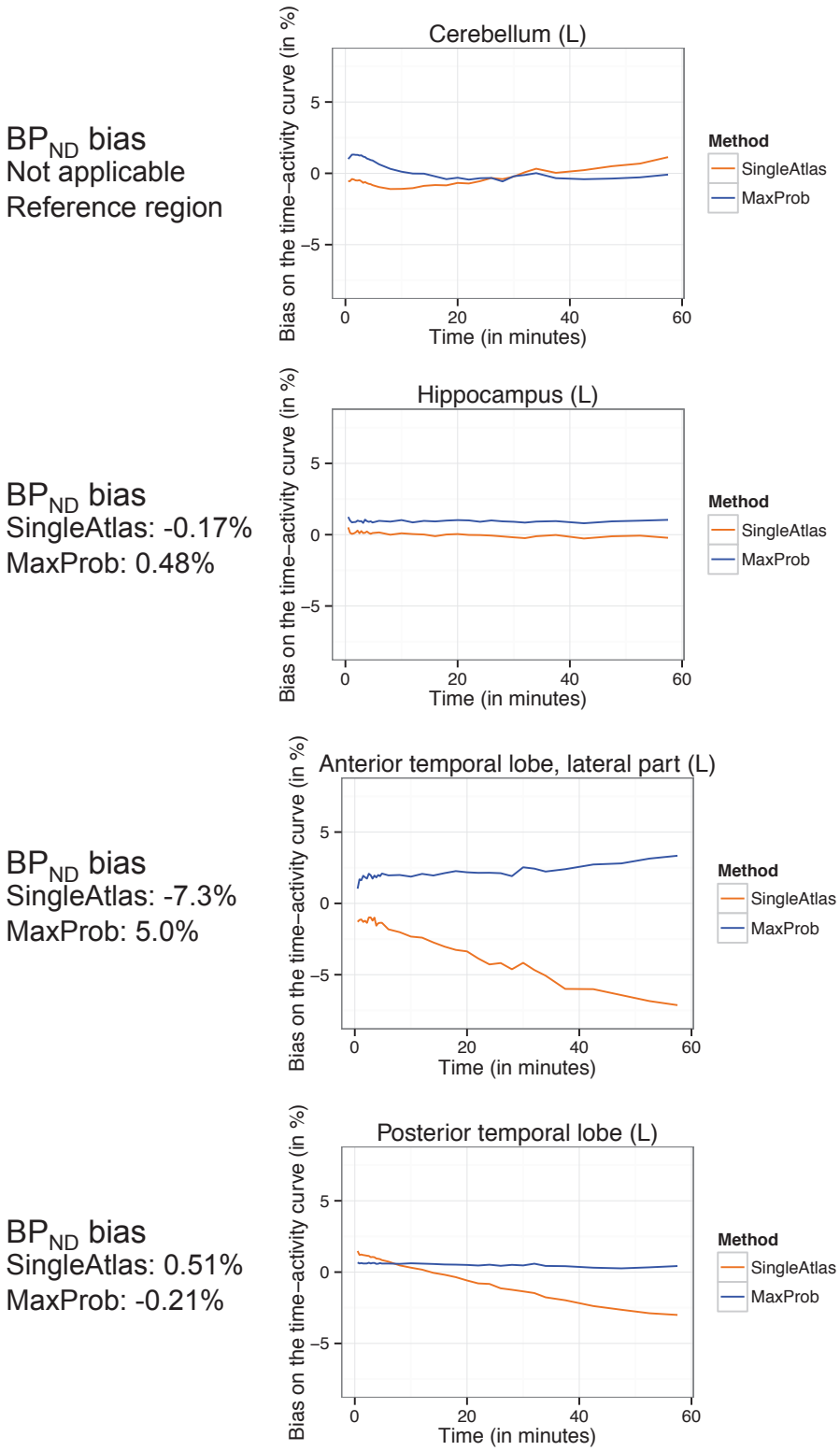

Figure 39: Mean bias over time for the PET frames across subjects for *SingleAtlas* and *MaxProb* MRAC methods, i.e. during the 60-minute [^{18}F]MPPF PET acquisition, for selected representative regions (see text). Resulting BP$_{ND}$ biases are also given (left panel). There is no evident relation between the bias on TACs and the bias on regional BP$_{ND}$.

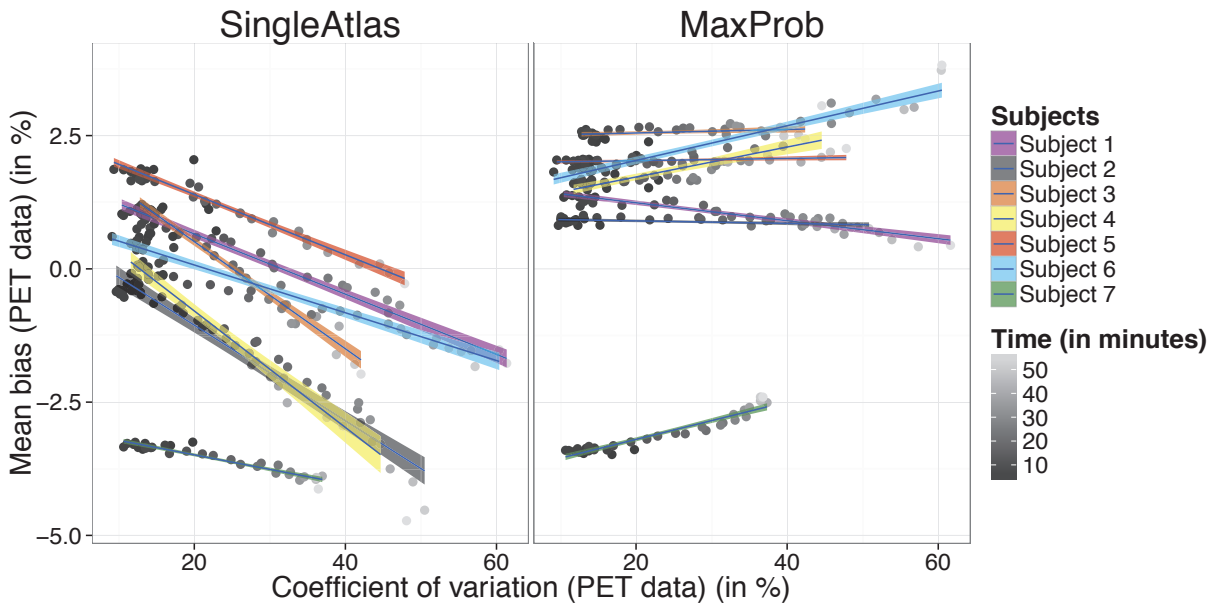

Figure 40: Mean bias (in %) across 44 brain regions, per subject and per MRAC method as a function of the coefficient of variation of tracer activity (i.e. tracer distribution inhomogeneity). Time-dependency is shown in levels of grey. Linear regression was performed per subject. The shade around linear regression shows the standard error of the slope (95% confidence interval).

3.3.4 Bias dependence on spatial tracer distribution and pseudo-CT quality

The plot of the slopes obtained by linear regression of the data presented in Figure 40, versus the global mean absolute error (MAE) between the ground truth CT and the pseudo-CT computed within the head mask for *SingleAtlas* and *MaxProb* methods, is shown in Figure 41. The figure suggests a correlation between the dependence of the bias with the image uniformity, expressed with the slope, and the quality of the generated pseudo-CT. It also shows that *MaxProb* generated more accurate pseudo-CTs than *SingleAtlas*, yielding dynamic activity measurements with a bias that was less dependent on the activity distribution.

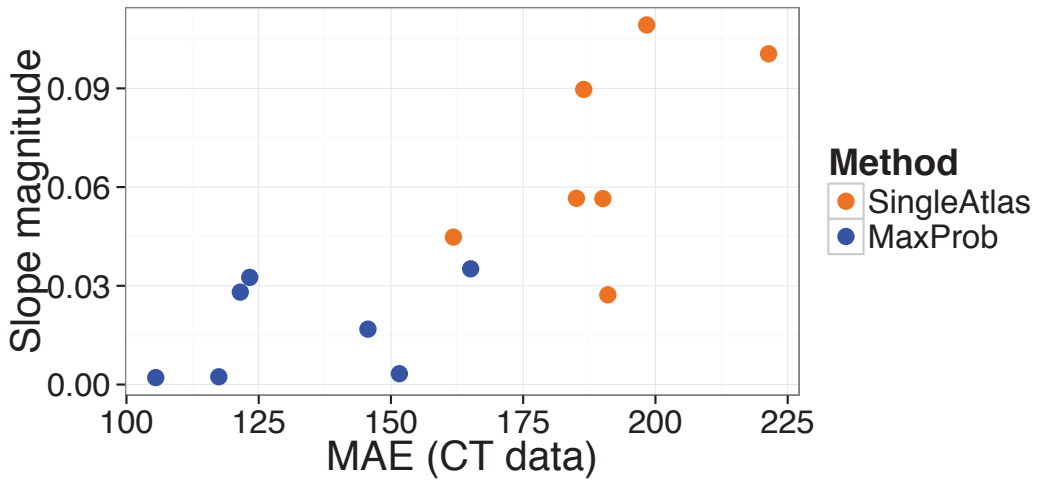

Figure 41: Slope magnitude of linear regression between activity coefficient of variation and mean bias on dynamic PET data *versus* mean absolute error (MAE) between the ground truth CT and pseudo-CT, per subject and per MRAC method. MAE was computed within the head mask (see Chapter 2, section 2.2.4). Larger errors in the pseudo-CT accuracy are associated with a larger coefficient of variation, i.e. a more heterogeneous tracer distribution.

3.3.5 Effect of the reconstruction algorithm

We investigated whether the results obtained with FBP2D PET reconstruction presented the same behaviour as results obtained with OP-OSEM3D. Mean bias over the 44 ROIs studied, computed per frame and per subject, is shown in Figure 42 for the same features as in Figure 40. Similarly to Figure 40, linear regressions for *SingleAtlas* demonstrated a higher dependence of regional bias on the COV, which was not the case for the *MaxProb* approach. This observation was supported by the mean slope of linear regressions across the seven subjects: -4.7 for *SingleAtlas* and 1.2 for *MaxProb* (Figure 42). Overall, similar behaviour was obtained with PET reconstructed with OP-OSEM3D and PET reconstructed with FBP2D. These data confirmed that the magnitude of bias was amplified with the heterogeneity of tracer spatial distribution of the PET frame for *SingleAtlas* but remained stable for *MaxProb*, irrespective of the reconstruction method.

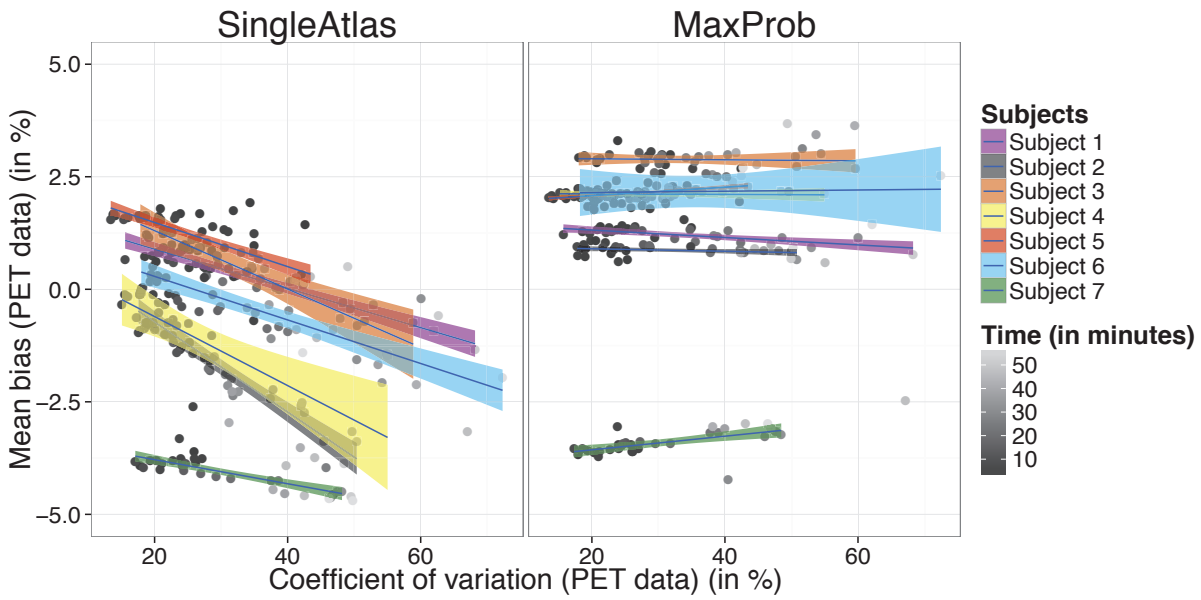

Figure 42: Mean bias (in %) across 44 brain regions, per subject and per MRAC method, as a function of the coefficient of variation of tracer activity. PET data was reconstructed with the filtered back-projection algorithm (compare the corresponding graph for OP-OSEM3D reconstruction in Figure 40). Time-dependency is shown in grey colour-scale. Linear regression was performed per subject. The shade around linear regression shows the standard error of the slope (confidence interval of 95%). The results obtained with FBP2D were very similar to those obtained with the iterative reconstruction algorithm (Figure 40).

3.3.6 Effect of scatter correction

An exploratory study of the effect of scatter correction on the variation of PET quantification bias over time was performed for one subject. Dynamic PET data were reconstructed without scatter correction using ground-truth CT and *SingleAtlas* pseudo-CT AC methods. We computed the bias on PET data corrected with *SingleAtlas* pseudo-CT, compared to PET data corrected with ground-truth CT, for one single brain region that had shown large bias (Figure 43, similar to the graphs in Figure 39) and the average bias over the 44 ROIs studied (shown in Figure 44, similar to Figure 40 and Figure 42). PET without scatter correction was compared to the corresponding PET series previously reconstructed including scatter correction.

Error on TACs as a function of time, for the anterior temporal lobe, left lateral part, is shown in Figure 43, for PET data reconstructed with and without scatter correction. Both curves had similar trend: the error was around 0.5% at the beginning of the acquisition and reached -10% for PET without scatter correction and -12% for PET with scatter correction in the last frames.

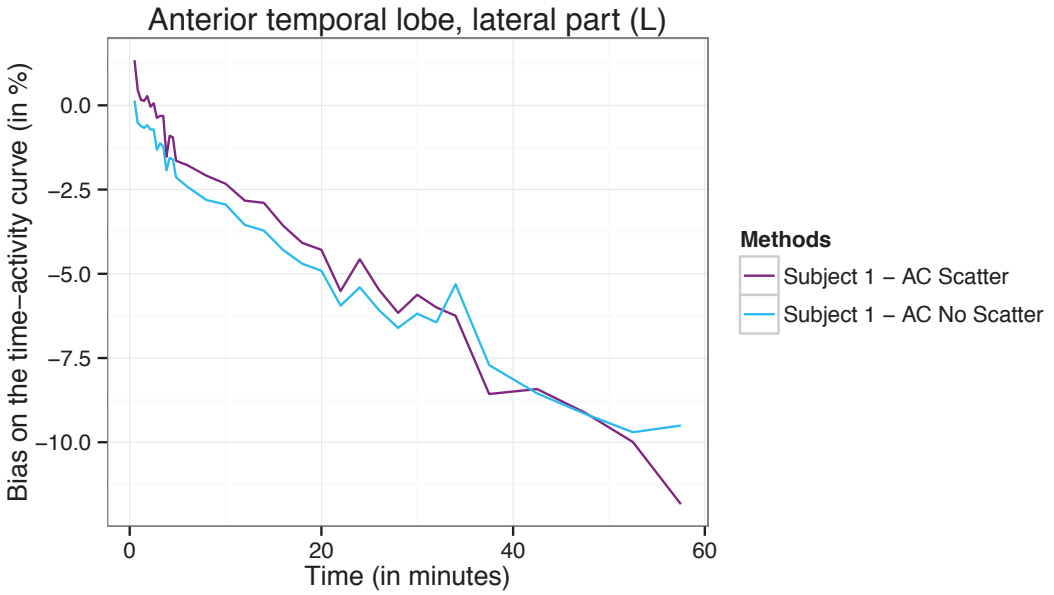

Figure 43: Bias over time for the PET frames for one subject and for *SingleAtlas*, i.e. during the 60-minute [^{18}F]MPPF PET acquisition, for label anterior temporal lobe, left lateral part. PET data was reconstructed with OP-OSEM3D algorithm with AC and scatter correction (in purple) and without scatter correction (in blue).

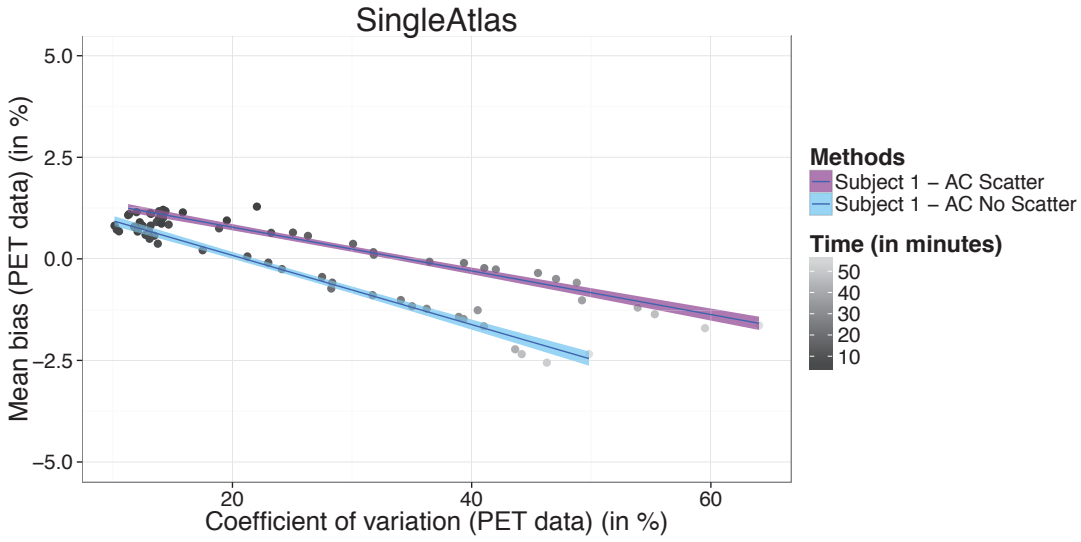

Figure 44: Mean bias (in %) across 44 brain regions, for one subject and for *SingleAtlas* MRAC method as a function of the coefficient of variation of tracer activity (between regions). Time-dependency is shown in levels of grey. The shade around linear regression shows the standard error of the slope (confidence interval of 95%). PET data was reconstructed with OP-OSEM3D algorithm with AC and scatter correction (in purple) and with AC but without scatter correction (in blue). Scatter correction only explains a small part of the evolution of bias across time.

Mean bias across the 44 brain regions studied (Figure 44) decreased from 1.3% to -1.7% for PET data reconstructed with scatter correction and from 0.9% to -2.5% when scatter correction was not taken into account. The bias magnitude increased with the COV in both cases, with and without scatter correction. In this example, the slope of the linear regression was even higher in absolute terms for PET data not corrected for scatter (-8.5) than the slope for PET data with scatter correction (-5.4).

Scatter correction had a minor contribution to the amplification of the magnitude of bias over the dynamic acquisition but did not seem to explain the entirety of the phenomenon.

3.3.7 Effect of head motion

Head motion was estimated on dynamic PET data reconstructed without AC. Each frame of the dynamic PET series was rigidly coregistered to a reference space (frame 12) using minctracc tools (McConnell Imaging Center, Montreal, Canada). Translation and rotation parameters were extracted from the matrices generated by the coregistration step, per time frame (in minutes) and per subject. Motion parameters as a function of time are shown in Figure 45.

The amount of movement was calculated as follows (**Equation 10**):

$$Amount\ of\ movement = \sqrt{(t_x^2 + t_y^2 + t_z^2)} \qquad \textbf{(Equation 10)}$$

were t_x, t_y and t_z refer to translations in x, y and z directions, whereas rotations were neglected.

To assess the relation between head motion and the influence of MRAC method, we calculated the correlation between the amount of movement and the bias on PET data along the dynamic acquisition per subject, per time frame. The mean R^2 coefficient across subjects was 0.24, indicating that motion artefacts did not explain our new finding of time-dependent (i.e. tracer distribution-dependent) changes in PET quantification due to the influence of the attenuation map.

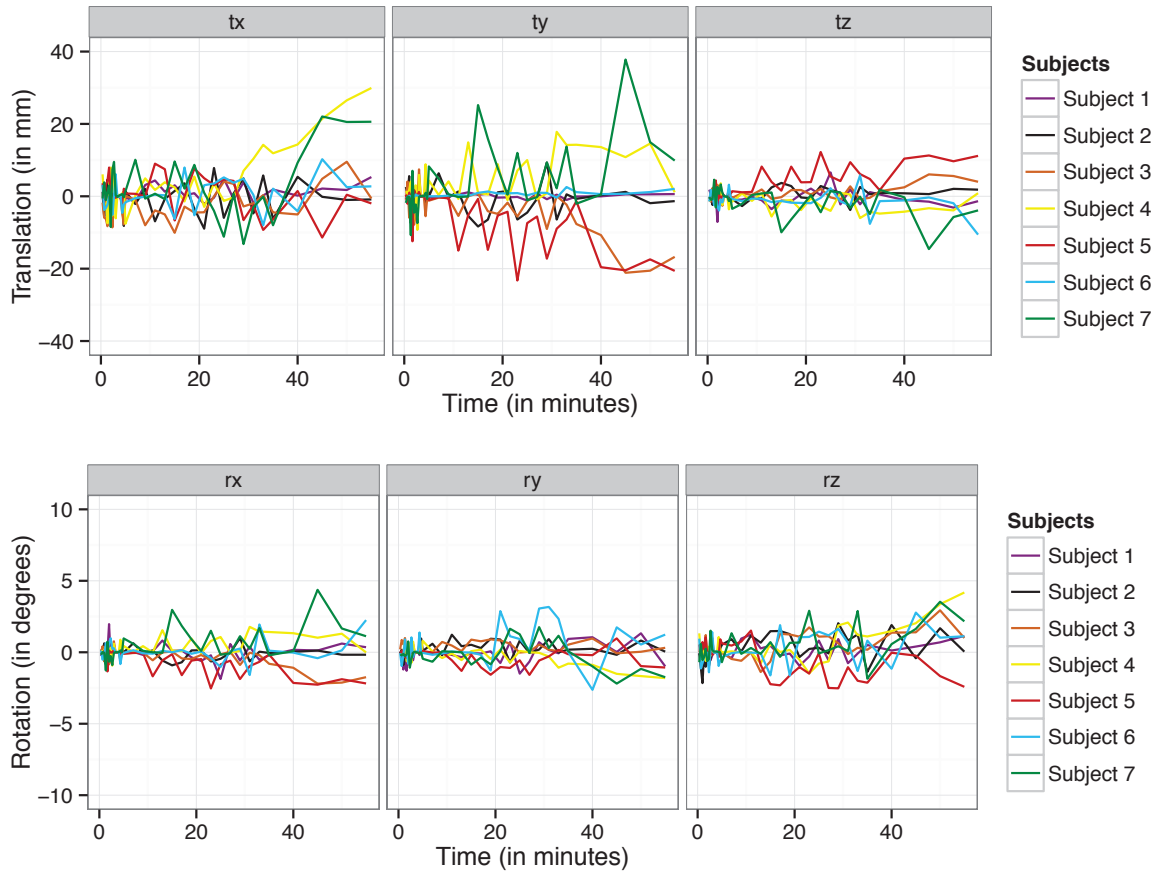

Figure 45: Motion estimation along the dynamic acquisition, per subject (translation and rotation parameters).

3.4 Discussion

PET-MR scanners are currently largely used for research, and full quantification with kinetic modelling will often be required. Most papers focused on the evaluation of new AC methods in PET-MR systems have used static [^{18}F]FDG PET data. If few studies (Burgos et al., 2015; Ladefoged et al., 2016) have demonstrated different performance of MRAC method depending on the PET tracer used, little attention has been paid to this phenomenon until now.

To our knowledge, this work highlights for the first time that inaccurate attenuation maps introduce bias in measured TACs that depends on the spatial distribution of the tracer in the head. Note that a similar finding has recently (and independently to this work) been reported in the context of PET/CT lung imaging (Holman et al., 2016). In dynamic acquisitions, the spatial distribution of the tracer within the brain can change across time from being rather uniform (early frames: blood flow /

perfusion) to very contrasted (late frames: specific binding) (cf. Figure 37). In this situation, inaccurate attenuation maps will not only bias the measured TACs in magnitude but also in shape, with unpredictable repercussions at the kinetic parameter computation level (cf. Figure 39). In addition, with inaccurate attenuation maps, varying performance is to be expected for late static images for tracers with heterogeneous distribution in the brain, which we have shown with late [^{18}F]MPPF compared to late [^{18}F]FDG uptake. Results presented in Figure 40 and Figure 41 illustrate this finding.

The reconstruction step is complex. However, if the activity value present in a single voxel of a reconstructed image is conceptualized simply as a linear combination of projection bin values corrected (e.g. multiplied) by their associated attenuation correction factors, it is easy to perceive the link between count distribution in projection space and bias in voxel values when attenuation correction factors are inaccurate. If the count distribution was uniform, the voxel value would not be very biased even given slightly incorrect attenuation correction factors. A mathematical framework that describes the quantification error in the PET image due to an inaccurate μ-map has been introduced in Thielemans et al. (2008). In our study, the results obtained with the dynamic evaluation on [^{18}F]MPPF PET data showed a strong similar tendency (Figure 40) for six of seven subjects assessed.

Note that other phenomena could explain the dependence of PET bias on tracer spatial distribution: changing counting statistics across time can influence the reconstruction algorithm as well as the scatter correction. In addition, we explored possible head motion artefacts.

In this work, we showed that the dependence of PET bias on tracer spatial distribution was purely the result of an inaccurate μ-map, by verifying the observations reported in Figure 40 (OP-OSEM3D reconstructions) with the same data reconstructed with FBP2D (Figure 42). The similar behaviour shown by the linear regressions in the two figures confirmed that the biases did not depend on the reconstruction method, and in particular that their evolution across time was not due to convergence properties that can vary with changing counting statistics when using iterative reconstruction methods. Note that higher standard errors of the slope were found in linear regressions for FBP2D data than for OP-OSEM3D reconstructions. This higher uncertainty appears to be produced by the unequal distribution of time frames across COV contributing to the estimation of the linear regression; most of the time frames of dynamic acquisitions had a small COV, and only a few time frames had higher COV. This phenomenon might be explained by the lower inter-regional

standard deviation in FBP2D reconstructions due to the intrinsic lack of contrast in those images, in particular for short temporal frames.

We also verified that this evolution was not caused by inaccuracies introduced during the scatter correction, a step that uses the attenuation map and whose performance could be influenced by the statistics and activity distribution within each emission time frame. The results (section 3.3.6) showed that the scatter correction only explains a small part of the error and its evolution across time, a finding which is supported by results reported by Burgos et al. (2014b) in the context of static PET acquisitions.

The low correlation found between the amount of motion and the bias on dynamic data suggests that head motion did not explain the amplification of bias across the dynamic acquisition. Note that the phenomenon of bias amplification across time (i.e. the evaluation of tracer spatial distribution) was also observed with simulated dynamic PET data that do not contain any motion artefact (see Chapter 4). In further work, motion correction will be applied to real dynamic data.

The MAE values obtained for pseudo-CT evaluation (Figure 41) were consistent with those reported in Burgos et al. (2014). *MaxProb* values were equivalent to those of the multi-atlas method described in Burgos et al. (2014), and *SingleAtlas* had similar MAE scores to the AC method based on the *UTE* image (the vendor's method implemented on the scanner). This may suggest that the *UTE* method could also lead to considerable bias across time in dynamic data.

The cerebellum contains few receptors belonging to the most frequently studied neurotransmitter systems, and it is relatively spared in neurodegenerative disease. Therefore, it is routinely used as a reference region for modelling or internal standardization (e.g. standard uptake value ratios for amyloid-beta PET imaging). Correct quantification of cerebellar radioactivity concentrations is therefore particularly important but had not been obtained with standard vendor implementations (Andersen et al. 2014). We argue that this problem has now been solved with multi-atlas approaches. The local errors observed in the cerebellar region with the *MaxProb* method (Chapter 2, Figure 28) averaged out over the entire cerebellum (Figure 39 and Chapter 2, Figure 27) and did not affect the kinetic modelling (Figure 36 and Figure 39). BP_{ND} computation relies on the complex modelling of the activity concentration over time. We found no obvious correlations between biases in cerebellar activity estimates and biases in the resulting BP_{ND}.

3.5 Conclusion and perspectives

Detailed evaluation of the impact of two MRAC methods on dynamic [^{18}F]MPPF PET data was provided in this chapter.

Data presented demonstrate that an inaccurate attenuation correction map (e.g. the *SingleAtlas* method), combined with inhomogeneous spatial tracer distribution, can lead to a non-constant bias of the activity measure across time, and this may distort kinetic parameter estimation. In contrast, *MaxProb* generated more accurate attenuation maps and entailed little bias of [^{18}F]MPPF activity for both TACs, especially during the first two thirds of the measurement period, and BP_{ND}. This study also shows that a cerebellar reference curve obtained for PET-MR data attenuation corrected via *MaxProb* can be used for kinetic modelling, opening the way for dynamic PET studies on hybrid PET-MR systems.

More research is necessary to fully understand the impact of MRAC on BP_{ND} modelling. Further investigation will involve applying the *MaxProb* method to more subjects and other PET tracers. In the next chapter we will evaluate the actual impact of inaccuracies due to MRAC on detectability of neurophysiological processes with PET-MRI. This will be essential for sensitivity evaluation of PET-MRI used to elucidate pathophysiological processes.

4 Chapter 4

Effect of AC on a bolus-infusion [^{11}C]raclopride PET study of endogenous dopamine release: validation on simulated data and application to a real study of transcranial direct current stimulation (tDCS)

Dynamic PET studies and PET kinetic modelling are often used in brain research to characterize cerebral neurophysiological processes. Some of these studies are focused on the release of an endogenous ligand induced by indirect pharmacologic challenge, or by a functional task; a process that can essentially only be studied noninvasively with PET or SPECT *in vivo*. Comparisons between groups of subjects under different conditions (e.g. test vs. control) are generally performed. In most cases, the differences highlighted between groups are small, usually around 5%, and localized in specific and small brain regions. Volkow et al. (1994) used [^{11}C]raclopride, a D2 receptor radioligand that is sensitive to endogenous dopamine, to investigate the dopamine release in response to a neurochemical challenge with a psychostimulant drug. In this study, the percentage change of [^{11}C]raclopride binding with respect to placebo was around 4% in the striata. In another pharmacological protocol, Mottolese et al. (2014) investigated the role of oxytocin in the inhibitory regulation of 5-HT signalling using [^{18}F]MPPF, a PET tracer for $5HT_{1A}$ serotoninergic receptors. They showed that oxytocin administration induced a significant mean BP_{ND} increase of around 3% in dorsal raphe nucleus and some limbic structures (hippocampus, insula, amygdala). In the study reported by Zald et al. (2004), healthy humans performed card selection tasks for monetary rewards and changes induced by this cognitive task in endogenous dopamine transmission were measured with [^{11}C]raclopride. Increases in BP in the left medial caudate nucleus (around 9%) with simultaneous significant decreases in other areas of the caudate and putamen (around 8%) were reported. In a different type of protocol (Zubieta et al., 2001), the function of the opioid system and μ-opioid receptors in the brains of healthy human subjects undergoing sustained pain was examined with [^{11}C]carfentanil, a selective μ-receptor radiotracer. Reductions in regional μ-opioid receptor availability (B_{max}/K_d) from placebo to sustained pain around 5% were obtained. These studies have been carried out on standalone PET cameras or PET/CT systems in the last decades and are now being transposed to PET-MR (Aiello et al., 2015; Galazzo et al., 2016; Sander et al., 2015; Villien et al.,

2014; Wey et al., 2014). Simultaneous PET-MR systems provide the opportunity to combine PET and MR imaging to better characterize neuronal mechanisms and brain responses to pathologies. However, as we have demonstrated in the two last chapters, MRAC can introduce important biases in PET quantification and affect the parameters derived from kinetic modelling. If an AC method produces substantial bias in reconstructed PET data, in particular in the cerebellum which is often used as reference region for PET modelling (Andersen et al., 2014), small variations between groups of subjects might not be detectable.

In this chapter we assess the impact of MRAC on PET quantification and kinetic modelling using realistic simulated PET data (Monte-Carlo simulation) in a bolus-infusion [^{11}C]raclopride protocol. We focus on the detectability of neurophysiological processes with PET-MR by modelling a tracer displacement produced by endogenous dopamine release; several magnitudes of variation are considered. We constituted a simulated database that included the main sources of variation of attenuation, *i.e.* the brain anatomy and evolution of the spatial distribution of the tracer across the acquisition time. We compare our multi-atlas AC method *(MaxProb)* with the sequence-based AC method implemented by the vendor on the mMR (*UTE*) and the ground-truth CT-based AC approach to determine the sensitivity and specificity of detection of each MRAC method. Finally, our multi-atlas AC methodology is applied to a real simultaneous PET-MR study aiming to demonstrate endogenous DA release after tDCS.

The results presented in this chapter have been presented in the conferences BrainPET 2017 (results on simulated data) and PSMR 2017 (results on real data).

4.1 Materials and methods

4.1.1 Simulated PET data

Dynamic [^{11}C]raclopride PET data was simulated using the PET-SORTEO platform (Reilhac et al., 2004), recently adapted to the geometry of the Siemens mMR Biograph (Reilhac et al., 2016). This simulation tool uses a Monte Carlo technique to generate realistic PET data from voxelized descriptions of tracer distributions, in accordance with the scanner geometry and physical characteristics. PET-SORTEO accounts for all the major sources of noise and biases that can occur within the acquisition of PET images and permits faithful reproduction of the image formation

process. PET-SORTEO requires as input two 3D-volumes (phantoms) containing the anatomical regions of interest for emission and attenuation, and the tracer activity in tissues across time (TAC per label). The following section describes how those elements have been defined in this study.

4.1.1.1 Materials

4.1.1.1.1 Structural test database for simulations

Datasets of 21 subjects (11 male, 10 female) [mean age ± SD, 41 ± 19 y; range, 15-68 y] were obtained from the King's College London & Guy's and St Thomas' PET Centre at St Thomas Hospital, London. The North East – York Research Ethics Committee (including consultation with the Medicines and Healthcare products Regulatory Agency (MHRA)), the radiation protection committee (ARSAC), the local Research & Development Committee, and the Higher Research Authority had approved the study (15/NE/0203) and all patients had given informed consent. Each subject had a brain PET-MR acquisition on a fully-integrated PET-MR scanner (Siemens Biograph mMR, Siemens Healthcare, Erlangen, Germany) after a brain PET/CT examination (GE Discovery 710) on the same day.

Three-dimensional anatomical T1-weighted sequences (MPRAGE) (TE=2.62 ms, TR=1700 ms, flip angle=9°) were reconstructed on 224 x 256 x 176 matrices with voxel dimensions of 1.06 x 1.06 x 1.1 mm^3. An ultra short echo time (UTE) image was acquired with the vendor-provided sequence (TE1=0.07 ms, TE2=2.46 ms, TR=11.94 ms, flip angle=10°) and reconstructed on 192 x 192 x 102 matrices with a voxel size of 1.56 x 1.56 x 1.56 mm^3.

A low dose CT (140 KVP, 512 x 512 x 47 matrix size, 1.36 x 1.36 x 3.27 mm^3 voxels) was acquired on the PET/CT for each subject.

4.1.1.1.2 Functional test database for simulations

Dynamic [^{11}C]raclopride PET datasets with bolus-infusion were obtained for ten subjects (4 male, 6 female) [mean age ± SD, 24.8 ± 2.35 y; range, 22-29 y]. The dose injected was 297 ± 42 MBq of [^{11}C]raclopride . Acquisitions were realized on a mCT Biograph PET/CT system.

4.1.1.2 MRI segmentation

The T1 MR images were anatomically segmented into 95 brain structures with the multi-atlas based MAPER procedure (Heckemann et al., 2010). A supplementary region, the cerebellar vermis, was added to the segmentation. This structure was manually delineated in the stereotaxic space. After computing the deformation field from the subject's space to MNI space using the *Segment* function of SPM12 on the T1 MR image, the cerebellar vermis was warped to the subject space by applying the inverse transformation. Probabilistic maps of white matter (WM), grey matter (GM) and cerebrospinal fluid (CSF) were generated in the subject space with SPM12 (*Segment* function).

4.1.1.3 Phantom generation

Emission and attenuation phantoms were created for each subject, in their individual space, from the MRI and CT data, as follows:

Preprocessing

Coregistration of CT to the MRI: The CT image was aligned with the MR image using the rigid registration tool *reg_aladin* from the NiftyReg software suite, optimizing normalized cross correlation for the image pair (http://cmictig.cs.ucl.ac.uk/wiki/index.php/NiftyReg (Ourselin et al., 2001)). The coregistered CT image was resampled to the T1 MRI resolution using cubic B-spline interpolation. The MRI was chosen as reference space to register the CT to the Biograph mMR space.

Cleaning of CT background: The background of the coregistered CT image was cleaned in order to eliminate the head support from the image. For this, a head mask of the CT image was generated as described in Chapter 2 (section 2.2.4) and the coregistered CT image was masked by this head mask.

Segmentation of CT: The CT image was thresholded into three tissue classes (bone, soft tissue and air) using the same thresholds as defined in Chapter 2 (section 2.2.1.2).

Emission phantom

Fifteen regions of interest were defined for the emission phantoms:

- Air
- Soft tissue
- Bone
- CSF and ventricles
- GM
- WM
- Cerebellar GM
- Cerebellar WM
- Cerebellar vermis
- Caudate nucleus (left) / Caudate nucleus (right)
- Nucleus accumbens (left) / Nucleus accumbens (right)
- Putamen (left) / Putamen (right)

Labels for air (label #1), soft tissue (including brain, neck and scalp - label #2) and bone (label #3) were directly obtained from the segmented CT. The neck region was added to the segmented CT as follows: the entire UTE image was binarized and holes were filled (UTE mask). The head region (binarized segmented CT) was subtracted from the UTE mask to obtain a mask of the neck region. The neck area was labelled as soft tissue. All the other labels were added to this image by the superposition principle. A mask of CSF (label #4) was generated by thresholding at > 0.9 and binarizing the CSF probability map obtained with SPM12 (*Segment* function). A mask of WM (label #6) was created by thresholding and binarizing the WM probability map (SPM12, *Segment* function) at > 0.5. In order to avoid holes in the brain, a different approach was used for the GM mask (label #5). This was built by removing WM from the brain. For this, the MAPER MRI segmentation (brain regions) was masked with the inverse mask of WM. Ventricles were extracted from the MAPER MRI segmentation and added to CSF label. Finally, the following ROIs were directly extracted from the MAPER MRI segmentation (see section 4.1.1.2) and overlaid onto the emission phantom: cerebellum GM (label #7) and WM (label #8) (right and left cerebellum combined), vermis (label #9), caudate right and left (labels #10 and #11), accumbens right and left (labels #12 and #13), putamen right and left (labels #14 and #15).

Attenuation phantom

Attenuation maps consisted of thresholded CTs with the neck area added from the *UTE* μ-map. A refinement step, in which CSF and GM probability map information was combined, was used to reduce the volume of bone structure (slightly overestimated by the simple threshold). Furthermore, the background of all images was set to 0 to reduce the simulation time. Finally, the neck region was extracted from the *UTE* μ-map and added to the attenuation phantom to compensate for the short CT field of view (described below). An example of MRI, CT, emission and attenuation maps for one subject of the database is given in Figure 46.

Both emission and attenuation phantoms were finally resampled to UTE resolution to ensure spatial matching with PET coordinates in the Biograph mMR.

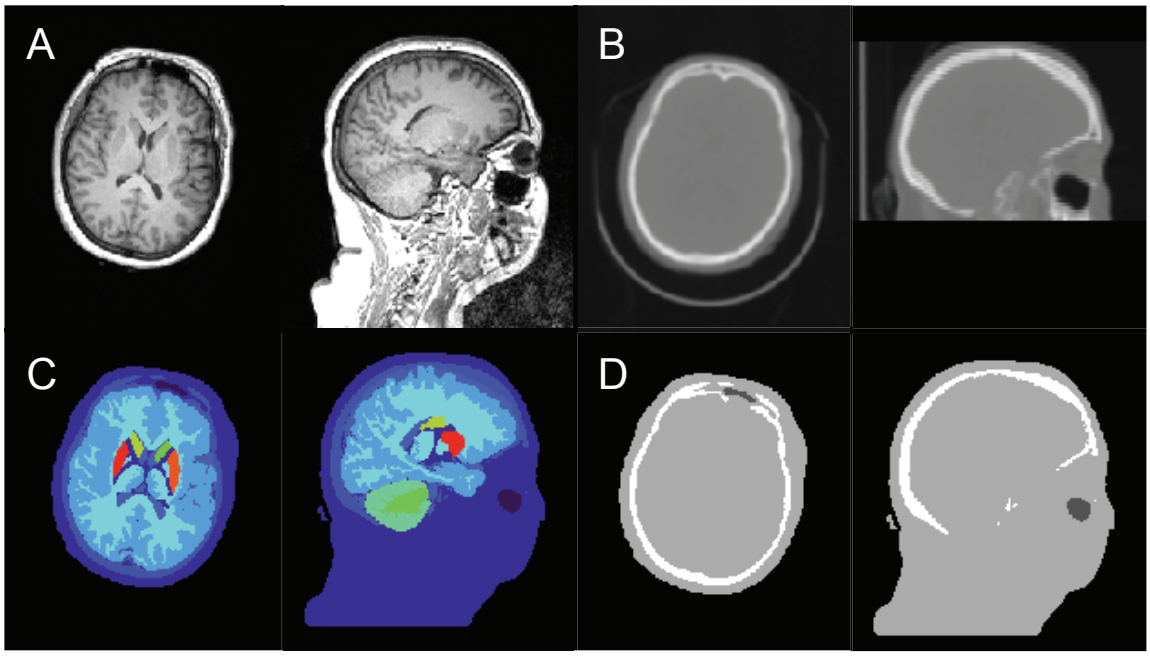

Figure 46: Example for one subject. T1-weighted MR image (A), CT image (B), emission phantom (C) and attenuation phantom (D).

4.1.1.4 Input kinetics

Input time-activity-curves

Input TACs for PET-SORTEO simulations were derived from real PET/CT data. Regional TACs were extracted from the bolus-infusion [^{11}C]raclopride data described in section "Functional database" (4.1.1.1.2), for the 15 ROIs described in section 4.1.1.3. Each TAC was first normalized by the area under the curve for WM (label #5), per subject. WM is devoid of dopaminergic receptors and provides a measure of free tracer in tissue. The TACs were then averaged across all subjects. Finally, averaged TACs were multiplied by the mean area under the curve for WM across subjects, in order to obtain realistic activity values. The TACs for caudate, putamen and accumbens were corrected for partial volume effect with geometric matrix transfer (GMT) methodology and resolution adapted to the mMR scanner (Frouin et al., 2002; Rousset et al., 2007).

The activity at time zero was set to 0 Bq/mL. Final TACs were corrected for partial volume effect (Rousset et al., 1998). The following rearrangements were performed: TACs for caudate nucleus and nucleus accumbens were averaged and this final curve was associated to both labels, TAC for air was set to 0 Bq/mL, TAC for vermis, which is devoid of dopaminergic D2 receptors, was set to TAC for cerebellum GM. Figure 47 shows the resulting TACs used as input for the PET-SORTEO simulations.

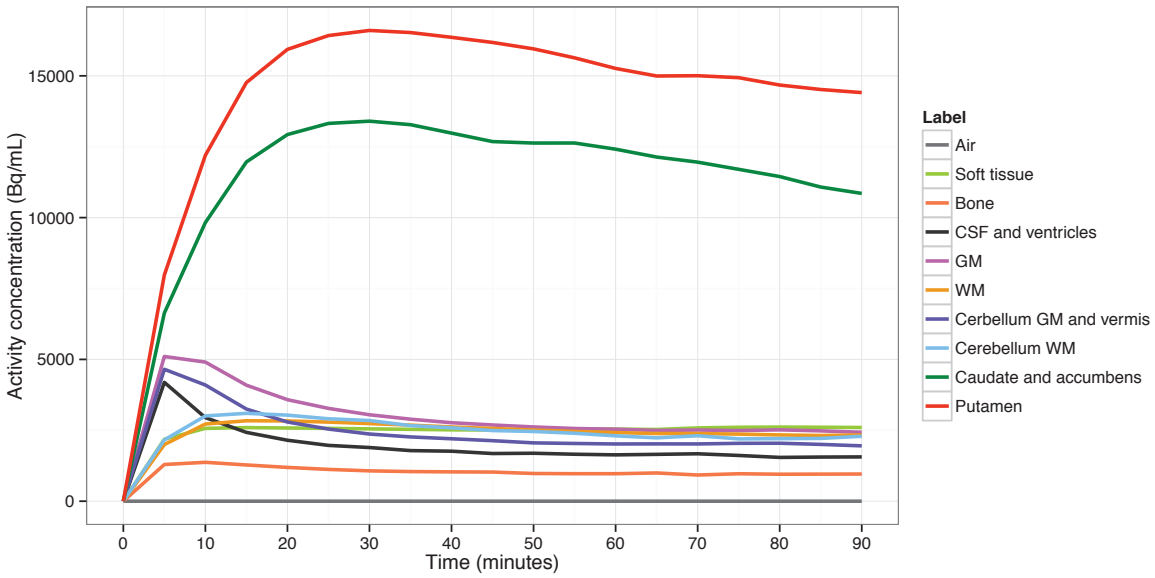

Figure 47: Regional TACs calculated from real PET/CT data and used as input for PET-SORTEO simulations.

Note that this single set of TACs was used as input for simulating data for all the 21 subjects in our dataset. Inter-subject variability was hence only supported by the anatomical variability of the emission and attenuation phantoms.

Modelling the PET displacement produced by endogenous dopamine release

In this section we model the effect of endogenous dopamine on [^{11}C]raclopride binding in the striata yielded by the tDCS. The endogenous dopamine release was modelled with a decreasing exponential function as proposed in Endres and Carson (1998) (**Equation 11**):

$$DA(t) = \frac{C_{max}.\Omega}{t_P - t_D}.t.(1 - t_D).\Pi_{(t_P - t_D)}\left(t - t_D - \frac{t_P - t_D}{2}\right) + C_{max}.\Omega.e^{-(t-t_P)/\tau}.u(t - t_P)$$ (Equation 11)

where C_{max} is the maximal radioactivity concentration of the TAC, Ω represents the percentage [^{11}C]raclopride radioactivity decrease compared to C_{max}. Several magnitudes of variation were considered, the displacement peak decrease was expressed in % compared to the peak of PET TAC: Ω = {5%, 10%, 25%} (stim05, stim10 and stim25 respectively). τ is the time constant of the exponential that characterises the time interval of return to equilibrium. τ was set to 30 min for all experiments. Π(t) is the rectangular function, u(t) is the unit step function, t_D is the onset time of the activation and t_P is the peak time of maximal response magnitude. t_D was set to 40 minutes and t_P to 45 minutes. To generate the effect of endogenous dopamine release on [^{11}C]raclopride binding, the curve of dopamine release was subtracted from the initial TACs in caudate, accumbens and putamen. The effect of stimulation was lateralized to the left side of the brain and applied to the three structures of the striatum: caudate nucleus, nucleus accumbens and putamen. An example of initial TAC for caudate, curve of dopamine release and TAC modelling the PET displacement for the left caudate nucleus are shown in Figure 48. Figure 49 shows final TACs for all ROIs, with a stimulation of 10%.

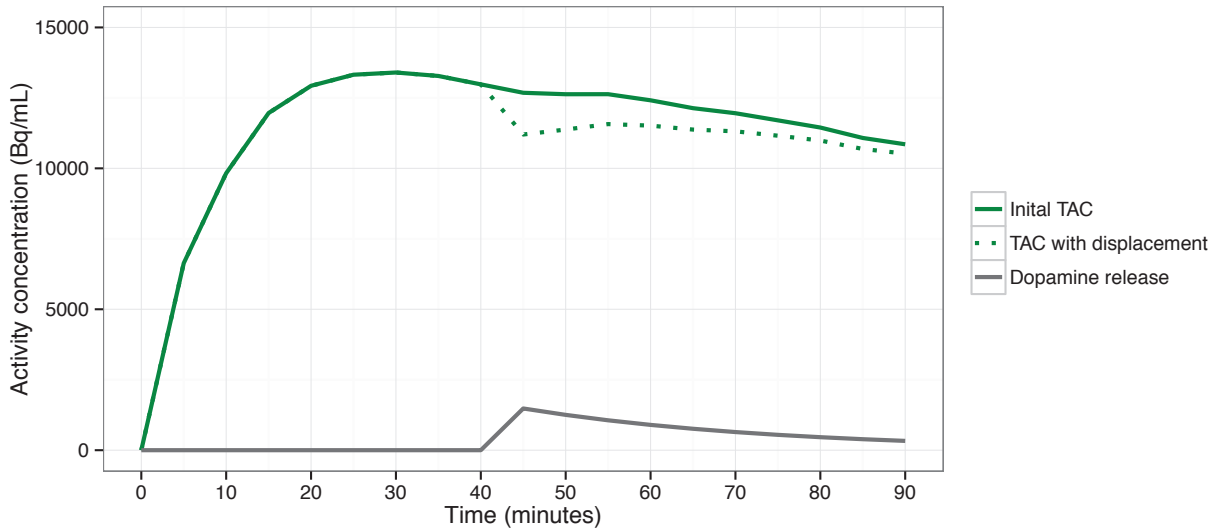

Figure 48: Model of the PET displacement produced by endogenous dopamine release on TAC (Ω = 10%) for caudate nucleus (L). Dopamine concentration linearly increases from the time of onset to the peak, and then exponentially decreases.

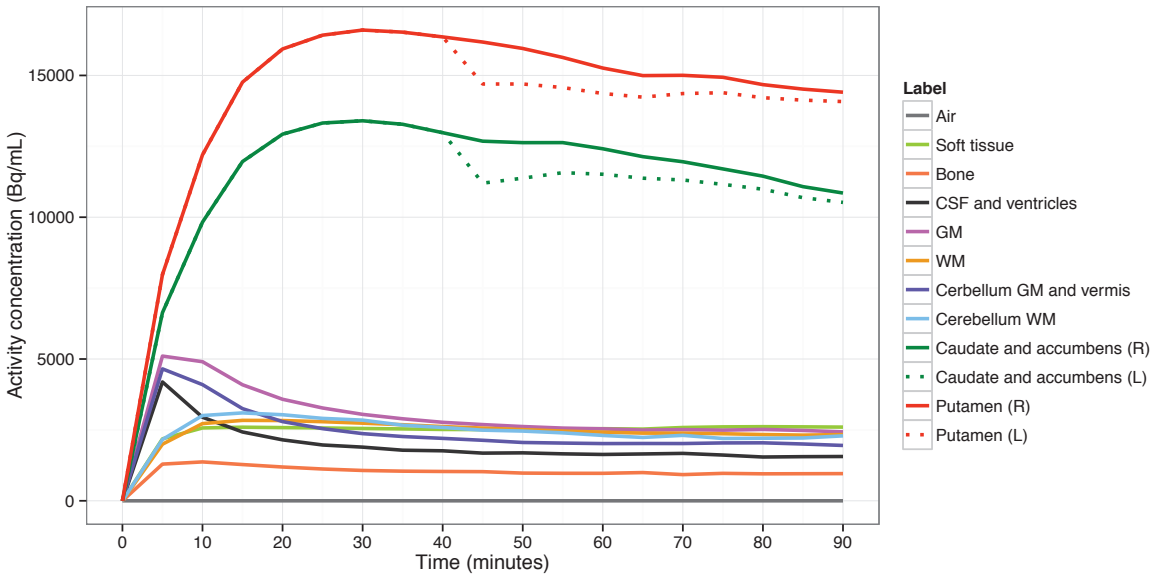

Figure 49: TACs with PET displacement (Ω = 10%) used as input for PET-SORTEO simulations.

For each subject, PET data were simulated with a placebo condition, i.e. without any stimulation (using TACs from Figure 47) and the three magnitudes of PET signal decrease (Ω, described above) for the active conditions (TACs from Figure 49).

4.1.1.5 Reconstruction of simulated PET

Simulated PET data was reconstructed with the Siemens off-line reconstruction software (e7tools, Siemens Medical Solutions, Knoxville, USA). Raw data were rebinned into 18 frames of 5 minutes for dynamic reconstruction. Images were reconstructed with the OP-OSEM3D algorithm incorporating the point spread function (PSF), using 12 iterations of 21 subsets. Data correction (normalization, attenuation and scatter correction) was integrated in the reconstruction process and Gaussian post-reconstruction filtering (FWHM = 4 mm) was used. A zoom of 3 was applied to the reconstructions, yielding a voxel size of $0.9 \times 0.9 \times 2.03$ mm^3 in a matrix of $256 \times 256 \times 127$ voxels.

4.1.1.6 Attenuation maps for simulated PET

For attenuation correction, three different attenuation maps were used in this study: 1) a CT-based μ-map, considered as gold standard, 2) the vendor-provided MR-based μ-map (*UTE*) and 3) our multi-atlas-based μ-map *MaxProb* (Merida et al., 2017, 2015) using the same atlas database as described in Chapter 2. The coregistred CT was resampled to UTE resolution. CT and *MaxProb* pseudo-CT intensities (in Hounsfield Units) were converted to attenuation coefficients at 511 keV with the standard bilinear transform (Carney et al., 2006) that takes into account the CT energy (kVp). The *UTE* μ-map was obtained from the UTE MR sequence and consisted in three discrete attenuation coefficients for bone, soft tissue, and air. This method is directly implemented in the Siemens mMR system (Catana et al., 2010).

Given that the three μ-maps had different neck coverage - in particular the individual CT had a reduced field of view - a generic neck area containing soft tissue only was added to all μ-maps. The neck section was derived from the *UTE* μ-map by automatic segmentation and binarization of the image. Resulting μ-maps are shown in Figure 50.

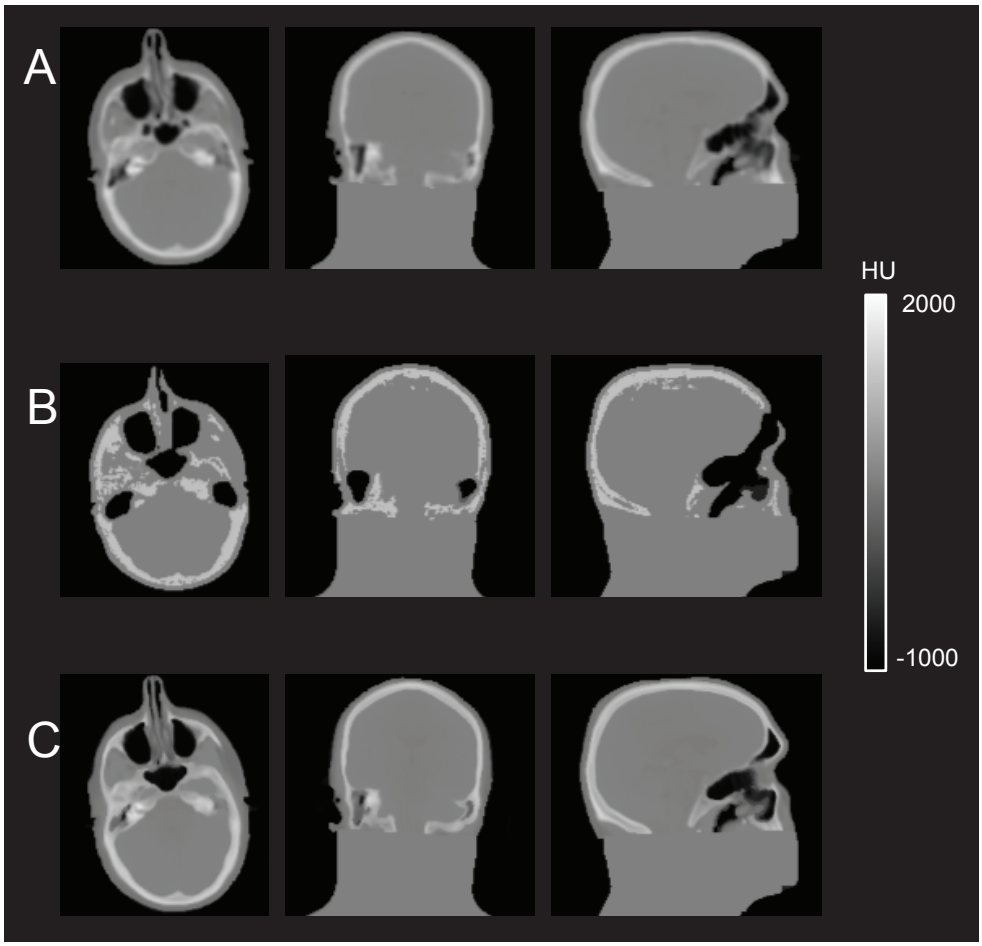

Figure 50: μ-maps with common neck. CT μ-map (A), *MaxProb* μ-map (B), *UTE* μ-map (C)

4.1.1.7 Data analysis of simulated data

4.1.1.7.1 Kinetic analysis

Time-activity curves (TACs) were extracted from the simulated PET series, for the striatal regions (caudate nucleus, nucleus accumbens and putamen) and for the cerebellar grey matter excluding vermis (no specific binding, reference region for modelling), considered here as the reference region. Regional extraction was performed with the labels defined in the emission phantom for each subject. To estimate the BP_{ND}, tissue-to-reference 5-min binding ratios (BR) were deduced from these TACs for all striatal regions, at equilibrium (Pinborg et al., 2005).

Parametric BR images were generated from the 90-minute dynamic series, for the following time-interval after the injection of the tracer:

- Baseline: 30 – 40 minutes
- Stimulation (stim): 40 – 55 minutes
- Post-simulation 1 (post1): 55 – 70 minutes
- Post-simulation 2 (post2): 70 – 85 minutes

4.1.1.7.2 Evaluation of PET quantification

Evaluation of PET quantification was performed by comparing the PET data reconstructed with the three attenuation maps: *MaxProb*, *UTE* and gold standard CT ($PET_{MaxProb}$ and PET_{UTE} to PET_{CT}, respectively). Bias on TACs and bias on tissue-to-reference BR curves was computed as follows:

$$Error_{TAC}\ (\%) = \frac{\mathrm{PET_{MRAC}} - \mathrm{PET_{CTAC}}}{\mathrm{PET_{CTAC}}} \times 100 \qquad \text{(Equation 12)}$$

$$Error_{BR}\ (\%) = \frac{\mathrm{BR_{MRAC}} - \mathrm{BR_{CTAC}}}{\mathrm{BR_{CTAC}}} \times 100 \qquad \text{(Equation 13)}$$

Regional errors were also computed on parametric BR images, per time-interval.

MRAC methods were compared on these quality criteria using paired Wilcoxon signed-rank tests. The threshold of statistical significance was set at a p-value of 0.05, divided by the number of comparisons (three in this study) to correct for multiple comparisons (Bonferroni, 1936).

4.1.1.7.3 Detection of endogenous dopamine variation

The 21 subjects included in this study were split into two groups: a group of 11 subjects receiving the dopaminergic stimulation (active group) and a group of 10 subjects that did not undergo stimulation (placebo group). The effect of dopaminergic stimulation was characterized at the regional and at the voxel level by means of the BR. The impact of the AC methods on group differentiation was studied.

4.1.1.7.3.1 Regional analysis

The PET displacement induced by dopamine release was quantified by calculating relative variations of BR (Δ) for three time-intervals: stim, post1 and post2. BR variations were compared to the BR at baseline (Equation 14).

$$\Delta\ (\%) = \frac{\mathrm{BR}_{\{\mathrm{stim;post1;post2}\}} - \mathrm{BR}_{\mathrm{baseline}}}{\mathrm{BR}_{\mathrm{baseline}}} \times 100 \qquad \text{(Equation 14)}$$

In addition, to take into account the large intra-group variability of Δ, the difference change of [^{11}C]raclopride binding in active group with respect to placebo (Δ_{DIFF}) was computed.

4.1.1.7.3.2 Voxel-wise analysis

Parametric BR images were normalized to MNI space (voxel size of 2 x 2 x 2 mm^3) and blurred using a Gaussian kernel with a standard deviation of 8 mm. Voxel-based analysis to assess differences between PET_{CTAC} and PET_{MRAC} was performed with SPM12 on BR images using an ANOVA with the factors subjects, conditions (placebo vs. active groups), AC method and time-interval (baseline, stim, post1, post2). The interaction between group, AC method and time-interval was included in the model. The AC method was added as main effect.

To assess the effect of stimulation between placebo and active groups, we tested if the difference between baseline and stim (either post1 or post2) in the active group was larger than the difference between baseline and stim (either post1 or post2) in the placebo group. This contrast was tested independently for each stimulation magnitude (stim05, stim10 and stim25).

The statistical parametric maps resulting from the above analysis were thresholded at p=0.001, uncorrected. Clusters of significant differences within a mask of striatal regions (caudate, accumbens and putamen) were extracted. For each AC method contrast, we calculated the number of voxels corresponding to a significant difference of Δ between between placebo and active groups, by adding up the spatial extent (k) of all significant clusters found in the mask. This metric was used to assess the sensitivity of detection of *UTE* and *MaxProb* MRAC methods, compared to CTAC.

4.1.2 Real PET-MR data

Data from the first brain PET-MR protocol, carried out at the CERMEP, that investigates the neurophysiological impact of fronto-temporal transcranial direct current stimulation in healthy subjects, were used. This study is still in progress and placebo and active groups have not been identified, thus preliminary data are shown in this work.

4.1.2.1 Protocol

Transcranial direct current stimulation (tDCS) consists in applying a weak constant current between two electrodes placed on the surface of the head, above two cortical areas. This stimulation technique can modify brain functions and is emerging as a prospective therapy for neurologic, psychiatric and addictive disorders. Some imaging reports suggest that tDCS effects are not restricted to the brain areas located under the electrodes, but spread through distributed cortical networks functionally connected with the targets, and reach subcortical areas. As the cortex is densely connected with basal ganglia areas, tDCS effects are probably capable of reaching subcortical areas with dopaminergic transmission. For this reason, and taking into account the dopaminergic pathophysiological hypothesis of schizophrenia, the effect of fronto-temporal tDCS on dopaminergic transmission is of major interest. This project, lead by Marie-Françoise Suaud-Chagny and Clara Fonteneau in the PSYR^2 team from the Centre de Recherche en Neurosciences de Lyon (CRNL), aims to study tDCS effects on dopaminergic transmission and characterize the neurochemical mechanisms involved in this process, on healthy subjects.

This study included two groups of subjects, one with active and one with placebo (sham) fronto-temporal tDCS (with anodal stimulation over the left dorsolateral prefrontal cortex and cathodal stimulation over the left temporo-parietal junction). Subjects were randomized, and the study was double-blind with a 2-arm parallel group design. The stimulation started 40 minutes after the injection of the tracer and lasted 30 minutes. The protocol (Figure 51) comported brain activity and connectivity measures (ASL, resting state and DTI). In PET, [^{11}C]raclopride radiotracer was used to measure D2 receptor occupancy variation between the baseline and the stimulation states.

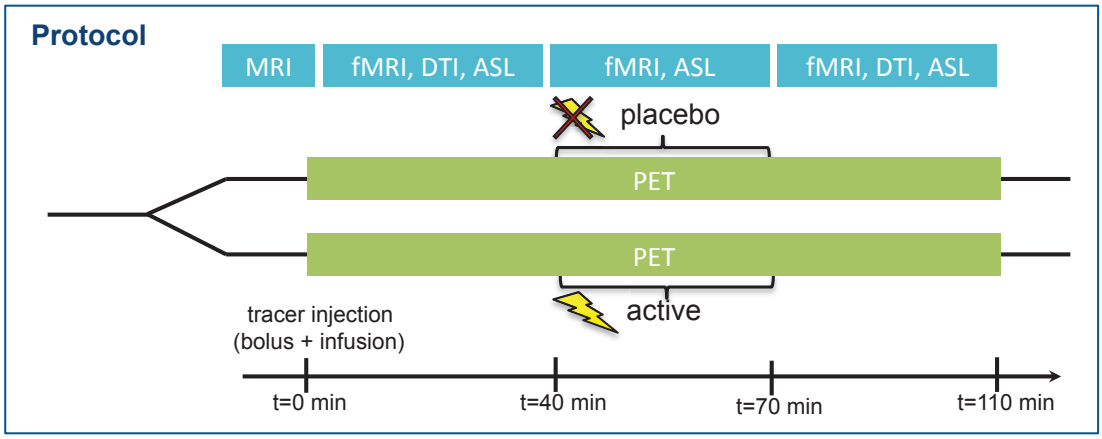

Figure 51: Protocol of simultaneous PET-MR study with tDCS

4.1.2.2 Data

Eighteen subjects (8 males, 10 females) [mean age ± SD, 25.6 ± 2.9 y; range, 22-34 y] had a simultaneous PET-MR exam (Siemens mMR Biograph). Three-dimensional anatomical T1-weighted sequences (MPRAGE) (TE= 2.34 ms, TR=2300 ms, flip angle=8°) were acquired and reconstructed in a 256 × 256 × 176 matrix with voxel dimensions of 0.97 x 0.97 x 1 mm^3. UTE AC sequences (TE1=0.07 ms, TE2=2.46 ms, TR=11.94 ms, flip angle=10°) were acquired and reconstructed in a 192 x 192 x 102 matrix (voxel size: 1.56 x 1.56 x 1.56 mm^3). The scan protocol also included other functional sequences - BOLD, ASL and DTI - not analysed in this work. All subjects had a 110-minute dynamic PET examination with a [^{11}C]raclopride bolus-infusion, acquired in listmode.

4.1.2.3 PET reconstruction and motion correction

PET data were corrected for head motion with the *Eber* algorithm (event-by-event rebinner; (Reilhac et al., 2017)), which directly corrects the listmode data by rebinning the detected events according to the estimated inter-frame motion. This approach presents the advantage to correct for motion artefacts with high temporal resolution (100 seconds) and also to correct for the spatial misalignment between emission data and attenuation data that is not taken into account in traditional motion correction implementations. For motion estimation, dynamic PET data were first reconstructed without AC in 63 frames of 100s each. Each reconstructed PET volume of the reconstructed PET series was coregistered onto the reference volume (mean image of the frames 3

to 5) with rigid body and cross-correlation (minctracc). Translations, and rotations were of each time interval were stored in a text file. Then the 63 motion correction matrices were applied to the listmode data, rebinned in sinograms of 21 regular 5-minute (300s) frames. Finally, images were reconstructed from the corrected sinograms with AC, and the OP-OSEM3D algorithm incorporating PSF, using 12 iterations and 21 subsets. A zoom of 3 was applied to the reconstructions, yielding a voxel size of 0.9 × 0.9 × 2.03 mm^3 in a matrix of 256 × 256 × 127 voxels. The 10 first seconds of PET acquisition preceding the tracer injection were excluded for PET image reconstruction. Both *MaxProb* and *UTE* MRAC approaches were used for AC.

4.1.2.4 Data analysis of real data

Time-activity curves (TACs) were extracted from the striatal regions (caudate and putamen) and from the cerebellum, considered as the reference region. The same methodology as presented for the simulated data (section 4.1.1.7.1) was used. Only the temporal intervals for parametric BR images were defined differently:

- Baseline: 30 – 40 minutes
- Stimulation (stim): 45 – 70 minutes
- Post-simulation 1 (post1): 75 – 90 minutes
- Post-simulation 2 (post2): 90 – 105 minutes

Tissue-to-reference BR were deduced from these TACs for striatal regions. Parametric BR images were generated for the following time-intervals after the injection of the tracer: baseline (30-40 min), stim (45-70 min), post1 (75-90 min) and post2 (90-105 min).

Intraregional means and standard deviations of BRs were extracted from the BR images. Results were compared with or without applying *Eber* motion correction, incorporating *UTE* or *MaxProb* AC. An analysis of variance was performed with a Tukey honest significant difference (HSD) test for each time-interval.

4.2 Results

4.2.1 Simulated PET data

In this section we report the results obtained with simulated [^{11}C]raclopride PET data. First, the accuracy of PET quantification achieved using *UTE* and *MaxProb* MRAC compared to CTAC is assessed. Then, a group analysis is performed to differentiate the placebo group from the active group under several stimulation conditions. The three AC approaches (CT, *UTE* and *MaxProb*) are compared in this context.

4.2.1.1 PET quantification

4.2.1.1.1 Activity curves and BR curves

Figure 52 and Figure 53 show an example of activity curves and curves of BR obtained from the Monte-Carlo simulation for one subject at each stimulation condition (placebo, stim05, stim10 and stim25). Curves are provided for each striatal ROI and the cerebellar reference region. The four time-intervals, defined to study the effect of the stimulation across the acquisition time, are displayed in colour in the figures.

The effect of stimulation (applied to labels in left hemisphere only) was well visible at stim25 and corresponds to a drop of both TAC and BR curve after 40 minutes of acquisition. This effect was however less evident at stim05, in particular in the accumbens, in which data had higher noise levels. Note that even though caudate and accumbens ROIs had the same input TAC for PET-SORTEO simulation, activity and BR obtained were inferior for accumbens due to substantial partial volume effect in such small structures. Regional BRs extracted in the parametric BR images per stimulation condition, time-interval and AC approach are shown in Figure 54.

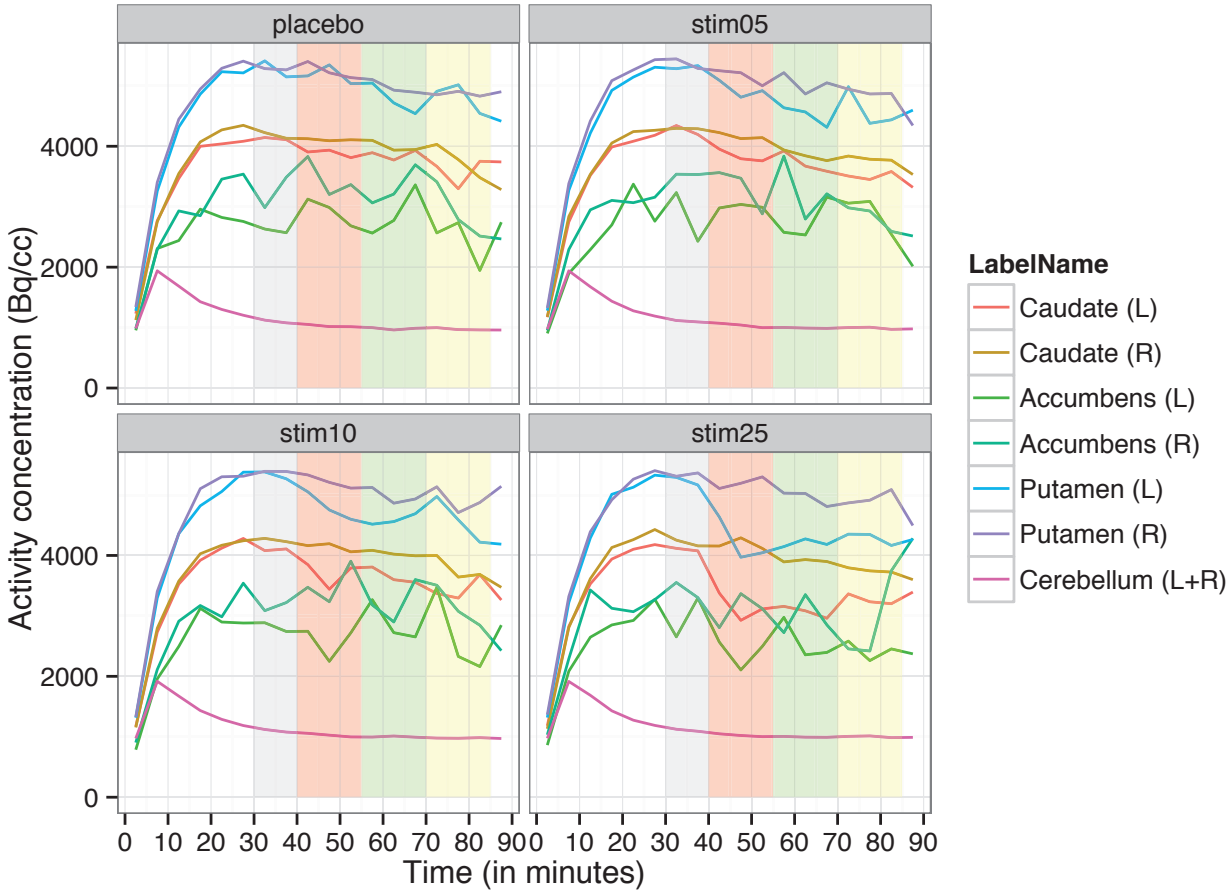

Figure 52: Example of TACs obtained for one simulated subject randomly selected, per ROI, for all stimulation conditions tested (i.e. placebo, stim05, stim10, stim25) and with CTAC. Time-intervals are displayed in colours in the background of the graph as follows: baseline in grey, stim in red, post1 in green and post2 in yellow. Dopamine release was only simulated for the caudate, putamen and accumbens on the left.

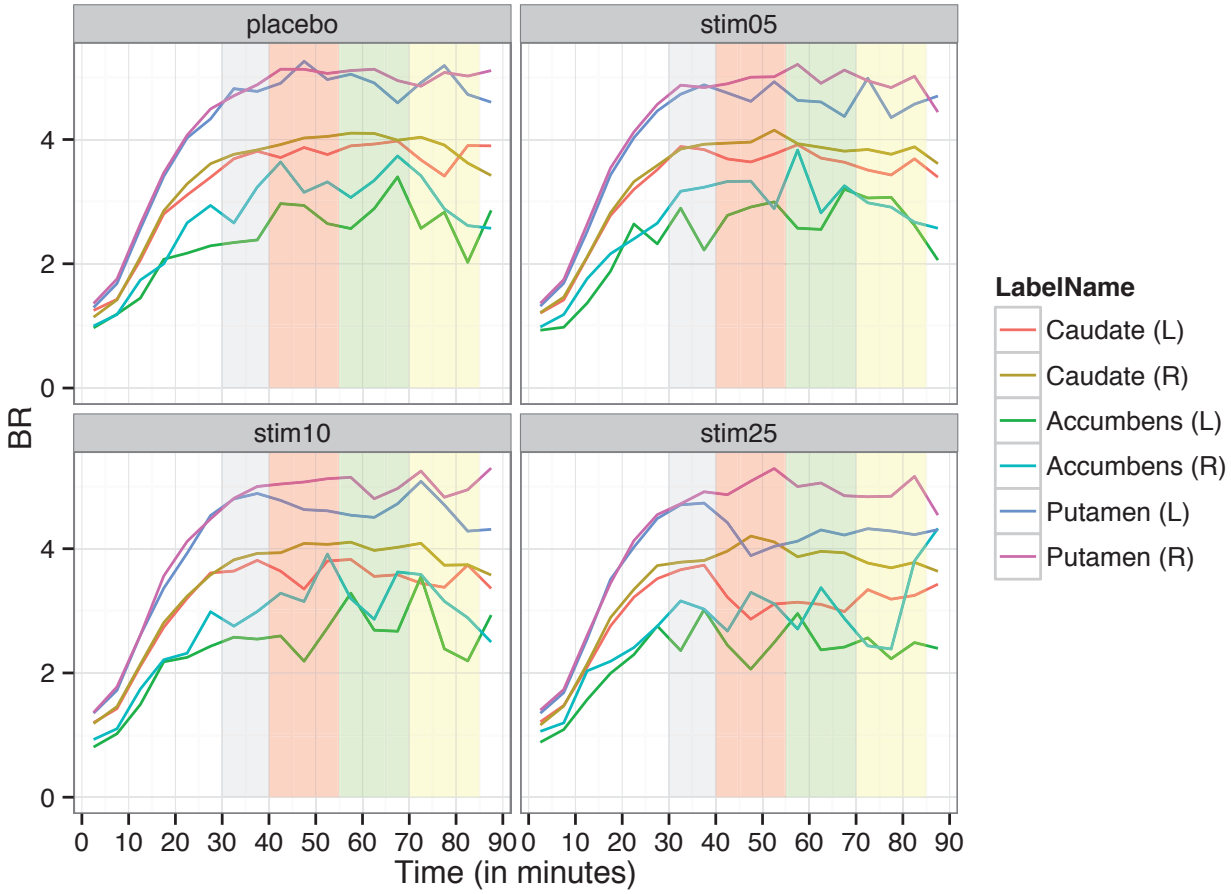

Figure 53: Example of curves of BR estimated with a simple target-over-reference model with cerebellum as reference region, shown for one randomly selected simulated subject. Curves are shown for CTAC per ROI, for all stimulation conditions tested (i.e. placebo, stim05, stim10, stim25). Time-intervals are displayed in colors in the background of the graph as follows: baseline in grey, stim in red, post1 in green and post2 in yellow.

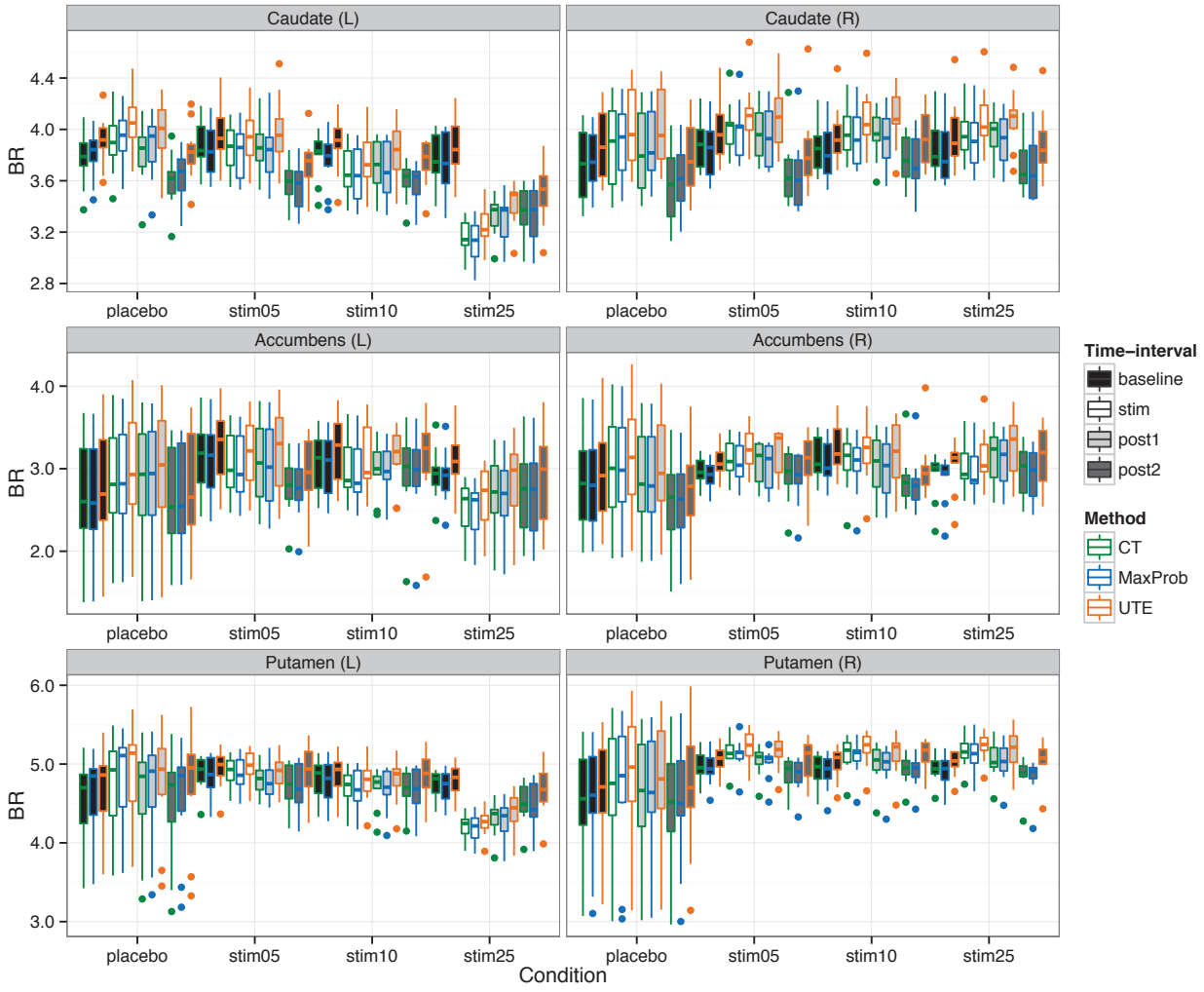

Figure 54: Mean BR across subjects, per ROI and stimulation condition, for the CT, *UTE* and *MaxProb* AC methods. Results are shown for the placebo group (n=11) and the active group (stimulated on the left; stim05, stim10 and stim25) (n=10). With *UTE*, BR were generally higher than those obtained with CT or *MaxProb*, The effect of stimulation can be seen in the differences between right and left labels, in particular for stim25.

4.2.1.1.2 Quantification error

Mean errors computed as a function of time for selected regions that were obtained with *UTE* and *MaxProb* are shown in Figure 55 and Figure 56. The graphs report the bias on the time-activity curves (Figure 55) and BR curves (Figure 56) across time for the striata (caudate, accumbens and putamen) and the cerebellum. Figures of mean absolute error for the TACs and BR curves across all subjects are provided in the Appendix (Figure 68 and Figure 69).

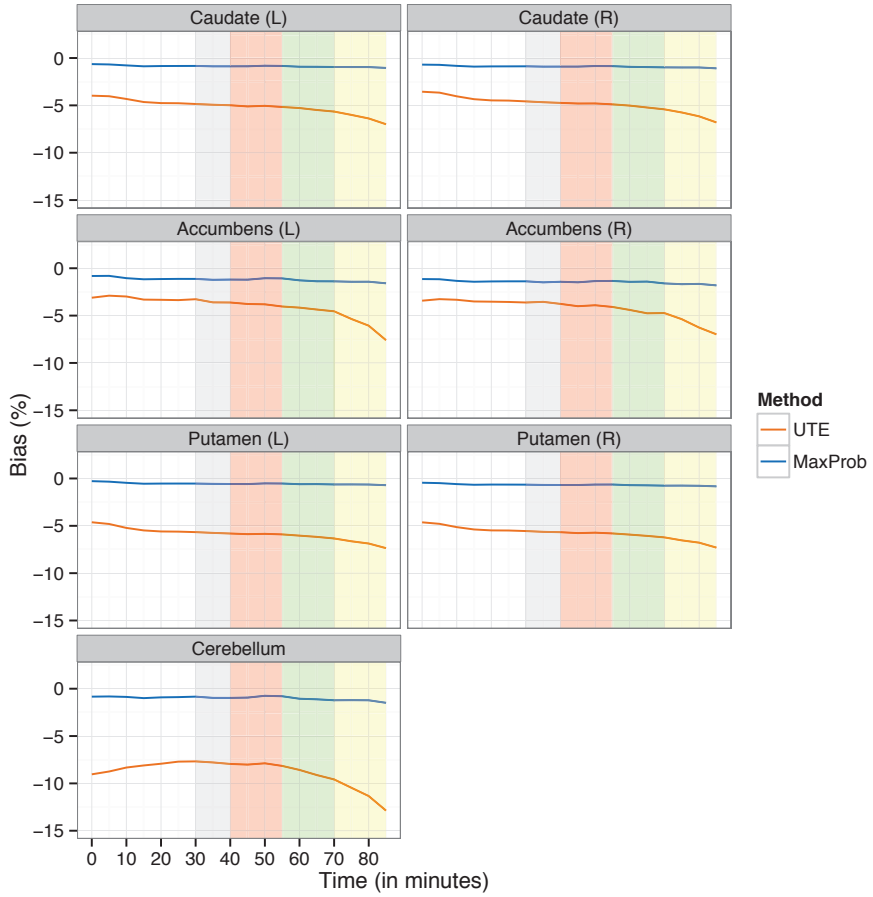

Figure 55: Mean bias over time for the PET frames across all subjects (n=21) for the *UTE* and *MaxProb* MRAC methods, i.e. during the 90-minute [^{11}C]raclopride PET acquisition, for striatal regions and cerebellum. Background features as above (Figure 52). Note the time-dependence of bias for UTE but not MRAC.

For the cerebellum, mean bias on time-activity-curves varied over time from -7.7 (lower error) to -12.9% (higher error) with *UTE* and from -0.7 to -1.6% with *MaxProb*. Mean bias in the striata (caudate, accumbens and putamen) varied from -3.8 to -7.2% for *UTE* and from -0.7 to -1.2% for *MaxProb*. The magnitude of bias tended to increase at later time-intervals for *UTE*, whereas it remained stable with *MaxProb*. For *UTE*, the magnitude of bias in the cerebellum decreased between 0 and 30 minutes, stabilized until minute 50 and increased until the end of the acquisition.

BRs calculated after *UTE* AC were substantially affected by quantification errors obtained in the cerebellum. The inverse U shape of bias time course in the cerebellar TACs (Figure 56) translated into a U shaped bias time course for the BRs. Mean error on BR reached +6.7% for *UTE* and were highly variable over time. However, with *MaxProb*, the mean error on BR did not fluctuate and remained below +1% for all striatal regions.

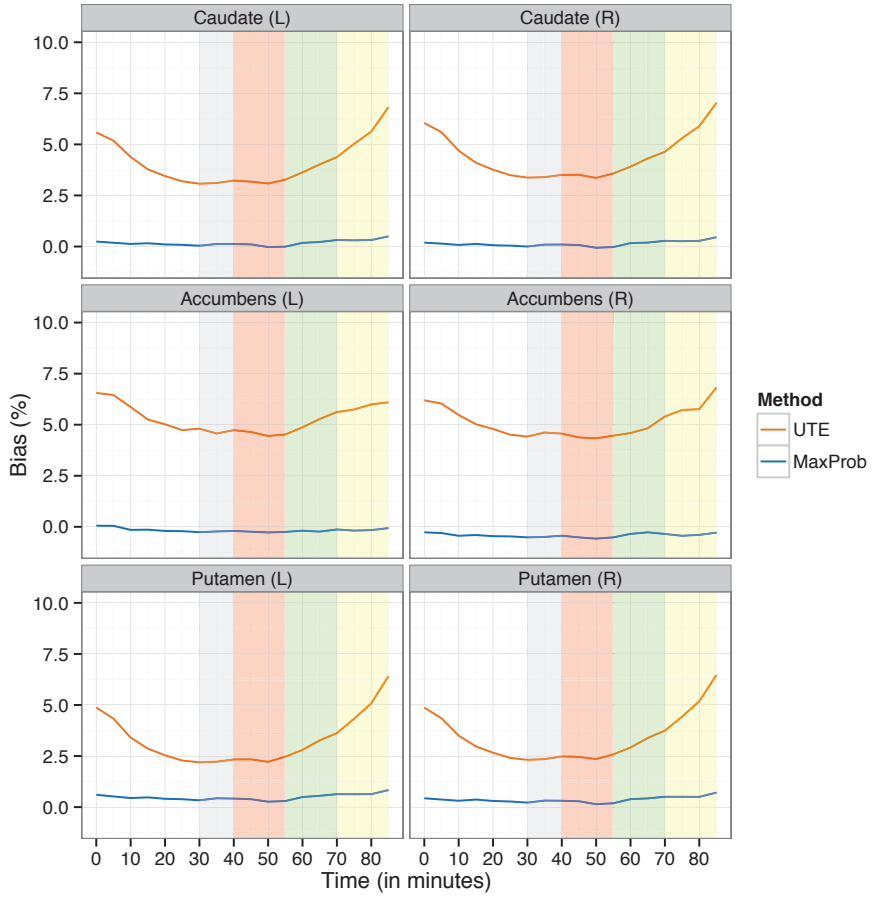

Figure 56: Mean bias over time for the BR estimated with a simple 5 min target-to-reference model with cerebellum as reference region, across all subjects (n=21) for the *UTE* and *MaxProb* MRAC methods. Background features as above (Figure 52).

Figure 57 shows the regional bias for parametric images of BR extracted for each time-interval. This figure shows similar data to Figure 56, but several frames were averaged per time-interval, and between-subject variability is shown. Again, regional BR errors for all time-intervals were close to zero with *MaxProb*, whereas the bias was higher and increased at the later time-intervals for *UTE* AC. The dispersion of the error across all subjects was higher for *UTE* than for *MaxProb*, especially at interval post2. Paired Wilcoxon signed-rank tests showed that differences in BR between CT and UTE were significant, whereas no significant differences between CT and *MaxProb* were found.

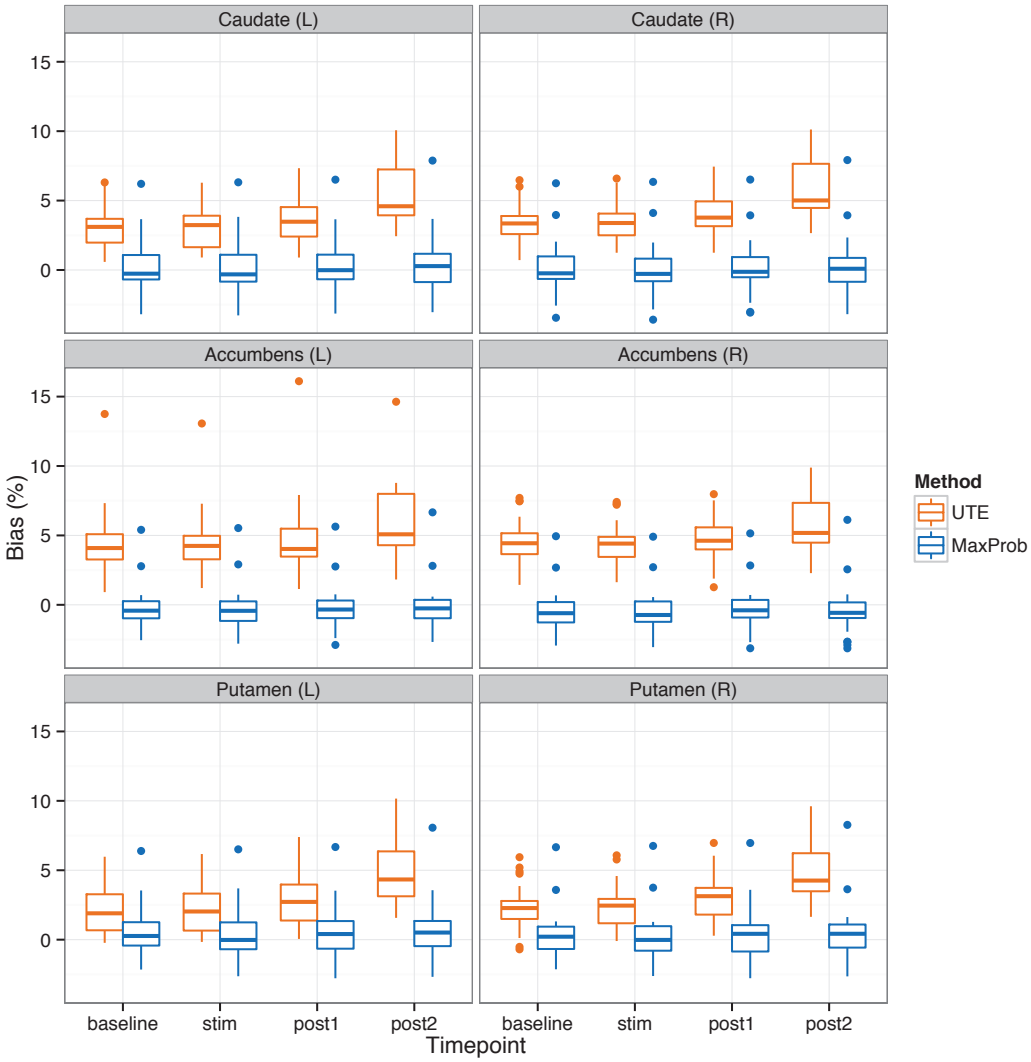

Figure 57: Boxplots of regional bias on parametric BR images across all simulated subjects (n=21), per time-interval, for the *UTE* and *MaxProb* MRAC approaches. Outliers are represented as dots.

Figure 58 shows the images of mean bias calculated on parametric BR images obtained with *UTE* and *MaxProb*, compared to CTAC for each time-interval. With *UTE*, the bias in the striatum was between 4 and 6% at the beginning of the acquisition (baseline and stim) and increased to 8% at the end of the dynamic acquisition (post2). With *MaxProb*, the local bias remained under 1% for all time-intervals.

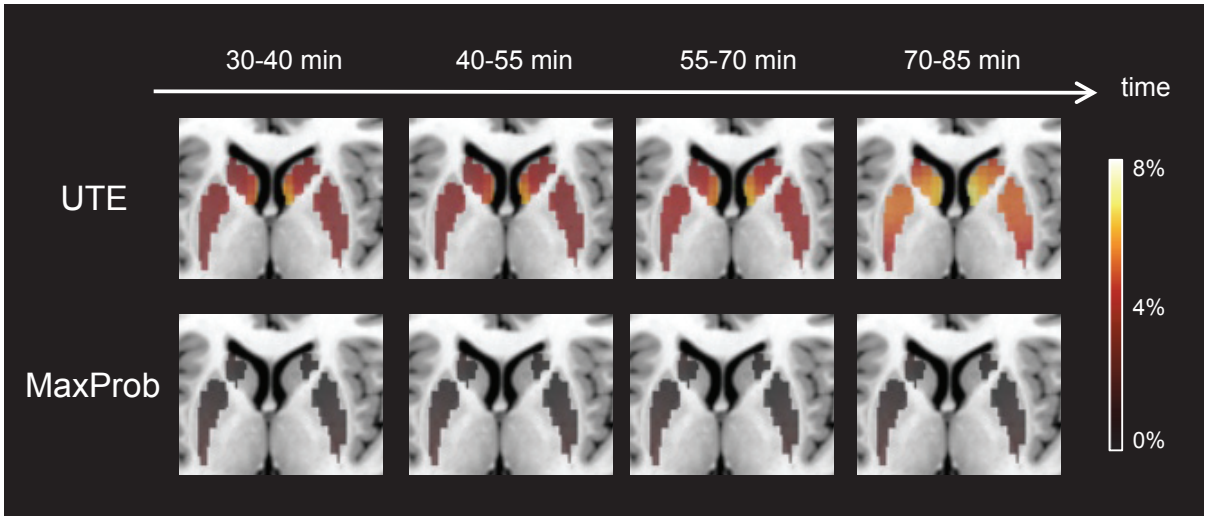

Figure 58: Mean of 21 bias images between BR_{CTAC} and BR_{MRAC}, per time point, in standard stereotaxic space. Color scale: percentage error. The bias images are masked by the mask of the striatum.

4.2.1.1.3 Outliers

In the analysis of PET quantification, we found 16 subjects that had regional errors superior to 5% with *UTE* and two of them presented regional biases on BR superior to 10%. With *MaxProb* only one subject had a bias on BR superior to 5% (which corresponds to one of the outliers with bias superior to 10% with *UTE*). An example is shown in Figure 59.

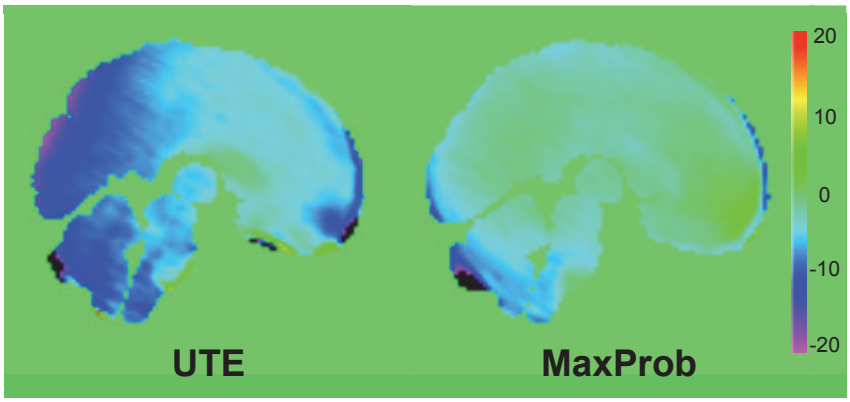

Figure 59: Example of an outlier subject. The parametric images of relative difference between PET_{MRAC} and PET_{CTAC}, obtained with *MaxProb* (left) and *UTE* (right) MRAC approaches are shown. The images of relative differences were computed on averaged dynamic PET series in MNI space, and masked by a brain mask.

The parametric images of relative difference between PET_{MRAC} and PET_{CTAC} for the outlier subject that had regional errors superior to 5% for *MaxProb* and superior to 10% for *UTE* are shown in Figure 59. For *MaxProb*, abnormal underestimation of PET was observed in the inferior area of the cerebellum (error around -7%). In comparison, quantification error for *UTE* was propagated in a larger area (all posterior brain, including cerebellum) and had higher quantification error rates (around -15%).

4.2.1.2 Detection of endogenous dopamine variation

4.2.1.2.1 Regional analysis

Figure 60 shows the mean variation of BR (Δ) between baseline and other time-intervals across placebo and active groups under different stimulation conditions. As ROIs in the right hemisphere did not undergo stimulation, conditions stim05, stim10 and stim25 in these regions represent test/retest data.

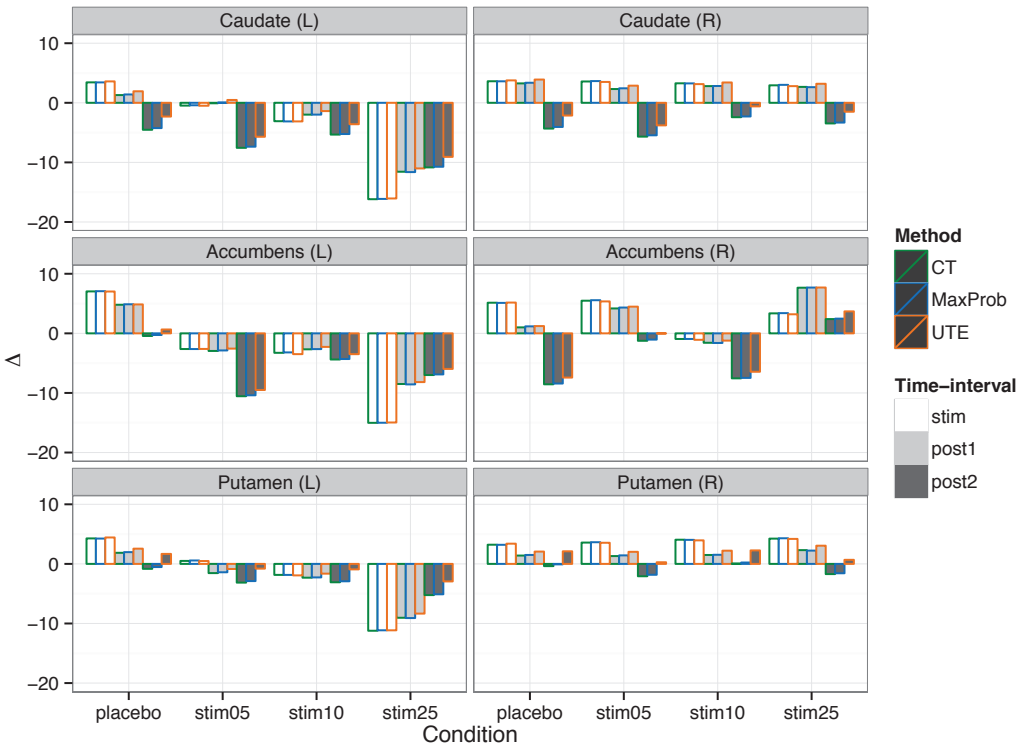

Figure 60: Mean variation of BR between baseline and other time-intervals, Δ (in %), per stimulation condition, for the CT, *UTE* and *MaxProb* AC methods. Results are shown for the placebo group (n=11) and the active group (stim05, stim10 and stim25) (n=10). Figure of boxplot is given in the Appendix (Figure 70).

Characteristic patterns of Δ compared with placebo (Figure 60) were identified for all conditions in the right hemisphere that represents the condition without PET displacement. For those regions, stim and post1 had similar and positive Δ which suggests that BR at stim and post1 was larger than BR at baseline. Conversely, post2 had negative Δ which represents a decrease of BR at post2 compared to BR at baseline. Those patterns were similar for all ROIs and time-intervals in the right hemisphere as well as for the placebo condition in the left hemisphere. Note that no stimulation was applied in the right hemisphere, and all Δ should be constant and close to zero, however high variability (from -4 to 4 for caudate right) between time-intervals was observed. In the left hemisphere, the effect of stimulation tended to increase values of Δ (indicating greater difference to baseline implying dopamine release), and patterns observed in the placebo condition were inversed. For conditions stim05, stim10 and stim25, the Δ magnitude increased at time-interval stim. This showed that BR at stim was inferior to BR at baseline. At post1 and post2, Δ increased progressively, until returning to equilibrium.

Δ ratios computed with *UTE* tended to be both under and over estimated compared to CT, depending on the time-interval, in particular at post2. At stim, differences between UTE and CT were not significant, however they were systematically significant at time-intervals post1 (except in accumbens with stim05 and stim25) and post2 (paired Wilcoxon signed-rank test). In contrast, Δ ratios obtained with *MaxProb* were very close to those obtained with CT and no significant differences were found.

The differences of mean Δ between active and placebo groups are shown in Figure 61. Differences of mean Δ were calculated to take into account inter-subject Δ and inter-time-interval variations and thus highlight the effect of PET displacement in the active group. The effect of stimulation was almost unsubstantial in ROIs of right hemisphere except for the accumbens (this small region was more sensitive to noise and partial volume effect). On the contrary, for ROIs in the left hemisphere, the effect of stimulation was characterized by increasing amplitudes of the Δ difference from stim05 to stim25. At the stim time-interval, the Δ differences for left caudate and AC CT reached -3.9% for stim05, -6.5% for stim10 and -19.6% for stim25. Those values were close to the initial degree of stimulation imposed (i.e. 5, 10 and 25%) but remained slightly inferior. Δ_{DIFF} obtained with the MRAC approaches produced similar patterns than CTAC.

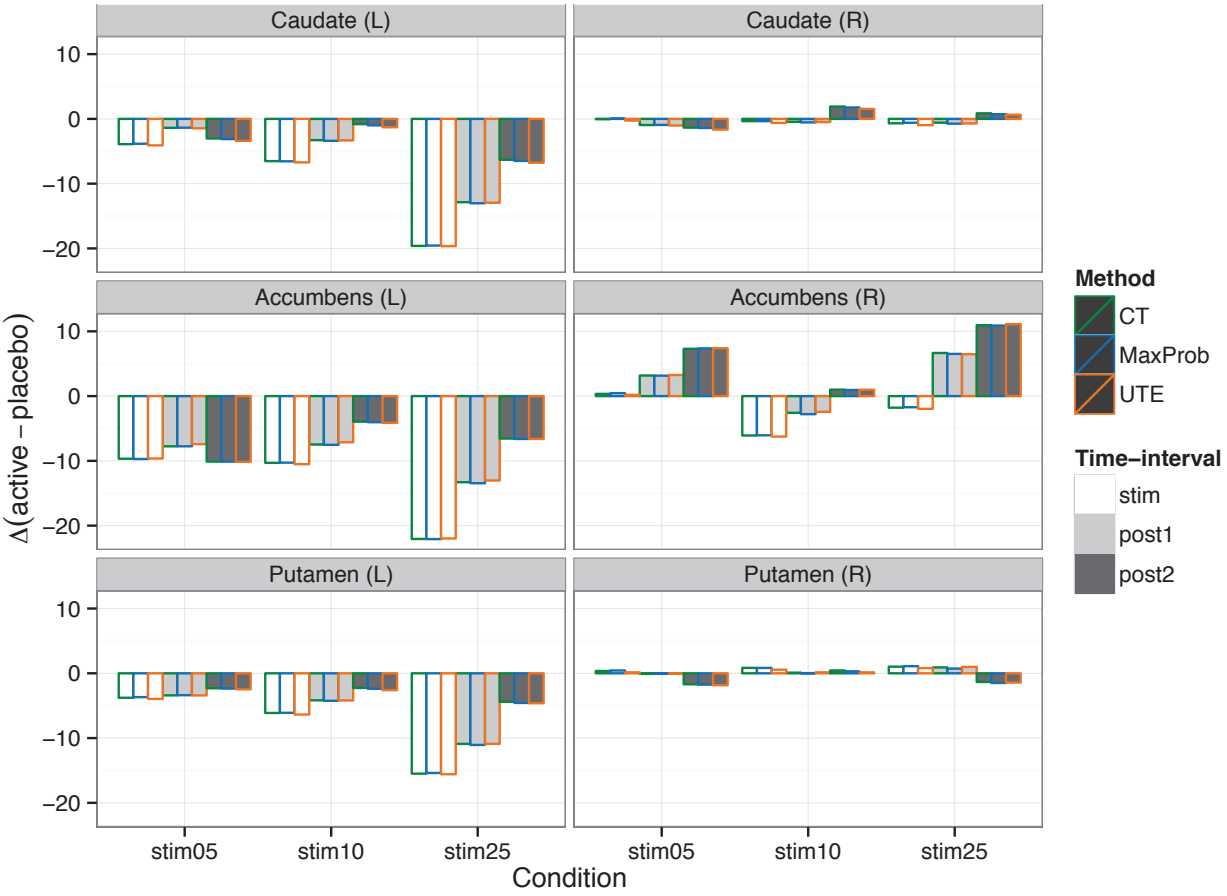

Figure 61: Mean delta difference between active (n=10) and placebo (n=11) groups, per stimulation condition, for the CT, *UTE* and *MaxProb* AC methods shown for the placebo group (n=11) and the active group (stim05, stim10 and stim25) (n=10).

4.2.1.2.2 Voxel-wise analysis

Figure 62 shows the t score maps of the differences in parametric images of BR, between active and placebo groups, obtained with CTAC, thresholded at p<0.001 uncorrected. The results are given for the three time-intervals studied (stim, post1 and post2), compared to baseline. The effect of stimulation across time was clearly lateralized to the left hemisphere, and was characterized by an important area of significant voxels showing BR reduction at time-interval stim, whereas the effect of stimulation on PET displacement was reduced for later time-intervals (post1 and post2) suggesting a return to equilibrium.

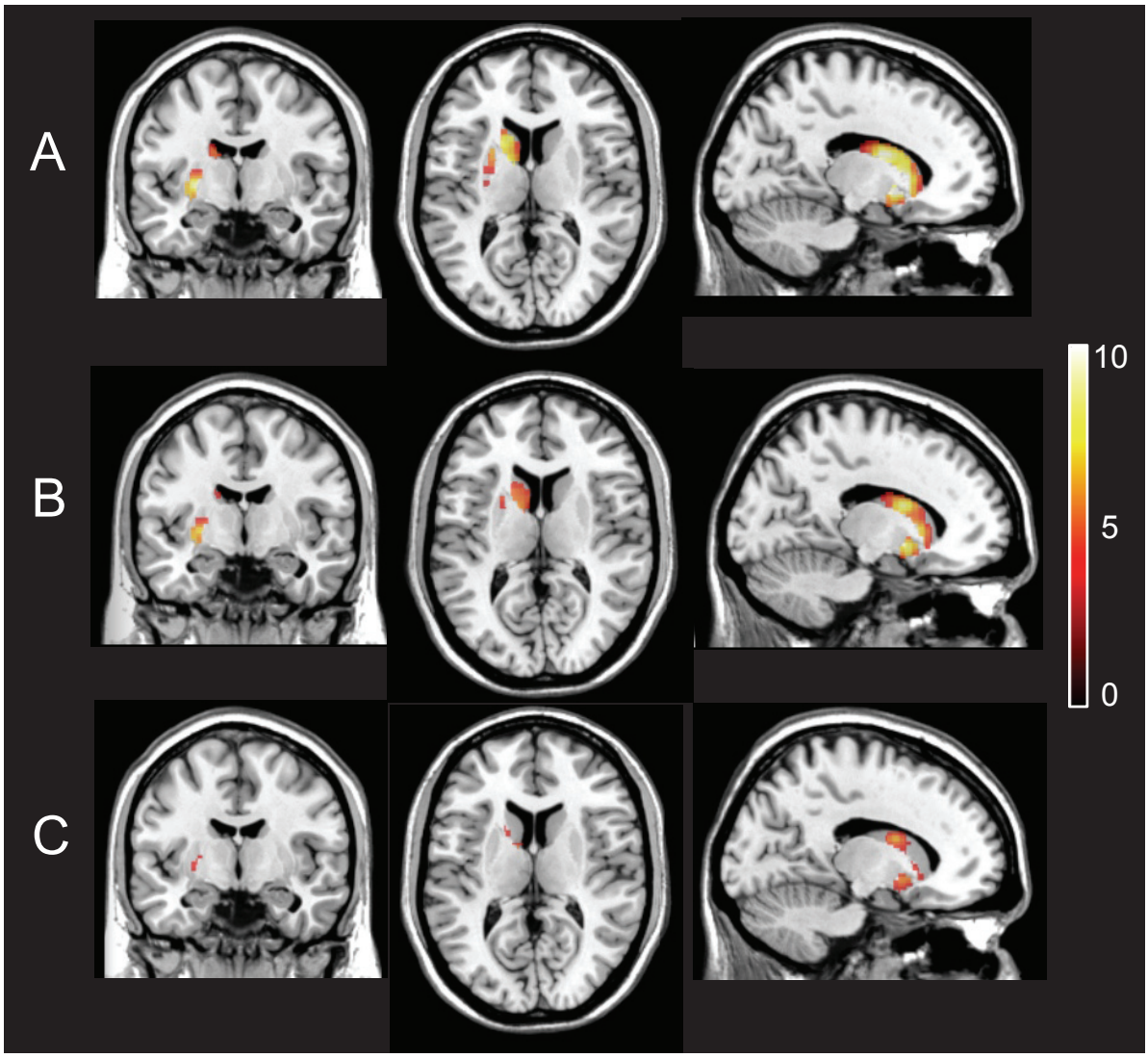

Figure 62: Comparison of parametric images of BR, between active (n=11) and placebo (n=10) groups for stim25, obtained with CTAC. The images show regions of BR reduction at time-intervals stim (A), post1 (B) and post2 (C), compared to baseline, at a significance level of p<0.001 uncorrected. Color scale: t statistic. Stimulation was applied on the left. Note that with ground truth CTAC, the dopamine release was detected in 97% of the striatal volume stimulated (for time-interval stim, with condition stim25).

Results obtained for the SPM analysis are summarized in Table 9. For each AC method, each condition and each time-interval, the total number of significant voxels showing BR decrease in the active group, compared to the placebo group, is given. The sensitivity of each AC method is reported in number of voxels and percentage compared to the simulated volume. The proportion (in %) of voxels detected with *UTE* or *MaxProb*, compared to CT, is also calculated (sensitivity relative to CT).

The sensitivity to detect the endogenous dopamine release of the CTAC, compared to the real striatal volume stimulated was assessed. At time-interval stim, we found a detection threshold of 97%, 26%

and 7% for stim25, stim10 and stim05 respectively (results also shown in Figure 62). In terms of sensitivity relative to CT, at stim25, both *MaxProb* and *UTE* MRAC methods were able to detect significant BR variations between baseline and other time-intervals, in the active group compared to the placebo group, with high sensitivity, but sensitivity was slightly inferior for *UTE*. At stim25, detection thresholds for stim, post1 and post2 were 100, 100 and 97% with *MaxProb* and 99, 98 and 89% with *UTE,* respectively. At stim05, *MaxProb* detected 94, 82 and 93% of the voxels with significant BR decrease for stim, post1 and post2, respectively. In contrast, *UTE* only detected 91, 62 and 77% of the voxels for the same time-intervals. Overall, *MaxProb* had a higher sensitivity than *UTE* in detecting group differences at the voxel level.

Table 9: Number of significant voxels obtained with the SPM analysis. Sensitivity compared to simulated volume is given in number of voxels (and %) per AC approach, stimulation condition and time-interval. Relative sensitivity of MRAC to CTAC is provided (in %).

		Sensitivity			**Relative sensitivity to CT**	
		CT	*MaxProb*	*UTE*	*MaxProb (%)*	*UTE (%)*
stim25	**stim**	1471 (97%)	1471 (97%)	1457 (96%)	100	99
	post1	1308 (86%)	1308 (86%)	1276 (84%)	100	98
	post2	532 (35%)	517 (31%)	473 (31%)	97	89
stim10	**stim**	395 (26%)	357 (24%)	351 (23%)	90	89
	post1	154 (10%)	154 (10%)	119 (8%)	100	77
	post2	92 (6%)	92 (6%)	73 (5%)	100	79
stim05	**stim**	101 (7%)	95 (6%)	92 (6%)	94	91
	post1	100 (7%)	82 (5%)	62 (4%)	82	62
	post2	231 (15%)	214 (14%)	178 (12%)	93	77

4.2.2 Real data

In this section, we describe the results obtained when applying *UTE* or *MaxProb* AC solutions combined with Eber motion correction algorithm to real PET-MR data acquired on the Siemens mMR Biograph system.

4.2.2.1 Notable specific case

The example of one subject of the study that showed important motion artefacts was employed to illustrate the impact of motion artefacts on both image quality and TACs. With this example we provide an indication about the effect of applying the Eber algorithm. Averages of dynamic PET images, uncorrected and corrected for motion, are reported in Figure 63. Due to the motion, the uncorrected image produced an effect of blurring in particular at the top of the head. Another consequence of this motion artefact is the underestimation of PET uptake in the striatal regions, compared to PET data corrected for motion. Figure 65 shows the BR curves across time for the given subject. In the absence of motion correction (top), regional BR decreased after 30 minutes, whereas the BR was recovered after applying Eber motion correction (bottom).

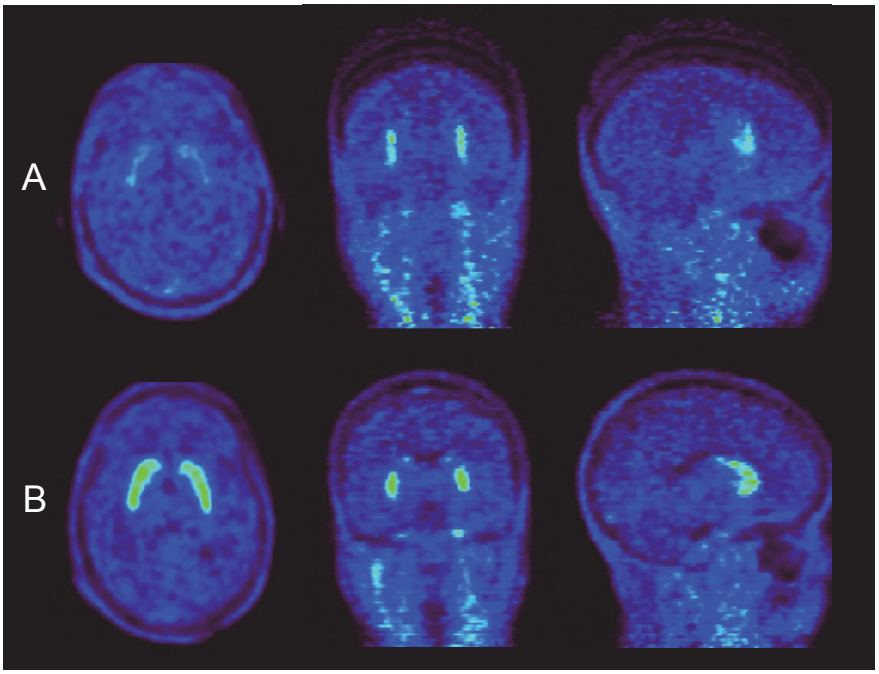

Figure 63: [^{11}C]raclopride bolus-infusion study over 110 minutes uncorrected (A) and corrected (B) for motion. Mean images are shown. In both cases, *MaxProb* MRAC was applied.

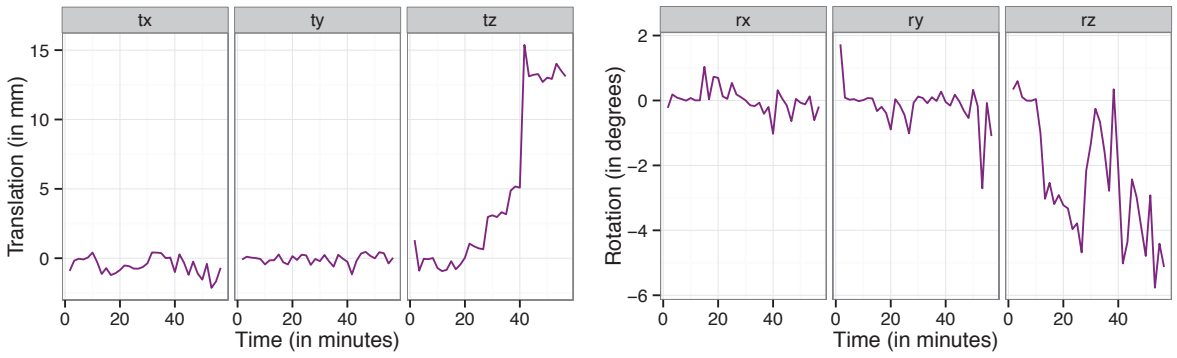

Figure 64: Motion estimation along the dynamic acquisition, for subject shown in Figure 63 (translation and rotation parameters).

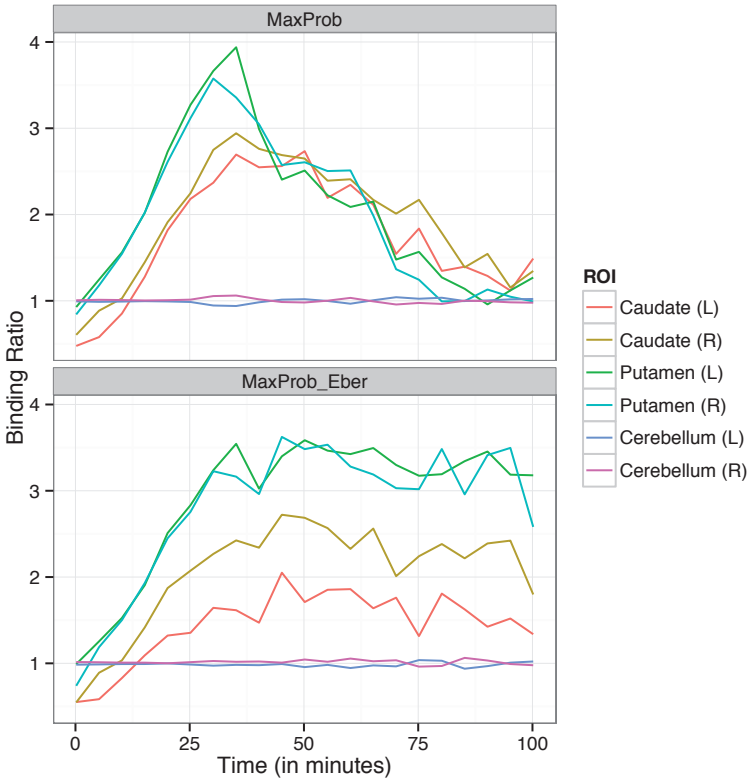

Figure 65: Example of BR curves per ROI, for one subject with important motion before (top) and after Eber motion correction (bottom). *MaxProb* AC was applied in both cases.

4.2.2.2 Quantitative results

Quantitative results are reported in Figure 66. In this figure, standard deviation of intra-regional BR extracted in striatal regions (caudate and putamen) is given per time-interval and AC method. When applying Eber motion correction, at baseline, the mean standard deviation over subjects and striatal regions decreased from 1.23 to 1.09 for *UTE* and from 1.16 to 1.03 for *MaxProb*. Significant improvement ($p<0.001$) produced by motion correction was seen for baseline and stim. Concerning differences between MRAC methods, at baseline, no significant differences were found between *UTE* and *MaxProb*, with or without Eber motion correction. At stim and post2, the BR standard deviation was significantly ($p<0.05$) reduced with *MaxProb*, compared to *UTE* AC. For example, at post2, the BR standard deviation was 1.65 for *UTE_Eber*, and 1.52 for *MaxProb_Eber*.

Overall, both *MaxProb* AC and Eber motion correction contributed jointly and individually to decrease the intra-regional variance of regional BR.

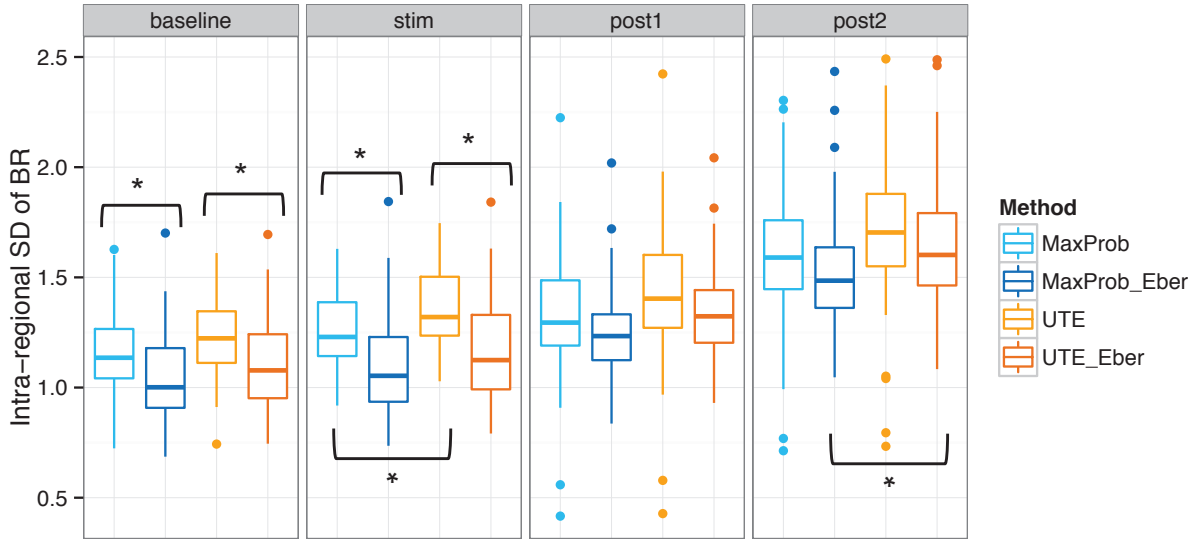

Figure 66: Boxplot of standard deviation of intra-regional BR, measured in all striatal regions, per time-interval, and per AC method applied. *: p <0.05 with the Tukey HDS test. Significant statistical tests for motion correction comparisons are indicated by brackets on the top of the graph, and significant statistical tests for AC comparisons at the bottom of the graph.

4.3 Discussion

PET quantification

Quantitative evaluation obtained with simulated [^{11}C]raclopride bolus-infusion PET data were consistent with results based on real acquisitions of dynamic [^{18}F]MPPF bolus PET data, shown in the previous chapter. The *MaxProb* method obtained similar performance in both studies that were based on two different PET tracers and targeted different ROIs due to the different specific tracer binding patterns. In addition, a similar order of magnitude was reached on the error calculated for the parameters estimated by kinetic modelling (i.e. BP_{ND} and BR). Our results also demonstrate, as suggested in Chapter 3, that *UTE* AC had similar behaviour to the *SingleAtlas* method: quantification bias tended to be increased with time-dependent tracer spatial distribution. However, quantification errors in the cerebellum with *UTE* were higher than those obtained with *SingleAtlas*, underlining again the need for alternative AC approaches in dynamic PET-MR studies. Our study based on simulated [^{11}C]raclopride PET data also permitted to confirm that motion artefacts did not explain

our finding of time-dependent (i.e. tracer distribution-dependent) changes in PET quantification due to the influence of the attenuation map. Indeed, while real data may suffer from head motion artefacts, simulated data is motion- free.

Outliers

One subject of the simulation study had substantial quantification error in the cerebellum with both *MaxProb* and *UTE* MRAC approaches. This bias had an important impact on BR modelling. The source of bias in the cerebellum with *MaxProb* for the one outlier (regional error > 5%) was not completely identified. The errors produced by *UTE* AC were even higher than *MaxProb* for this subject and more extended to the posterior part of the brain Figure 59.

Simulated PET data

High variability was observed for Δ BR across all subjects obtained for a given condition, especially in the labels from right hemisphere that did not undergo stimulation so they represent test-retest data (Figure 60). In our simulation study, the same input TACs were used for all subjects (Figure 47 for the placebo group and Figure 49 for the active group). The intra-condition variability was thus due to the anatomical variability, PET noise integrated in the simulation process by PET-SORTEO, and partial volume effect. Note that a factor of around 3 was identified between input TACs and TACs extracted from simulated PET data that is explained by partial volume effect.

The mean Δ calculated across all subjects (placebo and active groups) at time-intervals stim and post1 relative to baseline was generally positive, around 5% (Figure 60). However, in cases where no stimulation was applied (placebo group and ROI in left hemisphere for active and placebo groups) a null Δ was expected. The positive difference can be explained by the fact that BR curves that did not completely reach the equilibrium at the baseline time-interval (minutes 30-40) so the BR at baseline was inferior to BR at stim and post1 (see Figure 53).

In bolus-infusion protocols, an equilibrium state is aimed at, in which the activity reaches a constant value, maintained until the end of the acquisition by a continuous administration of the tracer. In our simulation study, curves used as input TACs for PET-SORTEO (Figure 47 and Figure 52) showed a

slight activity decrease at later time-intervals. Our input TACs were obtained from real PET/CT data, so this small decrease reflected the behaviour obtained in real acquisitions. The main consequence of having this small decrease was the negative Δ obtained in the placebo condition for the time-interval post2 (Figure 60). Note that this phenomenon was largely compensated for in the difference of Δ (Figure 61).

Our study employed an exponential expression to model the extracellular dopamine concentration variation produced by an endogenous release (stimulation) and the displacement of PET tracer observable in PET. Due to this exponential expression, the maximal amplitude of stimulation (5, 10 and 25%) did not last during the entire interval of the stim time-intervals. After the impulsion created by stimulation, the exponential behaviour of our model produced an immediate start of the return to equilibrium of TACs in the striatum. As a consequence, the variation of BR captured in the time-interval (shown in Figure 61) was necessarily inferior to the maximal amplitude of stimulation of the initial stimulation.

In this study, substantial and significant differences were found for BR and Δ computed at regional level, between CT and *UTE*, in particular at later time-intervals (post2), whereas no significant differences were found between CT and *MaxProb*. It is possible that the quantification errors found for BR (especially with the *UTE* method see Figure 57) were partially cancelled out when computing the Δ and also when comparing placebo and active groups, and thus slightly affect the Δ (Figure 60) and the difference of Δ (Figure 61). Similar compensation of quantification errors have been shown by Galazzo et al. (2016) in a PET-MR study assessing refractory focal epilepsy with [^{18}F]FDG and ASL. Despite the quantification errors produced by the *UTE* AC, compared to CTAC, no differences were found for z-scores of the asymmetry index between the two AC approaches.

Real PET-MR data

Ground truth CT was not available in this study. For this reason, the evaluation could only be based on the intra-regional dispersion of BR values. The time-intervals used for the BR analysis were not exactly the same between simulated and real data. This was due to the fact that the implementation of both protocols evolved in parallel. In addition, real PET data between 40 and 45 minutes was not analysed with the BR, but will be integrated in further work.

We showed that both Eber and *MaxProb* (and the combination of both algorithms) improved PET signal quality relative to no motion correction and UTE, respectively. This evaluation needs to be continued when the study will be completed, to compare whether motion and attenuation correction algorithms reduce BR variability within each group of subjects (placebo and active). In this context, it will be interesting to investigate if the MRAC approach used has an impact on group differentiation.

Limitations of the simple tissue-to-reference ratio kinetic modelling

Our analysis was based on the simple tissue-to-reference ratio. However, this approach seemed too sensitive to the high levels of noise in regional TACs. A model that fits the data observed and that searches for a possible effect of endogenous dopamine release on the PET signal (Normandin et al., 2012) would be preferable to detect PET displacement.

4.4 Conclusion and perspectives

UTE produced high quantification bias on PET activities and simple tissue-to-reference ratios were importantly affected, in particular at later time-intervals of the dynamic acquisition. Conversely, accurate quantification was achieved with *MaxProb* and biases obtained on PET activity and BR were very close to zero.

We showed that compared to the standard MRAC approach *UTE*, the *MaxProb* multi-atlas MRAC enhanced sensitivity to detect physiological variations in a dynamic PET study.

To further investigate the sensitivity of MRAC methods in differentiating two groups of subjects, the model proposed by Normandin et al. (2012) can be applied to a new set of simulated PET data and to the tDCS PET-MR study. The simulations will be based on the analytic expression of ligand exchange between compartments of plasma, tissue and specific binding in region of interest and region of reference. The release of endogenous dopamine will be modelled with gamma functions. In this context, we will test several times of endogenous release to see whether a late stimulation is more impacted by *UTE* inaccuracies in the later frames of the dynamic acquisition. The parameters estimated by the lp-ntPET algorithm will be compared for each AC approach.

Used singly and together, Eber motion correction and multi-atlas *MaxProb* AC contributed to reduce the intra-regional variance of BR. Further work will investigate the sensitivity gain generated by the proposed methods in stimulation conditions aiming to evoked extracellular dopamine concentration variation by contrasting groups receiving an active or placebo stimulation. In addition, it will be interesting to correlate variations detected in the PET signal with the MRI data: anatomical and functional connectivity (DTI and BOLD fMRI) and brain activity (ASL).

General conclusion

To address the question of brain AC for PET-MR, I have achieved a multi-atlas procedure that generates a subject-specific μ-map. The proposed solution only requires a T1-weighted MRI of the subject, commonly acquired in clinical and research protocols, and a database of atlases.

The *MaxProb* method permitted generating pseudo-CT images with high accuracy and the bias of static PET quantification was reduced to less than 2%. In an independent multi-centric study published by Ladefoged et al. (2016), *MaxProb* also obtained very good results and was among the top three of eleven techniques proposed in the literature. In addition, we were the first to demonstrate in the brain that an inaccurate attenuation correction map combined with inhomogeneous spatial tracer distribution can lead to a non-constant bias of the activity measure across time. *MaxProb* multi-atlas AC is not affected by this phenomenon. Accurate quantification was also achieved with *MaxProb* on physiological parameters estimated from kinetic modelling, even when cerebellum was used as reference region. This will matter in research practice: From our simulation study we showed that compared to a standard approach (UTE), *MaxProb* multi-atlas MRAC enhanced sensitivity to detect physiological variations in a dynamic PET study.

Our initial goal to reduce PET quantification errors to less than 5% in PET-MR systems has been reached. The *MaxProb* software is starting to be distributed to other centres for academic collaborations, opening the way for a common MRAC method for dynamic PET studies on hybrid PET-MR systems.

Advantages of the new method

Our multi-atlas method *MaxProb* has the advantage of only needing a T1 MR image of the subject to compute its μ-map. This is interesting compared to methods that use other specific MR contrasts such as Dixon or UTE. First, because of the gain in acquisition time and second, due to the possibility to apply *MaxProb* to PET data acquired on other systems that cannot provide Dixon or UTE sequences, such as PET alone scanners (Oncovision, http://oncovision.com/caremibrain/) in which case a simple T1 could be acquired on a traditional MRI scanner in the context of a standard clinical

acquisition and coregistered post hoc, whereas UTE or Dixon contrasts are not usually acquired and not even available on some MRI systems.

Another benefit of the multi-atlas concept is its extensibility to children, and also to non-human species used in PET research such as non-human primates and cats, as I have suggested in chapter 2.

General limitations and future work

As previously mentioned, subjects with unusual anatomy that deviates too much from the norm represented by the MR-CT atlas pairs will not be well managed by the multi-atlas technique (e.g. post-operative skull defects, very large sinuses). To potentially overcome this issue, several strategies have been presented at the end of chapter 2 that consist in the combination of subject-specific anatomical information extracted from the MRI with the output of the multi-atlas technique.

Another point to consider is the limit of the CTAC used as reference method to assess new MRAC approaches. Even if the CT has been considered as the reference AC method by the scientific community, it is important to keep in mind that CT does not directly measure PET 511 keV photon attenuation by the tissues, and that an energy conversion needs to be applied. The mathematical relationship used for this conversion has been determined empirically and presents approximations (Burger et al., 2002). In addition, the linear conversion approach used defers from one constructor to another (Siemens vs. GE). To overcome this problem, PET simulation can be used, in which the true activity is known. My work in chapter 4 has partly addressed the problem, but did still use attenuation phantoms with discrete values. PET-SORTEO upgrades are necessary for permitting the use of continuous attenuation coefficients.

While our work so far has indicated that common anatomical or post-surgical variants have limited impact on brain PET quantification with *MaxProb*, further work should assess in detail the robustness of the multi-atlas approach. This will include testing subjects with specific anatomies such as large frontal sinuses, post-operative cases, subjects with low-quality images and children that may not be well represented by our atlas database.

Another axis of future investigation concerns the variability between two CT images of the same subject (test/retest data) compared to the variability between the real CT and the pseudo-CT

computed with the *MaxProb* multi-atlas approach. In parallel, the variability and reproducibility of μ-maps derived from the UTE will be studied.

The path to quantitative simultaneous PET-MR in neuroscience

In this last year, new studies and protocols have been proposed to better understand brain function and new applications have been identified (Sander et al., 2015; Villien et al., 2014; Wey et al., 2014). In addition to PET-MR bi-modality, some teams have recently worked on the combination of PET-MR with EEG (Neuner et al., 2015; Shah et al., 2012) to widen the range of parameters that can be assessed simultaneously.

Simultaneous PET-MR studies aim at highlighting small variations of PET signal (or kinetic parameters modeled from PET data) and thus require accurate AC that does not produce spatially variant bias (Galazzo et al., 2016). Now that accurate MRAC has been achieved with multi-atlas solutions (Ladefoged et al., 2016), more innovative brain PET-MR protocols can be developed to investigate physiological mechanisms, and in particular neurovascular coupling of the neurochemical brain at work.

My work forms part of studies which will now enable interesting developments in the domain of multi-modal analyses to integrate the complementary but simultaneous information derived from PET and MR (and sometimes EEG). The final aim could be a full understanding of spatio-temporal relationships between connectivity, neurotransmission, and neural activity.

Appendix

State-of-the-art in PET-MR attenuation correction

Author	Year	Journal	Family	Algorithm	Error reported	Pros and cons		
						Accuracy	Robustness	Ease of implementation
Mollet	2014	JNM	Transmission-based	External positron source in the PET FOV. Transmission data extracted from simultaneous transmission-emission scan using the TOF	8% in soft tissue and 17% in bones	-	+	--
Salomon	2011	IEEE TMI	Joint emission and attenuation estimation	MLAA with TOF and anatomical priors (T1-w MRI segmented into several clusters)	In the cerebellum, -5% with FDG and 41% with FCH			
Mehranian	2015	IEEE TMI	Joint emission and attenuation estimation	MLAA with TOF and anatomical priors (Dixon MRI segmented into 4 classes: lung, fat, air and cortical bone)	In the cerebellum, -7% with FDG and -2.5% with FCH	-	+	+
Benoit	2016	Phys Med Biol	Joint emission and attenuation estimation	MLAA with UTE and a discretized T1-w MRI as anatomical priors	From -5 to 2% in large brain regions			
Zaidi	2003	Med Phys	MRI segmentation with constant coefficients	Segmentation of the T1-w MRI into four tissue classes (air, skull, brain, and nasal sinuses) using a fuzzy c-means algorithm	Regional errors between -2 and 7%			
Anazodo	2015	Frontiers in Neuroscience	MRI segmentation with constant coefficients	Bone mask extracted from the T1-w MRI combined with the Dixon-based μ-map	Mean error of -14.1%			
Keereman	2010	JNM	MRI segmentation with constant coefficients	Bone, soft tissue and air are segmented by thresholding the corrected R2* map (UTE sequence)	Mean error of 11.4%	--	+	+
Catana	2010	JNM	MRI segmentation with constant coefficients	Segmentation into air, soft tissue and bone.Bone and air voxels enhanced by calculating normalized	Local errors between -20 and 20%			
Berker	2012	JNM	MRI segmentation with constant coefficients	Segmentation of two-point Dixon and UTE MRI into four tissue classes (bone, air, fat and soft tissue)	Mean error over eight brain regions 7.6%			
Poynton	2014	Am J Nucl Med Mol Imaging	MRI segmentation with constant coefficients	Segmentation of T1-weighted and UTE sequences with a probabilistic CT atlas	Regional absolute bias of 1.8% in cingulate and 5.5% in cerebellum			
Ladefoged	2015	Phys Med Biol	MRI segmentation with continuous coefficients for bone	UTE segmented into five tissue classes (brain, cerebrospinal fluid, tissue, air and bone) and polynomial model for bone intensities	Regional errors between -0.5 and 4%	++	+	+
Juttukonda	2015	Neuroimage	MRI segmentation with continuous coefficients for bone	Dixon and UTE segmented in 4 tissue classes (air, fat, soft tissue, and bone) Polynomial regression is then computed between the R2* map and CT intensities for bone tissue	Regional errors around ±1% in brain structures such as parietal, temporal and occipital lobes and cerebellum			
Johansson	2011	Med Phys	MR intensity and CT HU fitting	Gaussian mixture regression model to link MR and CT intensities	Local errors between -20 and 20%	-	+	-
Navalpakkam	2013	Investigative Radiology	MR intensity and CT HU fitting	Super-vector regression estimation with features extracted from Dixon, UTE, CT images to associate MR intensities to CT intensities	Regional errors around 5%			
Andreasen	2016	Med Phys	Patch-based	Patches extracted from a database of T1-w MRI and CT pairs combined via a similarity-weighted average	3.5% in the occipital lobe			
Torrado-Carvajal	2016	JNM	Patch-based	Intensity-based nearest neighbour search between patches extracted from a database of T1-w MRI and CT pairs	Local errors between -10 and 10%	+	+	-
Roy	2014	JNM	Patch-based	Patches extracted from a database of MRI and CT pairs and combined using a Bayesian framework	Error on PET quantification not available			
Schreibmann	2010	Med Phys	Template	Mapping the CT image of a single subject to the MRI patient space	Error on PET quantification not available			
Montandon	2005	Neuroimage	Template	PET template built from 17 registered to the subject's PET image The μ-map is then wrapped to the subject's space	Error on PET quantification not available			
Malone	2011	JNM	Template	MR template built from 10 subjects registered to the subject's MRI image The μ-map is then wrapped to the subject's space	Error around -1% in the cerebellum	+	-	+
Izquierdo-Garcia	2014	JNM	Template	CT template built from 15 subjects registered to the subject's MRI image	Regional errors between 2 and 6%			
Sekine	2015	JNM	Template	CT template generated from 50 subjects and registered to a LAVA MRI	Regional errors between 2 and 3%			
Burgos	2014	IEEE TMI	Multi-atlas	MRI and CT pairs database registered to the subject's MRI Registered CTs are fused with a weighted average depending on a similarity rank	Mean error in grey matter 0.99%	++	+	+
Mérida	2017	Phys Med Biol	Multi-atlas	MRI and CT pairs database registered to the subject's MRI Registered CTs that belong to the majority class are selected and fused by averaging intensities	Mean error in grey matter 0.26%			

Table 10: Abbreviation list of the 83 regions used in the ROI evaluation based on the Hammers_mith atlases (www.brain-development.org / Hammers et al. 2003, Gousias et al. 2008), with cerebellar vermis added

Abbreviation	Complete name
Hippocampus_r	Hippocampus (right)
Hippocampus_l	Hippocampus (left)
Amygdala_r	Amygdala (right)
Amygdala_l	Amygdala (left)
Ant_TL_med_r	Anterior temporal lobe, medial part (right)
Ant_TL_med_l	Anterior temporal lobe, medial part (left)
Ant_TL_inf_lat_r	Anterior temporal lobe, lateral part excluding superior temporal gyrus (right)
Ant_TL_inf_lat_l	Anterior temporal lobe, lateral part excluding superior temporal gyrus (left)
G_paraH_amb_r	Parahippocampal and ambient gyri (right)
G_paraH_amb_l	Parahippocampal and ambient gyri (left)
G_s_t_cent_r	Superior temporal gyrus, central part (right)
G_s_t_cent_l	Superior temporal gyrus, central part (left)
G_tem_midin_r	Middle and inferior temporal gyrus (right)
G_tem_midin_l	Middle and inferior temporal gyrus (left)
G_occtem_la_r	Fusiform (lateral occipitotemporal) gyrus (right)
G_occtem_la_l	Fusiform (lateral occipitotemporal) gyrus (left)
Cerebellum_r	Cerebellum (right)
Cerebellum_l	Cerebellum (left)
Brainstem	Brainstem
Insula_l	Insula (left)
Insula_r	Insula (right)
OL_rest_lat_l	Lateral remainder of occipital lobe (left)
OL_rest_lat_r	Lateral remainder of occipital lobe (right)
G_cing_a_s_l	Cingulate gyrus, anterior part (left)
G_cing_a_s_r	Cingulate gyrus, anterior part (right)
G_cing_p_l	Gyrus cinguli, posterior part (left)
G_cing_p_r	Gyrus cinguli, posterior part (right)
FL_mid_fr_G_l	Middlle frontal gyrus (left)
FL_mid_fr_G_r	Middlle frontal gyrus (right)
PosteriorTL_l	Posterior temporal lobe (left)
PosteriorTL_r	Posterior temporal lobe (right)
PL_rest_l	Inferiolateral remainder of parietal lobe (left)
PL_rest_r	Inferiolateral remainder of parietal lobe (right)
CaudateNucl_l	Caudate nucleus (left)
CaudateNucl_r	Caudate nucleus (right)

NuclAccumb_l	Nucleus accumbens (left)
NuclAccumb_r	Nucleus accumbens (right)
Putamen_l	Putamen (left)
Putamen_r	Putamen (right)
Thalamus_l	Thalamus (left)
Thalamus_r	Thalamus (right)
Pallidum_l	Pallidum (left)
Pallidum_r	Pallidum (right)
Corp_Callosum	Corpus callosum
LatVent_excl_TH_r	Lateral ventricle (excluding temporal horn) (right)
LatVent_excl_TH_l	Lateral ventricle (excluding temporal horn) (left)
TemporaHorn_r	Lateral ventricle, temporal horn (right)
TemporaHorn_l	Lateral ventricle, temporal horn (left)
ThirdVentricl	Third ventricle
FL_precen_G_l	Precentral gyrus (left)
FL_precen_G_r	Precentral gyrus (right)
FL_strai_G_l	Straight gyrus (left)
FL_strai_G_r	Straight gyrus (right)
FL_OFC_AOG_l	Anterior orbital gyrus (left)
FL_OFC_AOG_r	Anterior orbital gyrus (right)
FL_i_fr_G_l	Inferior frontal gyrus (left)
FL_i_fr_G_r	Inferior frontal gyrus (right)
FL_s_fr_G_l	Superior frontal gyrus (left)
FL_s_fr_G_r	Superior frontal gyrus (right)
PL_postce_G_l	Postcentral gyrus (left)
PL_postce_G_r	Postcentral gyrus (right)
PL_s_pa_G_l	Superior parietal gyrus (left)
PL_s_pa_G_r	Superior parietal gyrus (right)
OL_ling_G_l	Lingual gyrus (left)
OL_ling_G_r	Lingual gyrus (right)
OL_cuneus_l	Cuneus (left)
OL_cuneus_r	Cuneus (right)
FL_OFC_MOG_l	Medial orbital gyrus (left)
FL_OFC_MOG_r	Medial orbital gyrus (right)
FL_OFC_LOG_l	Lateral orbital gyrus (left)
FL_OFC_LOG_r	Lateral orbital gyrus (right)
FL_OFC_POG_l	Posterior orbital gyrus (left)
FL_OFC_POG_r	Posterior orbital gyrus (right)

S_nigra_l	Substantia nigra (left)
S_nigra_r	Substantia nigra (right)
Subgen_antCing_l	Subgenual frontal cortex (left)
Subgen_antCing_r	Subgenual frontal cortex (right)
Subcall_area_l	Subcallosal area (left)
Subcall_area_r	Subcallosal area (right)
Presubgen_antCing_l	Pre-subgenual frontal cortex (left)
Presubgen_antCing_r	Pre-subgenual frontal cortex (right)
G_s_t_a_l	Superior temporal gyrus, anterior part (left)
G_s_t_a_r	Superior temporal gyrus, anterior part (right)
Vermis	Vermis

Comparison to other multi-atlas approaches

In a preliminary work (Merida et al., 2015), we compared our *MaxProb* approach to other multi-atlas techniques. For this, we implemented two simplified variants (Best10 and Average) of the solution described in Burgos et al. (2014). In the Best10 method, the registered atlases are ranked by local MR intensity similarity as measured by the normalized cross-correlation and the 10 top-ranked atlases are then fused via simple (non-weighted) averaging of HU values. In the Average method, fusion is performed by non-weighted averaging of all registered CTs of the database. The influence of the number of atlases fused in pseudo-CT generation was studied.

We assessed the influence of the number of atlases fused on pseudo-CT accuracy (Jaccard index), fusing increasing numbers of atlases ranked by similarity as in the Best10 method. Figure 4 shows the mean Jaccard (in %) obtained for bone, air and soft tissue, depending of the number of atlases fused. We found that for all tissues, the number of atlases to fuse that produced maximal overlap was around ten (Figure 67). Above this optimal number, the accuracy decreased, echoing the results reported by Aljabar et al. (2009) for regional brain segmentations. The right endpoint in the curves (39 atlases) corresponds to the Average method, in which all atlases in the database are selected. The first point corresponds to the best atlas in the ranking, per voxel, and gave better performance than the *SingleAtlas* method introduced in Chapter 2, thanks to the selection process at the voxel level.

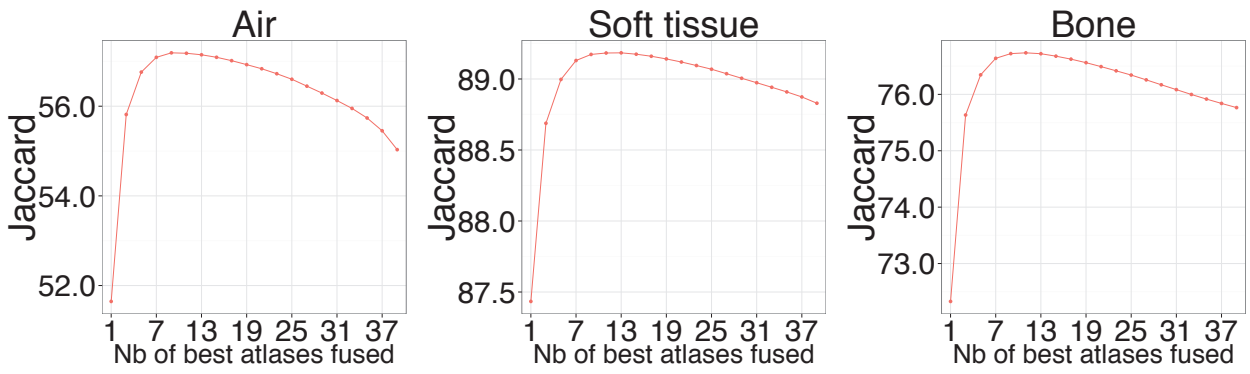

Figure 67: Pseudo-CT accuracy (mean Jaccard, in %) depending of the number of atlases fused. Note the different scales for the y axis.

Supplemental figures for Chapter 4

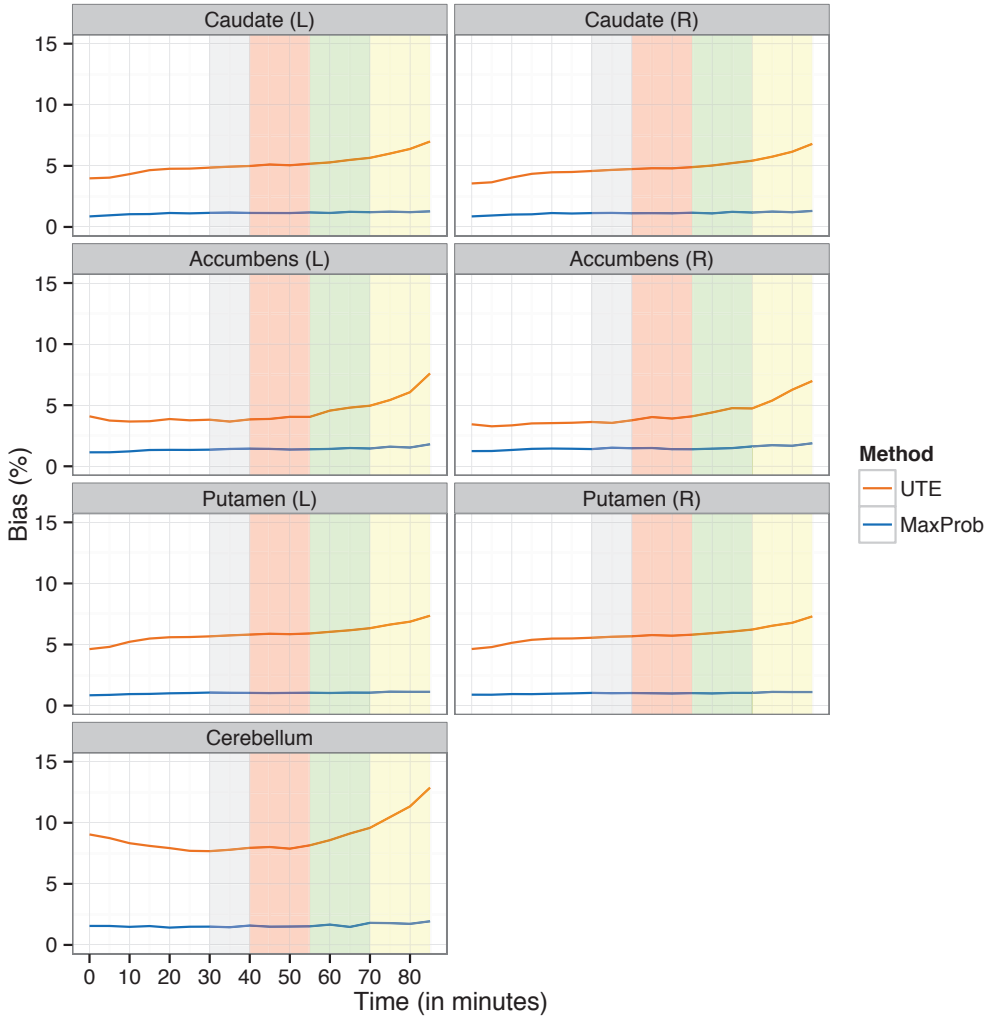

Figure 68: Mean absolute bias over time for the PET frames across subjects for *UTE* and *MaxProb* MRAC methods, i.e. during the 100-minute [^{11}C]Raclopride PET acquisition, for striatal regions and cerebellum.

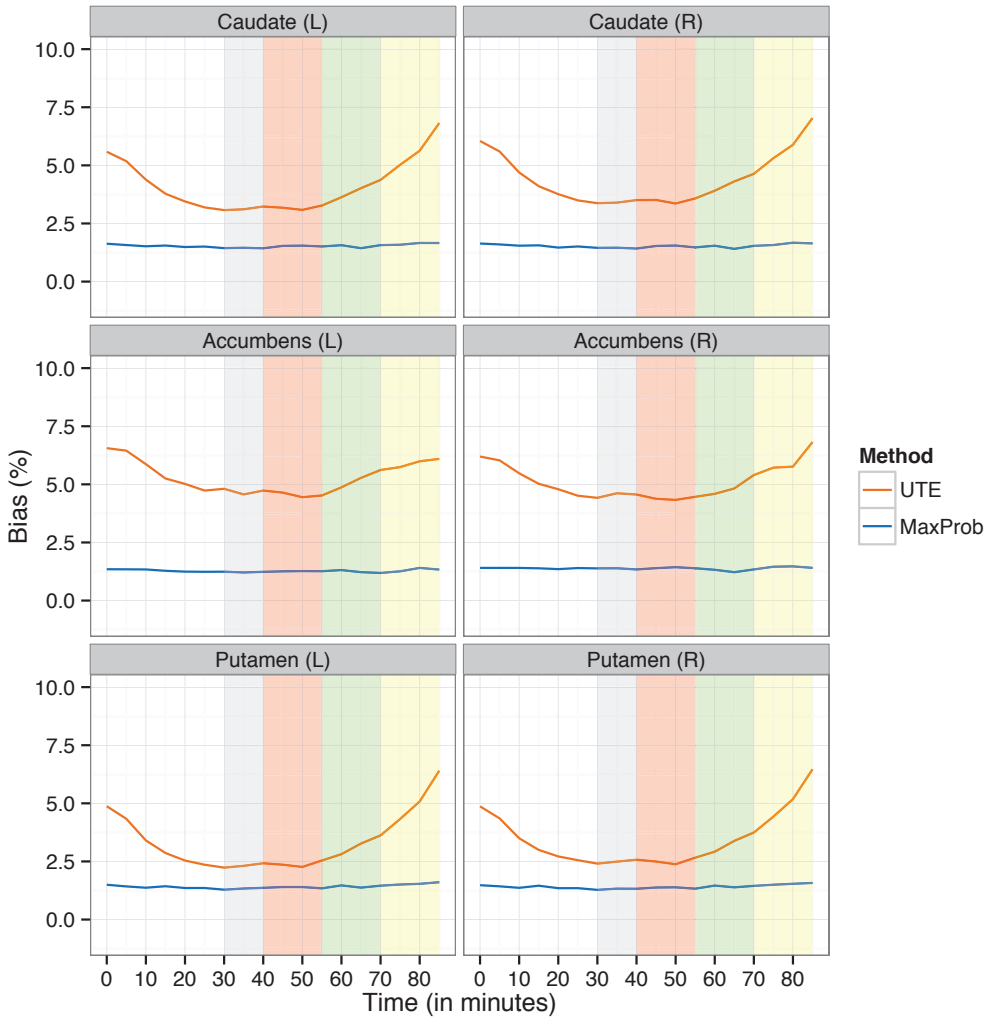

Figure 69: Mean absolute bias over time for the BR estimated from simple tissue-to-reference model with cerebellum as reference region, across subjects for *UTE* and *MaxProb* MRAC methods.

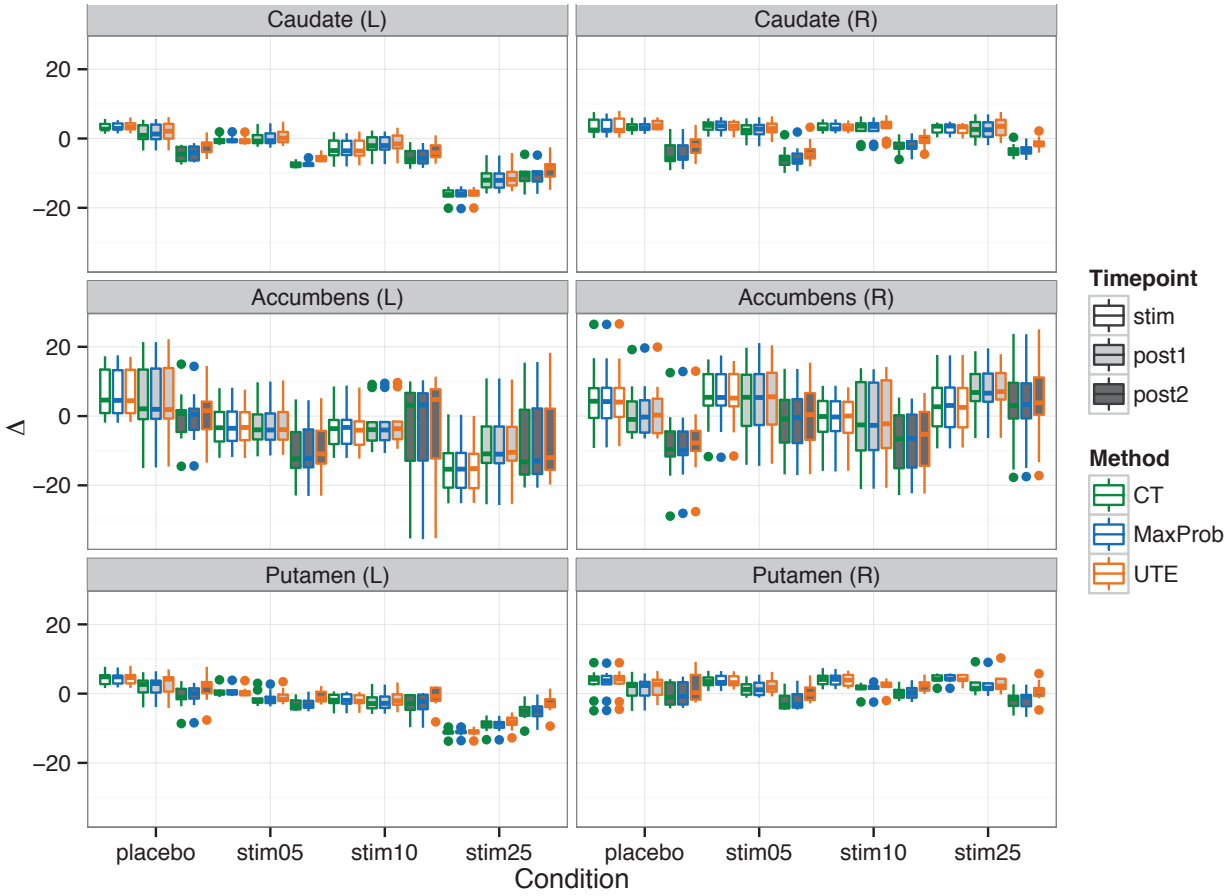

Figure 70: BR between baseline and other time-intervals, Δ (in %), per stimulation condition, for the CT, *UTE* and *MaxProb* AC methods. Results are shown for the placebo group (n=11) and the active group (stim05, stim10 and stim25) (n=10).

Multi-centric study

NeuroImage 147 (2017) 346–359

Contents lists available at ScienceDirect

NeuroImage

journal homepage: www.elsevier.com/locate/neuroimage

A multi-centre evaluation of eleven clinically feasible brain PET/MRI attenuation correction techniques using a large cohort of patients

Claes N. Ladefoged[a], Ian Law[a], Udunna Anazodo[b], Keith St. Lawrence[b], David Izquierdo-Garcia[c], Ciprian Catana[c], Ninon Burgos[d], M. Jorge Cardoso[d,e], Sebastien Ourselin[d,e], Brian Hutton[f], Inés Mérida[g,h], Nicolas Costes[g], Alexander Hammers[g,i], Didier Benoit[a], Søren Holm[a], Meher Juttukonda[j], Hongyu An[j], Jorge Cabello[k], Mathias Lukas[k], Stephan Nekolla[k], Sibylle Ziegler[k], Matthias Fenchel[l], Bjoern Jakoby[l,o], Michael E. Casey[m], Tammie Benzinger[n], Liselotte Højgaard[a], Adam E. Hansen[a], Flemming L. Andersen[a,*]

[a] Department of Clinical Physiology, Nuclear Medicine and PET, Rigshospitalet Copenhagen, Denmark
[b] Lawson Health Research Institute, London, ON, Canada
[c] Athinoula A. Martinos Center for Biomedical Imaging, Department of Radiology, Massachusetts General Hospital and Harvard Medical School, Charlestown, MA, USA
[d] Translational Imaging Group, Centre for Medical Image Computing, University College London, NW1 2HE, London, UK
[e] Dementia Research Centre, Institute of Neurology, University College London, WC1N 3AR, London, UK
[f] Institute of Nuclear Medicine, University College London, London, UK
[g] LILI-EQUIPEX – Lyon Integrated Life Imaging: hybrid MR-PET, CERMEP Imaging Centre, Lyon, France
[h] Siemens Healthcare France SAS, Saint-Denis, France
[i] King's College London & Guy's and St Thomas' PET Centre, Division of Imaging Sciences and Biomedical Engineering, King's College London, London, UK
[j] Joint Department of Biomedical Engineering, The University of North Carolina at Chapel Hill and North Carolina State University, Chapel Hill, NC 27599, USA
[k] Nuklearmedizinische Klinik und Poliklinik, Klinikum rechts der Isar, Technische Universitaet Muenchen, Munich, Germany
[l] Siemens Healthcare GmbH, Erlangen, Germany
[m] Siemens Medical Solutions USA, Inc., Knoxville, TN, USA
[n] Mallinckrodt Institute of Radiology, Washington University, St. Louis, MO 63130, USA
[o] University of Surrey, Guildford, Surrey, UK

ARTICLE INFO

Keywords:
Attenuation correction
PET/MRI
Brain

ABSTRACT

Aim: To accurately quantify the radioactivity concentration measured by PET, emission data need to be corrected for photon attenuation; however, the MRI signal cannot easily be converted into attenuation values, making attenuation correction (AC) in PET/MRI challenging. In order to further improve the current vendor-implemented MR-AC methods for absolute quantification, a number of prototype methods have been proposed in the literature. These can be categorized into three types: template/atlas-based, segmentation-based, and reconstruction-based. These proposed methods in general demonstrated improvements compared to vendor-implemented AC, and many studies report deviations in PET uptake after AC of only a few percent from a gold standard CT-AC. Using a unified quantitative evaluation with identical metrics, subject cohort, and common CT-based reference, the aims of this study were to evaluate a selection of novel methods proposed in the literature, and identify the ones suitable for clinical use.

Methods: In total, 11 AC methods were evaluated: two vendor-implemented (MR-AC_{DIXON} and MR-AC_{UTE}), five based on template/atlas information (MR-$AC_{SEGBONE}$ (Koesters et al., 2016), MR-$AC_{ONTARIO}$ (Anazodo et al., 2014), MR-AC_{BOSTON} (Izquierdo-Garcia et al., 2014), MR-AC_{UCL} (Burgos et al., 2014), and MR-$AC_{MAXPROB}$ (Merida et al., 2015)), one based on simultaneous reconstruction of attenuation and emission (MR-AC_{MLAA} (Benoit et al., 2015)), and three based on image-segmentation (MR-AC_{MUNICH} (Cabello et al., 2015), MR-$AC_{CAR\text{-}RIDR}$ (Juttukonda et al., 2015), and MR-$AC_{RESOLUTE}$ (Ladefoged et al., 2015)). We selected 359 subjects who were scanned using one of the following radiotracers: [^{18}F]FDG (210), [^{11}C]PiB (51), and [^{18}F] florbetapir (98). The comparison to AC with a gold standard CT was performed both globally and regionally, with a special focus on robustness and outlier analysis.

Results: The average performance in PET tracer uptake was within ± 5% of CT for all of the proposed methods,

* Corresponding author.
E-mail address: fling@rh.dk (F.L. Andersen).

http://dx.doi.org/10.1016/j.neuroimage.2016.12.010
Received 9 June 2016; Accepted 5 December 2016
Available online 14 December 2016

with the average ± SD global percentage bias in PET FDG uptake for each method being: MR-AC_{DIXON} (−11.3 ± 3.5)%, MR-AC_{UTE} (−5.7 ± 2.0)%, MR-$AC_{ONTARIO}$ (−4.3 ± 3.6)%, MR-AC_{MUNICH} (3.7 ± 2.1)%, MR-AC_{MLAA} (−1.9 ± 2.6)%, MR-$AC_{SEGBONE}$ (−1.7 ± 3.6)%, MR-AC_{UCL} (0.8 ± 1.2)%, MR-$AC_{CAR\text{-}RiDR}$ (−0.4 ± 1.9)%, MR-$AC_{MAXPROB}$ (−0.4 ± 1.6)%, MR-AC_{BOSTON} (−0.3 ± 1.8)%, and MR-$AC_{RESOLUTE}$ (0.3 ± 1.7)%, ordered by average bias. The overall best performing methods (MR-AC_{BOSTON}, MR-$AC_{MAXPROB}$, MR-$AC_{RESOLUTE}$ and MR-AC_{UCL}, ordered alphabetically) showed regional average errors within ± 3% of PET with CT-AC in all regions of the brain with FDG, and the same four methods, as well as MR-$AC_{CAR\text{-}RiDR}$, showed that for 95% of the patients, 95% of brain voxels had an uptake that deviated by less than 15% from the reference. Comparable performance was obtained with PiB and florbetapir.

Conclusions: All of the proposed novel methods have an average global performance within likely acceptable limits (± 5% of CT-based reference), and the main difference among the methods was found in the robustness, outlier analysis, and clinical feasibility. Overall, the best performing methods were MR-ACBOSTON, MR-ACMAXPROB, MR-ACRESOLUTE and MR-ACUCL, ordered alphabetically. These methods all minimized the number of outliers, standard deviation, and average global and local error. The methods MR-ACMUNICH and MR-ACCAR-RiDR were both within acceptable quantitative limits, so these methods should be considered if processing time is a factor. The method MR-ACSEGBONE also demonstrates promising results, and performs well within the likely acceptable quantitative limits. For clinical routine scans where processing time can be a key factor, this vendor-provided solution currently outperforms most methods. With the performance of the methods presented here, it may be concluded that the challenge of improving the accuracy of MR-AC in adult brains with normal anatomy has been solved to a quantitatively acceptable degree, which is smaller than the quantification reproducibility in PET imaging.

1. Introduction

Positron emission tomography/magnetic resonance imaging (PET/MRI) combines the powerful and functional imaging of PET for assessment of patients in oncology (Hillner et al., 2008) and neurology (Heiss, 2009) with MRI's excellent soft-tissue characterization, contrast, and power to provide additional functional information like perfusion and diffusion. A likely key clinical application of simultaneous PET/MRI is in neurological disorders, in particular in dementia (Bailey et al., 2015; Drzezga et al., 2014; Dukart et al., 2011). In order to accurately quantify the radioactivity concentration measured by PET, emission data need to be corrected for photon attenuation.

Currently, two fully integrated simultaneous whole-body human PET/MRI systems are commercially available: the Biograph mMR (Siemens Healthcare GmbH, Erlangen, Germany) and the Signa PET/MRI (GE Healthcare, Waukesha WI, USA). The vendor-implemented attenuation correction (AC) method in the Signa PET/MRI system is based on an atlas of MRI/CT pairs used to derive the approximate size and location of bones and air cavities (Wollenweber et al., 2013) but is yet to be fully evaluated on a large patient cohort (Sekine et al., 2016a). Two AC-methods are implemented in the Biograph mMR system. They are both segmenting the MR image into tissue classes: the two-point Dixon-Water-Fat sequence (Dixon) based on Martinez-Möller et al. (2009), which can lead to underestimation of PET tracer uptake near the skull (Andersen et al., 2014), and the ultrashort echo time sequence (UTE), based on a similar acquisition method as Catana et al. (2010) and a different segmentation method based on a voxel-based classifier, which is challenged by remaining segmentation errors in the skull base and near the frontal sinuses (Dickson et al., 2014). A third, atlas-based AC method is currently being developed (Koesters et al., 2016; Paulus et al., 2015).

To further improve the quantitative accuracy, a number of methods have been proposed in the literature. These can be categorized into three types: template/atlas-based, segmentation-based, and reconstruction-based. The template/atlas-based methods create a pseudo-CT image by co-registering database-subjects to a patient's MR image. The atlas or template can be based on pairs of CT and dual UTE (Delso et al., 2014b; Roy et al., 2014), CT and anatomical MRI (Dixon, T1, and/or T2-weighted sequences) (Anazodo et al., 2014; Andreasen et al., 2015; Burgos et al., 2014; Izquierdo-Garcia et al., 2014; Merida et al., 2015; Schreibmann et al., 2010; Sekine et al., 2016a; Torrado-Carvajal et al., 2016). Some methods also use probabilistic measures or machine learning techniques to compare with an atlas or template (Chan et al., 2013; Chen et al., 2015; Hofmann et al., 2008; Johansson et al., 2011; Navalpakkam et al., 2013; Poynton et al., 2014; Yang et al., 2013). Alternatives to template/atlas-based methods are the segmentation-based methods, which derive attenuation maps purely from MR images. These methods usually segment the T1 (Fei et al., 2012; Zaidi et al., 2003) or UTE images (Cabello et al., 2015; Catana et al., 2010; Juttukonda et al., 2015; Ladefoged et al., 2015) into multiple tissue classes, each assigned a mean linear attenuation coefficient (LAC). Furthermore, a number of UTE-based methods calculate a patient specific bone density (Cabello et al., 2015; Juttukonda et al., 2015; Ladefoged et al., 2015) using the normalized logarithmic difference between the UTE images (R_2^* map) (Keereman et al., 2010). A number of methods also exist employing special MRI sequences with modified sampling schemes using either short echo time (STE)/Dixon (Khateri et al., 2015) or improved UTE sequences, using point-wise encoding time reduction with radial acquisition (PETRA) (Grodzki et al., 2012), using zero TE (ZTE) (Wiesinger et al., 2016), or using triple UTE (Aitken et al., 2014; Berker et al., 2012; Su et al., 2015). Finally, maximum-likelihood reconstruction-based methods, where activity and attenuation are simultaneously reconstructed based on maximum-likelihood (Nuyts et al., 1999), using either time-of-flight information (TOF) (Mehranian and Zaidi, 2015; Rezaei et al., 2012, 2014; Salomon et al., 2011) or non-TOF information using MR-priors (Benoit et al., 2015), are yet to be evaluated for PET/MRI-brain applications. The methods using TOF would currently be limited to the Signa PET/MRI system or the sequential Ingenuity TF PET/MRI system (Philips Healthcare, Cleveland, OH) (Zaidi et al., 2011). However, recently, a TOF-based MLAA implementation failed to show additional benefit for attenuation correction in PET/MR imaging compared to a robust atlas-based method (Mehranian et al., 2016).

The proposed methods demonstrate improvements compared to the currently vendor-implemented AC, and many studies report deviations in PET uptake after AC of only a few percent from a gold standard CT-AC; or conclude that the methods are ready for clinical use on the basis of quantitative accuracy (Burgos et al., 2014; Izquierdo-Garcia et al., 2014; Ladefoged et al., 2015). There are publications indicating the desire for more accuracy in PET brain attenuation correction (Andersen et al., 2014; Dickson et al., 2014; Hitz et al., 2014), but whether the problem of AC has been solved fully is still debatable (Bailey et al., 2015).

There is currently no consensus on a method for summarizing evaluations, and this lack of standardization of metrics makes direct

comparisons across the published AC methods difficult. The methods rely on different gold/silver standards or make use of cohorts with different diseases or imaging tracers. The cohorts are of varying sizes, from 5 (Navalpakkam et al., 2013) to 92 subjects (Juttukonda et al., 2015), which might not be enough to ensure robustness and capture potential outliers in a clinical setting.

In this work, we present the performance of prototype methods within a multi-centre study, which include:

- A large patient cohort (n=359) who were scanned with three different radiotracers ([^{18}F]fluoro-D-glucose (FDG), [^{11}C] Pittsburgh-compound-B (PiB), and [^{18}F]florbetapir), allowing for detailed evaluation of outliers and robustness.
- Patients recruited from clinical populations with established or emerging clinical indications for both PET and MRI, and therefore well-suited for evaluating regional effects of brain MR-AC.
- A unified comparison between 11 PET/MRI brain AC methods using identical metrics and a common CT-based reference: two vendor-implemented (Dixon and UTE), five based on template/atlas-based information (Anazodo et al., 2014; Burgos et al., 2014; Izquierdo-Garcia et al., 2014; Koesters et al., 2016; Merida et al., 2015), one based on simultaneous reconstruction of attenuation and emission (Benoit et al., 2015), and three based on image-segmentation (Cabello et al., 2015; Juttukonda et al., 2015; Ladefoged et al., 2015).

The methods were assessed both globally and regionally using multiple metrics, including a detailed robustness and outlier analysis across the whole patient group. We also compared the methods by assessing the time that was required to execute the methods, referring to the actual run-time and scan-time of the corresponding sequences. While time may not be of high importance in a research setting, a clinical setup may demand high requirements for this factor in order to provide a timely diagnosis and acceptable patient management and throughput. The aim of this study was to evaluate the proposed methods and identify the ones suitable for clinical use by performing a unified quantitative evaluation.

2. Materials and methods

All patient studies were performed using a fully-integrated PET/MRI system (Siemens Biograph mMR, Siemens Healthcare, Erlangen, Germany) (Delso et al., 2011). For the purpose of obtaining a reference low-dose CT image of the head, whole-body PET/CT systems were used (Biograph TruePoint 40 and Biograph TruePoint 64, Siemens Healthcare) (Jakoby et al., 2009).

2.1. Patients

Data sets were obtained retrospectively from two different centers; Rigshospitalet, University Hospital Copenhagen, Denmark, and Washington University, St. Louis, United States of America. The Rigshospitalet data were comprised from data sets from the complete cohort of patients referred for a clinical FDG PET/MRI brain examination, either in neuro-oncology or dementia, as well as the complete cohort of subjects having undergone PiB PET/MRI examinations. These cohorts included healthy subjects and patients with mild cognitive impairment (MCI), Alzheimer's disease (AD), or clinical dementia. In total, 210 subjects with FDG PET/MRI scans (5 healthy volunteers, 4 neuro-oncological patients, 201 MCI, AD or clinical dementia patients) and 51 subjects scanned with PiB (1 healthy volunteer, 50 MCI, AD or clinical dementia patients) were consecutively selected between November 2013 and April 2015. From Washington University, data sets were obtained from 98 subjects referred for a florbetapir examination (3 very mild dementia, 95 MCI or clinical dementia patients).

Of a total of 359 PET/MRI brain studies from the two centers, 22 studies were excluded (9 FDG, 3 PiB and 10 florbetapir). Exclusion was due to metal implant-induced artifacts in the brain images (3 subjects) or data errors due to corruption or missing raw-data (19 subjects) leaving 337 studies available for analysis. The local ethics committees had approved the original studies and all patients gave informed consent.

2.2. Imaging protocol

2.2.1. PET

The PET scan information is given in Table 1. Patients were positioned head first with their arms down on the fully-integrated PET/MRI system. Data were acquired over a single bed position of 25.8 cm covering the head and neck for 10/20/15 min for FDG/PiB/florbetapir respectively (Table 1 for initiation of scan). For the purpose of this study, the PET data from the PET/MR acquisition were reconstructed using 3D Ordinary Poisson-Ordered Subset Expectation Maximization (OP-OSEM) with 4/3/4 iterations, 21 subsets, and 3/5/5 mm Gaussian post filtering for FDG/PiB/florbetapir, respectively, on 344×344 matrices (2.1×2.1×2.0 mm^3 voxels) in line with the respective clinical protocols.

2.2.2. MRI

The scan protocol included two-point Dixon images using the vendor-provided DIXON-VIBE AC sequence with repetition time (TR)/echo time 1 (TE1)/echo time 2 (TE2)=2300/1.23/2.46 ms, flip angle 10°, coronal orientation, voxel size of 2.6×2.6×3.12 mm^3, 19 s acquisition time; a UTE AC sequence with TR/TE1/TE2=11.94/0.07/2.46 ms, a flip angle of 10°, axial orientation, field of view (FOV) of 300 mm^2, reconstructed on 192×192×192 matrices (1.6×1.6×1.6 mm^3 voxels), 100 s acquisition time; and a T1w MPRAGE with TR/TE=1900/2.44 ms (FDG/PiB) and 2300/2.95 ms (florbetapir), inversion time=900 ms, flip angle=9°, sagittal orientation, reconstructed on 512×512×192 matrices (0.49×0.49×1 mm^3 voxels) (FDG/PiB) and 256×240×176 matrices (1.05×1.05×1.2 mm^3 voxels) (florbetapir), 300 s acquisition time. The patients injected with FDG or PiB were all imaged using the software version VB20P, whereas those injected with florbetapir were imaged with VB18P, which included a work-in-progress version of the UTE sequence. Due to the difference in version

Table 1
Patient information.

Tracer	Originating center	N (fat/water inverted)	Male/ Female	Age (min-max) in years	Injected tracer (±SD) in MBq	Scan start p.i. (min-max) in min
[^{18}F]FDG	Rigshospitalet, Copenhagen Denmark	201 (9)	108/93	68 (23–96)	203 (±20)	51 (24–134)
[^{11}C]PiB	Rigshospitalet, Copenhagen Denmark	48 (1)	2424	68 (39–85)	426 (±75)	43 (37–100)
[^{18}F]florbetapir	Washington University, North Carolina, USA	88 (3)	21/67	71 (41–91)	353 (±30)	0 n=75, or 52 (49–60) n=13

p.i.: post injection.

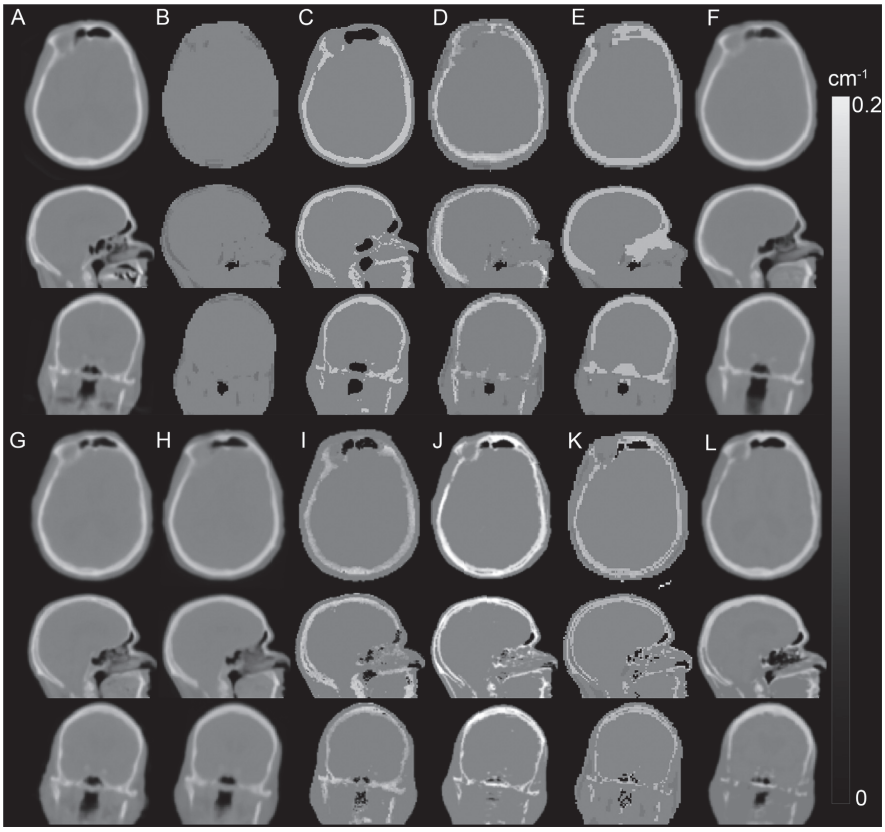

Fig. 1. Attenuation correction images for a sample patient that minimizes the difference of the overall brain error to the median error across all methods. (A) CT, (B) Dixon, (C) UTE, (D) Segbone, (E) Ontario, (F) Boston, (G) UCL, (H) MaxProb, (I) MLAA, (J) Munich, (K) CAR-RiDR, (L) RESOLUTE.

numbering, mainly expressed in the UTE sequences, the tracers were evaluated separately.

2.2.3. CT

A low dose CT (120 kVp, 36 mAs, 74 slices, 0.6×0.6×3 mm^3 voxels) was acquired from each patient to be used as gold standard. The CT images were acquired either on the same day as the PET/MRI examination (FDG and PiB) or within 8.3 ± 6 days of each other with no surgical procedures in between (florbetapir).

2.3. Creating the attenuation maps

In all, nine proposed MR-AC methods were selected for evaluation. These were selected to be representative of the three major types of

Table 2
Jaccard distance for overlap with bone ($\mu > 0.101\ cm^{-1}$) segmented from MR-AC_{CT} shown for each method and tracer. Results are shown for full head and further subdivided into top and bottom representing the area above and below the eyes. The best results are highlighted in bold. Note the Dixon method is left out due to there not being any bone present.

	FDG			PiB			Florbetapir		
	Full	**Top**	**Bottom**	**Full**	**Top**	**Bottom**	**Full**	**Top**	**Bottom**
UTE	0.56 ± 0.06	0.62 ± 0.10	0.51 ± 0.05	0.57 ± 0.06	0.65 ± 0.09	0.51 ± 0.04	0.32 ± 0.07	0.38 ± 0.12	0.27 ± 0.04
Segbone	0.54 ± 0.04	0.63 ± 0.07	0.48 ± 0.04	0.56 ± 0.03	0.65 ± 0.04	0.49 ± 0.03	N/A	N/A	N/A
Ontario	0.60 ± 0.04	0.74 ± 0.05	0.52 ± 0.05	0.60 ± 0.05	0.73 ± 0.07	0.52 ± 0.04	0.63 ± 0.05	0.75 ± 0.07	0.55 ± 0.04
Boston	0.74 ± 0.06	0.79 ± 0.08	0.69 ± 0.07	0.78 ± 0.04	0.83 ± 0.05	0.73 ± 0.04	0.78 ± 0.03	0.81 ± 0.06	0.75 ± 0.03
UCL	0.80 ± 0.04	0.83 ± 0.05	**0.77** ± 0.05	0.80 ± 0.04	0.83 ± 0.05	0.78 ± 0.04	**0.82** ± 0.03	**0.85** ± 0.04	**0.80** ± 0.03
MaxProb	**0.81** ± 0.04	**0.85** ± 0.05	**0.77** ± 0.04	**0.82** ± 0.02	0.84 ± 0.04	**0.79** ± 0.03	0.80 ± 0.03	0.83 ± 0.04	0.78 ± 0.03
MLAA	0.59 ± 0.07	0.67 ± 0.09	0.53 ± 0.06	0.51 ± 0.07	0.60 ± 0.09	0.44 ± 0.06	0.36 ± 0.09	0.37 ± 0.15	0.35 ± 0.05
Munich	0.72 ± 0.04	**0.85** ± 0.05	0.63 ± 0.05	0.73 ± 0.04	**0.86** ± 0.05	0.64 ± 0.04	0.72 ± 0.03	**0.85** ± 0.04	0.63 ± 0.04
CAR-RiDR	0.50 ± 0.07	0.62 ± 0.09	0.40 ± 0.06	0.50 ± 0.06	0.62 ± 0.08	0.41 ± 0.06	0.46 ± 0.06	0.60 ± 0.09	0.36 ± 0.05
RESOLUTE	0.68 ± 0.04	**0.85** ± 0.04	0.56 ± 0.04	0.69 ± 0.03	0.84 ± 0.04	0.58 ± 0.04	0.68 ± 0.03	**0.85** ± 0.03	0.54 ± 0.04

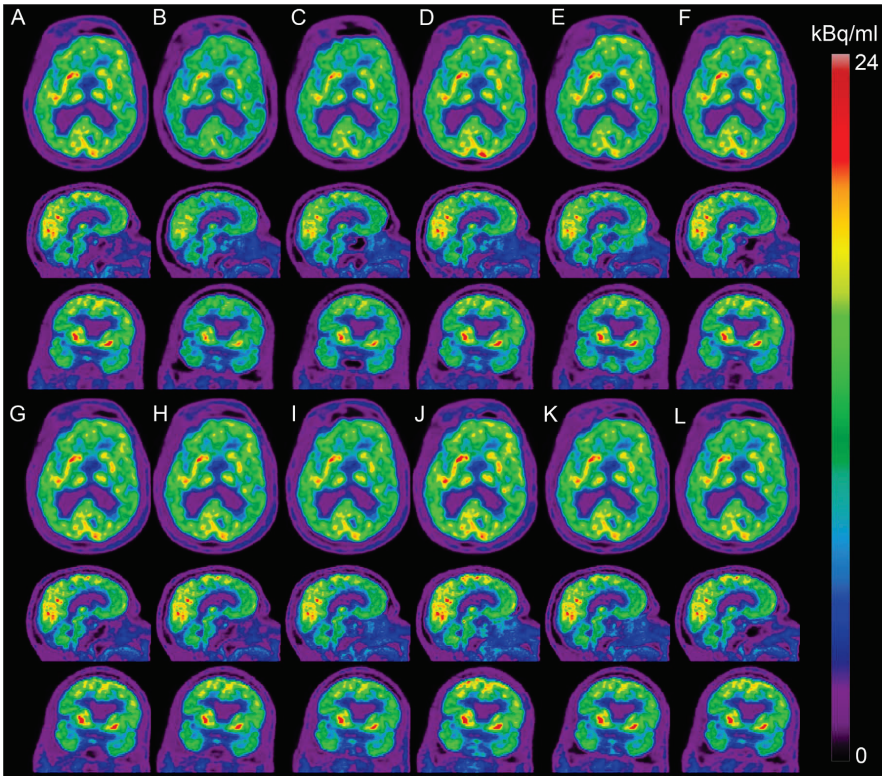

Fig. 2. PET images for a sample patient that minimizes the difference of the overall brain error to the median error across all methods. (A) CT, (B) Dixon, (C) UTE, (D) Segbone, (E) Ontario, (F) Boston, (G) UCL, (H) MaxProb, (I) MLAA, (J) Munich, (K) CAR-RiDR, (L) RESOLUTE.

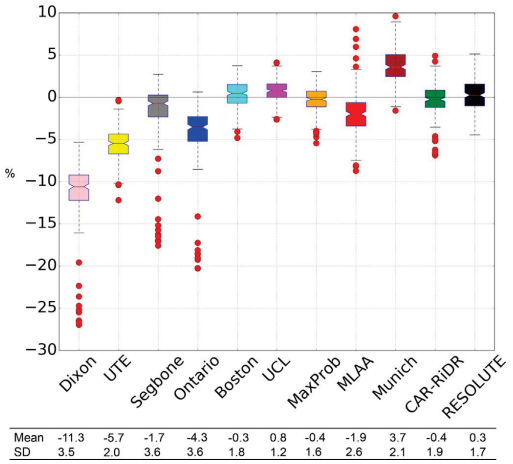

Fig. 3. Global performance of all methods for the FDG patients (n=201, including patients with fat/water tissue inversion). The median (red line), 25th and 75th percentiles (box), 1.5*IQR (whiskers), outliers (red dots), mean and SD are shown for each method. (For interpretation of the references to color in this figure legend, the reader is referred to the web version of this article.)

MR-AC categories (template/atlas-based, segmentation-based, and reconstruction-based), and had to be applicable to the Siemens mMR data available. Furthermore, they should be implemented on a central site (Copenhagen). Twelve attenuation maps were created. First, vendor-provided MR-based attenuation maps (MR-AC_{DIXON} and MR-AC_{UTE}) were derived using the DIXON VIBE sequence and the UTE MR sequence. Next, the nine proposed brain MR-AC methods were used. A brief introduction of each method is given below. We refer to the original publications for detailed explanations. Finally, for each subject, the CT image was co-registered to the T1 image using a 6-parameter rigid alignment procedure (minctracc, McConnell Imaging Center, Montreal, Canada) with normalized mutual information as objective function. The patient bed and head-holder were extracted manually from the CT images using an oval ROI (OsiriX software) applied to each transverse CT slice. The attenuation values were then converted from HUs to LACs at 511 keV by using a standard bi-linear scaling approach (Carney et al., 2006) as implemented in the Siemens PET/CT systems used. The co-registered CT attenuation map was substituted into the UTE attenuation file (MR-AC_{CT}) to facilitate use of routine reconstruction. We blurred the resulting image with a 4 mm Gaussian filter to simulate PET/CT reconstructions. Due to the limited coverage in the neck region by the acquired CT, we replaced the missing area by the values from MR-AC_{DIXON}. To ensure a fair comparison, this replacement was also performed in all the other attenuation maps.

All attenuation maps, except for MR-AC_{DIXON}, were created in the

image space defined by the method, and post-resampled and placed into the UTE file just as the reference CT. Since the CT image was co-registered to the T1 image, we also co-registered the Dixon and UTE images to the T1 image, and aligned the MR-AC maps of the methods defined using either of these.

All of the methods presented in this study, except for two, had been made available and were processed in Copenhagen. The MR-$AC_{SEGBONE}$ attenuation maps were created by Siemens, and MR-AC_{UCL} attenuation maps were created in London, as the CT/MRI database could not be shared at the time of this study.

2.3.1. Template/Atlas-based methods (Segbone, Ontario, Boston, UCL, MaxProb)

- ***Siemens Healthcare GmbH - Segbone:*** The prototype method by Siemens Healthcare (Koesters et al., 2016; Paulus et al., 2015) is a template-based method, where an MR model image of the skull region is non-rigidly registered to an individual subject exclusively on the Dixon input images. A pre-aligned skull mask is then brought to subject space, and attenuation values greater than soft-tissue are superimposed on the original Dixon attenuation map. This method is still a work-in-progress. The attenuation map is denoted MR-$AC_{SEGBONE}$.
- ***London Ontario:*** The method by Anazodo et al. (2014) uses the SPM8 function 'new segment' to extract a bone probability map from each individual's T1 MPRAGE image. The bone map defined by voxels with probability above 80% are, following a post-processing procedure, superimposed on MR-AC_{DIXON} and assigned the constant value 0.143 cm^{-1}. The resulting attenuation map is denoted MR-$AC_{ONTARIO}$.
- ***Boston MGH***: The method by Izquierdo-Garcia et al. (2014) also uses SPM8 to extract patient specific tissue probability maps from the individual's intensity normalized T1 MPRAGE image and register these to a template of co-aligned probability maps of 15 subjects. The averaged corresponding CT template is then back-warped to patient space, converted to LACs, blurred with a 4 mm Gaussian filter, and used as the template-based AC map MR-AC_{BOSTON}.
- ***London UCL***: The method by Burgos et al. (2014) non-linearly aligns a database of 41 T1-CT pairs to the intensity-normalized T1 image of a patient. At each voxel, a patch is extracted and the local normalized correlation coefficient is calculated between the patient T1 and each of the T1 images in the database. A weighting vector is calculated from the coefficients ranking each T1-CT pair relative to the other pairs, and used to obtain a target CT voxel value. The resulting synthesized CT image is converted to LACs, blurred with a 4 mm Gaussian filter, and denoted MR-AC_{UCL}.
- ***Lyon - MaxProb***: The method by Merida et al. (2015) is similar to Burgos et al. (2014) by also aligning a database of 27 T1-CT pairs to an intensity normalized T1 MPRAGE image of a patient, but deviates in the method used to combine the database into a target CT image. The authors discretize the CT images into air, soft tissue and bone voxels, calculate the modal tissue type across the database, and assign the mean of the CT values from the database subjects with that tissue type to the voxel. The final fused image is converted to LACs, blurred with a 4 mm Gaussian filter, and denoted MR-$AC_{MaxProb}$.

2.3.2. Maximum-likelihood reconstruction-based

- ***Copenhagen - MLAA:*** The method by Benoit et al. (2015) is a reconstruction-based method aimed at optimizing the existing non-TOF MLAA technique. The method uses the individual's MR-AC_{UTE} and a discretized version of the individual's T1 image as prior information to the MLTR algorithm. A heuristically determined schema assigns the value for α_j based on the two prior images, as well as the update term calculated in each MLTR iteration step. The final image of the MLAA algorithm is denoted MR-AC_{MLAA}.

2.3.3. Segmentation-based (Munich, CAR-RiDR, RESOLUTE)

- ***Munich***: The method by Cabello et al. (2015) uses the individual's UTE TE1 and TE2 images to extract air, soft tissue as well as the bone signal, which is extracted using R_2^* and scaled to LACs by normalizing to the maximum intensity and thresholding using an empirically chosen value. The intensity of the bone voxels from the R_2^* map are equalized by the mean and maximum values from a CT-based database. The resulting image is blurred with a 3 mm Gaussian filter, and denoted MR-AC_{MUNICH}.
- ***University of North Carolina - CAR-RiDR***: The method by Juttukonda et al. (2015) also uses the individual's UTE TE images to extract air, soft tissue and R_2^* signal. By fitting a sigmoid-best-fit to a set of 98 R_2^*-CT relationship pairs, the authors convert the measured R_2^* signal to a continuous CT value. The resulting image is denoted MR-$AC_{CAR\text{-}RiDR}$.
- ***Copenhagen - RESOLUTE***: The method by Ladefoged et al. (2015) segments brain, CSF, soft tissue, and air from the UTE TE images, and also uses R_2^* to extract a bone signal, which is converted to LACs using a set of R_2^*-CT relationship pairs from 10 training patients. To limit possible bias from regions with known R_2^* noise (Delso et al., 2014a), and because the amount of included bone is higher compared to Cabello et al. (2015), Juttukonda et al. (2015), the threshold for included bone was regionally varied within the head. The resulting image is blurred with a 4 mm Gaussian filter and denoted MR-$AC_{RESOLUTE}$.

2.4. Image analysis

As Dixon-based methods may suffer from fat/water inversion (Ladefoged et al., 2014), we excluded the patients with inversion from further analysis in most of the metrics. This was the case for nine FDG, one PiB, and three florbetapir patients. To avoid bias in the results, the patients with fat/water inversion are excluded in most figures. When included, it will be clearly stated. The methods directly affected by the inversion are MR-$AC_{SEGBONE}$, MR-$AC_{ONTARIO}$ and MR-$AC_{CAR\text{-}RiDR}$.

2.4.1. Global attenuation map performance

To evaluate the performance precision of the methods based on the attenuation maps, we measured the Jaccard-index for the bone compared to CT-derived attenuation maps. We defined bone as being greater than 0.101 cm^{-1}, representing values above soft-tissue.

2.4.2. Global PET performance

As a prior step to evaluating the global PET performance, we first created individual brain masks. We moved all patient data to common MNI space using ANTs (Avants et al., 2011) by non-rigidly registering the patients' T1 images to the ICBM 152 2009a template (Fonov et al., 2009). The MNI brain mask was back-warped to patient space, and the PET image reconstructed with the CT attenuation map was thresholded at >20% of the maximum intensity value. Finally, the intersection between the two masks was calculated and used as the final mask of the brain, and used throughout this manuscript when referring to the brain region. Next, the voxel-wise percent difference relative to PET_{CT}, defined as:

$$Rel_{\%} = \frac{PET_x - PET_{CT}}{PET_{CT}} \times 100, \quad (1)$$

as well as the absolute percent difference, defined as:

$$Abs_{\%} = \frac{|PET_x - PET_{CT}|}{PET_{CT}} \times 100, \quad (2)$$

were calculated for the PET images corrected with each of the evaluated

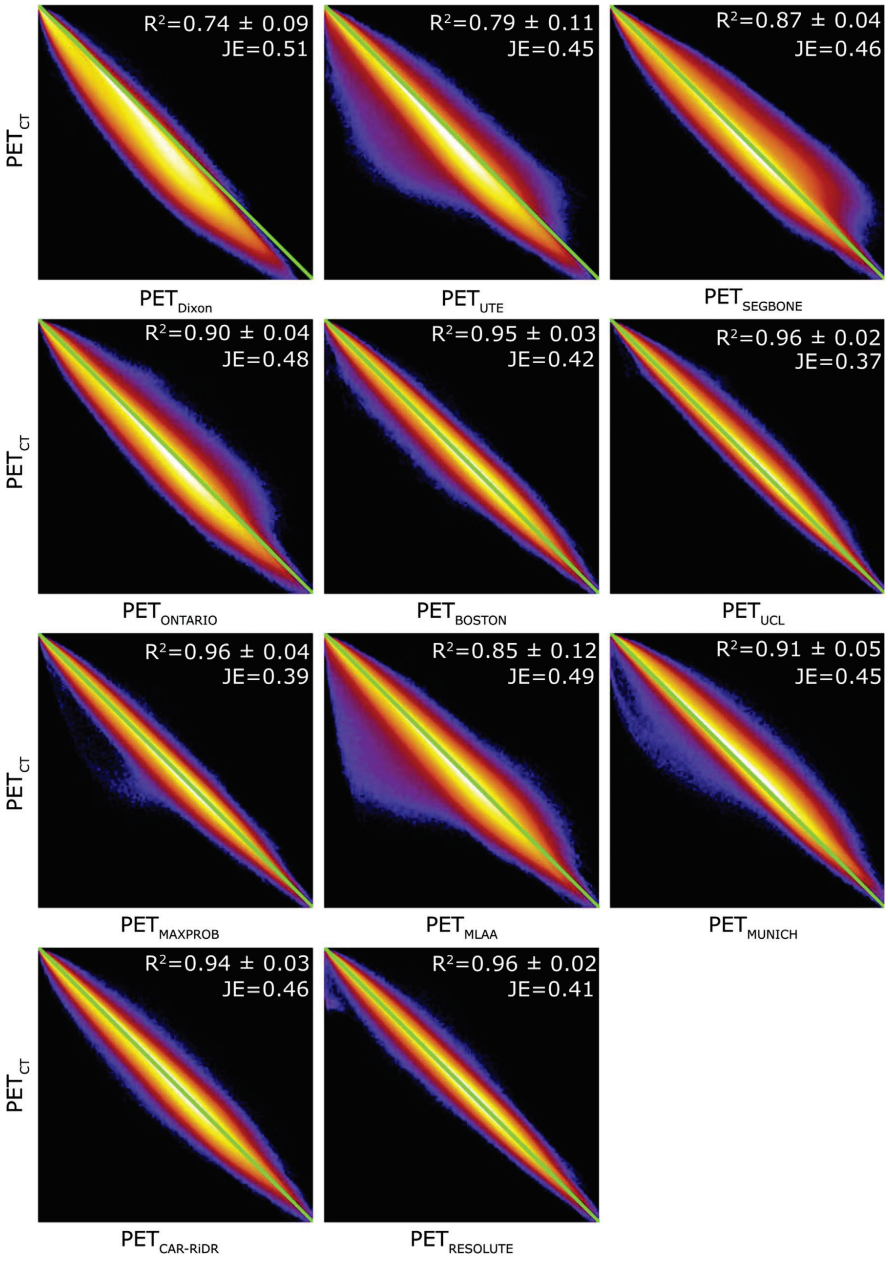

Fig. 4. Summed joint histograms of PET activity within the brain mask for FDG (n=192, excluding patients with fat/water tissue inversion) for PET_{CT} versus each of the methods. The R^2 scores are average ± SD of the individual patients. The joint entropy (JE) is calculated for all patients.

methods (PET_X). We calculated the averaged performance of $Rel_{\%}$ and $Abs_{\%}$ for the full brain across all patients for each of the methods. We computed the distribution of $Rel_{\%}$ errors for each of the methods using a histogram analysis. Finally, we computed the voxel-wise correlation between PET_{CT} and each of the proposed methods for all voxels within the brain. We plotted the correlations in a joint histogram, and

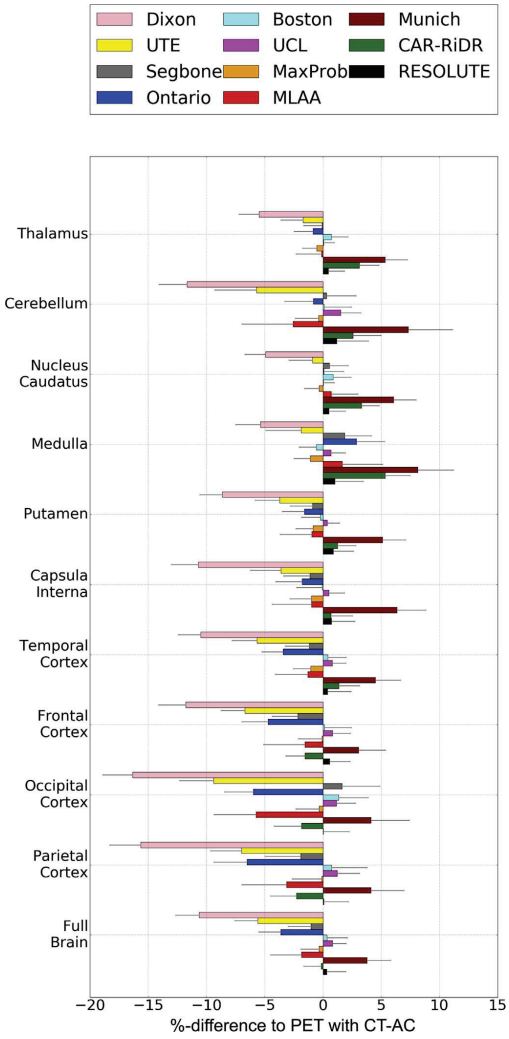

Fig. 5. Global and regional ROI analysis across all FDG patients (n=192, excluding patients with fat/water tissue inversion). The gray lines indicate 1 SD.

computed the goodness-of-fit value (R^2) to the identity line for each of the patients.

2.4.3. Regional PET performance

To evaluate the regional PET performance, we back-warped the anatomical predefined regions from MNI space (Collins et al., 1999; Fonov et al., 2009) to each patient, and extracted the mean $Rel_{\%}$ for each region in the template. We furthermore calculated the average and standard deviation $Rel_{\%}$-images across all patients for each of the methods for visual evaluation.

2.4.4. Analysis of robustness and outliers

To estimate the number of outliers for each method, we introduced a novel metric. The metric calculates the percentage of patients with at least x% of the brain within $\pm y$% in the $Rel_{\%}$ images, where x varies from 0–100 and y={5,10,15}. A perfect method therefore has 100% of the patients within ± 0% in the $Rel_{\%}$ images. To understand the reason for the worst outliers, we then analyzed the three FDG patients with the worst performance based on the ± 10% threshold and categorized the error. We present the worst outlier of each method.

3. Results

3.1. Global attenuation map evaluation

Fig. 1 shows the axial, sagittal and coronal views for each attenuation method for a single sample patient. The representative sample patient was chosen objectively to be that which minimizes the difference to the median $Rel_{\%}$ error (Eq. (1)) across all methods.

The Jaccard similarity coefficient for bone for each tracer-group was comparable. For the largest group (FDG) the averaged scores ranged between 0.50–0.81 for the entire head, 0.40–0.77 in the bottom of the head covering from the eye socket and downwards, and 0.51–0.85 for the top of the head. The overall best performance was seen for MR-AC_{BOSTON}, MR-$AC_{MAXPROB}$, MR-AC_{MUNICH}, MR-$AC_{RESOLUTE}$ and MR-AC_{UCL}, in alphabetical order, with Jaccard indices of 0.68–0.81 in the entire head, and 0.79–0.85 in the top of the head. The individual result for all tracer-groups and methods are shown in Table 2. Note that MR-$AC_{SEGBONE}$ was not evaluated on florbetapir-data, and thus no results are available.

3.2. Global PET performance

The reconstructed PET images for the sample patient in Fig. 1 are shown for the same slice in Fig. 2. Visually comparing the maximum uptake areas in PET_{CT}, it is apparent that PET_{DIXON} and PET_{UTE} underestimate the PET uptake, whereas all the alternative methods improve the performance. For this patient, the average error for the entire brain was between −3.3% (Ontario) and 3.9% (Munich) for the proposed methods, and −10% and −5.3% for Dixon and UTE, respectively. The global $Rel_{\%}$ performance for the entire brain is shown for all 201 FDG patients and 11 methods in the boxplot in Fig. 3. The average performance was within ± 5% of PET_{CT} for all of the proposed methods, with the best performance seen for MR-AC_{BOSTON}, MR-$AC_{CAR\text{-}RiDR}$, MR-$AC_{MAXPROB}$, MR-$AC_{RESOLUTE}$, and MR-AC_{UCL}, ordered alphabetically. MR-AC_{DIXON} showed −11% and MR-AC_{UTE} showed −7%. The global $Abs_{\%}$ performance for the entire brain is summarized for each method and tracer in Supplementary Table 1. The global histogram analysis is shown in Supplemental Figs. 1–3 for the three tracers. The averaged voxel-wise joint histograms are shown for PET_{CT} versus each of the proposed methods in Fig. 4 (FDG) and Supplemental Figs. 4–5 (PiB and Florbetapir). The highest correlation with the unity line was for FDG obtained by MR-$AC_{RESOLUTE}$ (0.96 ± 0.02), MR-AC_{UCL} (0.96 ± 0.02), MR-$AC_{MAXPROB}$ (0.96 ± 0.04), MR-AC_{BOSTON} (0.95 ± 0.03), and MR-$AC_{CAR\text{-}RiDR}$ (0.94 ± 0.03).

3.3. Regional PET performance

The regional $Rel_{\%}$ performance for the anatomical regions defined in the MNI template is shown in Fig. 5 for FDG and Supplemental Figs. 6–7 for PiB and Florbetapir. The best performance across all regions was again found with MR-AC_{BOSTON}, MR-$AC_{CAR\text{-}RiDR}$, MR-$AC_{MAXPROB}$, MR-$AC_{RESOLUTE}$ and MR-AC_{UCL}, ordered alphabetically. Only MR-$AC_{MAXPROB}$ and MR-$AC_{RESOLUTE}$, ordered alphabetically, had an average ± 1 SD error across all tracers below ± 5% in all regions. The averaged absolute difference, $Abs_{\%}$, is shown in Supplemental Figs. 8–9 for each of the regions and tracers. The average and standard deviation images of the $Rel_{\%}$ calculated for each FDG patient are shown in Figs. 6 and 7, respectively, and in Supplemental Figs. 10–13

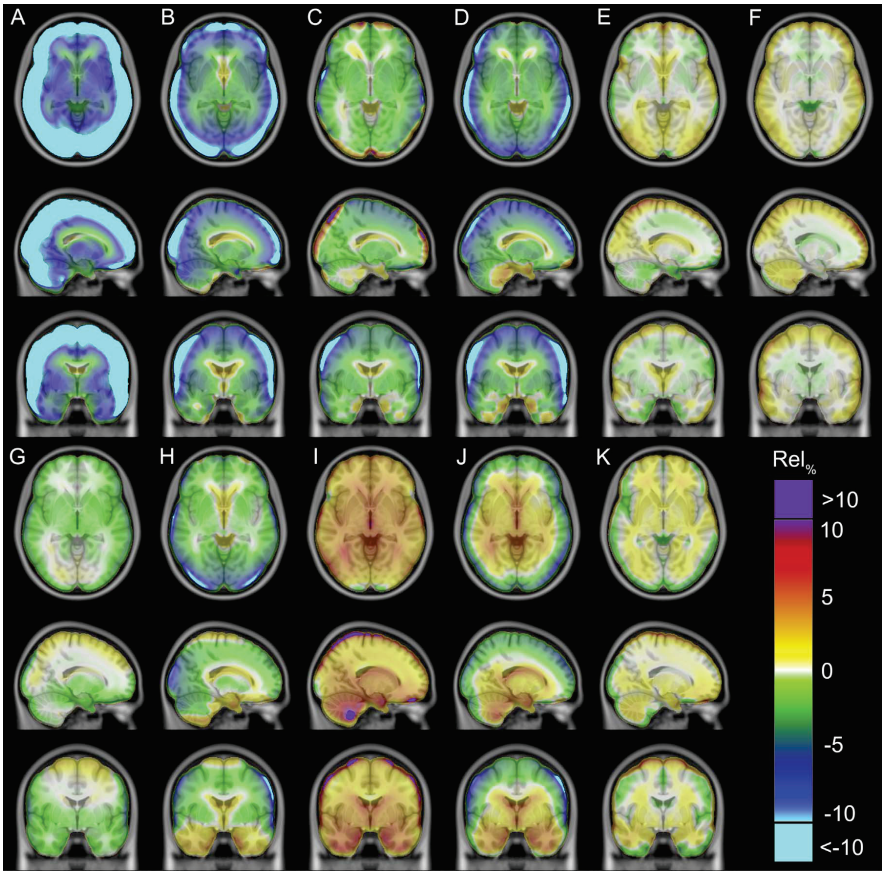

Fig. 6. Averaged $Rel_{\%}$ images across all FDG patients (n=201, including patients with fat/water tissue inversion) for each method: (A) Dixon, (B) UTE, (C) Segbone, (D) Ontario, (E) Boston, (F) UCL, (G) MaxProb, (H) MLAA, (I) Munich, (J) CAR-RiDR, (K) RESOLUTE.

for PiB and florbetapir. Considering all regions in the brain and all tracers, the overall best performance in terms of error and robustness was seen for MR-AC_{BOSTON}, MR-$AC_{MAXPROB}$, MR-$AC_{RESOLUTE}$ and MR-AC_{UCL}, ordered alphabetically.

3.4. Analysis of robustness and outliers

The result of the outlier analysis is shown in Fig. 8 for errors within ± 5%, ± 10%, and ± 15% (FDG) and Supplemental Fig. 14 (PiB and florbetapir). The proposed methods exceed the performance of the current Dixon and UTE methods. The cutoff where all of the patients are within ± 10% of PET_{CT} is achieved for MR-AC_{BOSTON}, MR-$AC_{MAXPROB}$, MR-$AC_{RESOLUTE}$ and MR-AC_{UCL}, ordered alphabetically, and at 90% of the brain, and between 60% and 80% for the other methods. At ± 15%, there is a clear separation between five of the methods (MR-AC_{BOSTON}, MR-$AC_{CAR\text{-}RiDR}$, MR-$AC_{MAXPROB}$, MR-$AC_{RESOLUTE}$ and MR-AC_{UCL}, ordered alphabetically) and the remaining methods. The robustness of each method can be assessed in the standard deviation images (Fig. 7). The best performance was obtained by MR-AC_{UCL} in the center of the brain, shortly followed by MR-$AC_{MAXPROB}$, MR-AC_{BOSTON} and MR-$AC_{RESOLUTE}$. In the cortical regions, the best performance was obtained by MR-$AC_{RESOLUTE}$ and MR-$AC_{CAR\text{-}RiDR}$. The three patients with the worst performance are categorized in Table 3, and the worst outlier is shown for each method in Supplemental Fig. 15.

In general, the worst outliers in the template/atlas-based methods (MR-$AC_{ONTARIO}$, MR-AC_{BOSTON}, MR-AC_{UCL}, MR-$AC_{MAXPROB}$) all have the same error category – the bone density is over or underestimated. Only a single case is due to registration errors (#1 in MR-$AC_{MAXPROB}$). The effect of the error is greatest in the cortical regions, with errors up to 30% locally.

The general errors in the proposed segmentation-based methods (MR-AC_{MUNICH}, MR-$AC_{CAR\text{-}RiDR}$, MR-$AC_{RESOLUTE}$) are over/under estimation of bone in air/tissue interface areas, resulting in local errors of up to 25% in the medulla and cerebellum. For the vendor-provided methods, the worst outliers were due to missing bone (MR-AC_{DIXON}) and underestimated bone density (MR-AC_{UTE}).

4. Discussion

This study facilitates a framework for comparing a large number of state-of-the-art methods using multiple metrics, and does so across a large patient cohort. We aimed to represent a broad spectrum of published methods, showing promises of clinical feasibility, and

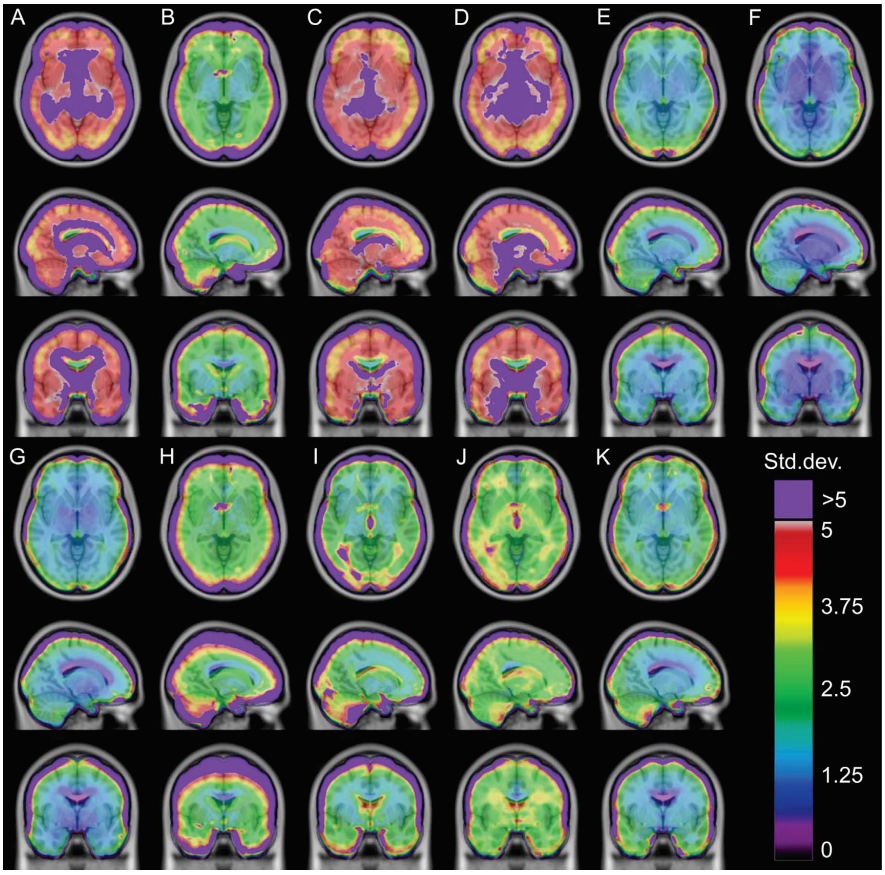

Fig. 7. Standard deviation images across all FDG $Rel_{\%}$ images (n=201, including patients with fat/water tissue inversion) for each method: (A) Dixon, (B) UTE, (C) Segbone, (D) Ontario, (E) Boston, (F) UCL, (G) MaxProb, (H) MLAA, (I) Munich, (J) CAR-RiDR, (K) RESOLUTE.

selected nine methods that were applicable to our large cohort of Siemens mMR examinations. Adding the vendor-provided methods, Dixon and UTE, we evaluated 11 methods for obtaining an MR-AC image. The key findings for the proposed methods were: almost all achieved relative errors below ± 5% globally and in all regions of the brain; the methods essentially differed in robustness, clinical feasibility, and outliers. Dixon and UTE have been included as current vendor references and confirm earlier results from Andersen et al. (2014), Dickson et al. (2014) with a tendency to global underestimation of activity.

The cerebellum is a region that is often used for normalization purposes, especially in kinetic modeling, and therefore requires extra attention. Considering the average ± 1 SD, the best performance is obtained with $MR\text{-}AC_{BOSTON}$ and $MR\text{-}AC_{MAXPROB}$, shortly followed by most of the other methods; the only methods exceeding ± 5% were $MR\text{-}AC_{MLAA}$ and $MR\text{-}AC_{MUNICH}$ (Fig. 5). The maximum error in the cerebellum was 6–9% from the reference for most of the proposed methods (Supplemental Fig. 16), except for $MR\text{-}AC_{CAR\text{-}RiDR}$ (14%), $MR\text{-}AC_{MLAA}$ and $MR\text{-}AC_{MUNICH}$ (17%).

The result of the attenuation map evaluation (Table 2) illustrates that the multi-atlas and multi-registration based methods ($MR\text{-}AC_{UCL}$, $MR\text{-}AC_{MAXPROB}$) have the highest overall bone accuracy, with equally good results achieved in the upper part of the head by R_2^*-based methods ($MR\text{-}AC_{MUNICH}$, $MR\text{-}AC_{RESOLUTE}$). This area-dependent difference could be explained by the challenges reported in air/tissue interface areas originating from the UTE sequence, such as the mouth and esophagus (Delso et al., 2014a). Metal implant-induced artifacts resulting in overestimation of bone in the mouth area especially affects the accuracy of the R_2^*-based methods, but obviously also the remaining methods. Of all methods, two of the R_2^*-based methods ($MR\text{-}AC_{CAR\text{-}RiDR}$ and $MR\text{-}AC_{RESOLUTE}$) had the lowest standard deviation in the cortical regions near the bone (Fig. 7). This can be explained by the fact that these methods extract patient specific bone density, whereas the template/atlas-based methods use an average CT value. This can in some cases lead to local under- or overestimation of the PET signal of up to 20% (Table 3, Supplemental Fig. 15). It should be noted that for the subjects where the CT include the dental region, the CTs were also affected by metal implants resulting in streak artifacts, which could bias the results further.

The template/atlas-based methods generally produced attenuation maps very similar to the CT-based attenuation maps, but they are based on the assumption that any new subject can be represented by a template, a local combination of atlas patients, or by a non-rigid registration to a template. The template/atlas-based methods are

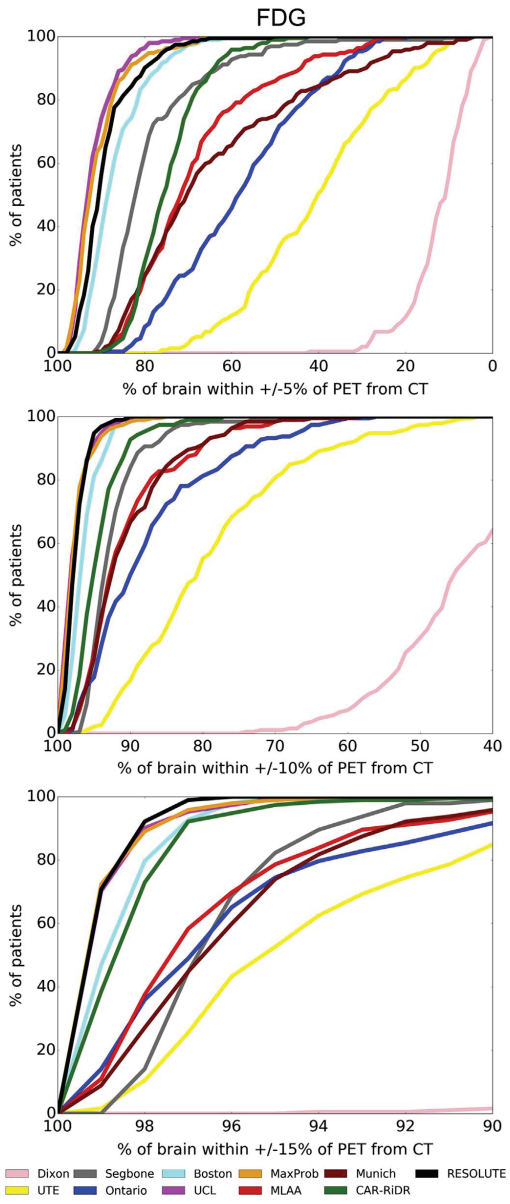

Fig. 8. Outlier analysis for the FDG patients (n=192, excluding patients with fat/water tissue inversion). Note different scale of x-axis.

therefore also potentially challenged by abnormal anatomy and patient surgery. The template/atlas-based methods are, furthermore, currently only optimized and tested for adults, as the application to children might require a purpose specific MRI/CT database. We did not include children, or any patients who have undergone anatomy-changing surgery in this study.

Most subjects chosen came from dementia studies, as this disease has the potential to be a key clinical application of PET/MRI (Bailey et al., 2015). The disease is clinically imaged with FDG, or amyloid binding radiotracers such as PiB or florbetapir, with the majority of patients having relatively widely distributed uptake in the brain, making the tracers well suited for a large-scale evaluation of MR-AC methods. The overall performance was, generally, similar across the three tracers for all methods (Supplemental Figs. 1–3).

When considering patient management, the acquisition time and number of steps required for generating AC maps has also to be taken into account. A potential challenge for the template/atlas-based methods is the long computation time due to multiple registrations for each patient in the database (Table 4). The MR-AC$_{MAXPROB}$ and MR-AC$_{UCL}$ methods currently require at least an hour of processing time for each attenuation map, whereas the MR-AC$_{MUNICH}$ and MR-AC$_{CAR\text{-}RiDR}$ methods only take a few seconds. The shorter processing time is usually a key argument for choosing the segmentation-based methods in fast-paced clinical services, whereas accuracy is much more important than speed in research applications. The MR-AC$_{SEGBONE}$ prototype requires less than 2 min of processing time, with further potential for speed-up. The processing time for multi-atlas methods could be shortened by code optimization and by reducing the number of database studies using pre-selection of the candidates more likely to match the patient (e.g. using gender, age, etc.) (Aljabar et al., 2009) but this requires further evaluation. An alternative is to use the newly proposed one-registration multi-atlas approach, which, however, comes at the cost of a lower accuracy in bone extraction compared to the multi-atlas approach (Arabi and Zaidi, 2016). In line with this, recent result on GE Signa system has shown, that compared to the clinical single-atlas, multi-atlas (MR-AC$_{UCL}$) is more accurate especially in regions close to the skull base (Sekine et al., 2016b). The emission-based method, MLAA, is currently computationally intensive, and relies on multiple MR sequences, which might complicate its use in a clinical setting.

We excluded a single machine-learning-based AC-method (Chen et al., 2015) from this study, as it had excessively long processing time for each patient (> 4 days), making it infeasible both in clinical routine and in this study in its current state.

4.1. Limitations

The use of a CT as gold standard is debatable. The CT image does not fully cover the FOV of the MR and PET area, and is further subject to streak artifacts from dental implants. Since the CT images are not simultaneously acquired with the PET/MRI, they are also subject to non-rigid movement, e.g. jaw movement and swallowing, not accounted for during the rigid registration. In lack of a true gold standard, such as a transmission scan with a rotating source, we considered the CT to be the reference.

The cohort, mainly consisting of patients with dementia and age-matched controls, represents an ageing population. This study did not include data to test the performance of these MR-AC methods on brain scans from younger patients. Furthermore, the study cohort did not include patients with focal PET lesions. Therefore, the performance of these methods in brain tumor patients has yet to be evaluated in most cases, although evaluation of individual methods (e.g. MR-AC$_{BOSTON}$) has already been performed in challenging brain tumors as in Izquierdo-Garcia et al. (2014).

The data from Washington University (florbetapir) were used to train the mapping of bone values from HU to LACs in the MR-AC$_{CAR\text{-}RiDR}$ method (Juttukonda et al., 2015). This could potentially bias the results.

5. Conclusion

All of the proposed methods have an average global performance within likely acceptable limits (± 5% of CT-based reference), and

Engineering Sciences. Funding was also received from the National Institute for Health Research University College London Hospitals Biomedical Research Centre (NIHR BRC UCLH/UCL High Impact Initiative BW.mn.BRC10269) and the EPSRC (EP/K005278/1). In Lyon, this work was supported by a CIFRE studentship jointly funded by Siemens and the French national agency for research and Technology (ANRT). Funding was also received from the French national 'invest for the future' programs (LILI – Lyon Integrated Life Imaging: hybrid MR-PET ANR-11-EQPX-0026) and the hospital University Institute CESAME (Brain and Mental Health ANR-10-IBHU-0003). In Munich, this work was supported by the European Union Seventh Framework Program (FP7) under Grant Agreement n° 602621 Trimage and n° 294582- MUMI. In Boston, this work was supported by the NIH National Institute of Biomedical Imaging and Bioengineering (NIBIB) grant number 1R01EB014894.

Appendix A. Supporting information

Supplementary data associated with this article can be found in the online version at http://dx.doi.org/10.1016/j.neuroimage.2016.12.010.

References

Aitken, A.P., Giese, D., Tsoumpas, C., Schleyer, P., Kozerke, S., et al., 2014. Improved UTE-based attenuation correction for cranial PET-MR using dynamic magnetic field monitoring. Med. Phys. 41, 012302.

Aljabar, P., Heckemann, R.A., Hammers, A., Hajnal, J.V., Rueckert, D., 2009. Multi-atlas based segmentation of brain images: atlas selection and its effect on accuracy. Neuroimage 46 (3), 726–738.

Anazodo, U.C., Thiessen, J.D., Ssali, T., Mandel, J., Gunther, M., et al., 2014. Feasibility of simultaneous whole-brain imaging on an integrated PET-MRI system using an enhanced 2-point Dixon attenuation correction method. Front. Neurosci. 8, 434.

Andersen, F.L., Ladefoged, C.N., Beyer, T., Keller, S.H., Hansen, A.E., et al., 2014. Combined PET/MR imaging in neurology: MR-based attenuation correction implies a strong spatial bias when ignoring bone. Neuroimage 84, 206–216.

Andreasen, D., Van Leemput, K., Hansen, R.H., Andersen, J.A., Edmund, J.M., 2015. Patch-based generation of a pseudo CT from conventional MRI sequences for MRI-only radiotherapy of the brain. Med. Phys. 42, 1596–1605.

Arabi, H., Zaidi, H., 2016. One registration multi-atlas-based pseudo-CT generation for attenuation correction in PET/MRI. Eur. J. Nucl. Med. Mol. Imaging 43, 2021–2035.

Avants, B.B., Tustison, N.J., Song, G., Cook, P.A., Klein, A., et al., 2011. A reproducible evaluation of ANTs similarity metric performance in brain image registration. Neuroimage 54, 2033–2044.

Bailey, D.L., Pichler, B.J., Guckel, B., Barthel, H., Beer, A.J., et al., 2015. Combined PET/MRI: Multi-modality Multi-parametric Imaging Is Here: Summary Report of the 4th International Workshop on PET/MR Imaging, February 23–27, 2015, Tubingen, Germany. Mol. Imaging Biol. vol. 17, pp. 595–608.

Benoit, D., Ladefoged, C.N., Rezaei, A., Keller, S.H., Andersen, F.L., Højgaard, L., Hansen, A.E., Holm, S., Nuyts, J., 2016. Optimized MLAA for quantitative non-TOF PET/MR of the brain. Phys. Med. Biol. 61 (24), 8854.

Berker, Y., Franke, J., Salomon, A., Palmowski, M., Donker, H.C., et al., 2012. MRI-based attenuation correction for hybrid PET/MRI systems: a 4-class tissue segmentation technique using a combined ultrashort-echo-time/Dixon MRI sequence. J. Nucl. Med. 53, 796–804.

Burgos, N., Cardoso, M.J., Thielemans, K., Modat, M., Pedemonte, S., et al., 2014. Attenuation correction synthesis for hybrid PET-MR scanners: application to brain studies. IEEE Trans. Med. Imaging 33, 2332–2341.

Cabello, J., Lukas, M., Forster, S., Pyka, T., Nekolla, S.G., et al., 2015. MR-based attenuation correction using ultrashort-echo-time pulse sequences in dementia patients. J. Nucl. Med. 56, 423–429.

Carney, J.P., Townsend, D.W., Rappoport, V., Bendriem, B., 2006. Method for transforming CT images for attenuation correction in PET/CT imaging. Med. Phys. 33, 976–983.

Catana, C., van der Kouwe, A., Benner, T., Michel, C.J., Hamm, M., et al., 2010. Toward implementing an MRI-based PET attenuation-correction method for neurologic studies on the MR-PET brain prototype. J. Nucl. Med. 51, 1431–1438.

Chan, S.-L.S., Jeffree, R.L., Fay, M., Crozier, S., Yang, Z., et al., 2013. Automated Classification of Bone and Air Volumes for Hybrid PET-MRI Brain Imaging. International Conference on Digital Image Computing: Techniques and Applications (DICTA), Hobart, Australia, pp. 1–8.

Chen, Y., Juttukonda, M., Su, Y., Benzinger, T., Rubin, B.G., et al., 2015. Probabilistic air segmentation and sparse regression estimated pseudo CT for PET/MR attenuation correction. Radiology 275, 562–569.

Collins, D.L., Zijdenbos, A., Baaré, W.C., Evans, A., 1999. ANIMAL+INSECT: improved cortical structure segmentation. In: Kuba, A., Šáamal, M., Todd-Pokropek, A. (Eds.), Information Processing in Medical Imaging. Springer, Berlin, Heidelberg, 210–223.

Delso, G., Fürst, S., Jakoby, B., Ladebeck, R., Ganter, C., et al., 2011. Performance measurements of the Siemens mMR integrated whole-body PET/MR scanner. J. Nucl. Med. 52, 1914–1922.

Delso, G., Carl, M., Wiesinger, F., Sacolick, L., Porto, M., et al., 2014a. Anatomic evaluation of 3-dimensional ultrashort-echo-time bone maps for PET/MR attenuation correction. J. Nucl. Med. 55, 780–785.

Delso, G., Zeimpekis, K., Carl, M., Wiesinger, F., Hullner, M., et al., 2014b. Cluster-based segmentation of dual-echo ultra-short echo time images for PET/MR bone localization. EJNMMI Phys. 1, 7.

Dickson, J.C., O'Meara, C., Barnes, A., 2014. A comparison of CT- and MR-based attenuation correction in neurological PET. Eur. J. Nucl. Med. Mol. Imaging 41, 1176–1189.

Drzezga, A., Barthel, H., Minoshima, S., Sabri, O., 2014. Potential clinical applications of PET/MR imaging in neurodegenerative diseases. J. Nucl. Med. 55, 47S–55S.

Dukart, J., Mueller, K., Horstmann, A., Barthel, H., Moller, H.E., et al., 2011. Combined evaluation of FDG-PET and MRI improves detection and differentiation of dementia. PLoS One 6, e18111.

Fei, B., Yang, X., Nye, J.A., Aarsvold, J.N., Raghunath, N., et al., 2012. MRPET quantification tools: registration, segmentation, classification, and MR-based attenuation correction. Med. Phys. 39, 6443–6454.

Fonov, V.S., Evans, A.C., McKinstry, R.C., Almli, C., Collins, D., 2009. Unbiased nonlinear average age-appropriate brain templates from birth to adulthood. Neuroimage 47, S102.

Grodzki, D.M., Jakob, P.M., Heismann, B., 2012. Ultrashort echo time imaging using pointwise encoding time reduction with radial acquisition (PETRA). Magn. Reson. Med. 67, 510–518.

Heiss, W.D., 2009. The potential of PET/MR for brain imaging. Eur. J. Nucl. Med. Mol. Imaging 36, 105–112.

Hillner, B.E., Siegel, B.A., Liu, D., Shields, A.F., Gareen, I.F., et al., 2008. Impact of positron emission tomography/computed tomography and positron emission tomography (PET) alone on expected management of patients with cancer: initial results from the National Oncologic PET Registry. J. Clin. Oncol. 26, 2155–2161.

Hitz, S., Habekost, C., Furst, S., Delso, G., Forster, S., et al., 2014. Systematic comparison of the performance of integrated whole-body PET/MR imaging to conventional PET/CT for 18F-FDG b.rain imaging in patients examined for suspected dementia. J. Nucl. Med. 55, 923–931.

Hofmann, M., Steinke, F., Scheel, V., Charpiat, G., Farquhar, J., et al., 2008. MRI-based attenuation correction for PET/MRI: a novel approach combining pattern recognition and atlas registration. J. Nucl. Med. 49, 1875–1883.

Izquierdo-Garcia, D., Hansen, A.E., Forster, S., Benoit, D., Schachoff, S., et al., 2014. An SPM8-based approach for attenuation correction combining segmentation and nonrigid template formation: application to simultaneous PET/MR brain imaging. J. Nucl. Med. 55, 1825–1830.

Jakoby, B.W., Bercier, Y., Watson, C.C., Bendriem, B., Townsend, D.W., 2009. Performance characteristics of a new LSO PET/CT scanner with extended axial field-of-view and PSF reconstruction. IEEE Trans. Nucl. Sci. 56, 633–639.

Johansson, A., Karlsson, M., Nyholm, T., 2011. CT substitute derived from MRI sequences with ultrashort echo time. Med. Phys. 38, 2708–2714.

Juttukonda, M.R., Mersereau, B.G., Chen, Y., Su, Y., Rubin, B.G., et al., 2015. MR-based attenuation correction for PET/MRI neurological studies with continuous-valued attenuation coefficients for bone through a conversion from R2* to CT-Hounsfield units. Neuroimage 112, 160–168.

Keereman, V., Fierens, Y., Broux, T., De Deene, Y., Lonneux, M., et al., 2010. MRI-based attenuation correction for PET/MRI using ultrashort echo time sequences. J. Nucl. Med. 51, 812–818.

Khateri, P., Saligheh Rad, H., Jafari, A.H., Fathi Kazerooni, A., Akbarzadeh, A., et al., 2015. Generation of a four-class attenuation map for MRI-based attenuation correction of PET data in the head area using a novel combination of STE/Dixon-MRI and FCM clustering. Mol. Imaging Biol. 17, 884–892.

Koesters, T., Friedman, K.P., Fenchel, M., Zhan, Y., Hermosillo, G., et al., 2016. Dixon sequence with superimposed model-based bone compartment provides highly accurate PET/MR attenuation correction of the brain. J. Nucl. Med. 57, 918–924.

Ladefoged, C.N., Hansen, A.E., Keller, S.H., Holm, S., Law, I., et al., 2014. Impact of incorrect tissue classification in Dixon-based MR-AC: fat-water tissue inversion. EJNMMI Phys. 1, 101.

Ladefoged, C.N., Benoit, D., Law, I., Holm, S., Kjaer, A., et al., 2015. Region specific optimization of continuous linear attenuation coefficients based on UTE (RESOLUTE): application to PET/MR brain imaging. Phys. Med. Biol. 60, 8047–8065.

Martinez-Möller, A., Souvatzoglou, M., Delso, G., Bundschuh, R.A., Chefd'hotel, C., et al., 2009. Tissue classification as a potential approach for attenuation correction in whole-body PET/MRI: evaluation with PET/CT data. J. Nucl. Med. 50, 520–526.

Mehranian, A., Zaidi, H., 2015. Joint estimation of activity and attenuation in whole-body TOF PET/MRI using constrained Gaussian mixture models. IEEE Trans. Med. Imaging 34, 1808–1821.

Mehranian, A., Arabi, H., Zaidi, H., 2016. Quantitative analysis of MRI-guided attenuation correction techniques in time-of-flight brain PET/MRI. Neuroimage 130, 123–133.

Merida, I., Costes, N., Heckemann, R.A., Drzezga, A., Forster, S., et al., 2015. Evaluation of several multi-atlas methods for PSEUDO-CT generation in brain MRI-PET attenuation correction. IEEE. In: Proceedings of the 12th International Symposium on Biomedical Imaging (ISBI), New York, NY, USA. pp. 1431–1434.

Navalpakkam, B.K., Braun, H., Kuwert, T., Quick, H.H., 2013. Magnetic resonance-based attenuation correction for PET/MR hybrid imaging using continuous valued attenuation maps. Invest. Radiol. 48, 323–332.

Nuyts, J., Dupont, P., Stroobants, S., Benninck, R., Mortelmans, L., et al., 1999.

Simultaneous maximum a posteriori reconstruction of attenuation and activity distributions from emission sinograms. IEEE Trans. Med. Imaging 18, 393–403.
Paulus, D.H., Quick, H.H., Geppert, C., Fenchel, M., Zhan, Y., et al., 2015. Whole-body PET/MR imaging: quantitative evaluation of a novel model-based MR attenuation correction method including bone. J. Nucl. Med. 56, 1061–1066.
Poynton, C.B., Chen, K.T., Chonde, D.B., Izquierdo-Garcia, D., Gollub, R.L., et al., 2014. Probabilistic atlas-based segmentation of combined T1-weighted and DUTE MRI for calculation of head attenuation maps in integrated PET/MRI scanners. Am. J. Nucl. Med. Mol. Imaging 4, 160–171.
Rezaei, A., Defrise, M., Nuyts, J., 2014. ML-reconstruction for TOF-PET with simultaneous estimation of the attenuation factors. IEEE Trans. Med. Imaging 33, 1563–1572.
Rezaei, A., Defrise, M., Bal, G., Michel, C., Conti, M., et al., 2012. Simultaneous reconstruction of activity and attenuation in time-of-flight PET. IEEE Trans. Med. Imaging 31, 2224–2233.
Roy, S., Wang, W.T., Carass, A., Prince, J.L., Butman, J.A., et al., 2014. PET attenuation correction using synthetic CT from ultrashort echo-time MR imaging. J. Nucl. Med. 55, 2071–2077.
Salomon, A., Goedicke, A., Schweizer, B., Aach, T., Schulz, V., 2011. Simultaneous reconstruction of activity and attenuation for PET/MR. IEEE Trans. Med. Imaging 30, 804–813.
Schreibmann, E., Nye, J.A., Schuster, D.M., Martin, D.R., Votaw, J., et al., 2010. MR-based attenuation correction for hybrid PET-MR brain imaging systems using deformable image registration. Med. Phys. 37, 2101–2109.
Sekine, T., Buck, A., Delso, G., Ter Voert, E.E., Huellner, M., et al., 2016a. Evaluation of atlas-based attenuation correction for integrated PET/MR in human brain: application of a head atlas and comparison to true CT-based attenuation correction. J. Nucl. Med. 57, 215–220.
Sekine, T., Burgos, N., Warnock, G., Huellner, M., Buck, A., et al., 2016b. Multi-atlas-based attenuation correction for brain 18F-FDG PET imaging using a time-of-flight PET/MR scanner: comparison with clinical single-atlas- and CT-based attenuation correction. J. Nucl. Med. 57, 1258–1264.
Su, K.H., Hu, L., Stehning, C., Helle, M., Qian, P., et al., 2015. Generation of brain pseudo-CTs using an undersampled, single-acquisition UTE-mDixon pulse sequence and unsupervised clustering. Med. Phys. 42, 4974–4986.
Torrado-Carvajal, A., Herraiz, J.L., Alcain, E., Montemayor, A.S., Garcia-Canamaque, L., et al., 2016. Fast patch-based pseudo-CT synthesis from T1-weighted MR images for PET/MR attenuation correction in brain studies. J. Nucl. Med. 57, 136–143.
Wiesinger, F., Sacolick, L.I., Menini, A., Kaushik, S.S., Ahn, S., et al., 2016. Zero TE MR bone imaging in the head. Magn. Reson. Med. 75, 107–114.
Wollenweber, S.D., Ambwani, S., Delso, G., Lonn, A.H.R., Mullick, R., et al., 2013. Evaluation of an atlas-based PET head attenuation correction using PET/CT & MR patient data. IEEE Trans. Nucl. Sci. 60, 3383–3390.
Yang, Z., Choupan, J., Sepehrband, F., Reutens, D., Crozier, S., 2013. Tissue classification for PET/MRI attenuation correction using conditional random field and image fusion. Int. J. Mach. Learn. Comput. 3, 87–92.
Zaidi, H., Montandon, M.L., Slosman, D.O., 2003. Magnetic resonance imaging-guided attenuation and scatter corrections in three-dimensional brain positron emission tomography. Med. Phys. 30, 937–948.
Zaidi, H., Ojha, N., Morich, M., Griesmer, J., Hu, Z., et al., 2011. Design and performance evaluation of a whole-body Ingenuity TF PET-MRI system. Phys. Med. Biol. 56, 3091–3106.

Synthèse

Introduction

L'imagerie hybride simultanée IRM-TEP est une nouvelle technique d'imagerie médicale innovante combinant l'imagerie par résonance magnétique (IRM) et la tomographie par émission de positons (TEP). Le couplage de ces deux modalités d'imagerie de pointe ouvre aujourd'hui de nouveaux axes de recherche et va fournir des outils innovants pour explorer les fonctions cérébrales. Pour cela, il est indispensable de corriger l'atténuation des photons par les tissus afin d'obtenir une quantification précise du signal TEP. Traditionnellement, en imagerie TEP/CT (TEP couplée au scanner à rayons-X), les cartes de radiodensité utilisées pour la correction d'atténuation sont directement dérivées de l'image de CT. En IRM-TEP, les rayons-X ont été remplacés par l'IRM et la carte d'atténuation n'est plus disponible. Il est alors nécessaire de trouver une alternative pour calculer la carte d'atténuation du sujet à partir de son image IRM.

Méthodes

J'ai mis au point une méthode multi-atlas (*MaxProb*) qui permet de construire une carte d'atténuation spécifique à l'anatomie du sujet. J'utilise l'image IRM du sujet, et une base de données de 40 paires d'images IRM et CT de référence (les atlas). La carte d'atténuation est générée en combinant les informations contenues dans la base de données. Les atlas sont d'abord recalés dans l'espace du sujet par transformation non-linéaire. Les CT recalés sont ensuite segmentés en trois classes tissulaires (air, tissus mous et os) puis fusionnés au niveau du voxel par un processus de classe majoritaire. L'intensité finale d'un voxel du pseudo-CT est déterminée en moyennant les unités Hounsfield des atlas CT appartenant à la classe majoritaire. La carte d'atténuation est finalement dérivée du pseudo-CT généré.

Nous avons évalué l'impact de la qualité du pseudo-CT sur les images TEP reconstruites, par rapport aux images TEP reconstruites avec le CT de référence. Nous avons également comparé la méthode *MaxProb* à une méthode plus simple qui n'utilise qu'un atlas (*SingleAtlas*), ainsi qu'à la méthode fournie dans le scanner par le constructeur (UTE).

Les performances de *MaxProb* on été évaluées sur des données statiques et dynamiques ainsi que sur des données TEP simulées et réelles. Les images de TEP [^{18}F]FDG statiques, très couramment utilisées en routine clinique et recherche, présentent une distribution homogène du traceur ce qui permet une évaluation globale. Nous avons évalué notre méthode sur des données TEP [^{18}F]FDG de 23 sujets. Nous avons choisi des données de TEP dynamique au [^{18}F]MPPF (un antagoniste sélectif des récepteurs 5-HT_{1A}) afin d'explorer l'impact de la distribution spatiale du traceur qui varie au cours du temps lors d'une acquisition TEP. Cette évaluation dynamique a été réalisée sur sept sujets. Nous avons également simulé des données TEP dynamique afin de reproduire une étude de bolus-infusion utilisant le traceur [^{11}C]raclopride. Vingt-et-un sujets ayant chacun quinze régions d'intérêt définies à partir de l'IRM ont été inclus. Le potentiel de liaison non-déplaçable a été estimé par simple ratio entre région d'intérêt et région de référence (cervelet) dans le caudé, putamen et noyaux accumbens, à l'équilibre. L'évaluation est réalisée au niveau régional mais aussi au niveau du voxel pour les images de radioactivité, les courbes d'activité et les paramètres cinétiques (potentiel de liaison non-déplaçable).

Résultats

En TEP statique [^{18}F]FDG, le biais moyen variait entre 0 et 1% pour 73 des 84 régions cérébrales étudiées et une seule région a obtenu une erreur de 2.5%. L'analyse SPM de données TEP corrigées avec *MaxProb* a montré des différences significatives dans moins de 0.02% du volume cérébrale, alors que pour *SingleAtlas* nous avons obtenu des différences significatives dans plus de 20% du cerveau.

Sur les données de [^{18}F]MPPF dynamiques, la plupart des erreurs régionales sur le BP étaient comprises entre -1 et +3% (biais maximal à 5%) pour *MaxProb*. Avec *SingleAtlas*, les erreurs étaient plus importantes et présentaient une plus grande variabilité. Le biais sur la quantification TEP était amplifié au cours de l'acquisition dynamique avec *SingleAtlas* mais pas avec *MaxProb*. Nous avons montré que cet effet est dû à l'interaction entre la distribution spatiale du traceur qui varie au cours du temps et le degré d'erreur sur les cartes d'atténuation.

Sur les données simulées, nous avons mis en évidence qu'une bonne quantification sur les paramètres physiologiques estimés par modélisation cinétique a également été obtenue avec

MaxProb, même lorsque le cervelet (entouré par les os du crâne) est utilisé comme région de référence. De plus, par rapport à la méthode de correction d'atténuation standard (UTE), *MaxProb* améliore la sensibilité de détection des variations physiologiques mesurées en TEP dynamique.

Conclusion

La correction d'atténuation multi-atlas avec la méthode *MaxProb* permet une bonne quantification sur les scanners hybrides IRM-TEP, ce qui ouvre la voie à de nouveaux protocoles d'imagerie dynamique et simultanée en IRM-TEP.

Personal publications

Journal papers

I. Mérida, A. Reilhac, J. Redouté, R.A. Heckemann, N. Costes, A. Hammers: Multi-atlas attenuation correction supports full quantification of static and dynamic brain PET data in PET-MR. Phys. Med. Biol., 2017.

C.N. Ladefoged, I. Law, U. Anazodo, K. St. Lawrence, D. Izquierdo-Garcia, C. Catana, N. Burgos, M.J. Cardoso, S. Ourselin, B. Hutton, **I. Mérida**, N. Costes, A. Hammers, D. Benoit, S. Holm, M. Juttukonda, H. An, J. Cabello, M. Lukas, S. Nekolla, S. Ziegler, M. Fenchel, B. Jakoby, M.E. Casey, T. Benzinger, L. Højgaard, A.E. Hansen and F.L. Andersen: A multi-centre evaluation study of eleven PET/MRI brain attenuation correction methods on a large cohort of patients: ready for clinical implementation. Neuroimage, 2016.

Conference papers

I. Mérida, N. Costes, R.A. Heckemann, A. Drzezga, S. Förster, A. Hammers: Evaluation of several multi-atlas methods for pseudo-CT generation in brain MRI-PET attenuation correction. Biomedical Imaging (ISBI) IEEE 12th International Symposium, 2015.

C.N. Ladefoged, I. Law, U. Anazodo, K. St. Lawrence, D. Izquierdo-Garcia, C. Catana, N. Burgos, M.J. Cardoso, S. Ourselin, B. Hutton, **I. Mérida**, N. Costes, A. Hammers, D. Benoit, S. Holm, M. Juttukonda, H. An, J. Cabello, M. Lukas, S. Nekolla, S. Ziegler, M. Fenchel, B. Jakoby, M.E. Casey, T. Benzinger, L. Højgaard, A.E. Hansen and F.L. Andersen: Multi-center evaluation of eleven PET/MRI brain attenuation correction methods. IEEE NSS-MIC, 2016.

Conference abstracts

I. Mérida, C. Fonteneau, A. Reilhac, J. Redouté, Z. Irace, M.F. Suaud-Chagny, A. Hammers, N. Costes: Motion correction and multi-atlas attenuation correction applied to a simultaneous bolus/infusion PET-MR brain study. PSMR 2017. *Oral presentation.*

A. Reilhac, **I. Mérida**, Z. Irace, M. C. Stephenson, C. Chen, J. J. Totman, D. W. Townsend, F. Hayad ,N. Costes: Development, validation and application of a rebinner with rigid motion correction for the mMR scanner. PSMR 2017.

I. Mérida, A. Hammers, J. Redouté, C. McGinnity, C. Fonteneau, M.F. Suaud-Chagny, A. Reilhac, N. Costes: Attenuation correction with a multi-atlas method for brain PET-MR imaging: assessment with realistic simulated [^{11}C]raclopride bolus-infusion PET data. Brain&BrainPET 2017. *Poster presentation.*

A. Reilhac, T. Sjoholm, B.A. Thomas, Z. Irace, **I. Mérida**, M. Villien, J. Redoute, N. Costes: Validation and application of PET-SORTEO for the geometry of the Siemens mMR scanner. PSMR 2016.

I. Mérida, N. Costes, J. Redouté, R.A. Heckemann, A. Reilhac, A. Hammers: PET-MR attenuation correction with a maximum probability method: low bias stable over time in dynamic acquisitions. PSMR 2016. *Poster presentation.*

I. Mérida, N. Costes, R.A. Heckemann, A. Hammers: Pseudo-CT generation in brain MR-PET attenuation correction: comparison of several multi-atlas methods. EJNMMI Phys., PSMR 2015. *Oral presentation.*

Glossary

[^{18}F]FDG: fludeoxyglucose

[^{18}F]MPPF: 2'-Methoxyphenyl-(N-2'-pyridinyl)-p-18F-fluoro-benzamidoethylpiperazine

1TC: one-tissue compartment model

2TC: two-tissue compartment model

AC: attenuation correction

ACF: attenuation correction factor

ANOVA: analysis of variance

APD: avalanche photodiodes

ASL: arterial spin labelling

BBB: blood-brain barrier

BOLD: blood oxygen level dependent

BP: binding potential

BP_{ND}: non-displaceable binding potential

BR: binding ratio

CBF: cerebral blood flow

COV: coefficient of variation

CRNL: Centre de recherche en neurosciences de Lyon

CSF: cerebrospinal fluid

CT: x-ray computed tomography

CTAC: CT-based attenuation correction

DTI: diffusion tensor imaging

Eber: event-by-event rebinner

EEG: electroencephalography

FBP: Filtered-back projection

fMRI: functional magnetic resonance imaging

FOV: field of view

FWHM: full width at half maximum

GM: grey matter

HSD: honest significant difference

HU: Hounsfield units

keV: kilo electronvolt

KVP: peak kilovoltage

LAVA: liver-accelerated volume acquisition

LOR: line of response

MAE: mean absolute error

MAPER: multi-atlas propagation with enhanced registration

MEG: magnetoencephalography

MLAA: maximum-likelihood reconstruction of attenuation and activity

MNI: Montreal Neurological Institute

MPRAGE: magnetisation-prepared rapid gradient-echo

MRAC: MR-based attenuation correction

MRI: magnetic resonance imaging

NHP: non-human primate

OSEM: ordered subset expectation maximization

PET: positron emission tomography

PETRA: pointwise encoding time reduction with radial acquisition

PSF: point spread function

R2: spin-spin relaxation rate

R2*: spin-spin relaxation rate with local magnetic field inhomogeneities

RF: radio-frequency

ROI: region of interest

SD: standard deviation

SiPM: silicon photomultiplier

SORTEO: simulation of realistic tridimensional emitting objects

SPECT: single-photon emission computed tomography

SPM: Statistical Parametric Mapping

SRTM: simplified reference tissue model

SUV: standardized uptake value

SUVr: standardized uptake value ratio

SV: super vector

T1: spin-lattice relaxation time

T2: spin-spin relaxation time

T2*: spin-spin relaxation time with local magnetic field inhomogeneities

TAC: time activity curve

tDCS: transcranial direct current stimulation

TE: echo time

TOF: time of flight

TR: repetition time

UTE: ultra-short echo time

UTE1: first-echo image when referring to the UTE sequence

UTE2: second-echo image when referring to the UTE sequence

WM: white matter

ZTE: zero echo time

μ-map: attenuation map

List of figures

List of tables

Bibliography

1. Aasheim, L.B., P, A.K., Goa, E., Asta, H., 2015. PET / MR brain imaging : evaluation of clinical UTE-based attenuation correction. J. Neuclear Med. doi:10.1007/s00259-015-3060-3
2. Aiello, M., Salvatore, E., Cachia, A., Pappata, S., Cavaliere, C., Prinster, A., Nicolai, E., Salvatore, M., Baron, J.C., Quarantelli, M., 2015. Relationship between simultaneously acquired resting-state regional cerebral glucose metabolism and functional MRI: A PET/MR hybrid scanner study. Neuroimage 113, 111–121. doi:10.1016/j.neuroimage.2015.03.017
3. Alessio, A., Kinahan, P., 2006. PET image reconstruction, in: Henkin, R. (Ed.), Nuclear Medicine. Elsevier, Philadelphia.
4. Aljabar, P., Heckemann, R.A., Hammers, A., Hajnal, J. V, Rueckert, D., 2009. Multi-atlas based segmentation of brain images: Atlas selection and its effect on accuracy. Neuroimage 46, 726–738. doi:10.1016/j.neuroimage.2009.02.018
5. Anazodo, U.C., Thiessen, J.D., Ssali, T., Mandel, J., Günther, M., Butler, J., Pavlosky, W., Prato, F.S., Thompson, R.T., St. Lawrence, K.S., 2015. Feasibility of simultaneous whole-brain imaging on an integrated PET-MRI system using an enhanced 2-point Dixon attenuation correction method. Front. Neurosci. 9, 1–11. doi:10.3389/fnins.2014.00434
6. Andersen, F.L., Ladefoged, C.N., Beyer, T., Keller, S.H., Hansen, A.E., Højgaard, L., Kjær, A., Law, I., Holm, S., Andersen, F.L., Ladefoged, C.N., Beyer, T., Keller, S.H., Hansen, A.E., Højgaard, L., Kjær, A., Law, I., Holm, S., 2014. Combined PET/MR imaging in neurology: MR-based attenuation correction implies a strong spatial bias when ignoring bone. Neuroimage 84, 206–216. doi:10.1016/j.neuroimage.2013.08.042
7. Andersen, J.B., Henning, W.S., Lindberg, U., Ladefoged, C.N., Højgaard, L., Greisen, G., Law, I., 2015. Positron emission tomography/magnetic resonance hybrid scanner imaging of cerebral blood flow using 15O-water positron emission tomography and arterial spin labeling magnetic resonance imaging in newborn piglets. J. Cereb. Blood Flow Metab. 35, 1703–1710. doi:10.1038/jcbfm.2015.139
8. Andreasen, D., Leemput, K. Van, Hansen, R.H., Andersen, J.A.L., Edmund, J.M., Mri, P.E.T., 2016. Patch-based generation of a pseudo CT from conventional MRI sequences for MRI- only radiotherapy of the brain Patch-based generation of a pseudo CT from conventional MRI sequences for MRI-only radiotherapy of the brain 1596. doi:10.1118/1.4914158
9. Benoit, D., Ladefoged, C., Rezaei, A., Keller, S.H., Andersen, F., Hojgaard, L., Hansen, A., Holm, S., Nuyts, J., 2016. Optimized MLAA for quantitative non-TOF PET/MR of the brain. Phys. Med. Biol. 8854–8874. doi:10.1002/elan.
10. Berker, Y., Franke, J., Salomon, a., Palmowski, M., Donker, H.C.W., Temur, Y., Mottaghy, F.M., Kuhl, C., Izquierdo-Garcia, D., Fayad, Z. a., Kiessling, F., Schulz, V., 2012. MRI-Based Attenuation Correction for Hybrid PET/MRI Systems: A 4-Class Tissue Segmentation Technique Using a Combined Ultrashort-Echo-Time/Dixon MRI Sequence. J. Nucl. Med. 53, 796–804. doi:10.2967/jnumed.111.092577
11. Beyer, T., Townsend, D.W., Brun, T., Kinahan, P.E., Charron, M., Roddy, R., Jerin, J., Young, J., Byars, L., Nutt, R., 2000. A combined PET/CT scanner for clinical oncology. J. Neuclear Med. 41, 1369–1379.
12. Bisdas, S., Ritz, R., Bender, B., Braun, C., Pfannenberg, C., Reimold, M., Naegele, T., Ernemann, U., 2013. Metabolic mapping of gliomas using hybrid MR-PET imaging: feasibility of the method and spatial distribution of metabolic changes. Invest. Radiol. 48, 295–301.
13. Bitar, R., Leung, G., Perng, R., Tadros, S., Moody, A.R., Sarrazin, J., McGregor, C., Christakis, M., Symons, S., Nelson, A., Roberts, T.P., 2006. MR pulse sequences: what every radiologist wants to know but is afraid to ask. Radiographics 26, 513–537. doi:10.1148/rg.262055063
14. Bonferroni, C.E., 1936. Teoria statistica delle classi e calcolo delle probabilità. Pubbl. del R Ist.

Super. di Sci. Econ. e Commer. di Firenze 8, 3–62.
15. Burger, C., Goerres, G., Schoenes, S., Buck, a., Lonn, a., Von Schulthess, G., 2002. PET attenuation coefficients from CT images: Experimental evaluation of the transformation of CT into PET 511-keV attenuation coefficients. Eur. J. Nucl. Med. 29, 922–927. doi:10.1007/s00259-002-0796-3
16. Burgos, N., Cardoso, M.J., Thielemans, K., Modat, M., Dickson, J., Schott, J.M., Atkinson, D., Arridge, S.R., Hutton, B.F., 2015. Multi-contrast attenuation map synthesis for PET / MR scanners : assessment on FDG and Florbetapir PET tracers. Eur J Nucl Med Mol Imaging 42, 1447–1458. doi:10.1007/s00259-015-3082-x
17. Burgos, N., Cardoso, M.J., Thielemans, K., Modat, M., Pedemonte, S., Dickson, J., Barnes, A., Ahmed, R., Mahoney, C.J., Schott, J.M., Duncan, J.S., Atkinson, D., Arridge, S.R., Hutton, B.F., Ourselin, S., 2014a. Attenuation Correction Synthesis for Hybrid PET-MR Scanners: Application to Brain Studies. IEEE Trans. Med. Imaging 33, 2332–2341. doi:10.1109/TMI.2014.2340135
18. Burgos, N., Thielemans, K., Cardoso, M.J., Markiewicz, P., Jiao, J., Dickson, J., Duncan, J.S., Atkinson, D., Arridge, S.R., Hutton, B.F., Ourselin, S., 2014b. Effect of Scatter Correction When Comparing Attenuation Maps : Application to Brain PET / MR. IEEE Nucl. Sci. Symp. Conf. Rec.
19. Büther, F., Vrachimis, A., Becker, A., Stegger, L., 2016. Impact of MR-safe headphones on PET attenuation in combined PET/MRI scans. EJNMMI Res. 6, 1–5. doi:10.1186/s13550-016-0178-7
20. Buvat, I., Frey, E.C., Green, A.J., Ljungberg, M., 2014. Quantitative Nuclear Medicine Imaging: concepts, requirements, and methods, IAEA Human. ed. Vienna.
21. Cabello, J., Lukas, M., Förster, S., Pyka, T., Nekolla, S.G., Ziegler, S.I., 2015. MR-Based Attenuation Correction Using Ultrashort-Echo- Time Pulse Sequences in Dementia Patients. J. Nucl. Med. 56, 423–429. doi:10.2967/jnumed.114.146308
22. Cardoso, M.J., Clarkson, M.J., Ridgway, G.R., Modat, M., Fox, N.C., Ourselin, S., 2011. LoAd: A locally adaptive cortical segmentation algorithm. Neuroimage 56, 1386–1397. doi:10.1016/j.neuroimage.2011.02.013
23. Carney, J.P.J., Townsend, D.W., Rappoport, V., Bendriem, B., 2006. Method for transforming CT images for attenuation correction in PET/CT imaging. Med. Phys. 33, 976–983. doi:10.1118/1.2174132
24. Catana, C., Drzezga, A., Heiss, W.-D., Rosen, B.R., 2012. PET/MRI for neurologic applications. J. Nucl. Med. 53, 1916–25. doi:10.2967/jnumed.112.105346
25. Catana, C., van der Kouwe, A., Benner, T., Michel, C.J., Hamm, M., Fenchel, M., Fischl, B., Rosen, B., Schmand, M., Sorensen, A.G., 2010. Toward implementing an MRI-based PET attenuation-correction method for neurologic studies on the MR-PET brain prototype. J. Nucl. Med. 51, 1431–1438. doi:10.2967/jnumed.109.069112
26. Chen, S., Tyan, Y., Lai, J., Chang, C., 2016. Automated Determination of Arterial Input Function for Dynamic Susceptibility Contrast MRI from Regions around Arteries Using Independent Component Analysis 2016.
27. Coombs, B.D., Szumowski, J., Coshow, W., 1997. Two-point Dixon technique for water-fat signal decomposition with B0 inhomogeneity correction. Magn. Reson. Med. 38, 884–9. doi:10.1002/mrm.1910380606
28. Costes, N., Merlet, I., Zimmer, L., Lavenne, F., Cinotti, L., Delforge, J., Luxen, A., Pujol, J.-F., Le Bars, D., 2002. Modeling [18 F]MPPF positron emission tomography kinetics for the determination of 5-hydroxytryptamine(1A) receptor concentration with multiinjection. J. Cereb. Blood Flow Metab. 22, 753–65. doi:10.1097/00004647-200206000-00014
29. Delso, G., Furst, S., Jakoby, B., Ladebeck, R., Ganter, C., Nekolla, S.G., Schwaiger, M., Ziegler, S.I., 2011. Performance Measurements of the Siemens mMR Integrated Whole-Body PET/MR Scanner. J. Nucl. Med. 52, 1914–1922. doi:10.2967/jnumed.111.092726
30. Delso, G., Wiesinger, F., Sacolick, L.I., Kaushik, S.S., Shanbhag, D.D., Martin, H., 2015. Clinical Evaluation of Zero-Echo-Time MR Imaging for the Segmentation of the Skull. J. Nucl. Med. 417–422. doi:10.2967/jnumed.114.149997
31. Dickson, J.C., O'Meara, C., Barnes, A., 2014. A comparison of CT- and MR-based attenuation

correction in neurological PET. Eur. J. Nucl. Med. Mol. Imaging 41, 1176–1189. doi:10.1007/s00259-013-2652-z
32. Drzezga, A., Barthel, H., Minoshima, S., Sabri, O., 2014. Potential Clinical Applications of PET/MR Imaging in Neurodegenerative Diseases. J. Nucl. Med. 55, 47S–55S. doi:10.2967/jnumed.113.129536
33. Endres, C.J., Carson, R.E., 1998. Assessment of dynamic neurotransmitter changes with bolus or infusion delivery of neuroreceptor ligands. J. Cereb. Blood Flow Metab. 18, 1196–1210.
34. Fahey, F.H., 2002. Data Acquisition in PET Imaging. J. Nucl. Med. Technol. 30, 39–49.
35. Fayad, H., Lamare, F., Merlin, T., Visvikis, D., 2016. Motion correction using anatomical information in PeT/cT and PeT/Mr hybrid imaging. Q. J. Nucl. Med. Mol. Imaging 60, 12–24.
36. Frohwein, L.J., Schlicher, D., Heß, M., Büther, F., Schäfers, K.P., 2016. Markerless Attenuation Correction for Flexible MRI RF Surface Coils in Hybrid PET/MRI, in: PSMR.
37. Frouin, V., Comtat, C., Reilhac, A., Grégoire, M.-C., 2002. Correction of partial-volume effect for PET striatal imaging: fast implementation and study of robustness. J. Nucl. Med. 43, 1715–1726.
38. Fung, E., Carson, R.E., 2013. Cerebral blood flow with [15O]water PET studies using image-derived input function and MR-defined carotid centerlines. Phys. Med. Biol. doi:10.1124/dmd.107.016501.CYP3A4-Mediated
39. Galazzo, I.B., Mattoli, M.V., Pizzini, F.B., De Vita, E., Barnes, A., Duncan, J.S., Jager, R., Golay, X., Bomanji, J.B., Koepp, M., Groves, A.M., Fraioli, F., 2016. Cerebral metabolism and perfusion in MR-negative individuals with refractory focal epilepsy assessed by simultaneous acquisition of 18F-FDG PET and arterial spin labeling. NeuroImage Clin. 11, 648–657. doi:10.1016/j.nicl.2016.04.005
40. Gibby, W., 2005. Basic principles of magnetic resonance imaging. Neurosurg. Clin. N. Am. 16, 1–64.
41. Gousias, I.S., Rueckert, D., Heckemann, R. a., Dyet, L.E., Boardman, J.P., Edwards, a. D., Hammers, A., 2008. Automatic segmentation of brain MRIs of 2-year-olds into 83 regions of interest. Neuroimage 40, 672–684. doi:10.1016/j.neuroimage.2007.11.034
42. Grodzki, D.M., Jakob, P.M., Heismann, B., 2012. Ultrashort Echo Time Imaging Using Pointwise Encoding Time Reduction With Radial Acquisition (PETRA). Magn. Reson. Med. 518, 510–518. doi:10.1002/mrm.23017
43. Gunn, R.N., Lammertsma, A.A., Cunningham, V.J., 1997. Parametric Imaging of Ligand-Receptor Binding in PET Using a Simplified Reference Region Model. Neuroimage 287, 279–287.
44. Gutierrez, D., Montandon, M.L., Assal, F., Allaoua, M., Ratib, O., Lövblad, K.O., Zaidi, H., 2012. Anatomically guided voxel-based partial volume effect correction in brain PET: Impact of MRI segmentation. Comput. Med. Imaging Graph. 36, 610–619. doi:10.1016/j.compmedimag.2012.09.001
45. Hammers, A., Allom, R., Koepp, M.J., Free, S.L., Myers, R., Lemieux, L., Mitchell, T.N., Brooks, D.J., Duncan, J.S., 2003. Three-dimensional maximum probability atlas of the human brain, with particular reference to the temporal lobe. Hum. Brain Mapp. 19, 224–247. doi:10.1002/hbm.10123
46. Heckemann, R.A., Hajnal, J. V, Aljabar, P., Rueckert, D., Hammers, A., 2006. Automatic anatomical brain MRI segmentation combining label propagation and decision fusion. Neuroimage 33, 115–126. doi:10.1016/j.neuroimage.2006.05.061
47. Heckemann, R.A., Keihaninejad, S., Aljabar, P., Rueckert, D., Hajnal, J. V., Hammers, A., 2010. Improving intersubject image registration using tissue-class information benefits robustness and accuracy of multi-atlas based anatomical segmentation. Neuroimage 51, 221–227. doi:10.1016/j.neuroimage.2010.01.072
48. Hoa, D., Micheneau, A., Gahide, G., Le Bars, E., Taourel, P., 2008. L'IRM pas à pas, Sauramps m. ed. Montpellier.
49. Holman, B.F., Cuplov, V., Hutton, B.F., Groves, A.M., Thielemans, K., 2016. The effect of respiratory induced density variations on non-TOF PET quantitation in the lung. Phys. Med. Biol. 61, 3148–3163. doi:10.1088/0031-9155/61/8/3148

50. Hsu, S., Cao, Y., Lawrence, T.S., 2015. Quantitative characterizations of ultrashort echo (UTE) images for supporting air – bone separation in the head. Phys. Med. Biol. 2869, 2869. doi:10.1088/0031-9155/60/7/2869
51. Hudson, H.M., Larkin, R.S., 1994. Accelerated Image Reconstruction Using Ordered Subsets of Projection Data. IEEE Trans. Med. Imaging 13, 601–609. doi:10.1109/42.363108
52. Hutton, B., Nuyts, J., Zaidi, H., 2006. Iterative Reconstruction Methods, in: Zaidi, H. (Ed.), Quantitative Analysis in Nuclear Medicine Imaging.
53. Hutton, B.F., Thomas, B.A., Erlandsson, K., Bousse, A., Reilhac-Laborde, A., Kazantsev, D., Pedemonte, S., Vunckx, K., Arridge, S.R., Ourselin, S., 2012. What approach to brain partial volume correction is best for PET/MRI? Nucl. Instruments Methods Phys. Res. Sect. A Accel. Spectrometers, Detect. Assoc. Equip. 702, 29–33. doi:10.1016/j.nima.2012.07.059
54. Innis, R.B., Cunningham, V.J., Delforge, J., Fujita, M., Gjedde, A., Gunn, R.N., Holden, J., Houle, S., Huang, S.-C., Ichise, M., Iida, H., Ito, H., Kimura, Y., Koeppe, R.A., Knudsen, G.M., Knuuti, J., Lammertsma, A.A., Laruelle, M., Logan, J., Maguire, R.P., Mintun, M.A., Morris, E.D., Parsey, R., Price, J.C., Slifstein, M., Sossi, V., Suhara, T., Votaw, J.R., Wong, D.F., Carson, R.E., 2007. Consensus Nomenclature for *in vivo* Imaging of Reversibly Binding Radioligands. J. Cereb. Blood Flow Metab. 27, 1533–1539. doi:10.1038/sj.jcbfm.9600493
55. Izquierdo-Garcia, D., Hansen, A.E., Forster, S., Benoit, D., Schachoff, S., Furst, S., Chen, K.T., Chonde, D.B., Catana, C., 2014. An SPM8-Based Approach for Attenuation Correction Combining Segmentation and Nonrigid Template Formation: Application to Simultaneous PET/MR Brain Imaging. J. Nucl. Med. 55, 1825–1830. doi:10.2967/jnumed.113.136341
56. Jaccard, P., 1901. Distribution de la flore alpine dans le Bassin des Dranses et dans quelques régions voisines. Bull. la Société Vaudoise des Sci. Nat. 37, 241–272.
57. Jiao, J., Bousse, A., Thielemans, K., Burgos, N., Weston, P., Markiewicz, P., Schott, J., D., A., Arridge, S., Hutton, B.F., Ourselin, S., 2016. Direct Parametric Reconstruction with Joint Motion Estimation/Correction for Dynamic Brain {PET} Data. IEEE Trans. Med. Imag. 36, 203–213. doi:10.1109/TMI.2016.2594150
58. Johansson, A., Karlsson, M., Nyholm, T., 2011. CT substitute derived from MRI sequences with ultrashort echo time. Med. Phys. 38, 2708–2714. doi:10.1118/1.3578928
59. Juttukonda, M.R., Mersereau, B.G., Chen, Y., Su, Y., Rubin, B.G., Benzinger, T.L.S., Lalush, D.S., An, H., 2015. MR-based attenuation correction for PET / MRI neurological studies with continuous-valued attenuation coef fi cients for bone through a conversion from R2 * to CT-Houns fi eld units. Neuroimage 112, 160–168. doi:10.1016/j.neuroimage.2015.03.009
60. Keereman, V., Fierens, Y., Broux, T., De Deene, Y., Lonneux, M., Vandenberghe, S., 2010. MRI-based attenuation correction for PET/MRI using ultrashort echo time sequences. J. Nucl. Med. 51, 812–818. doi:10.2967/jnumed.109.065425
61. Kinahan, P.E., Townsend, D.W., Beyer, T., Sashin, D., 1998. Attenuation correction for a combined 3D PET/CT scanner. Med. Phys. 25, 2046–2053. doi:10.1118/1.598392
62. Koesters, T., Friedman, K.P., Fenchel, M., Zhan, Y., Hermosillo, G., Babb, J., Jelescu, I.O., Faul, D., Boada, F.E., Shepherd, T.M., 2016. Dixon sequence with superimposed model-based bone compartment provides highly accurate PET/MR attenuation correction of the brain. JNM 8, 583–592. doi:10.1002/aur.1474.Replication
63. Ladefoged, C., Law, I., Anazodo, U., St Lawrence, K., Izquierdo-Garcia, D., Catana, C., Burgos, N., Cardoso, M.J., Ourselin, S., Hutton, B., Mérida, I., Costes, N., Hammers, A., Benoit, D., Holm, S., Juttukonda, M., An, H., Cabello, J., Lukas, M., Nekolla, S., Ziegler, S., Fenchel, M., Jakoby, B., Casey, M.E., Benzinger, T., Højgaard, L., Hansen, A.E., Andersen, F.L., 2016. A multi-centre evaluation of eleven clinically feasible brain PET/MRI attenuation correction techniques using a large cohort of patients. Neuroimage 147, 346–359. doi:10.1016/j.neuroimage.2016.12.010
64. Ladefoged, C.N., Benoit, D., Law, I., Holm, S., Kjaer, A., Hojgaard, L., Hansen, A.E., Andersen, F., 2015. Region specific optimization of continuous linear attenuation coefficients based on UTE (RESOLUTE): application to PET / MR brain imaging. Phys. Med. Biol. 60, 8047–8065. doi:10.1088/0031-9155/60/20/8047

65. Lammertsma, A.A., Hume, S.P., 1996. Simplified reference tissue model for PET receptor studies. Neuroimage 4, 153–8. doi:10.1006/nimg.1996.0066
66. Larsson, A., Johansson, A., Axelsson, J., Nyholm, T., Asklund, T., Riklund, K., Karlsson, M., 2013. Evaluation of an attenuation correction method for PET/MR imaging of the head based on substitute CT images. Magn. Reson. Mater. Physics, Biol. Med. 26, 127–136. doi:10.1007/s10334-012-0339-2
67. Le Pogam, A., Lamare, F., Hatt, M., Fernandez, P., Le Rest, C.C., Visvikis, D., 2013. MRI data driven partial volume effects correction in PET imaging using 3D local multi-resolution analysis. Nucl. Instruments Methods Phys. Res. Sect. A Accel. Spectrometers, Detect. Assoc. Equip. 702, 39–41. doi:10.1016/j.nima.2012.08.038
68. Malone, I.B., Ansorge, R.E., Williams, G.B., Nestor, P.J., Carpenter, T.A., Fryer, T.D., 2011. Attenuation correction methods suitable for brain imaging with a PET/MRI scanner: a comparison of tissue atlas and template attenuation map approaches. J. Nucl. Med. 52, 1142–1149. doi:10.2967/jnumed.110.085076
69. Manber, R., Thielemans, K., Hutton, B., Wan, M.Y.S., McClelland, J.R., Barnes, A., Arridge, S., Ourselin, S., Atkinson, D., 2016. Joint PET-MR respiratory motion models for clinical PET motion correction. Phys. Med. Biol. 61, 6515–6530. doi:10.1088/0031-9155/61/17/6515
70. Martinez-Möller, A., Souvatzoglou, M., Delso, G., Bundschuh, R. a, Chefd'hotel, C., Ziegler, S.I., Navab, N., Schwaiger, M., Nekolla, S.G., 2009. Tissue classification as a potential approach for attenuation correction in whole-body PET/MRI: evaluation with PET/CT data. J. Nucl. Med. 50, 520–526. doi:10.2967/jnumed.108.054726
71. McKee, B.T., Hiltz, L.G., 1994. Attenuation correction for three-dimensional PET using uncollimated flood-source transmission measurements. Phys. Med. Biol. 39, 2043–2058. doi:10.1088/0031-9155/39/11/015
72. Mehranian, A., Arabi, H., Zaidi, H., 2016. Vision 20/20: Magnetic resonance imaging-guided attenuation correction in PET/MRI: Challenges, solutions, and opportunities. Med. Phys. 43, 1130–1155. doi:10.1118/1.4941014
73. Mehranian, A., Zaidi, H., 2015. Joint estimation of activity and attenuation in whole-body TOF PET / MRI using constrained Gaussian mixture models. IEEE Trans. Med. Imaging 34, 1808–1821. doi:10.1109/TMI.2015.2409157
74. Merida, I., Costes, N., Heckemann, R.A., Drzezga, A., Förster, S., Hammers, A., 2015. Evaluation of several multi-atlas methods for pseudo-CT generation in brain MRI-PET attenuation correction, in: Biomedical Imaging (ISBI), 2015 IEEE 12th International Symposium on. pp. 1431–1434. doi:10.1109/ISBI.2015.7164145
75. Merida, I., Reilhac, A., Redouté, J., Heckemann, R.A., Costes, N., Hammers, A., 2017. Multi-atlas attenuation correction supports full quantification of static and dynamic brain PET data in PET-MR. Phys. Med. Biol. 62, 2834–2858. doi:doi.org/10.1088/1361-6560/aa5f6c
76. Modat, M., Ridgway, G.R., Taylor, Z. a., Lehmann, M., Barnes, J., Hawkes, D.J., Fox, N.C., Ourselin, S., 2010. Fast free-form deformation using graphics processing units. Comput. Methods Programs Biomed. 98, 278–284. doi:10.1016/j.cmpb.2009.09.002
77. Mollet, P., Keereman, V., Bini, J., Izquierdo-garcia, D., Fayad, Z.A., Vandenberghe, S., 2014. Improvement of attenuation correction in time-of-flight PET/MR imaging with a positron-emitting source. J. Nucl. Med. 55, 329–36. doi:10.2967/jnumed.113.125989
78. Montandon, M.L., Zaidi, H., 2005. Atlas-guided non-uniform attenuation correction in cerebral 3D PET imaging. Neuroimage 25, 278–286. doi:10.1016/j.neuroimage.2004.11.021
79. Mottolese, R., Redouté, J., Costes, N., Le Bars, D., Sirigu, A., 2014. Switching brain serotonin with oxytocin. Proc. Natl. Acad. Sci. U. S. A. 111, 8637–42. doi:10.1073/pnas.1319810111
80. Navalpakkam, B.K., Braun, H., Kuwert, T., Quick, H.H., 2013. Magnetic resonance-based attenuation correction for PET/MR hybrid imaging using continuous valued attenuation maps. Invest. Radiol. 48, 323–32. doi:10.1097/RLI.0b013e318283292f
81. Neuner, I., Mauler, J., Arrubla, J., Kops, E., Tellmann, L., Scheins, J., Herzog, H., Langen, K., Shah, J., 2015. Simultaneous trimodal MR-PET-EEG imaging for the investigation of resting state

networks in humans. EJNMMI Phys. 2, A71. doi:10.1186/2197-7364-2-S1-A71
82. Normandin, M.D., Schiffer, W.K., Morris, E.D., 2012. A linear model for estimation of neurotransmitter response profiles from dynamic PET data. Neuroimage 59, 2689–2699. doi:10.1016/j.neuroimage.2011.07.002
83. Nuyts, J., Dupont, P., Stroobants, S., Benninck, R., Mortelmans, L., Suetens, P., 1999. Simultaneous Maximum A Posteriori Reconstruction of Attenuation and Activity Distributions from Emission Sinograms. IEEE Trans. Med. Imaging 18, 393–403.
84. Nuyts, J., Matej, S., 2015. Image reconstruction, in: Nuclear Medicine Physics: A Handbook for Teachers and Students. IAEA.
85. Ourselin, S., Roche, A., Subsol, G., Pennec, X., Ayache, N., 2001. Reconstructing a 3D structure from serial histological sections. Image Vis. Comput. 19, 25–31. doi:10.1016/S0262-8856(00)00052-4
86. Parsey, R. V, Arango, V., Olvet, D.M., Oquendo, M. a, Van Heertum, R.L., John Mann, J., 2005. Regional heterogeneity of 5-HT1A receptors in human cerebellum as assessed by positron emission tomography. J. Cereb. Blood Flow Metab. 25, 785–793. doi:10.1038/sj.jcbfm.9600072
87. Paulus, D.H., Quick, H.H., Geppert, C., Fenchel, M., Zhan, Y., Hermosillo, G., Faul, D., Boada, F., Friedman, K.P., Koesters, T., 2015. Whole-Body PET/MR Imaging: Quantitative Evaluation of a Novel Model-Based MR Attenuation Correction Method Including Bone. J. Nucl. Med. 56, 1061–1066. doi:10.2967/jnumed.115.156000
88. Paulus, D.H., Tellmann, L., Quick, H.H., 2013. Towards improved hardware component attenuation correction in PET/MR hybrid imaging. Phys. Med. Biol. 58, 8021–40. doi:10.1088/0031-9155/58/22/8021
89. Pinborg, L.H., Ziebell, M., Frøkjaer, V.G., de Nijs, R., Svarer, C., Haugbøl, S., Yndgaard, S., Knudsen, G.M., 2005. Quantification of 123I-PE2I binding to dopamine transporter with SPECT after bolus and bolus/infusion. J. Nucl. Med. 46, 1119–27.
90. Pirotte, B., Goldman, S., Dewitte, O., Massager, N., Wikler, D., Lefranc, F., Ben Taib, N.O., Rorive, S., David, P., Brotchi, J., Levivier, M., 2006. Integrated positron emission tomography and magnetic resonance imaging-guided resection of brain tumors: a report of 103 consecutive procedures. J. Neurosurg. 104, 238–253.
91. Poynton, C.B., Chen, K.T., Chonde, D.B., Izquierdo-Garcia, D., Gollub, R.L., Gerstner, E.R., Batchelor, T.T., Catana, C., 2014. Probabilistic atlas-based segmentation of combined T1-weighted and DUTE MRI for calculation of head attenuation maps in integrated PET/MRI scanners. Am. J. Nucl. Med. Mol. Imaging 4, 160–71.
92. Reilhac, A., Lartizien, C., Costes, N., Sans, S., Comtat, C., Gunn, R.N., Evans, A.C., 2004. PET-SORTEO: A Monte Carlo-based simulator with high count rate capabilities. IEEE Trans. Nucl. Sci. 51, 46–52. doi:10.1109/TNS.2003.823011
93. Reilhac, A., Merida, I., Irace, Z., Stephenson, M.C., Chen, C., Totman, J.J., Townsend, D.W., Hayad, F., Costes, N., 2017. Development , validation and application of a rebinner with rigid motion correction for the mMR scanner, in: PSMR.
94. Reilhac, A., Soderlund, T., Thomas, B., Irace, Z., Mérida, I., Villien, M., Redouté, J., Costes, N., 2016. Validation and application of PET-SORTEO for the geometry of the Siemens mMR scanner, in: PSMR. pp. 1–2.
95. Rezaei, A., Defrise, M., Bal, G., Michel, C., Conti, M., Watson, C., 2012. Simultaneous Reconstruction of Activity and Attenuation in Time-of-Flight PET. IEEE Trans. Med. Imaging 31, 2224–2233.
96. Rogers, J.G., Harrop, R., Kinahan, P.E., 1987. The Theory of Three-Dimensional Image Reconstruction for PET. IEEE Trans. Med. Imaging 6, 239–243.
97. Rohlfing, T., Brandt, R., Menzel, R., Maurer, C.R., 2004. Evaluation of atlas selection strategies for atlas-based image segmentation with application to confocal microscopy images of bee brains. Neuroimage 21, 1428–1442. doi:10.1016/j.neuroimage.2003.11.010
98. Rousset, O., Rahmim, A., Alavi, A., Zaidi, H., 2007. Partial Volume Correction Strategies in PET. PET Clin. 2, 235–249. doi:10.1016/j.cpet.2007.10.005

99. Rousset, O.G., Ma, Y., Evans, A.C., 1998. Principle and Validation. J. Nucl. Med. 39.
100. Roy, S., Wang, W., Carass, A., Prince, J.L., Butman, J.A., Pham, D.L., 2014. PET Attenuation Correction Using Synthetic CT from Ultrashort Echo-Time MR Imaging. J. Nucl. Med. 2071–2078. doi:10.2967/jnumed.114.143958
101. Salomon, A., Goedicke, A., Schweizer, B., Aach, T., Member, S., Schulz, V., 2011. Simultaneous Reconstruction of Activity and Attenuation for PET / MR. IEEE Trans. Med. Imaging 30, 804–813.
102. Sander, C.Y., Hooker, J.M., Catana, C., Normandin, M.D., Alpert, N.M., Knudsen, G.M., Vanduffel, W., Rosen, B.R., Mandeville, J.B., 2013. Neurovascular coupling to D2/D3 dopamine receptor occupancy using simultaneous PET/functional MRI. Proc. Natl. Acad. Sci. U. S. A. 110, 11169–74. doi:10.1073/pnas.1220512110
103. Sander, C.Y., Hooker, J.M., Catana, C., Rosen, B.R., Mandeville, J.B., 2015. Imaging Agonist-Induced D2/D3 Receptor Desensitization and Internalization In Vivo with PET/fMRI. Neuropsychopharmacology 1–10. doi:10.1038/npp.2015.296
104. Sari, H., Erlandsson, K., Thielemans, K., Atkinson, D., Ourselin, S., Arridge, S., Hutton, B.F., 2015. Incorporation of MRI-AIF Information For Improved Kinetic Modelling of Dynamic PET Data. IEEE Trans. Nucl. Sci. 62, 612–618. doi:10.1109/TNS.2015.2426952
105. Savio, A., Fünger, S., Tahmasian, M., Rachakonda, S., Sorg, C., Grimmer, T., Calhoun, V., Drzezga, A., 2017. Resting state networks as simultaneously measured with fMRI and PET. doi:10.2967/jnumed.116.185835
106. Schreibmann, E., Nye, J. a, Schuster, D.M., Martin, D.R., Votaw, J., Fox, T., 2010. MR-based attenuation correction for hybrid PET-MR brain imaging systems using deformable image registration. Med. Phys. 37, 2101–2109. doi:10.1118/1.3377774
107. Schultz, C.C., Fusar-Poli, P., Wagner, G., Koch, K., Schachtzabel, C., Gruber, O., Sauer, H., Schlösser, R.G.M., 2012. Multimodal functional and structural imaging investigations in psychosis research. Eur. Arch. Psychiatry Clin. Neurosci. 262. doi:10.1007/s00406-012-0360-5
108. Sekine, T., Buck, A., Delso, G., Ter Voert, E.E.G.W., Huellner, M., Veit-Haibach, P., Warnock, G., 2015. Evaluation of Atlas-Based Attenuation Correction for Integrated PET/MR in Human Brain: Application of a Head Atlas and Comparison to True CT-Based Attenuation Correction. J. Nucl. Med. 57, 215–220. doi:10.2967/jnumed.115.159228
109. Sekine, T., Burgos, N., Warnock, G., Huellner, M., Buck, A., ter Voert, E.E.G.W., Cardoso, M.J., Hutton, B.F., Ourselin, S., Veit-Haibach, P., Delso, G., 2016. Multi-Atlas-Based Attenuation Correction for Brain 18F-FDG PET Imaging Using a Time-of-Flight PET/MR Scanner: Comparison with Clinical Single-Atlas- and CT-Based Attenuation Correction. J. Nucl. Med. 57, 1258–1264. doi:10.2967/jnumed.115.169045
110. Shah, N.J., Oros-Peusquens, A.M., Arrubla, J., Zhang, K., Warbrick, T., Mauler, J., Vahedipour, K., Romanzetti, S., Felder, J., Celik, A., Rota-Kops, E., Iida, H., Langen, K.J., Herzog, H., Neuner, I., 2012. Advances in multimodal neuroimaging: Hybrid MR-PET and MR-PET-EEG at 3 T and 9.4 T. J. Magn. Reson. 229, 101–115. doi:10.1016/j.jmr.2012.11.027
111. Sjölund, J., Forsberg, D., Andersson, M., Knutsson, H., 2015. Generating patient specific pseudo-CT of the head from MR using atlas-based regression. Phys. Med. Biol. 825, 825. doi:10.1088/0031-9155/60/2/825
112. Smith, S.M., Jenkinson, M., Woolrich, M.W., Beckmann, C.F., Behrens, T.E.J., Johansen-Berg, H., Bannister, P.R., De Luca, M., Drobnjak, I., Flitney, D.E., Niazy, R.K., Saunders, J., Vickers, J., Zhang, Y., De Stefano, N., Brady, J.M., Matthews, P.M., 2004. Advances in functional and structural MR image analysis and implementation as FSL. Neuroimage 23, S208-19. doi:10.1016/j.neuroimage.2004.07.051
113. Stegger, L., Martirosian, P., Schwenzer, N., Bisdas, S., Kolb, A., Pfannenberg, C., Claussen, C.D., Pichler, B., Schick, F., Boss, A., 2012. Simultaneous PET/MR imaging of the brain: feasibility of cerebral blood flow measurements with FAIR-TrueFISP arterial spin labeling MRI. Acta Radiol 53, 1066–1072. doi:10.1258/ar.2012.120191
114. Tahaei, M.S., Reader, A.J., 2016. Patch-based image reconstruction for PET using prior-image derived dictionaries. Phys. Med. Biol. 61, 6833–6855. doi:10.1088/0031-9155/61/18/6833

115. Thielemans, K., Asma, E., Manjeshwar, R.M., Ganin, A., Spinks, J.T., 2008. Image-based correction for mismatched attenuation in pet images. IEEE Nucl. Sci. Symp. Conf. Rec. 5292–5296. doi:10.1109/NSSMIC.2008.4774427
116. Tomasi, D., Wang, G., Volkow, N.D., 2013. Energetic cost of brain functional connectivity. doi:10.1073/pnas.1303346110/-/DCSupplemental.www.pnas.org/cgi/doi/10.1073/pnas.1303346110
117. Torrado-Carvajal, A., Herraiz, J.L., Hernandez-tamames, J.A., Jose-estepar, R.S., Eryaman, Y., Rozenholc, Y., Adalsteinsson, E., Wald, L.L., Malpica, N., 2015. Multi-Atlas and Label Fusion Approach for Patient-Specific MRI Based Skull Estimation. Magn. Reson. Med. 0, 1–11. doi:10.1002/mrm.25737
118. Tyler, D.J., Robson, M.D., Henkelman, R.M., Young, I.R., Bydder, G.M., 2007. Magnetic resonance imaging with ultrashort TE (UTE) PULSE sequences: Technical considerations. J. Magn. Reson. Imaging 25, 279–289. doi:10.1002/jmri.20851
119. Uppal, R., Catana, C., Ay, I., Benner, T., Sorensen, A.G., Caravan, P., 2011. Bimodal thrombus imaging: simultaneous PET/MR imaging with a fibrin-targeted dual PET/MR probe--feasibility study in rat model. Radiology 258, 812–820. doi:10.1148/radiol.10100881
120. Villien, M., Wey, H.-Y., Mandeville, J.B., Catana, C., Polimeni, J.R., Sander, C.Y., Zürcher, N.R., Chonde, D.B., Fowler, J.S., Rosen, B.R., Hooker, J.M., 2014. Dynamic functional imaging of brain glucose utilization using fPET-FDG. Neuroimage 100, 192–9. doi:10.1016/j.neuroimage.2014.06.025
121. Volkow, N.D., Wang, G.J., Fowler, J.S., Logan, J., Schlyer, D., Hitzemann, R., Lieberman, J., Angrist, B., Pappas, N., MacGregor, R., Burr, G., Cooper, T., Wolf, A.P., 1994. Imaging endogenous dopamine competition with [11C]raclopride in the human brain. Synapse 16, 255–262.
122. Werner, P., Barthel, H., Drzezga, A., Sabri, O., 2015. Current status and future role of brain PET/MRI in clinical and research settings. Eur. J. Nucl. Med. Mol. Imaging 42, 512–526. doi:10.1007/s00259-014-2970-9
123. Wey, H.Y., Catana, C., Hooker, J.M., Dougherty, D.D., Knudsen, G.M., Wang, D.J.J., Chonde, D.B., Rosen, B.R., Gollub, R.L., Kong, J., 2014. Simultaneous fMRI-PET of the opioidergic pain system in human brain. Neuroimage 102, 275–282. doi:10.1016/j.neuroimage.2014.07.058
124. Wiesinger, F., Sacolick, L.I., Menini, A., Kaushik, S.S., Ahn, S., Veit-Haibach, P., Delso, G., Shanbhag, D.D., 2016. Zero TE MR bone imaging in the head. Magn. Reson. Med. 75, 107–114. doi:10.1002/mrm.25545
125. Zaidi, H., Montandon, M.-L., Slosman, D.O., 2003. Magnetic resonance imaging-guided attenuation and scatter corrections in three-dimensional brain positron emission tomography. Med. Phys. 30, 937–948. doi:10.1118/1.1569270
126. Zald, D.H., Boileau, I., El-Dearedy, W., Gunn, R., McGlone, F., Dichter, G.S., Dagher, A., 2004. Dopamine Transmission in the Human Striatum during Monetary Reward Tasks. J. Neurosci. 24, 4105–4112. doi:10.1523/JNEUROSCI.4643-03.2004
127. Zubieta, J., Smith, Y., Bueller, J., Xu, Y., Kilbourn, M., Jewett, D., Meyer, C., Koeppe, R., Stohler, C., 2001. Regional mu opioid receptor regulation of sensory and affective dimensions of pain. Science (80-.). 293, 311–5. doi:10.1126/science.1060952